ARL-TR-9170 ● APR 2021

DEVCOM ARMY RESEARCH LABORATORY

Mid-Lift-to-Drag Ratio Rigid Vehicle Free-Flight Motion Characterization in Earth's Atmosphere

by T Gordon Brown and Thomas Harkins

Approved for public release; distribution is unlimited.

NOTICES

Disclaimers

The findings in this report are not to be construed as an official Department of the Army position unless so designated by other authorized documents.

Citation of manufacturer's or trade names does not constitute an official endorsement or approval of the use thereof.

Destroy this report when it is no longer needed. Do not return it to the originator.

ARL-TR-9170 ● APR 2021

Mid-Lift-to-Drag Ratio Rigid Vehicle Free-Flight Motion Characterization in Earth's Atmosphere

T Gordon Brown and Thomas Harkins
Weapons and Materials Research Directorate,
DEVCOM Army Research Laboratory

Approved for public release; distribution is unlimited.

REPORT DOCUMENTATION PAGE

Form Approved
OMB No. 0704-0188

Public reporting burden for this collection of information is estimated to average 1 hour per response, including the time for reviewing instructions, searching existing data sources, gathering and maintaining the data needed, and completing and reviewing the collection information. Send comments regarding this burden estimate or any other aspect of this collection of information, including suggestions for reducing the burden, to Department of Defense, Washington Headquarters Services, Directorate for Information Operations and Reports (0704-0188), 1215 Jefferson Davis Highway, Suite 1204, Arlington, VA 22202-4302. Respondents should be aware that notwithstanding any other provision of law, no person shall be subject to any penalty for failing to comply with a collection of information if it does not display a currently valid OMB control number.
PLEASE DO NOT RETURN YOUR FORM TO THE ABOVE ADDRESS.

1. REPORT DATE *(DD-MM-YYYY)*	2. REPORT TYPE	3. DATES COVERED (From - To)
April 2021	Technical Report	1 May 2018–31 January 2019

4. TITLE AND SUBTITLE
Mid-Lift-to-Drag Ratio Rigid Vehicle Free-Flight Motion Characterization in Earth's Atmosphere

5a. CONTRACT NUMBER

5b. GRANT NUMBER

5c. PROGRAM ELEMENT NUMBER

6. AUTHOR(S)
T Gordon Brown and Thomas Harkins

5d. PROJECT NUMBER
Interagency Agreement NNJ17ZA011

5e. TASK NUMBER

5f. WORK UNIT NUMBER

7. PERFORMING ORGANIZATION NAME(S) AND ADDRESS(ES)
DEVCOM Army Research Laboratory
ATTN: FCDD-RLW-WE
Aberdeen Proving Ground, MD 21005

8. PERFORMING ORGANIZATION REPORT NUMBER
ARL-TR-9170

9. SPONSORING/MONITORING AGENCY NAME(S) AND ADDRESS(ES)
NASA Johnson Space Center
2101 E NASA Parkway
Houston, TX 77058

10. SPONSOR/MONITOR'S ACRONYM(S)
JSC

11. SPONSOR/MONITOR'S REPORT NUMBER(S)

12. DISTRIBUTION/AVAILABILITY STATEMENT
Approved for public release; distribution is unlimited.

13. SUPPLEMENTARY NOTES

14. ABSTRACT
Flight experiments of gun-launched scale models of a conceptual airframe called the Co-Optimization Bluntbody Re-entry Analysis Mid-Lift-to-Drag (L/D) Rigid Vehicle (CobraMRV), being considered by NASA for future manned Mars missions, were conducted at the US Army Combat Capabilities Development Command in the fall of 2017. In-flight observations by test-range radars and high-speed video cameras were recorded and postprocessed to obtain CobraMRV state estimates useful for aerodynamic characterization of the CobraMRV shape. Because the image resolution of most of the recorded video was insufficient for automated computerized processing, manual processing was undertaken. Despite limited diagnostic fidelity, flight motion history observations appear suitable to enable characterization of aerodynamic damping. Methods employed and the CobraMRV state estimates obtained are detailed. Possible changes in procedures and additions to test-range equipment enabling improved accuracy of flight-body measurements are presented.

15. SUBJECT TERMS
human Mars mission airframe, flight experiments, pitching motion measurements, video image processing, Co-Optimization Bluntbody Re-entry Analysis Mid-Lift-to-Drag (L/D) Rigid Vehicle, CobraMRV

16. SECURITY CLASSIFICATION OF:			17. LIMITATION OF ABSTRACT	18. NUMBER OF PAGES	19a. NAME OF RESPONSIBLE PERSON
a. REPORT	b. ABSTRACT	c. THIS PAGE			Thomas Brown
Unclassified	Unclassified	Unclassified	UU	161	19b. TELEPHONE NUMBER (Include area code) (410) 306-0737

Standard Form 298 (Rev. 8/98)
Prescribed by ANSI Std. Z39.18

Contents

List of Figures v

List of Tables x

Acknowledgments xi

1. Introduction 1

2. Correlation of Data Sources 7

3. Estimation of CobraMRV Orientation from Video Images 8

3.1 Orientation Estimation from DB Camera Images 12

3.2 Orientation and Velocity Estimation from FC 1–5 Images 16

3.3 Orientation Estimation from DR Camera Images 19

3.4 Orientation Estimation from FF 1 Camera Images 20

4. Comparison with Previously Reported Pitch Estimates 32

5. Improving State Estimation Accuracy 39

5.1 Location and Orientation Estimation within an Individual Video Image 40

5.2 Location and Orientation Estimation of a Video Image in Gun Coordinates 42

6. Conclusions 42

7. References 44

Appendix A. Mechanical Design 45

Appendix B. Experimental Flight Log 54

Appendix C. Mechanical Fabrication 58

Appendix D. Physical Measurements **85**

Appendix E. Site Survey **91**

Appendix F. Results: Tube Round (TR) 40649 **93**

Appendix G. Results: Tube Round (TR) 40650 **100**

Appendix H. Results: Tube Round (TR) 40651 **107**

Appendix I. Results: Tube Round (TR) 40652 **114**

Appendix J. Results: Tube Round (TR) 40653 **121**

Appendix K. Results: Tube Round (TR) 40654 **128**

Appendix L. Results: Tube Round (TR) 40655 **135**

Appendix M. Results: Tube Round (TR) 40656 **142**

List of Symbols, Abbreviations, and Acronyms **147**

Distribution List **148**

List of Figures

Fig. 1 CobraMRV full-scale dimensions 1

Fig. 2 (left) Fabricated scale model of CobraMRV and (center and right) computer-aided design sabot package 2

Fig. 3 Test range instrumentation schematic 4

Fig. 4 Test-range photograph with fiducial stake and camera locations superimposed 6

Fig. 5 FC 2 video of TR 40654 passing Stake S2a 8

Fig. 6 CobraMRV orientation and yaw angles when the velocity vector is parallel to the shot line 10

Fig. 7 CobraMRV orientation and yaw angles, general case 10

Fig. 8 DB camera image of TR 40653 4 ms after tube exit 13

Fig. 9 CobraMRV orthogonal axis length in pixels in DB camera record of TR 40653 13

Fig. 10 Blow-up of DB camera image of TR 40653 at 4 ms 15

Fig. 11 TR 40653 axis orientation estimates in the gun coordinate system with corresponding pitch and yaw estimates from DB camera images 15

Fig. 12 FC 2 camera image of TR 40651, Frame 314 17

Fig. 13 FC 2 image of TR 40651 passing Stake S2a 18

Fig. 14 FC 2 image of TR 40654 passing Stake S2a 18

Fig. 15 Downrange speed vs. downrange distance CobraMRV TR 40651 19

Fig. 16 DR camera image of TR 40654, Frame 220 20

Fig. 17 Schematic of changing FF 1 image plane orientation while tracking CobraMRV in flight 21

Fig. 18 Image plane orientation with respect to shot line 22

Fig. 19 Errors in image plane orientation estimates 23

Fig. 20 FF 1 image taken 0.5 ms after launch of TR 40652 23

Fig. 21 FF 1 image taken 6.0 ms after launch of TR 40652 24

Fig. 22 Slant range to CobraMRV and CobraMRV length vs. time in FF 1 images of TR 40652 24

Fig. 23 FF 1 image taken 22.5 ms after launch of TR 40652 25

Fig. 24 FF 1 image taken 40.5 ms after launch of TR 40652 25

Fig. 25 FF 1 image taken 56.5 ms after launch of TR 40652 26

Fig. 26 FF 1 image taken 81.0 ms after launch of TR 40652 26

Fig. 27 FF 1 image taken 102.0 ms after launch of TR 40652 27

Fig. 28 Time history of estimated CobraMRV orientation for flight experiment TR 40652 28
Fig. 29 Time history of estimated CobraMRV AoA for flight experiment TR 40652..... 29
Fig. 30 CobraMRV elevation and pitch history for TR 40652 29
Fig. 31 CobraMRV azimuth and yaw history for TR 40652 30
Fig. 32 CobraMRV axis orientation history for TR 40652 31
Fig. 33 CobraMRV pitch, roll, and yaw for TR 40652 32
Fig. 34 Comparison of TR 40653 FF1 camera pitch vs. time estimates with model prediction 33
Fig. 35 Comparison of TR 40653 FF1 camera pitch vs. distance estimates with model prediction 34
Fig. 36 Comparison of TR 40653 FF 1 camera AoA vs. distance estimates with model prediction 35
Fig. 37 Pitch estimates at extrema and TR 40653 pitch history compared with Kestrel model prediction: (top) initial estimates vs. time and (bottom) revised estimates vs. downrange distance..... 36
Fig. 38 CobraMRV pitch vs. downrange distance from all processed images 37
Fig. 39 CobraMRV pitch vs. downrange distance before occurrence of significant roll 38
Fig. 40 CobraMRV axis orientation history before occurrence of significant roll for TR 40650 through TR 40655..... 39
Fig. 41 CobraMRV height vs. range for all eight flight experiments 40
Fig. A-1 Slug, simplified projectile, solid polyethylene cylindrical shape with obturator..... 47
Fig. A-2 Computer-aided design model of CobraMRV 48
Fig. A-3 Drawing 1 (overview) of MRV 1:200 scale at design physical characteristics..... 48
Fig. A-4 Drawing 2 (Ti body) of MRV 1:200 scale at design physical characteristics..... 49
Fig. A-5 Drawing 3 (Al lid) of MRV 1:200 scale at design physical characteristics..... 50
Fig. A-6 Transparent sabot package assembly 50
Fig. A-7 Sabot package (nonsymmetric): (left) orthogonal and (right) cutaway view..... 51
Fig. A-8 Mesh of sabot package (384.5e03 elements) 52
Fig. A-9 Sabot FEA: von Mises stress (exterior and interior)..... 52
Fig. A-10 Sabot FEA: factor of safety (interior) 53

Fig. C-1 CobraMRV 1:200 scale model as fabricated 59
Fig. D-1 MOI measurement table with MRV and fixture assembly (transverse)..... 87
Fig. D-2 MOI measurement table with MRV and fixture assembly (axial)..... 88
Fig. D-3 Optical comparitor measurement of MRV fixture location with reference to the pivot point 89
Fig. D-4 Typical quadratic fit of MOI and CG 90
Fig. F-1 Elevation angle vs. flight time in gun coordinates, TR 40649..... 94
Fig. F-2 Azimuth angle vs. flight time in gun coordinates, TR 40649..... 94
Fig. F-3 Pitch angle vs. flight time in gun coordinates, TR 40649..... 95
Fig. F-4 Yaw angle vs. flight time in gun coordinates, TR 40649 95
Fig. F-5 Angle of attack (AoA) vs. flight time in gun coordinates, TR 40649 96
Fig. F-6 Pitch angle vs. downrange distance in gun coordinates, TR 40649.... 96
Fig. F-7 Yaw angle vs. downrange distance in gun coordinates, TR 40649 97
Fig. F-8 AoA vs. downrange distance in gun coordinates, TR 40649..... 97
Fig. F-9 Pitch vs. yaw, TR 40649 98
Fig. F-10 Pitch, yaw, and roll angle estimates from Flight Follower 1 vs. flight time in gun coordinates, TR 40649..... 99
Fig. G-1 Elevation angle vs. flight time in gun coordinates, TR 40650..... 101
Fig. G-2 Azimuth angle vs. flight time in gun coordinates, TR 40650..... 101
Fig. G-3 Pitch angle vs. flight time in gun coordinates, TR 40650..... 102
Fig. G-4 Yaw angle vs. flight time in gun coordinates, TR 40650 102
Fig. G-5 Angle of attack (AoA) vs. flight time in gun coordinates, TR 40650..... 103
Fig. G-6 Pitch angle vs. downrange distance in gun coordinates, TR 40650.. 103
Fig. G-7 Yaw angle vs. downrange distance in gun coordinates, TR 40650 .. 104
Fig. G-8 AoA vs. downrange distance in gun coordinates, TR 40650..... 104
Fig. G-9 Pitch vs. yaw, TR 40650 105
Fig. G-10 CobraMRV speed from video and radar vs. downrange distance, TR 40650..... 106
Fig. H-1 Elevation angle vs. flight time in gun coordinates, TR 40651..... 108
Fig. H-2 Azimuth angle vs. flight time in gun coordinates, TR 40651..... 108
Fig. H-3 Pitch angle vs. flight time in gun coordinates, TR 40651..... 109
Fig. H-4 Yaw angle vs. flight time in gun coordinates, TR 40651 109
Fig. H-5 Angle of attack (AoA) vs. flight time in gun coordinates, TR 40651..... 110

Fig. H-6 Pitch angle vs. downrange distance in gun coordinates, TR 40651.. 110
Fig. H-7 Yaw angle vs. downrange distance in gun coordinates, TR 40651 .. 111
Fig. H-8 AoA vs. downrange distance in gun coordinates, TR 40651..... 111
Fig. H-9 Pitch vs. yaw, TR 40651 112
Fig. H-10 CobraMRV speed from video and radar vs. downrange distance, TR 40651 113
Fig. H-11 Pitch, yaw, and roll angle estimates from Flight Follower 1 vs. flight time in gun coordinates, TR 40651 113
Fig. I-1 Elevation angle vs. flight time in gun coordinates, TR 40652..... 115
Fig. I-2 Azimuth angle vs. flight time in gun coordinates, TR 40652..... 115
Fig. I-3 Pitch angle vs. flight time in gun coordinates, TR 40652..... 116
Fig. I-4 Yaw angle vs. flight time in gun coordinates, TR 40652 116
Fig. I-5 Angle of attack (AoA) vs. flight time in gun coordinates, TR 40652..... 117
Fig. I-6 Pitch angle vs. downrange distance in gun coordinates, TR 40652.. 117
Fig. I-7 Yaw angle vs. downrange distance in gun coordinates, TR 40652 .. 118
Fig. I-8 AoA vs. downrange distance in gun coordinates, TR 40652..... 118
Fig. I-9 Pitch vs. yaw, TR 40652 119
Fig. I-10 CobraMRV speed from video and radar vs. downrange distance, TR 40652..... 120
Fig. I-11 Pitch, yaw, and roll angle estimates from Flight Follower 1 vs. flight time in gun coordinates, TR 40652 120
Fig. J-1 Elevation angle vs. flight time in gun coordinates, TR 40653..... 122
Fig. J-2 Azimuth angle vs. flight time in gun coordinates, TR 40653 122
Fig. J-3 Pitch angle vs. flight time in gun coordinates, TR 40653..... 123
Fig. J-4 Yaw angle vs. flight time in gun coordinates, TR 40653 123
Fig. J-5 Angle of attack (AoA) vs. flight time in gun coordinates, TR 40653..... 124
Fig. J-6 Pitch angle vs. downrange distance in gun coordinates, TR 40653.. 124
Fig. J-7 Yaw angle vs. downrange distance in gun coordinates, TR 40653 .. 125
Fig. J-8 AoA vs. downrange distance in gun coordinates, TR 40653..... 125
Fig. J-9 Pitch vs. yaw, TR 40653 126
Fig. J-10 CobraMRV speed from video and radar vs. downrange distance, TR 40653..... 127
Fig. J-11 Pitch, yaw, and roll angle estimates from Flight Follower 1 vs. flight time in gun coordinates, TR 40653 127

Fig. K-1 Elevation angle vs. flight time in gun coordinates, TR 40654..... 129
Fig. K-2 Azimuth angle vs. flight time in gun coordinates, TR 40654..... 129
Fig. K-3 Pitch angle vs. flight time in gun coordinates, TR 40654..... 130
Fig. K-4 Yaw angle vs. flight time in gun coordinates, TR 40654 130
Fig. K-5 Angle of attack (AoA) vs. flight time in gun coordinates, TR 40654..... 131
Fig. K-6 Pitch angle vs. downrange distance in gun coordinates, TR 40654.. 131
Fig. K-7 Yaw angle vs. downrange distance in gun coordinates, TR 40654 .. 132
Fig. K-8 AoA vs. downrange distance in gun coordinates, TR 40654..... 132
Fig. K-9 Pitch vs. yaw, TR 40654 133
Fig. K-10 CobraMRV speed from video and radar vs. downrange distance, TR 40654..... 134
Fig. K-11 Pitch, yaw, and roll angle estimates from Flight Follower 1 vs. flight time in gun coordinates, TR 40654..... 134
Fig. L-1 Elevation angle vs. flight time in gun coordinates, TR 40655..... 136
Fig. L-2 Azimuth angle vs. flight time in gun coordinates, TR 40655..... 136
Fig. L-3 Pitch angle vs. flight time in gun coordinates, TR 40655..... 137
Fig. L-4 Yaw angle vs. flight time in gun coordinates, TR 40655 137
Fig. L-5 Angle of attack (AoA) vs. flight time in gun coordinates, TR 40655..... 138
Fig. L-6 Pitch angle vs. downrange distance in gun coordinates, TR 40655.. 138
Fig. L-7 Yaw angle vs. downrange distance in gun coordinates, TR 40655 .. 139
Fig. L-8 AoA vs. downrange distance in gun coordinates, TR 40655..... 139
Fig. L-9 Pitch vs. yaw, TR 40655 140
Fig. L-10 CobraMRV speed from video and radar vs. downrange distance, TR 40655..... 141
Fig. L-11 Pitch, yaw, and roll angle estimates from Flight Follower 1 vs. flight time in gun coordinates, TR 40655..... 141
Fig. M-1 Elevation angle vs. flight time in gun coordinates, TR 40656..... 143
Fig. M-2 Azimuth angle vs. flight time in gun coordinates, TR 40656..... 143
Fig. M-3 Pitch angle vs. flight time in gun coordinates, TR 40656..... 144
Fig. M-4 Yaw angle vs. flight time in gun coordinates, TR 40656 144
Fig. M-5 Pitch angle vs. downrange distance in gun coordinates, TR 40656.. 145
Fig. M-6 Yaw angle vs. downrange distance in gun coordinates, TR 40656 .. 145
Fig. M-7 CobraMRV speed from video and radar vs. downrange distance, TR 40656..... 146

List of Tables

Table 1 Test range camera specifications and locations 4
Table 2 Video data available for postflight analysis 5
Table 3 Fiducial stake locations 7
Table 4 Pixel resolution along CobraMRV axis in recorded videos 9
Table 5 CobraMRV azimuth with respect to image plane combinations 28
Table B-1 FE 1.1 Al MRV: sabot integrity 56
Table B-2 FE 1.2 Ti MRV: video characterization 57
Table E-1 Survey results 92

Acknowledgments

The authors thank Ron Sostaric from NASA Johnson for leadership, guidance, and sponsorship of this effort. The assembled team from NASA (Johnson and Ames) and the US Army Combat Capabilities Development Command Army Research Laboratory rose to the occasion to successfully demonstrate a rapid flight experiment focused on evaluating pitch damping of this nonsymmetric blunt body at supersonic high angle of attack. Breanna Johnson, Joseph Garcia, Ben Nikaido, and Javier Doll are recognized for contributions to the predictive aerodynamic behavior. The personnel at Transonic Experimental Facility (DEVCOM Army Research Laboratory) and Aberdeen Test Center are recognized for the efficient experimental conduct and support of complicated diagnostics, especially Eric Miller, Bill Aubry, Jared Kranz, Matt Krassenstein, and Martin Chidsey. Personnel at ARL and the DEVCOM Chemical and Biological Center (CBC) responsible for fabrication of the experimental hardware are also recognized for perseverance and diligence in meeting quality and schedule deadlines, especially Tom King and Rashad Scott. Ryan Decker is recognized for his contribution to the limited automated image analysis due to low resolution as well as his technical consultation. Ron Anderson, contractor for FSB, is thanked for his careful measurements leading to moments of inertia. Ryan Gilley of CBC is thanked for his careful measurement of the fabricated surfaces of the aluminum and titanium bodies for comparison to the model. Jim Garner is thanked for his leadership and guidance during project formulation and planning of the experiment at Transonic Experimental Facility.

1. Introduction

Entry, descent, and landing (EDL) technologies employed for previous unmanned Mars mission payloads such as the Mars Science Laboratory rover are not practicable for the much greater payloads and precision landing location requirements of future manned missions. A high-ballistic-number Mid-Lift-to-Drag Rigid Vehicle (MRV) concept initially designed using the Co-Optimization Bluntbody Re-entry Analysis (COBRA) shape optimization process (patent by Brown et al. 2014a) is the leading design for a manned flight vehicle capable of safe and successful EDL to the Mars surface. This shape, referred to as CobraMRV*, is shown in Fig. 1.

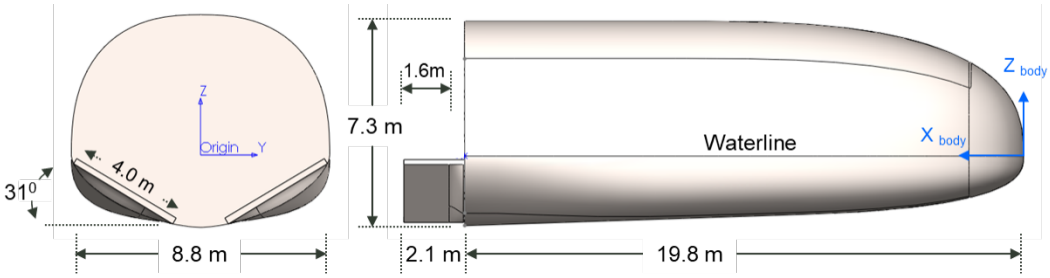

Fig. 1 CobraMRV full-scale dimensions

In May 2017, the NASA Lyndon B Johnson Space Center and the US Army Combat Capabilities Development Command Army Research Laboratory at Aberdeen Proving Ground (APG), Maryland, entered into an Interagency Agreement to support NASA's human Mars EDL work on Mid-Lift-to-Drag vehicle development research and trade studies. During September and November 2017, two series of cannon-launched flight experiments were conducted at APG with subscale CobraMRV models (Cerimele et al. 2017) with the goal of collecting data to aid understanding of the flight performance of the CobraMRV shape and to enable refinement and calibration of the computer models used to predict CobraMRV's flight behavior. Of primary interest was observation of CobraMRV pitching motion and damping characteristics. A four-petal sabot was designed to control the initial attitude of the CobraMRV at muzzle exit and to obturate the bore given the size and irregular shape of the flight body (Brown et al. 2018). To excite an aerodynamics response of the flight body in the pitch plane, the sabot was designed to have the projectile exit the tube with a pitch of 45°, no yaw, and no roll (Fig. 2).

* All subsequent references to these flight vehicles are shortened to CobraMRV.

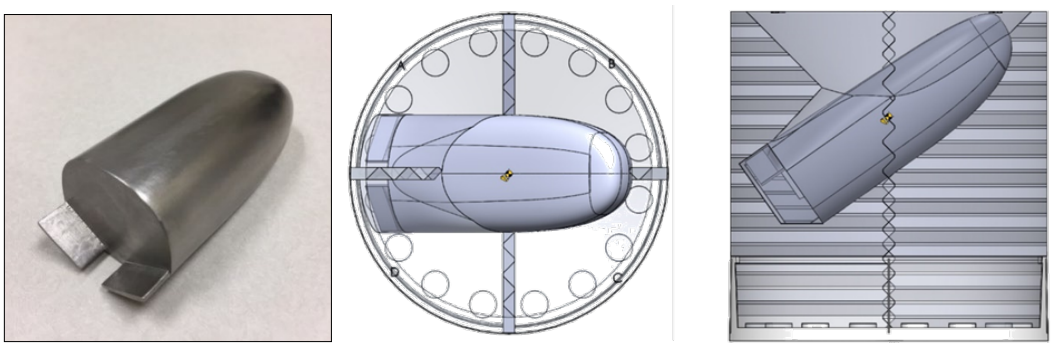

Fig. 2 (left) Fabricated scale model of CobraMRV and (center and right) computer-aided design sabot package

The initial series was conducted to provide propellant charge establishment and to demonstrate the structural integrity and proper sabot separation of this launch system using an early prototype CobraMRV-shaped aluminum (Al) payload. These firings were successfully completed on September 17, 2017. The free-flight motion of this payload was not measured.

The subsequent ballistic range experiment series was conducted to obtain free-flight motion characterization of the CobraMRV models. To this end, a 1:200 scale CobraMRV-shaped titanium flight body matching CobraMRV requirements of center of gravity, mass, and moments of inertia was designed and fabricated. In these flight experiments, the CobraMRV models were flat-fired from a 120-mm cannon at launch speeds of approximately Mach 3. Data recorded from ground-based range instrumentation including fixed and tracking Doppler radars, and fixed and tracking video cameras were used to estimate the models' position and attitude histories during free flight. This series consisted of firing eight units of the Ti CobraMRV scale model and took place during October 29 and November 2, 2017.

Mechanical designs of both the Al and Ti flight bodies as well as the sabot package are detailed in Appendix A. Experiment flight logs for firings of both the Al and Ti flight bodies are presented in Appendix B.

Initial postflight analysis efforts of some of the "best" recorded video yielded a limited number of discrete single-point, fixed-camera-derived pitch angle estimates from five of the flights and pitch-angle time histories from two of the flights. The matching of simulated flight data to this subset of the experimental measurements was described in earlier reports (Brown et al. 2018; Sostaric et al. 2019). Since that time, projectile position and attitude estimates have been completed via manual frame-by-frame analysis of all the usable recorded video from the eight flight experiments with the Ti flight bodies.

In this report, the test-range instrumentation setup is presented first to provide context for subsequent analysis of the collected data. Then, the position and attitude estimation methodologies used to extract measurements from the data are described and representative results shown. The complete set of estimates is presented graphically in the report appendixes. The corresponding numerical values of these estimates can be provided by the authors upon request.

While it is hoped that this larger dataset will support additional insights in understanding CobraMRV dynamics, it must be acknowledged that the accuracy of the attitude estimates presented herein are potentially adversely affected by various aspects of the range instrumentation and data acquisition systems. These are addressed when describing the video data estimation methodologies.

Sostaric et al. (2019) concluded with a statement that a flight experiment program employing CobraMRV models with onboard instrumentation could yield data from which a "full system identification approach to flight reconstruction could be achieved". Although a suitable onboard instrumentation and telemetry package had been demonstrated at DEVCOM Army Research Laboratory by Brown et al. (2014b), the added complexity and added expense of the sensor and telemetry systems were not pursued. Therefore, we conclude this report with a discussion of some modest modifications/additions to the test range that, while not expected to yield the quantity and quality of data possible with onboard systems, could enable appreciably improved accuracy of flight-vehicle state estimates over the results presented herein.

All eight CobraMRV test projectiles were fired at a quadrant elevation of 5.0 mil along a line of fire oriented 196.54° east of true north and terminating in a large sand pile approximately 250 m downrange. The same charge mass was used for all shots producing a spread of launch velocities from 1080.0 to 1144.7 m/s (μ = 1112.54 m/s, σ = 21.4 m/s). Seven fixed video cameras, two flight-follower video cameras with rotating-mirrors, a fixed head radar, and a tracking radar were employed at the test range to observe and record the test projectiles in flight.

The ballistic test range layout is shown schematically (not to scale) in Fig. 3. Two fixed cameras were positioned downrange on the line of fire beneath the flightpath, with one aimed back at the gun (downbore [DB] camera) to record the launch and sabot discard and the other aimed along the line of fire (downrange [DR] camera) to record the latter portion of the flight. Five fixed cameras (FCs) were positioned offset from and aimed perpendicular to the line of fire (designated FC 1–5). Two flight follower (FF) video cameras were positioned downrange from the gun and offset on either side of the line of fire (FF 1 and FF 2). Their fields of view (FOVs) were slewed during CobraMRV flight via rotating mirrors initially aimed at the

gun. When triggered by the muzzle exit detector, they began rotating at preset rates intended to keep the projectiles within the cameras' FOV as they progressed along their trajectories.

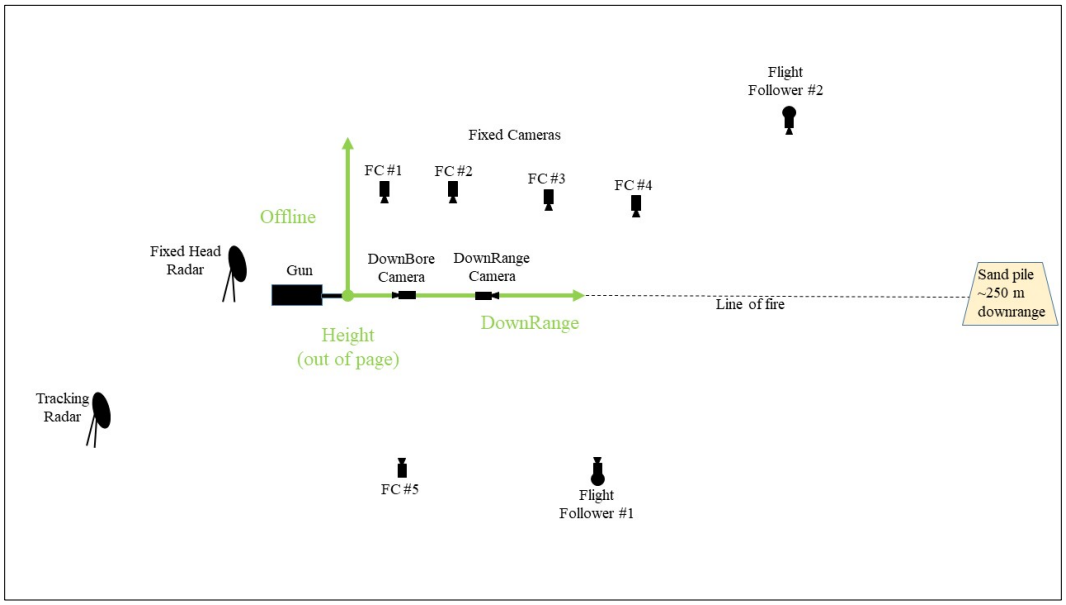

Fig. 3 Test range instrumentation schematic

The nine cameras comprised several different models, each with their own performance specifications. The characteristics most relevant to our analyses are given in Table 1. Also included in this table are the locations of the cameras relative to the gun muzzle (using range measurement convention as described by Murphy [1954]). The fixed-head radar was positioned 5.5 m behind and 3.1 m offline from the gun. The tracking radar was positioned 150.9 m behind and –37.6 m offline from the gun.

Table 1 Test range camera specifications and locations

Description	Fixed	Fixed	Fixed	Fixed	Fixed	Flight Follower	Flight Follower	Down Bore	Down Range
Designation	FC #1	FC #2	FC #3	FC #4	FC #5	FF #1	FF #2	DB	DR
Version	Phantom v7	Phantom v7.3	Phantom Miro M310	Phantom v7.3	Phantom v2511	Phantom v2511	Phantom v7.3	Phantom v7.3	Phantom v7.3
Pixels	800x600	800x600	1280x800	800x600	1280x512	1280x800	512x256	384x800	800x600
Rate (fps)	1000	6688	3200	6688	10000	10000	21052	10000	5000
Exposure (μs)	900.0	3.0	3.0	9.0	7.0	25.0	10.0	10.0	20.0
DownRange (m)	8.89	25.37	40.66	56.11	17.53	45.07	95.19	12.59	17.43
Offline (m)	12.56	12.09	11.63	7.06	-40.36	-37.27	50.11	-0.20	0.04
Height (m)	-1.03	-1.33	-1.59	-1.76	-1.36	-1.36	-1.68	-1.30	-1.31

CobraMRV position and attitude estimates were made using video recorded from the DB, DR, FC 1–4, and FF 1 cameras. Images from FC 5 were used to confirm successful launch and sabot discard. Images from FF 2 were not of sufficient quality to enable attitude estimation. As part of these manual analyses, CobraMRV velocity estimates when passing all five FC cameras were made from transit times of their respective FOVs. The radars were operated by Aberdeen Test Center (ATC) personnel who provided the authors with postprocessed position and velocity time histories from the tracking head radar. These times, positions, and velocities were assumed to be correct and were used as touchstones for interpretation of the video data.

All the video data sources from which position and/or attitude estimates were made for the eight flight experiments are shown in Table 2. The individual firings are designated by sequential tube round (TR) numbers per test-range naming protocol. Inter-firing adjustments were made to improve the video coverage as the test program progressed. Representative frames from each of these seven cameras are shown and discussed when the respective attitude estimation methodologies are described in Section 3.

Table 2 Video data available for postflight analysis

Tube Round	Attitude from FC #1	Attitude From FC #2	Attitude From FC #3	Attitude From FC #4	Attitude From DB	Attitude From DR	Attitude From FF #1
40649	N	N	N	N	N	N	Y
40650	Y	Y	N	N	N	Y	Y
40651	Y	Y	Y	Y	N	Y	Y
40652	Y	Y	Y	Y	N	Y	Y
40653	Y	Y	Y	Y	Y	Y	Y
40654	Y	Y	Y	Y	Y	Y	Y
40655	Y	Y	Y	Y	Y	Y	Y
40656	Y	Y	Y	Y	Y	Y	N

Figure 4 is an overhead photo of a portion of the test range extending from just behind the gun to approximately 90 m downrange. The shot line is indicated by the white line segment with tick marks at 10-m intervals. Red icons representing the seven FCs and FF 1 are superimposed on the picture at their respective locations. The two vectors attached to FC 1–5 indicate their respective approximate FOVs.

The black rectangles superimposed on the picture indicate the locations of six wooden stakes installed roughly parallel to the line of fire. These stakes served as fiducials within the FC 1–4 and FF 1 video images. Proceeding downrange, the stakes are designated as S1a, S1b, S2a, S2b, S3, and S4, where the numerals correspond to the FC within whose FOV they are located. The stakes were "2 × 4" boards (nominally 38 × 89 mm) attached to metal stands with clamps that accommodated plumb adjustments made using bubble levels. Their locations were measured initially with a laser rangefinder and are given in Table 3, where the dimensions are of the corner of the "2 × 4" nearest the gun. Inter-firing adjustments were made to restore plumb.

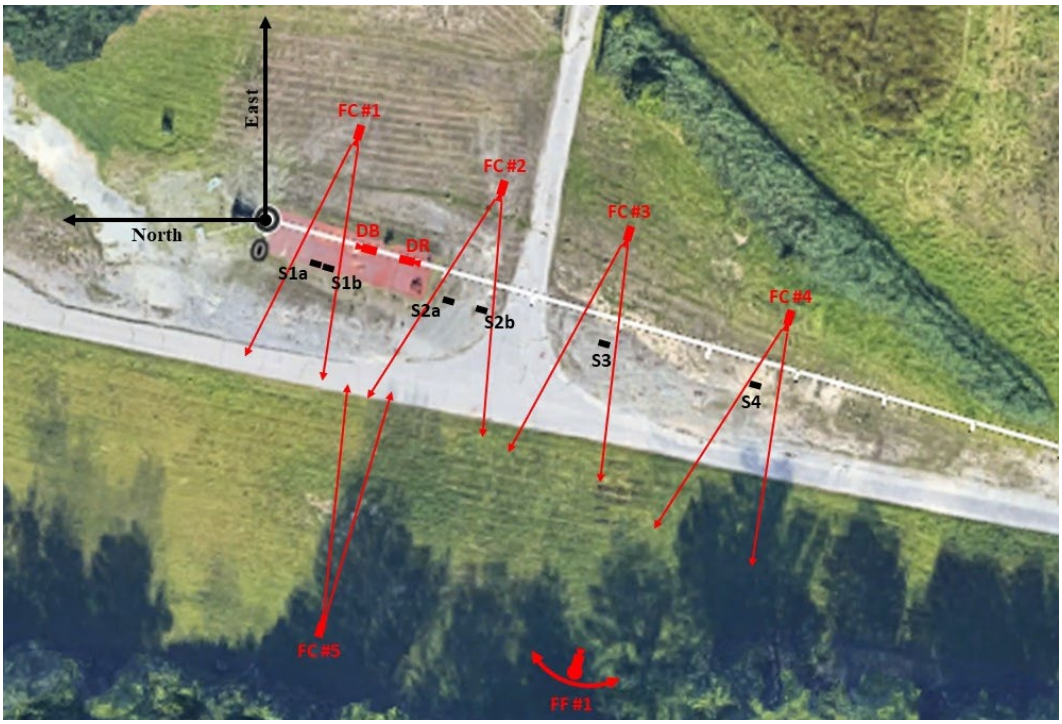

Fig. 4 Test-range photograph with fiducial stake and camera locations superimposed

Table 3 Fiducial stake locations

Designation	Down Range (m)	Offline (m)
S1a	8.0	-1.55
S1b	9.48	-1.34
S2a	22.93	-1.36
S2b	25.9	-1.59
S3	40.99	-1.4
S4	55.28	-1.4

2. Correlation of Data Sources

Correlation of the data from the tracking radar and FC 1–4, DB, DR, and FF 1 cameras was accomplished in one of two ways. Radar, DB, DR, and FF 1 data are time-correlated, as these recorders all employed the test-range inter-range group (IRIG) B time source. Because the FC 1–4 cameras used unsynchronized internal clocks to time stamp their recordings, their images were correlated to the radar data using estimated CobraMRV position data from the respective camera's recorded video.

Within each of the FC 1–4 video files, the individual frame in which the test projectile was nearest the line of sight (LOS) from the camera to a fiducial stake was found. For each of these images, the LOS from the camera position through the projectile midpoint was used to define a vertical plane located in the range coordinate system in which the projectile midpoint lay when the image was taken. The IRIG B time at which the projectile crossed this plane was computed by linear interpolation of the radar trajectory, providing a basis to synchronize the internal clocks of the FC cameras to the test range IRIG B time source. This procedure is illustrated by considering Fig. 5, which is a portion of Frame 313 from the FC 2 video record of TR 40654. In this frame, the CobraMRV (seen within the superimposed circle) is passing the right-hand edge of Fiducial Stake S2a as it traverses the FC 2 FOV from left to right. The LOS through the projectile midpoint is seen to intercept the fiducial stake at its downrange edge. As the stake location is given with respect to its up-range edge, the width of the stake gives the offset needed to define the downrange dimension of the intercept of the LOS in the plane containing the face of the stake. The vector from the FC 2 camera location (25.37,

12.09) to the downrange edge of Stake S2a (22.93 + 3.5/39.37, –1.36) defines the camera/projectile LOS vertical plane. The projectile location at the plane intercept is computed as (23.26, 0.016, 0.111) at postlaunch time of 22.92 ms. The time for Frame 313 was then set as 22.92 ms, and the times of the other frames in the FC 2 record for this flight were assigned using the FC 2 frame rate of 6688 fps.

Fig. 5 FC 2 video of TR 40654 passing Stake S2a

In most instances, the LOS through the projectile midpoint did not line up with a fiducial stake edge. The downrange location of the endpoint of the vector from the camera location to the plane containing the respective fiducial stake's face was given by scaling the offset of the projectile midpoint from the up-range edge using the stake width in that image (thus accounting for any foreshortening of the stake face due to non-orthogonality of the LOS).

3. Estimation of CobraMRV Orientation from Video Images

Immediately following the flight experiments, an attempt was made to obtain CobraMRV orientation measurements using the High-Fidelity Automated Launch Video Analysis methodology developed at the DEVCOM Armaments Center (AC), formerly Army Research, Development and Engineering Center, by Decker et al. (2013a, 2013b). This effort was largely unsuccessful because the projectile images did not have sufficient resolution to enable the automated shape extraction software to accurately identify the projectile orientation. Simulation analyses (Decker 2017)

had identified a minimum resolution requirement of approximately 100–125 pixels along the length of a nonrolled CobraMRV whose longitudinal (i.e., roll) axis is in the image plane to consistently achieve subdegree fidelity orientation measurements with the automated shape extraction software. Table 4 gives the estimated camera resolution in number of pixels along the CobraMRV longitudinal axis for the recorded video of each of the tube round/camera combinations for which orientation estimates were made. These resolution estimates were made from the numbers of pixels spanning objects of known sizes within the respective video files. There are two values for the DB, DR, and FF 1 cameras because their video records for each experiment include images with the CobraMRV at appreciably different distances from the cameras along the trajectories. The larger number of pixels in these entries correspond to the frame within the record with the projectile closest to the camera, and the smaller number corresponds to the greatest distance. With the single exception of the DB camera images, the resolutions of the recorded images ranged between 12% and 58% of Decker's minimum resolution requirement. Additionally, in many of the frames, the CobraMRV longitudinal axis was yawed with respect to the image plane and/or rolled with respect to the horizontal plane, thus potentially affecting automated orientation estimation accuracy even further.

Table 4 Pixel resolution along CobraMRV axis in recorded videos

Tube Round	Pixels Along Axis FC #1	Pixels Along Axis FC #2	Pixels Along Axis FC #3	Pixels Along Axis FC #4	Pixels Along Axis DB at range Min/Max	Pixels Along Axis DR at range Min/Max	Pixels Along Axis FF #1 at range Min/Max
40649	X	X	X	X	X	X	31/21
40650	20	21	X	X	X	52/33	30/21
40651	20	21	35	16	X	34/15	31/20
40652	20	22	46	16	X	39/14	31/20
40653	20	20	45	16	80/40	30/13	31/20
40654	20	20	46	17	68/41	52/12	30/16
40655	38	40	45	16	92/42	38/18	31/20
40656	39	42	58	17	88/42	40/18	X

In light of this, CobraMRV longitudinal axis orientations within the individual digital images were estimated by the authors manually by successively placing the cursor at our visual estimates of the fore and aft ends of that axis and recording the respective pixel locations within that image. The goals in undertaking the manual examination of the video records were to obtain CobraMRV orientation estimates

in the gun coordinate system seen in Fig. 3 and the corresponding pitch and yaw components of the projectile axis' angle of attack. The video images did not provide any objective quantitative means of estimating CobraMRV roll orientation.

Within the literature, different disciplines and even different authors sometimes use the terms pitch, yaw, and angle of attack to describe different angles and/or use different terms for the angles whose estimates we are reporting. Herein, these terms and angles are defined per Figs. 6 and 7.

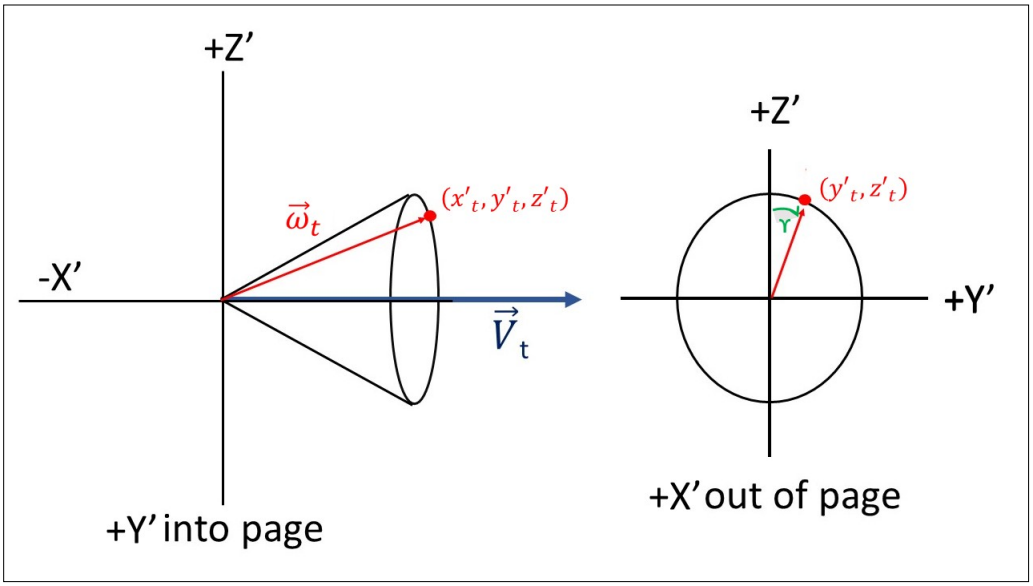

Fig. 6 CobraMRV orientation and yaw angles when the velocity vector is parallel to the shot line

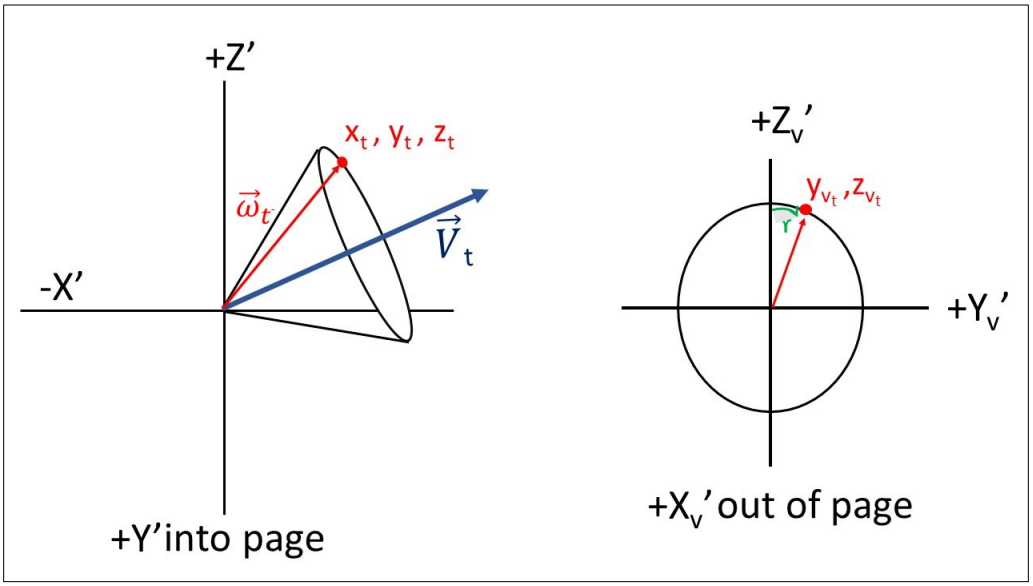

Fig. 7 CobraMRV orientation and yaw angles, general case

The (X', Y', Z') coordinate system in Fig. 6 is parallel to the gun coordinate system with its origin translated to the aft end of the CobraMRV longitudinal axis represented by the red vector $(\vec{\omega}_t)$. The forward end of the CobraMRV axis is located at (x'_t, y'_t, z'_t). The orientation of the CobraMRV axis in the gun coordinate system is given by two angles describing the projections of the CobraMRV axis onto the X', Z' vertical plane and the X', Y' horizontal plane. First, the elevation angle (θ_t) is computed as $\theta_t = \tan^{-1}\left({z'_t}/{x'_t}\right)$. Next, the azimuth angle (φ_t) is computed as $\varphi_t = \tan^{-1}\left({y'_t}/{x'_t}\right)$.

The magnitude of the angle between the CobraMRV longitudinal axis and the velocity vector $(\vec{V}_t)$ gives the angle of attack (AoA). After interpolating the velocity vector at the image time from the radar data, the AoA can be computed from the dot product formula: $\vec{\omega}_t \circ \vec{V}_t = |\vec{\omega}_t||\vec{V}_t| \cos(AoA)$. In the simple case portrayed in Fig. 6, where the velocity vector is parallel to the shot line, the AoA can alternatively be computed by $AoA = \tan^{-1}\left(\sqrt{\left(y'^2_t + z'^2_t\right)}\Big/ x'_t\right)$. This formulation conveys the useful visualization heuristic of the instantaneous AoA defining a cone about the velocity vector upon whose surface the CobraMRV's longitudinal axis lies. The height of the cone is x'_t, and the radius of the base is $\sqrt{\left(y'^2_t + z'^2_t\right)}$.

Computation of the pitch and yaw components of the AoA is illustrated in the right-hand portion of Fig. 6 that gives the view antiparallel to the velocity vector (i.e., looking back at the base of the cone from downrange of the CobraMRV location). Pitch (τ) is the component of AoA in the vertical plane containing $\vec{V}_t$ computed as $\tau_t = AoA\cos(\gamma) = AoA\left(\frac{z'_t}{\sqrt{(y'^2_t + z'^2_t)}}\right)$. Yaw (ρ) is the component in the plane containing $\vec{V}_t$ perpendicular to the vertical plane just described and is computed as $\rho_t = AoA\sin(\gamma) = AoA\left(\frac{y'_t}{\sqrt{(y'^2_t + z'^2_t)}}\right)$.

For most of the CobraMRV video images, $\vec{V}_t$ was not parallel to the shot line, and the geometry of Fig. 7 applies where the X',Y',Z' coordinate system, $(\vec{\omega}_t)$, and (x'_t, y'_t, z'_t) are defined as in Fig. 6. The CobraMRV elevation (θ_t) and azimuth (φ_t) in the gun coordinate system are computed as before.

The AoA is then computed from the dot product formula. The CobraMRV axis vector is transformed to the X_v', Y_v', Z_v' coordinate system, where $\vec{V}_t$ lies on the

$+X_v{}'$ axis, the $X_v{}', Z_v{}'$ plane is vertical and the $Y_v{}'$ axis completes the orthogonal triad. The pitch and yaw components are computed as before, mutatis mutandis.

The steps employed to transform the CobraMRV axis endpoints pixel locations in an image to (x'_t, y'_t, z'_t) coordinates differed depending on the source camera. Because exact camera aiming, lens characteristics, and pixel subtense data were not available for any of the image files, various assumptions and estimates were made to enable orientation estimate computations. Pixels were assumed to be square in every image as is typically the case for modern digital imagers and as verified by the observed pixel extent of objects of known dimensions.

3.1 Orientation Estimation from DB Camera Images

Pixels on the CobraMRV bodies in the DB camera images were assumed to be in planes parallel to the plane defined by the offline and height axes of the gun coordinate system (Fig. 3) with the CobraMRV CG in the downrange/height axes plane. Figure 8 is the DB camera image of TR 40653 taken 4 ms after tube exit. At this time, the CobraMRV is approximately 4.5 m downrange and sabot separation is completed. As previously noted, the sabot was designed to have the projectile exit the tube with a pitch of 45°, no yaw, and no roll. Visual examination of the downbore camera images yielded no evidence of any measurable roll in this early postlaunch interval. The first step in obtaining orientation estimates for the DB camera images was to estimate the pixel subtense (i.e., its angular width). This was done by counting the number of pixels across the midbody horizontal span of the CobraMRV, as indicated by the red brackets superimposed on Fig. 8. In this region the CobraMRV is 44.1 mm wide. Combining this width, the number of pixels, and the distance from the DB camera to the CobraMRV, the pixel subtense was estimated. The LOS distance at each of the processed image time steps in that video record was combined with the pixel subtense to compute the length (λ_t) of the CobraMRV in pixels at those times (Fig. 9).

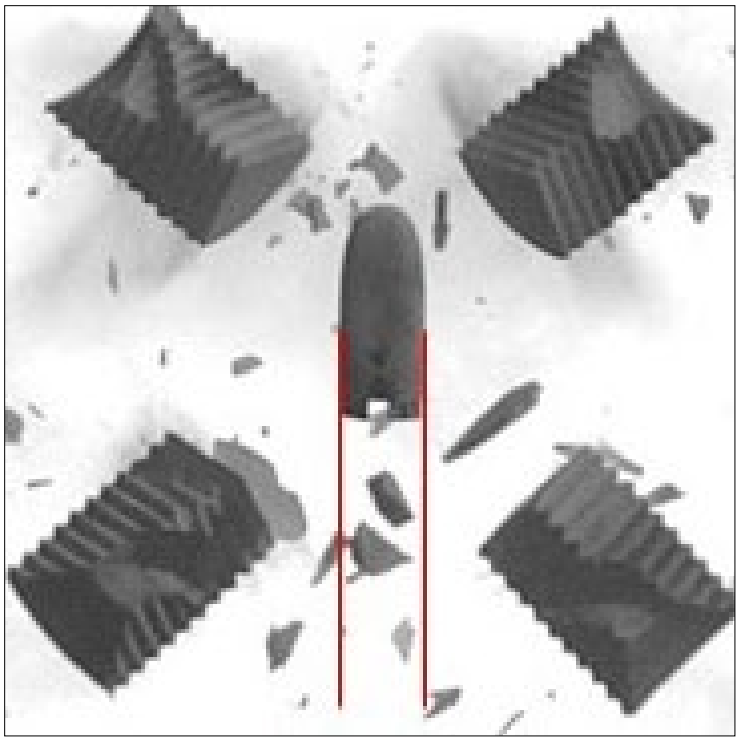

Fig. 8 DB camera image of TR 40653 4 ms after tube exit

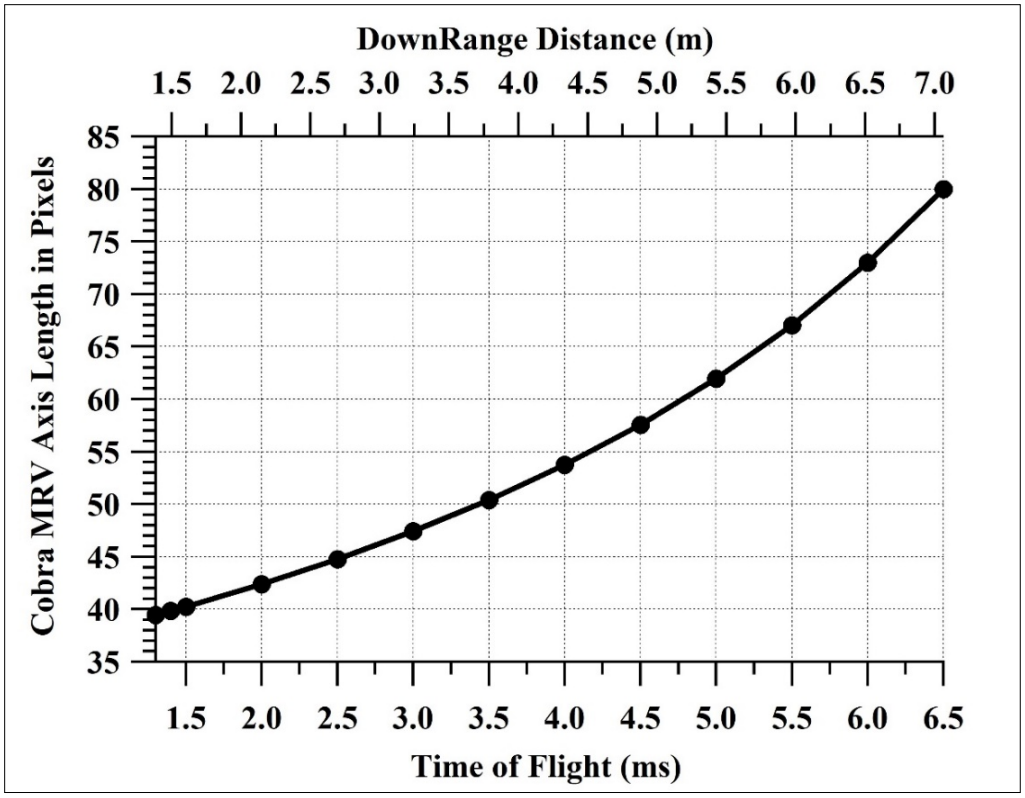

Fig. 9 CobraMRV orthogonal axis length in pixels in DB camera record of TR 40653

Figure 10 is a blow-up of the previous DB camera image with the visual estimates of the pixels at the fore (X) and aft (+) ends of the CobraMRV longitudinal axis indicated. Differencing these two locations gave the vertical (V_t: positive up) and horizontal (H_t: positive right) spans in pixels of the CobraMRV axis' projection onto the image plane at that time. Given the assumed orientation of the DB camera image plane, the height and cross-range locations of the forward end of the CobraMRV longitudinal axis are given by scaling the vertical and horizontal spans [i.e., $z'_t = (V_t/\lambda_t) * 99.96mm$ and $y'_t = (H_t/\lambda_t) * 99.96mm$, where 99.96 mm is the length of the CobraMRV longitudinal axis]. The downrange component of the axis location is then given by $x'_t = \sqrt{99.96^2 - (y'^2_t + z'^2_t)}$. The elevation and azimuth angles of the CobraMRV in the gun coordinate system are computed as $\theta_t = \tan^{-1}\left(z'_t / x'_t\right)$ and $\varphi_t = \tan^{-1}\left(y'_t / x'_t\right)$.

The first observational data points in all of the raw radar data files were from locations tens of meters downrange of the gun. Thus, all the processed location and velocity data in the intervals of the DB camera images were estimates based on polynomial fits through the subsequent radar observations. Using these velocity vector data, the CobraMRV longitudinal axis' AoA, pitch, and yaw estimates were computed as described in Fig. 7 and seen in Fig. 11. Also shown are the estimated elevation and azimuth components of the CobraMRV's orientation vector. Because the gun quadrant elevation is only 5 mil, the velocity vector of the CobraMRV is nearly along the gun coordinate system downrange axis throughout the interval covered by the DB camera. Hence, the pitch and elevation differ only slightly and are indistinguishable on the scale of the plot in Fig. 11. The available DB camera images for other flight experiments were processed in the same way.

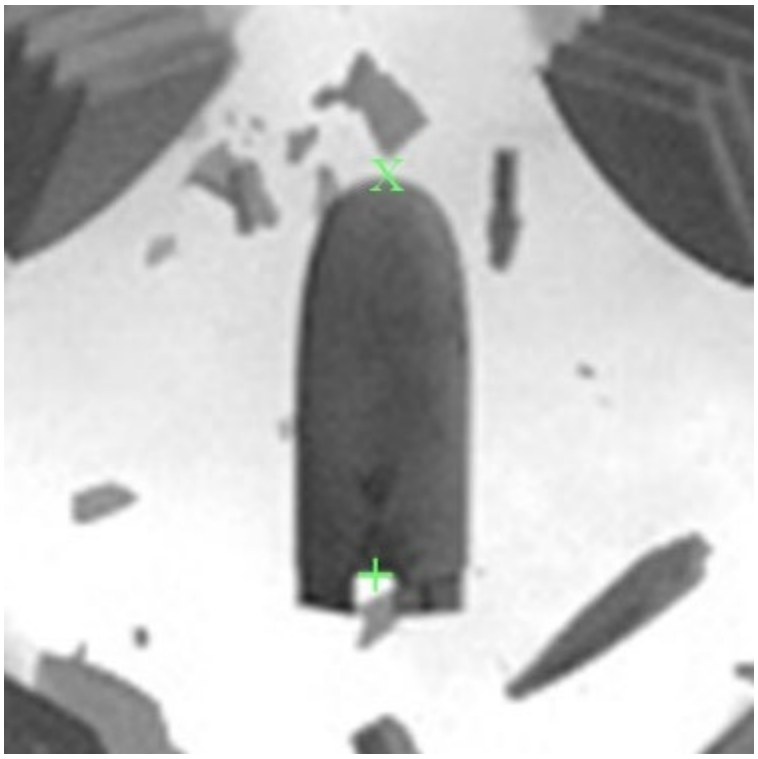

Fig. 10 Blow-up of DB camera image of TR 40653 at 4 ms

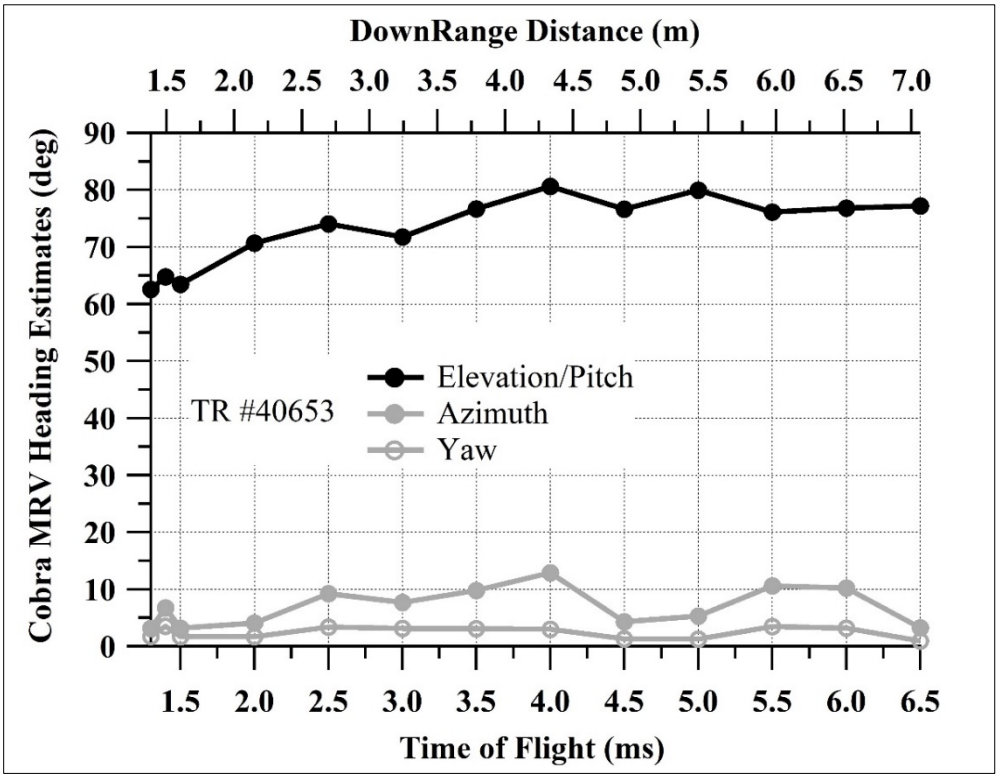

Fig. 11 TR 40653 axis orientation estimates in the gun coordinate system with corresponding pitch and yaw estimates from DB camera images

3.2 Orientation and Velocity Estimation from FC 1–5 Images

Images from the FC 1–4 fixed camera records were used to estimate CobraMRV elevation as it passed the respective fiducial stakes, and images from FC 1–5 were used to estimate the downrange speed as they passed the respective cameras. Pixels on the CobraMRV in these FC images were assumed to be in planes parallel to the plane defined by the downrange and height axes of the gun coordinate system.

Figure 12 is Frame 314 of the FC 2 camera images of TR 40651. The CobraMRV is seen within the superimposed circle. It first enters the FC 2 FOV at the left edge of Frame 310 of the recorded video and exits at the right edge after Frame 336. Pixel subtense of the FC 2 camera for this experiment was estimated from the number of pixels between the fiducial stakes (S2a and S2b) in the image, the length of the corresponding line segment between the stake locations, and the distance from the camera to the midpoint of that line segment. The pixel spatial resolution in meters per pixel along the shot line was scaled by the ratio of the distances from the camera to the shot line and from the camera to the line segment midpoint.[*] CobraMRV longitudinal axis length in pixels was then given by dividing the axis length (99.96 mm) by the pixel spatial resolution. This "calibration" was used for the subsequent elevation angle and speed estimates made from FC 2 images. Calibrations for the other FC cameras were made analogously based on elements within the images at known locations with known dimensions.

[*] In reality, the spatial extent of pixels along the shot line is not constant, but given the camera and fiducial location and orientation uncertainties and the relatively narrow FC cameras' FOV, this admittedly "crude" estimate was applied. As will be argued in Section 4, the presence of multiple, accurate fiducials in an image would enable more-accurate estimation techniques.

Fig. 12 FC 2 camera image of TR 40651, Frame 314

Elevation angle estimates were made for all available FC camera images in which the CobraMRVs are passing the fiducial stakes. Figure 13 is a blow-up of a portion of Frame 315 of the FC 2 video of TR 40651. At this time, the CobraMRV is along the LOS from FC 2 to the downrange edge of Stake S2a. As was done with the DB camera images, the pixels at the fore (X) and aft (+) ends of the CobraMRV axis were manually estimated, and the vertical and horizontal spans of the projection of that axis onto the image plane were computed. With the assumed orientations of the FC image planes being parallel to the shot line, the height and downrange locations of the forward end of the CobraMRV longitudinal axis are given by scaling the vertical and horizontal spans (i.e., $z'_t = (V_t/\lambda_t) * 99.96mm$ and $x'_t = (H_t/\lambda_t) * 99.96mm$). The magnitude of the cross-range component of the axis location is then given by $y'_t = \sqrt{99.96^2 - \left(x'^2_t + z'^2_t\right)}$. The polarity of y'_t is determined by inspection of the image (if apparent), continuity with the temporal sequence of the other images in the respective FC camera's record, and/or the polarity of H_t in the corresponding DR camera image when available. The elevation and azimuth angles of the CobraMRV in the gun coordinate system are then computed as before.

At the instant recorded in Fig. 13 when TR 40651 was passing the downrange edge of Stake S2a, H_t is positive, the CobraMRV was flying "pointy end forward", and

the elevation angle in the gun coordinate system was estimated as –58°. Figure 14 is a blow-up of a portion of Frame 313 of the FC 2 video of TR 40654 showing that CobraMRV at the same downrange distance. In this case, the horizontal span was negative and the elevation angle was estimated as –110°.

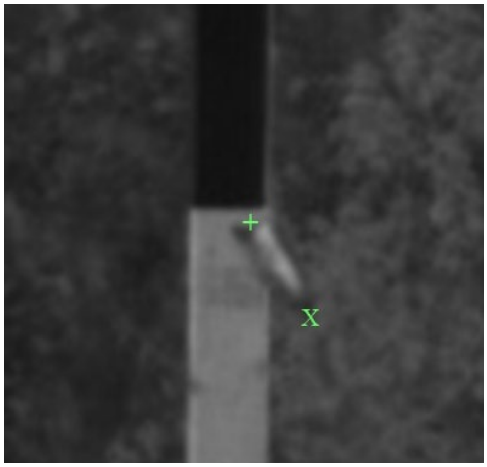

Fig. 13 FC 2 image of TR 40651 passing Stake S2a

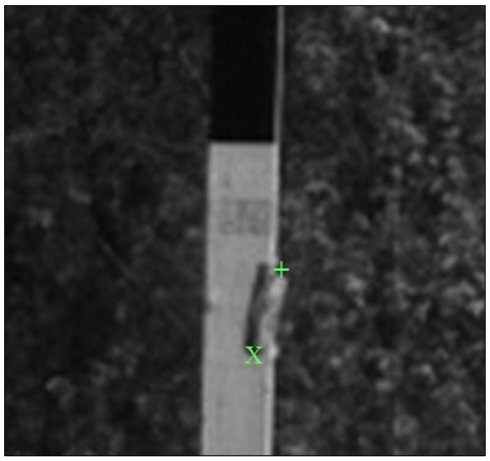

Fig. 14 FC 2 image of TR 40654 passing Stake S2a

CobraMRV speed when passing each of the FC cameras was estimated from the downrange distance along the trajectory within the respective camera FOV and the corresponding transit time. Distances were computed as the product of the estimated pixel size in meters per pixel along the shot line and the number of horizontal pixels in the image. Transit times were computed as the product of the number of frames in which the CobraMRV was visible and the camera frame rate. Figure 15 shows a comparison of the FC-camera-derived speed estimates for TR 40651 and the downrange speed given by the tracking radar for the first 70 m of travel. The camera-derived estimates are all within 3% of the corresponding radar values.

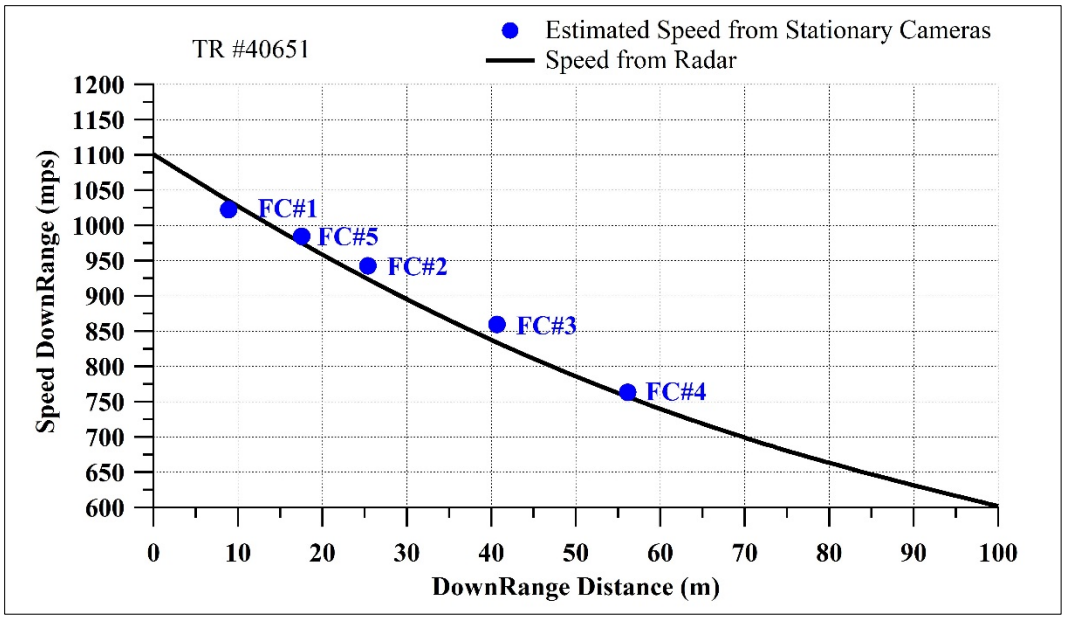

Fig. 15 Downrange speed vs. downrange distance CobraMRV TR 40651

3.3 Orientation Estimation from DR Camera Images

Figure 16 is the DR camera image of TR 40654 taken 44 ms after tube exit. At this time, the CobraMRV is approximately 44.3 m downrange and flying with considerable pitch and yaw. Pixel subtense was estimated from dimensions of Fiducial Stake S4 visible on the right hand side of the image. With the assumptions CobraMRV CG swerve was negligible and that pixels on the CobraMRV bodies in the DR camera images were in vertical planes perpendicular to the shot line,* axis orientation estimates were made in the same way as the estimates from the DB camera images after the horizontal span polarity was reversed (i.e., the azimuth component is positive when the forward end of the CobraMRV is to the left of its aft end in the DR image).

* When the DR camera videos are played, the CobraMRVs all have obvious left/right movement of various magnitudes, but lacking precise values of camera location, aiming, and image parameters, the stated assumptions were made to enable orientation estimates. The quantitative accuracy of the angular estimates is not known.

Fig. 16 DR camera image of TR 40654, Frame 220

Elevation and azimuth angles sometimes cannot be distinguished from their supplementary angles in individual DR camera images due to image quality. Using the vertical span measured for the image in Fig. 16, the angle between the CobraMRV axis and the horizontal plane was estimated by $\varepsilon_t = atan\left(\frac{V_t}{\lambda_t}\right)$ as approximately 65°, but whether the CobraMRVs tip is inclined toward or away from the camera cannot be discriminated. This type of difficulty was resolved either by maintaining continuity when a temporal sequence of images that included some non-ambiguous images was available or by examining the corresponding FF 1 image.

3.4 Orientation Estimation from FF 1 Camera Images

As was done with the preceding cameras, pixel subtense for the FF 1 images was estimated from frames in each video record that included objects of known dimensions at known locations. CobraMRV orientation estimates made using FF 1 images required additional computations because the image plane orientation was different for each frame in the video record of a flight experiment.

Beginning when the muzzle flash indicative of CobraMRV/sabot tube exit was detected, the FF 1 camera FOV was continuously slewed to track the CobraMRV in flight. Thus, the orientation of the locus of each of the sequential images recorded by the FF 1 camera is different. This is illustrated in Fig. 17 for two orientations.

The conventions for defining locus orientation (angles β_1 and β_3) are those used by the ATC personnel operating the FF cameras. For the FF 1 camera positioned 37.27 m to the right of the shot line and 45.07 m downrange of the gun, the camera orientation is defined as the angle between the image locus and the vector from FF 1 perpendicular to the shot line. In early flight (e.g., β_1) this angle is negative and in later flight (e.g., β_3) this angle is positive. The image plane containing the pixels on the CobraMRV body for each frame time is then defined as the vertical plane perpendicular to the locus at that time. As can be seen in Fig. 17, the angle between the image plane and the shot line is equal to the camera orientation angle (i.e., $\beta_2 = \beta_1$ and $\beta_4 = \beta_3$).

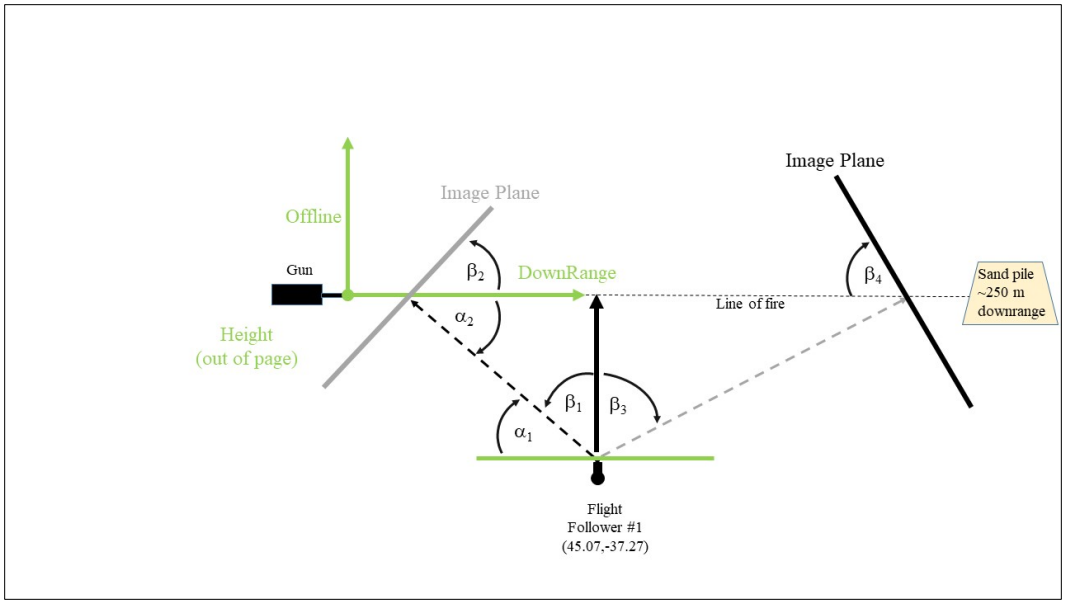

Fig. 17 Schematic of changing FF 1 image plane orientation while tracking CobraMRV in flight

As a time history of the FF 1 camera locus orientation was only available for the TR 40653 flight experiment, FF 1 image plane orientation estimates had to be made for the other seven flight experiments. Our first thought was to use the LOS from the camera to the CobraMRV as an estimate of the camera locus orientation. If the CobraMRV were always located at the horizontal midpoint in the temporal sequence of inflight recorded images, the camera orientation angle would equal the LOS angle from the camera location to the CobraMRV position. But this was not the case for any of eight FF 1 video records. The LOS angle history of TR 40653 was computed using the radar-derived CobraMRV positions. Figure 18 gives the image plane orientation histories obtained from the measured mirror orientations and the corresponding CobraMRV LOS angles.

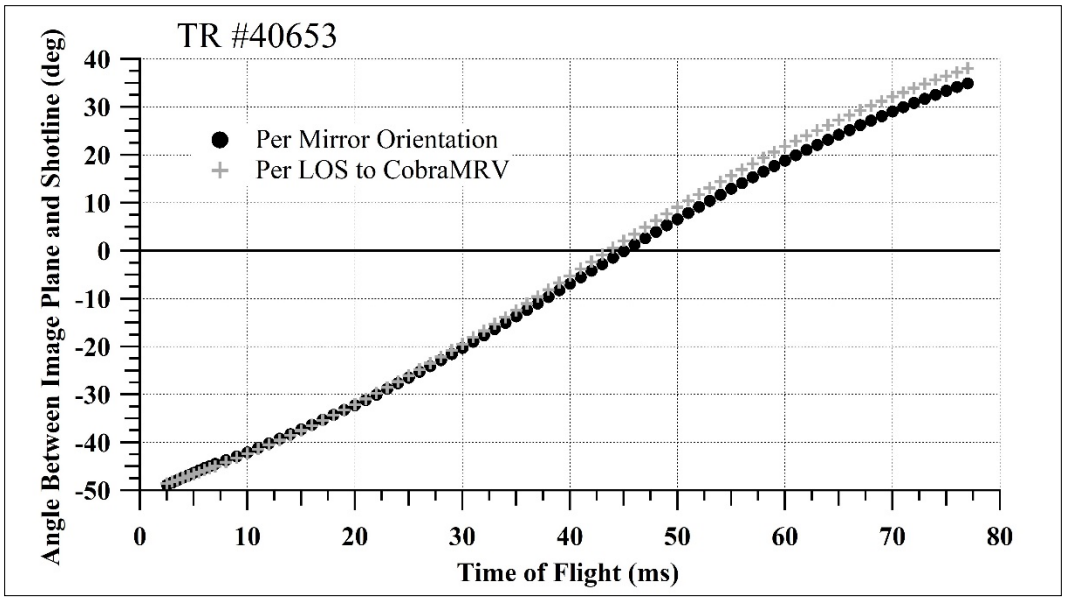

Fig. 18 Image plane orientation with respect to shot line

Assuming the mirror orientation history to be accurate, the error in image plane orientation estimates based on the CobraMRV LOS angles is plotted as the gray crosses in Fig. 19. The magnitude of this error generally increases with the mirror-based orientation lagging the LOS based orientation.* After making visual estimates of the pixels at the longitudinal axis endpoints in each image, the mean of the pixels' horizontal components was computed and differenced from the pixel column number at the image midpoint. Multiplying this offset value by the pixel subtense and adding that product to the LOS-based orientation, a "corrected" LOS-based orientation history was computed. The black curve in Fig. 19 gives the error when this corrected history was differenced from the mirror orientation history of TR 40653. This result encouraged the belief both that the radar and FF 1 time bases were synced and that the pixel subtense estimation methodology was reasonably accurate. Image plane orientations were estimated for the other seven flight experiments via this corrected LOS technique.

* This trend is confirmed in the TR 40653 video record by the CobraMRV outrunning the camera FOV at approximately 80 ms time of flight.

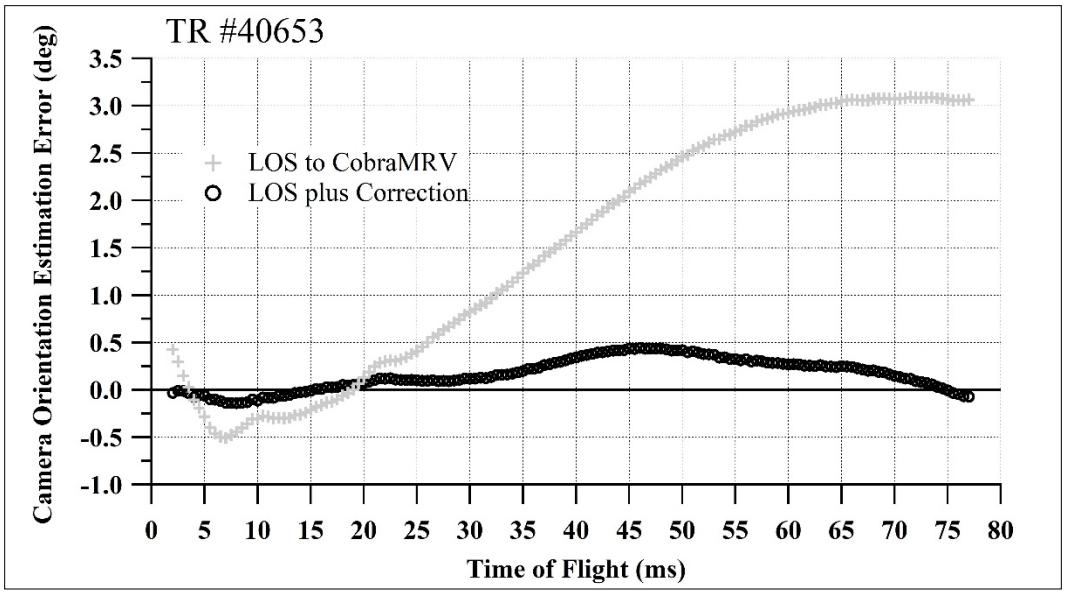

Fig. 19 Errors in image plane orientation estimates

Figures 20, 21, and 23–27 comprise a sequence of FF 1 images throughout the launch and flight of TR 40652. The photo in Fig. 20 was taken 0.5 ms after muzzle exit. At this time, the CobraMRV is approximately 0.55 m outside the tube but is not yet visible because it is still within the blast plume. The estimated orientation angle of the camera locus is –49.7°. The camera orientation has begun to translate at this time.

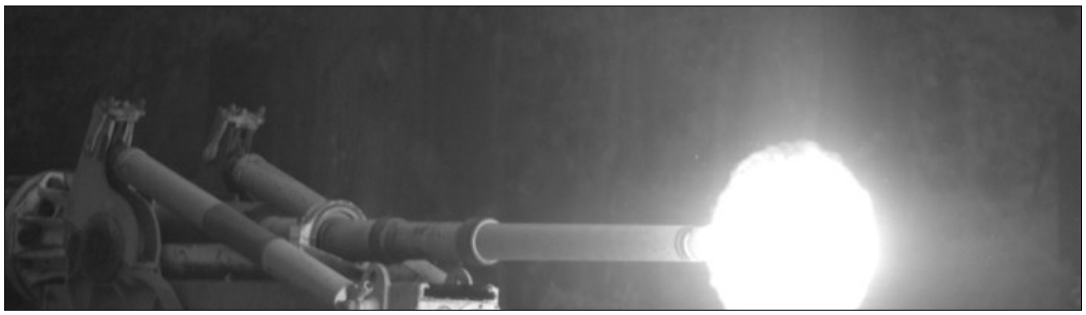

Fig. 20 FF 1 image taken 0.5 ms after launch of TR 40652

At 6.0 ms, Fig. 21 shows that the gun is no longer in the FF 1 FOV. By this time, the CobraMRV is approximately 6.6 m downrange, tilted upward, and approaching the first fiducial stake, S1a. The CobraMRV can be seen within the superimposed circle in Fig. 21. Also visible in this image are the four discarded sabot petals. The estimated orientation angle of the camera locus for this image is –45.2°. Two kinds of foreshortening in these FF 1 images need to be accounted for to make the desired orientation estimates. Similar to the DB and DR images, the length of the CobraMRV in pixels is a function of slant range from the camera to the CobraMRV.

Figure 22 gives the slant range and corresponding CobraMRV principal axis length for all the FF 1 images used for orientation estimates of TR 40652. The first was at 3.7 ms after tube exit, and the last was at 104.0 ms after tube exit with the minimum slant range and corresponding maximum resolution occurring when the projectile passes the FF 1 cameras downrange position. Additionally, the angles between the individual image planes and the shot line needed to be accounted for when estimating CobraMRV azimuth/yaw, as is described shortly.

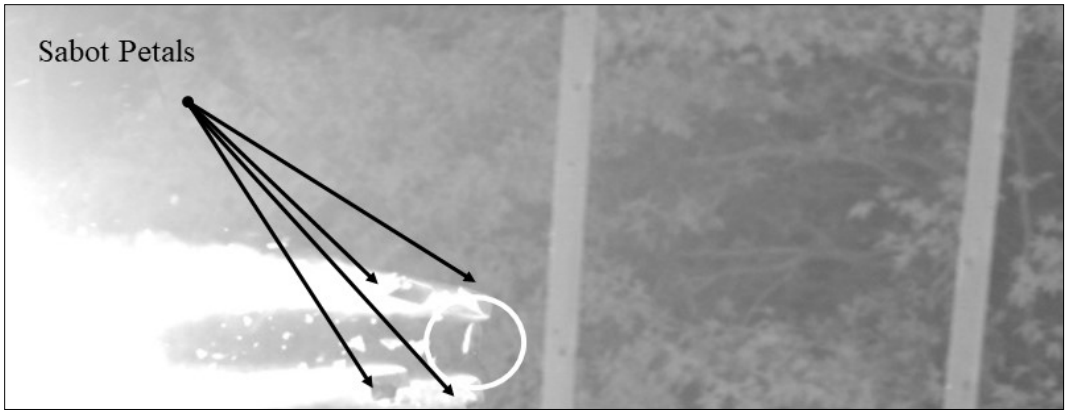

Fig. 21 FF 1 image taken 6.0 ms after launch of TR 40652

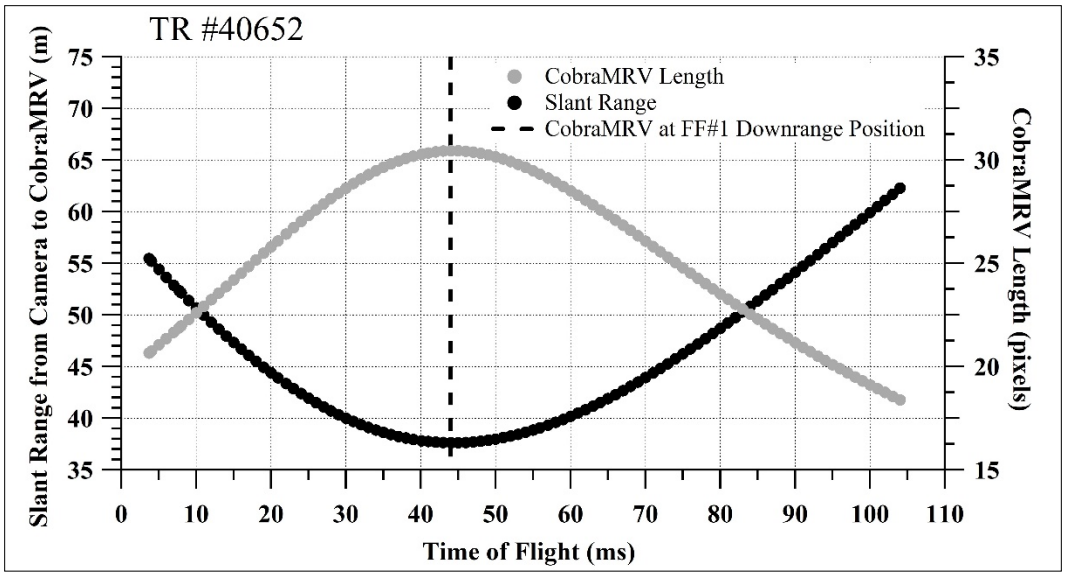

Fig. 22 Slant range to CobraMRV and CobraMRV length vs. time in FF 1 images of TR 40652

Figure 23 is the image taken 22.5 ms after tube exit. At this time, the CobraMRV is approximately 23.8 m downrange and the camera orientation is –29.6°. The CobraMRV is now tilted significantly downward.

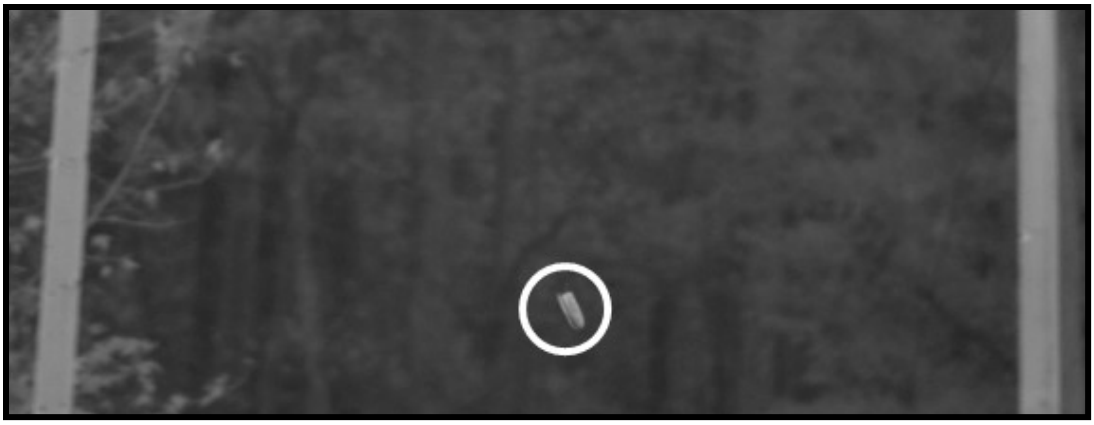

Fig. 23 FF 1 image taken 22.5 ms after launch of TR 40652

At 40.5 ms after launch (Fig. 24), the CobraMRV is approximately 41.3 m downrange. The camera orientation is –6.5°, and the CobraMRV is tilted slightly upward.

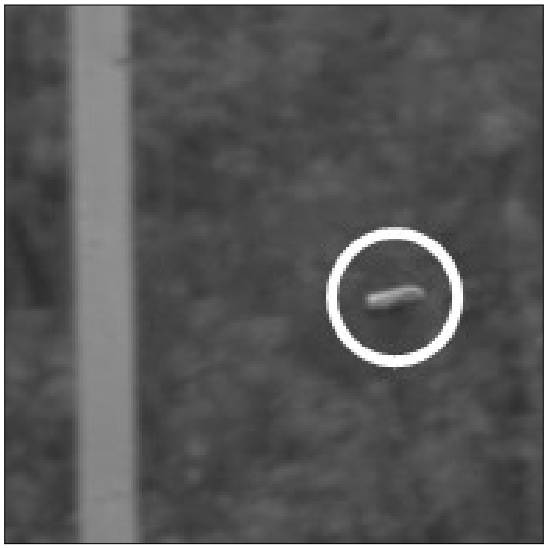

Fig. 24 FF 1 image taken 40.5 ms after launch of TR 40652

At 56.5 ms after launch (Fig. 25), the CobraMRV is approximately 55.9 m downrange. The camera orientation is +17.2°, and the CobraMRV is tilted upward and appears to be turned toward the camera.

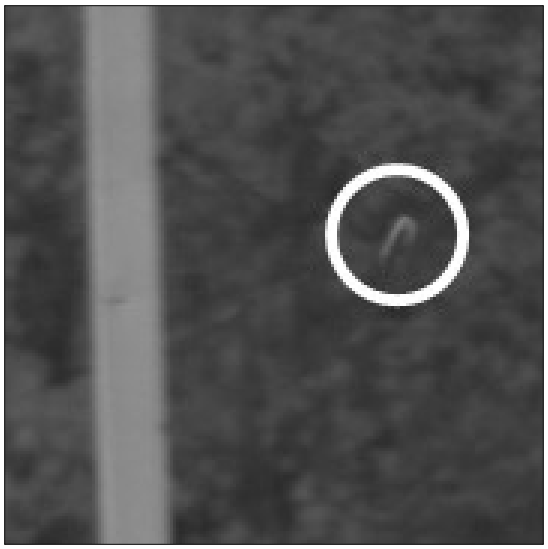

Fig. 25 FF 1 image taken 56.5 ms after launch of TR 40652

At 81.0 ms after launch (Fig. 26), the CobraMRV is approximately 76.6 m downrange. The camera orientation is +37.2°, and the CobraMRV is tilted downwards and appears to be turned away from the camera.

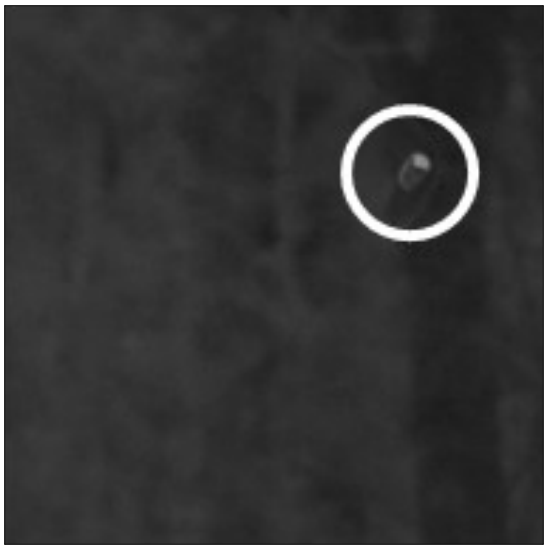

Fig. 26 FF 1 image taken 81.0 ms after launch of TR 40652

Finally, at 102.0 ms after launch (Fig. 27), the CobraMRV is approximately 93.0 m downrange. The camera orientation is +48.8°, and the CobraMRV is tilted upward and appears to be turned away from the camera.

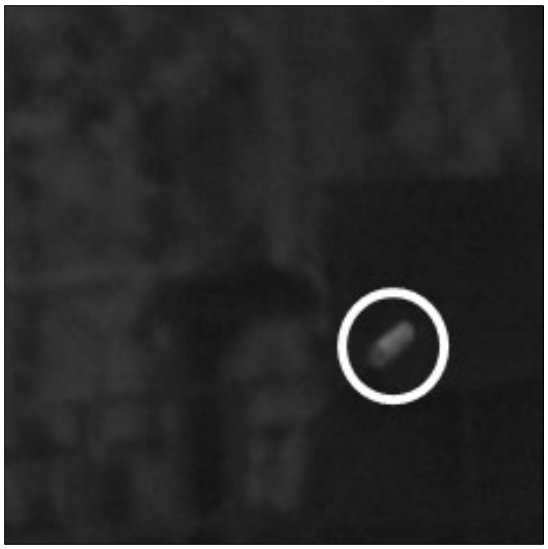

Fig. 27 FF 1 image taken 102.0 ms after launch of TR 40652

As the preceding sequence of images demonstrate, the FF 1 video records include images with every combination of CobraMRV tilt and turn with respect to instantaneous image plane. Pixels on the CobraMRV bodies in those images were assumed to be in the vertical plane estimated at that time step by the corrected LOS technique. After making visual estimates of the pixels at the fore and aft ends of the CobraMRV axis for each image, the elevation angle with respect to horizontal (ε_t) was computed as the arcsine of the ratio of the vertical span (V_t) to the longitudinal axis length in pixels (λ_t) at that slant range/time. The magnitude of the azimuth angle of the CobraMRV with respect to the image plane (δ_t) is given by the arccosine of the ratio of the horizontal span to the length of the projection of the CobraMRV axis onto the horizontal plane [i.e., $|\delta_t| = \text{acos}\{H_t/(\lambda_t * \cos(\varepsilon_t))\}$]. There are four possible values for δ_t depending on whether the CobraMRV's horizontal span is positive or negative and whether the CobraMRV is turned toward or away from the camera (see Table 5). It is not always clear on the basis of a single image whether δ_t is toward the camera or away from the camera (e.g., Figs. 20 and 21). This type of difficulty was resolved either by maintaining continuity within the temporal sequence of images and/or by examining the corresponding DR image. After this is determined, the azimuth angle in the gun coordinate system is given by combining the CobraMRV azimuth with respect to the image plane and the orientation of the image plane with respect to the shot line (i.e., $\psi_t = \delta_t - \beta_t$).

Table 5 CobraMRV azimuth with respect to image plane combinations

	Turned away from camera	Turned toward camera
$H_t > 0$	$\delta_t = \lvert\delta_t\rvert$	$\delta_t = -\lvert\delta_t\rvert$
$H_t < 0$	$\delta_t = 180 - \lvert\delta_t\rvert$	$\delta_t = -180 + \lvert\delta_t\rvert$

After computing the length of the projection of the CobraMRV longitutinal axis onto the X',Y' plane as $99.96mm * \cos(\varepsilon_t)$, the coordinates of the forward end of that axis are given by $z'_t = (V_t/\lambda_t) * 99.96mm$, $y'_t = 99.96mm * \cos(\varepsilon_t)\sin(\psi_t)$, and $x'_t = 99.96mm * \cos(\varepsilon_t)\cos(\psi_t)$. The AoA was computed from the dot product of the longitudinal axis orientation vector and the velocity vector (i.e., $AoA_t = \cos^{-1}\left(\frac{\vec{\omega}_t \cdot \vec{V}_t}{|\vec{\omega}_t||\vec{V}_t|}\right)$). The time history of CobraMRV axis orientation angles in the gun coordinate system estimated from the FF 1 video record of TR 40652 is shown in Fig. 28 and the corresponding AoA history in Fig. 29.

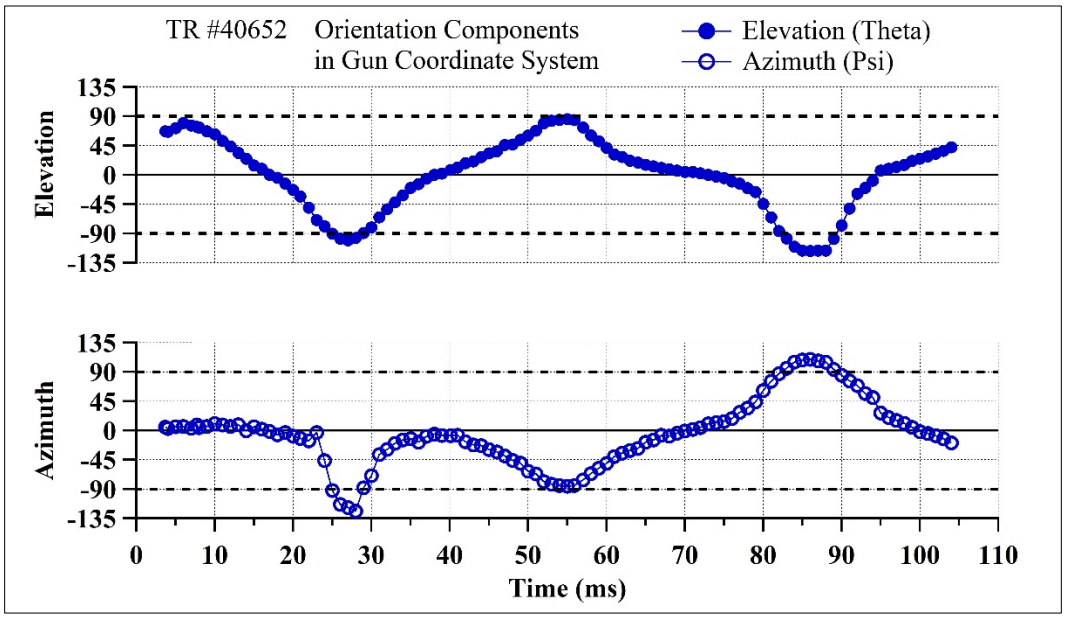

Fig. 28 Time history of estimated CobraMRV orientation for flight experiment TR 40652

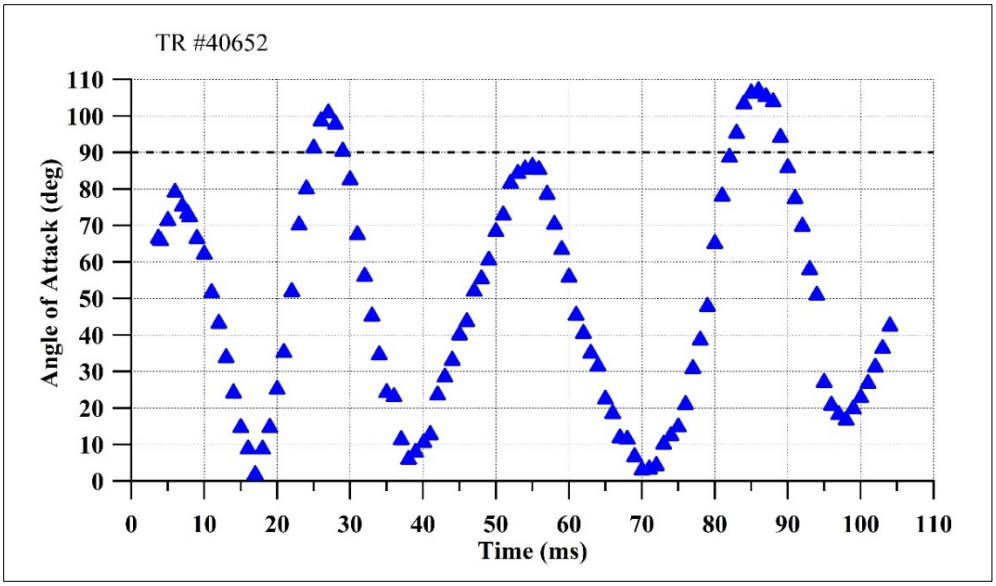

Fig. 29 Time history of estimated CobraMRV AoA for flight experiment TR 40652

Pitch (τ) and yaw (ρ) components of the AoA were obtained by solving for the rotation angle of the vector on the surface of the cone of radius AoA_t about the velocity vector collinear with $\vec{\omega}_t$. Resolving this into angles with respect to the velocity-vector-fixed horizontal and vertical planes yielded the pitch and yaw components, respectively. Superimposing these pitch estimates on the previously plotted gun coordinate system elevation estimates gives Fig. 30, and similarly superimposing these yaw estimates on the previously plotted azimuth estimates gives Fig. 31.

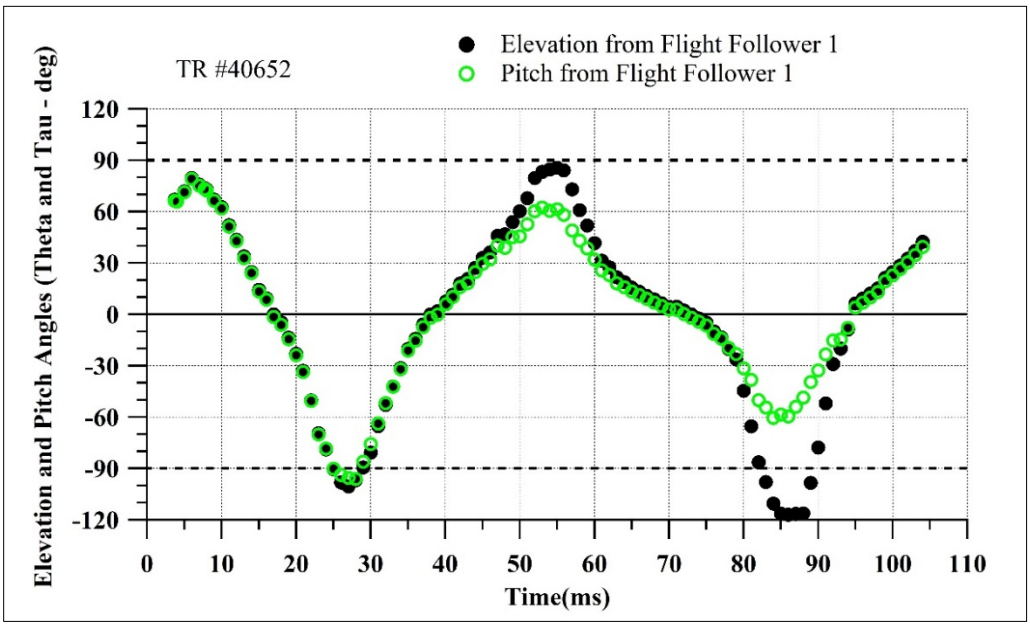

Fig. 30 CobraMRV elevation and pitch history for TR 40652

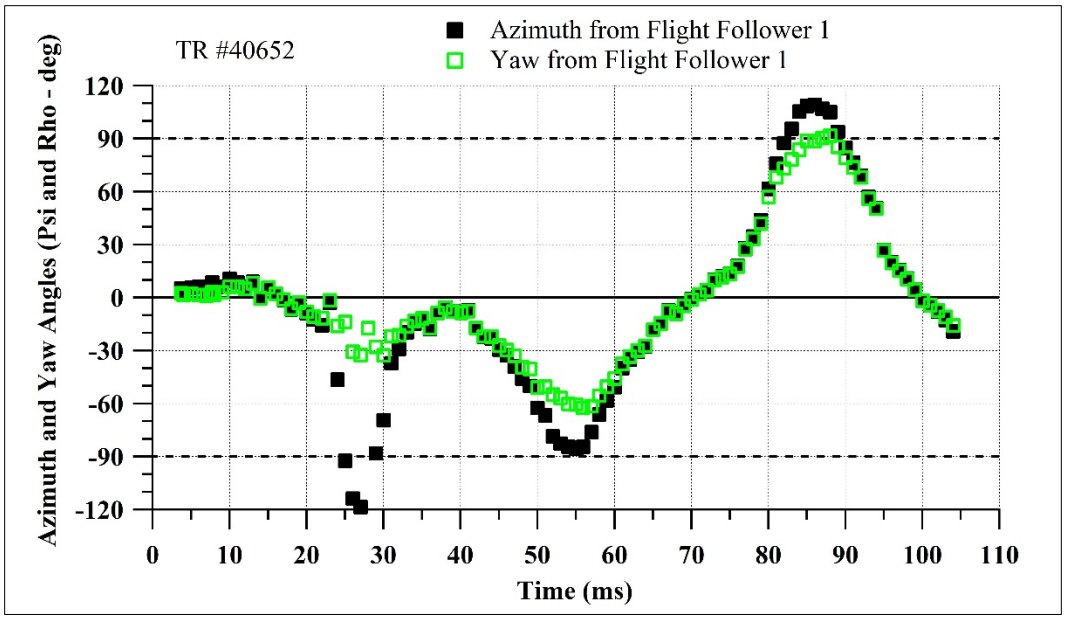

Fig. 31 CobraMRV azimuth and yaw history for TR 40652

In Fig. 32, pitch versus yaw is plotted as the gray dots. The blue dashed circle indicates an AoA magnitude of 90°. After fitting the pitch versus time and the yaw versus time estimates with high-order polynomials, the "smoothed" black line curve of fitted pitch versus fitted yaw was added. The black dot in the first quadrant near the positive pitch axis indicates the first measurement at 3.7 ms, and the succeeding "smoothed" measurements proceed along the curve until ending in the second quadrant at 104 ms time of flight. Recalling that the intent of the sabot design was to have the CobraMRVs exit the launch tube with +45° of pitch and no yaw or roll, the initial angular motion's being predominantly in the pitch plane is as expected, though of larger magnitude than was anticipated (Sostaric et al. 2019). Continuing on, the second yaw cycle is seen to lie approximately along a diagonal through the second and fourth quadrants with this apparent rotation beginning at approximately 40 ms. No attempt was made to aerodynamically interpret this motion as there were no CobraMRV roll data. Given that the CobraMRV shape is radially asymmetric, this absence precluded any such analysis.

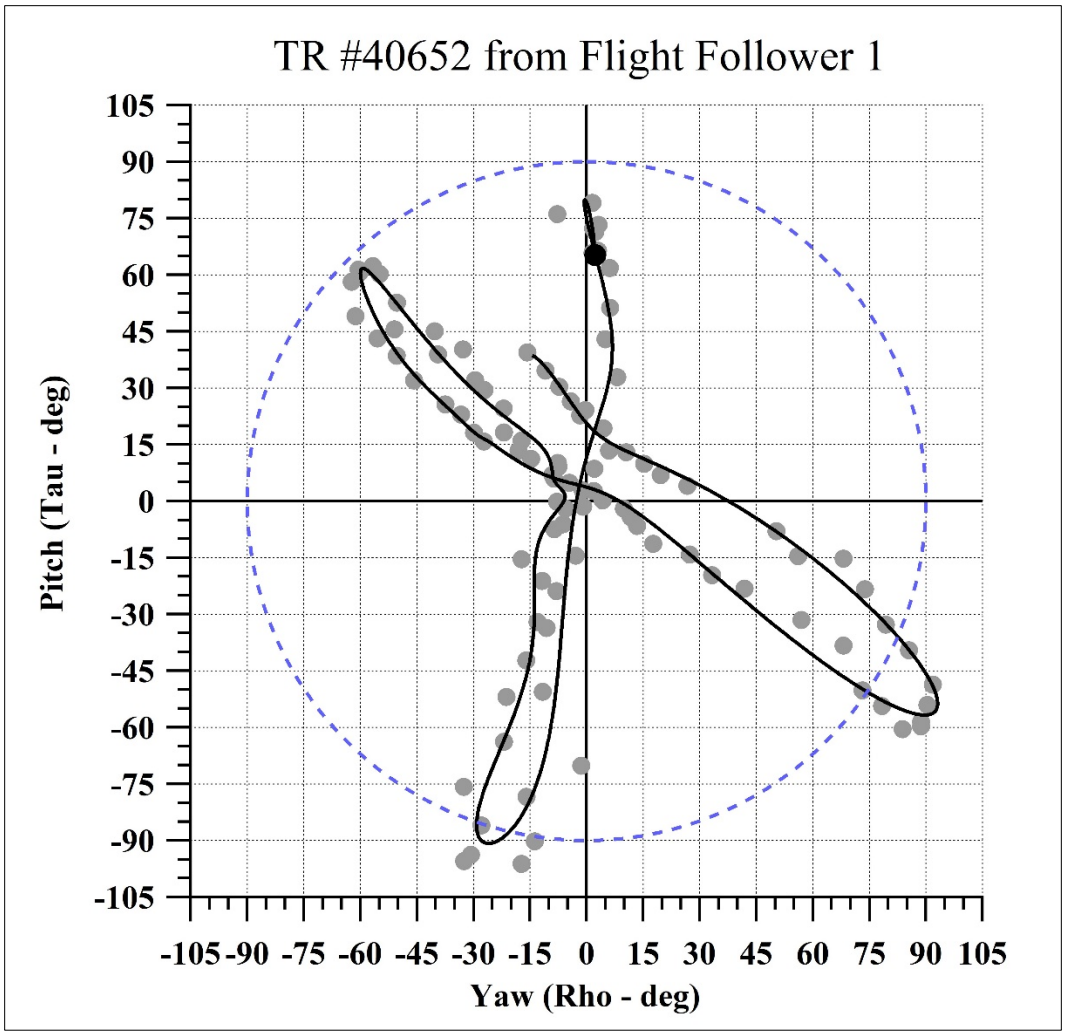

Fig. 32 CobraMRV axis orientation history for TR 40652

At this point, the authors stepped through the temporal sequence of FF 1 images and made a purely subjective informed guess of CobraMRV roll orientation in each of the processed images. This was done most often based on observation of the tail of the CobraMRV and its apparent roll with respect to horizontal in conjunction with a concern for continuity with previous and future observations. Much time was consumed attempting to reproduce the image geometries by positioning a CobraMRV airframe at the estimated viewing angle of the respective FF 1 frames and orienting the CobraMRV to reproduce the recorded image, but no quantitative accuracy claims are (or can reasonably be) made.

Figure 33 represents the pitch and yaw time history of the TR 40652 longitudinal axis with the addition of the roll history "guess". We observe that the beginning of significant growth in yaw apparently coincides with the beginning of observed CobraMRV roll, but no causal relationship is claimed. The correspondence of yaw

and roll was generally observed in all the FF 1 video records (see plots in Appendices F–M), but these plots are primarily included to show the regions of each flight experiment that we believe best satisfy the test objective of obtaining observations of pitching motion during intervals with little or no CobraMRV roll. For TR 40652, this would be the interval from launch until approximately 40 ms.

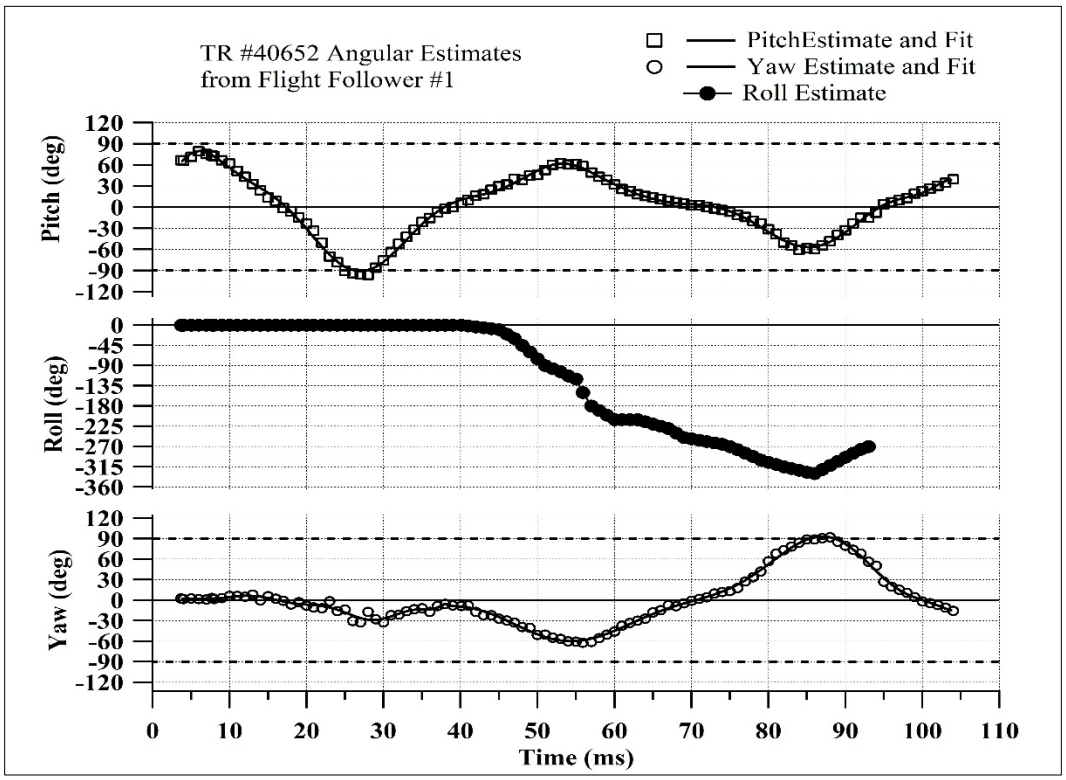

Fig. 33 CobraMRV pitch, roll, and yaw for TR 40652

Any future CobraMRV flight experiments should certainly include some means of obtaining roll orientation so that the interaction of roll and longitudinal axis orientation can be examined. All the FF 1 video records were analyzed in a similar manner to that of TR 40652.

4. Comparison with Previously Reported Pitch Estimates

As noted earlier, only a limited number of single-point pitch-angle estimates for five CobraMRV flights, and tracking-camera-derived estimated pitch-angle time histories for two of the flights, were available at the time of the modelling work described in Sostaric et al. (2019). Both the FC and FF pitch estimates used in that effort were computed from the ratio of rise over run of the CobraMRV within the respective images. Compensation for any out-of-plane components of the CobraMRV axis orientation and/or foreshortening arising from camera orientation

relative to the gun coordinate system were not attempted in these initial estimates. These (and other) shortcomings were noted at the time: "Flight video observations show that the vehicle begins to develop significant out-of-plane motion in roll and yaw after the first one-to-two cycles, which is not easily estimated using camera images. The onset of the roll and yaw oscillation does vary from shot to shot, and could explain the variation in pitch magnitude from shot to shot for the third set of data points near t = 0.05 s.* Further refinement of the flight data is needed" (p. 5).

In this effort, out-of-image plane components were estimated, radar-derived position data were incorporated into the estimation methodologies, angular and distance-related pixel foreshortenings were considered, and correspondences between images from multiple cameras were examined when making pitch estimates. In Fig. 34, the revised TR 40653 pitch-angle time history is shown with the initial estimated pitch history and Sostaric's Kestrel simulation model fit to those data. Though there are differences between the two sets of pitch estimates, they are in fact very similar, and a Kestrel fit to the revised pitch versus time data would no doubt be little changed.

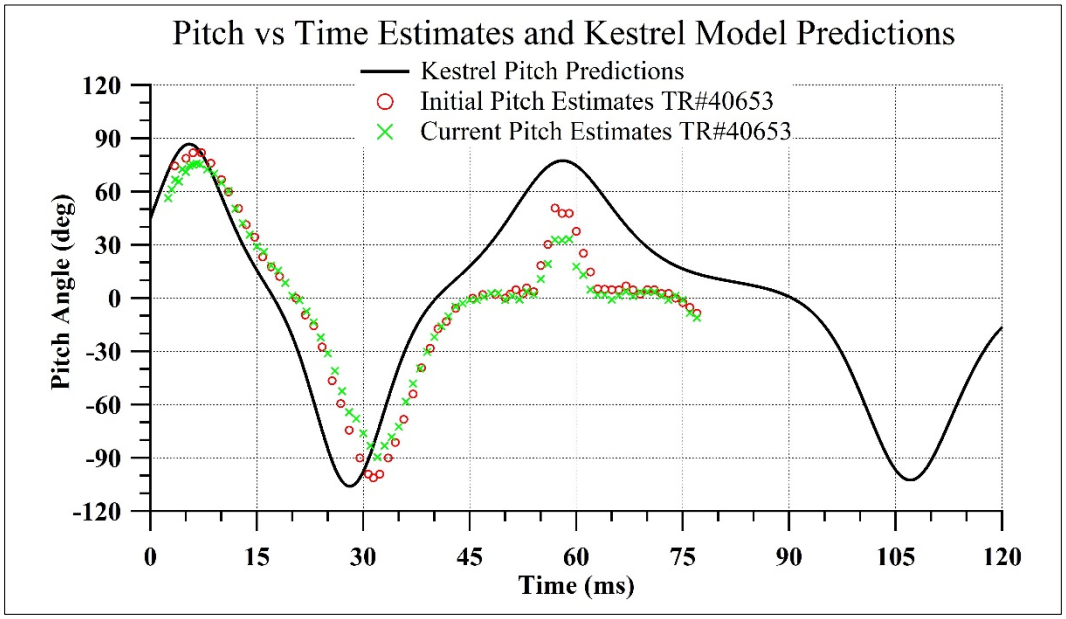

Fig. 34 Comparison of TR 40653 FF1 camera pitch vs. time estimates with model prediction

* These can be seen in Fig. 36a.

However, when the pitch histories are plotted versus their corresponding downrange locations as interpolated from the radar data along with the Kestrel fit,* the quality of the fit in frequency is seen to be not as good in the distance domain (Fig. 35). Whereas the two positive peaks of the measured data and the Kestrel prediction are well aligned in time, and the intermediate negative peak of the measured data lags somewhat, in downrange distance all three measured peaks lag the predicted peaks with the lag increasing at each peak. Examination revealed that the Kestrel simulation assumed the nominal launch speed of 1100 mps, whereas the subsequent radar analysis showed an 1128-mps launch. Also, comparison of the inflight velocity histories from the simulation output and the radar data shows significant differences in the two deceleration (total drag) histories.

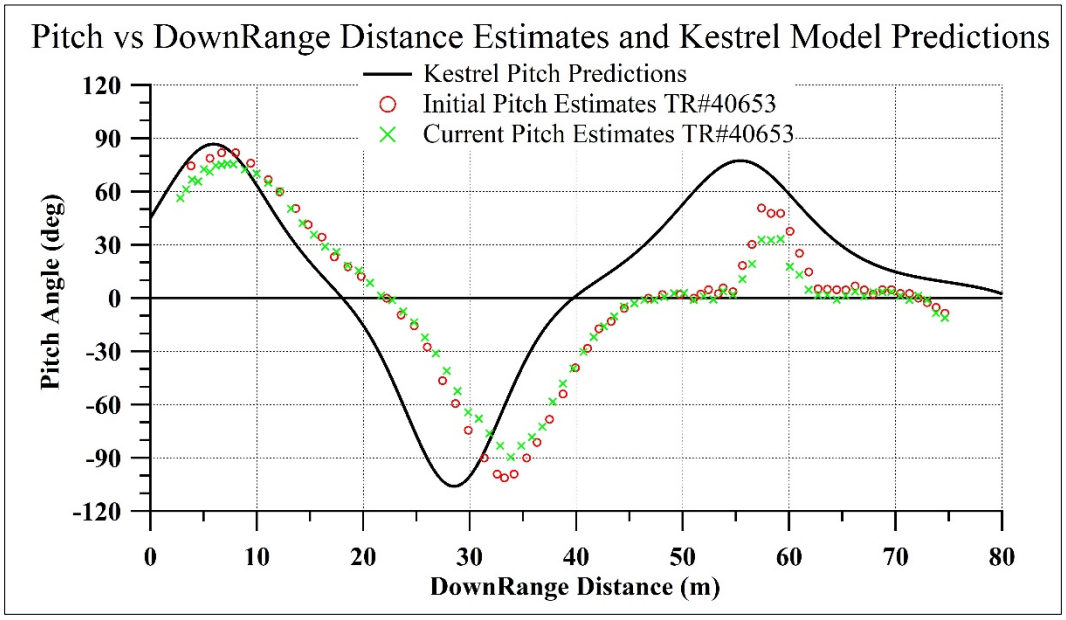

Fig. 35 Comparison of TR 40653 FF1 camera pitch vs. distance estimates with model prediction

As the simulation predicted angular history had no out of plane motion, the simulation predicted AoA is given by rectifying the pitch angle estimates. When this is plotted along with the revised TR 40653 measurements of AoA that include estimated out of plane components, we see a good match in magnitude (Fig. 36).

* The Kestrel downrange locations were estimated by integrating speed values computed from the body-fixed velocity components included in the simulation output.

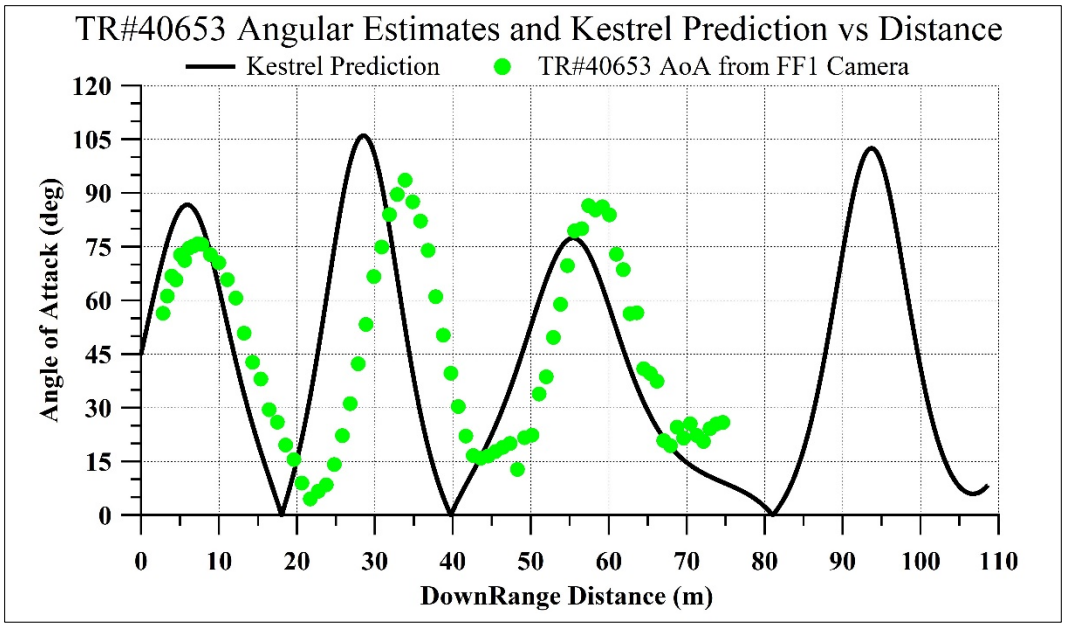

Fig. 36 Comparison of TR 40653 FF 1 camera AoA vs. distance estimates with model prediction

Figure 37 (top) is reproduced from Sostaric et al. (2019) and shows the estimated pitch history of TR 40653 (open red circles), estimated pitch at some of the maxima and minima of other TRs (filled circles), and the Kestrel fit to TR 40653 plotted versus time. Figure 37 (bottom) shows the corresponding revised estimates as well as some additional pitch extrema estimates and the Kestrel fit plotted versus downrange distance. As noted in regards to Fig. 34, the initial and revised pitch estimates do differ but their qualitative characteristics are similar and Sostaric's observations still apply: "A good match is observed … for the first full cycle in magnitude, along with a reasonably good match in frequency" (p. 5) with increasing variations in pitch magnitude and frequency for the different TRs beginning thereafter.

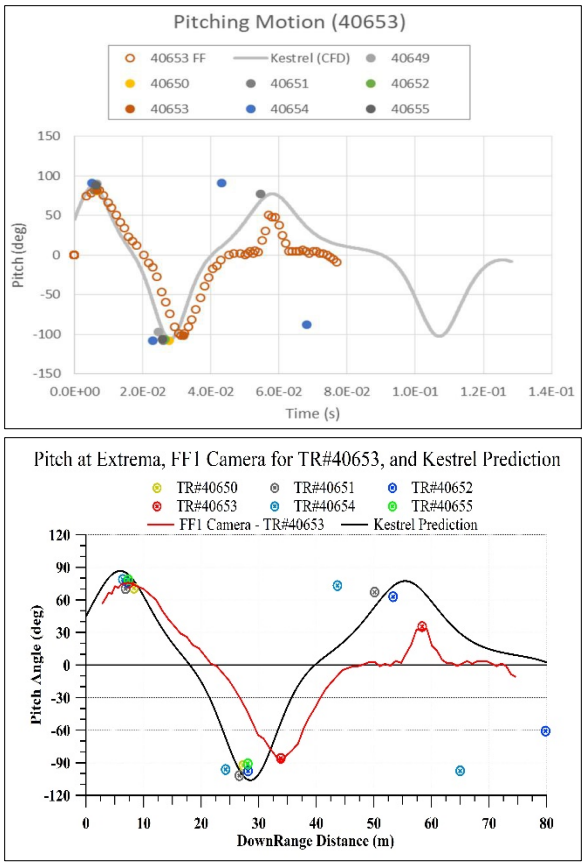

Fig. 37 Pitch estimates at extrema and TR 40653 pitch history compared with Kestrel model prediction: (top) initial estimates vs. time and (bottom) revised estimates vs. downrange distance

Figure 38 gives the full pitch-angle histories estimated from the FF 1 video records of TR 40650 through TR 40655.* The pitch angles are plotted versus the radar-derived downrange distances at the times when the individual images were recorded. Because the flight experiments were nearly flat-fired (quadrant elevation = 5 mil), the downrange distances can be essentially equated to the calibers of travel† and provide a basis for comparison of the angular histories of these six CobraMRVs with different launch speeds. All the available processed FF 1 pitch data for these TRs are shown in Fig. 38.

* TR 40649 was not included because it appears to begin to roll almost immediately after tube exit. The FF 1 video of TR 40650 is of lesser quality than other flights but seems to show that the round was launched with the CobraMRV axis not in the vertical plane, perhaps due to not correctly indexing the round when loading (though this is unprovable conjecture). Despite not appearing to have been launched at the desired orientation, this experiment is included in Figs. 38–40 because rolling motion was not observed in the subsequent images.

† Downrange distances and corresponding path lengths along the trajectories were compared for the radar-derived position histories. The average ratio of distance to path length for the first 100 m of downrange travel for TR 40650 through TR 40655 was 0.9995.

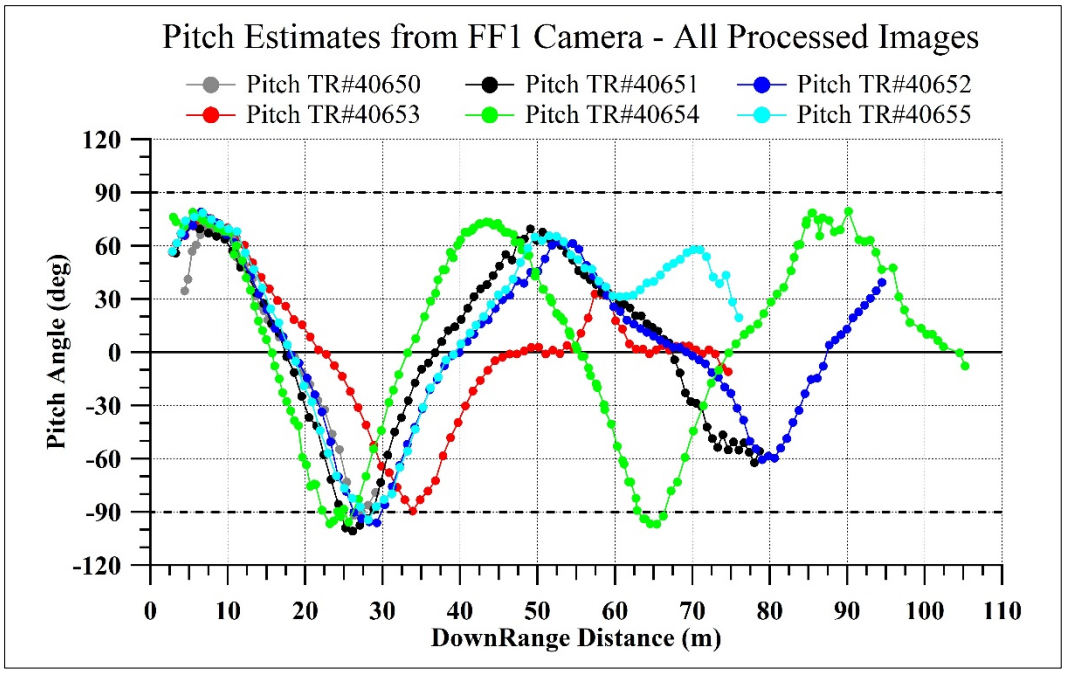

Fig. 38 CobraMRV pitch vs. downrange distance from all processed images

As the desired goal of these flight experiments was to observe pitching motion and damping characteristics, "the ideal flight is multiple pitch cycles with minimal out of plane movement and minimal yaw and roll attitude motion" (Sostaric et al. 2019, p. 4). When only those pitch angle estimates from the respective intervals from launch until the observation of appreciable CobraMRV roll are plotted versus downrange distance (Fig. 39), the pitch angle histories of these six flight experiments are very similar.

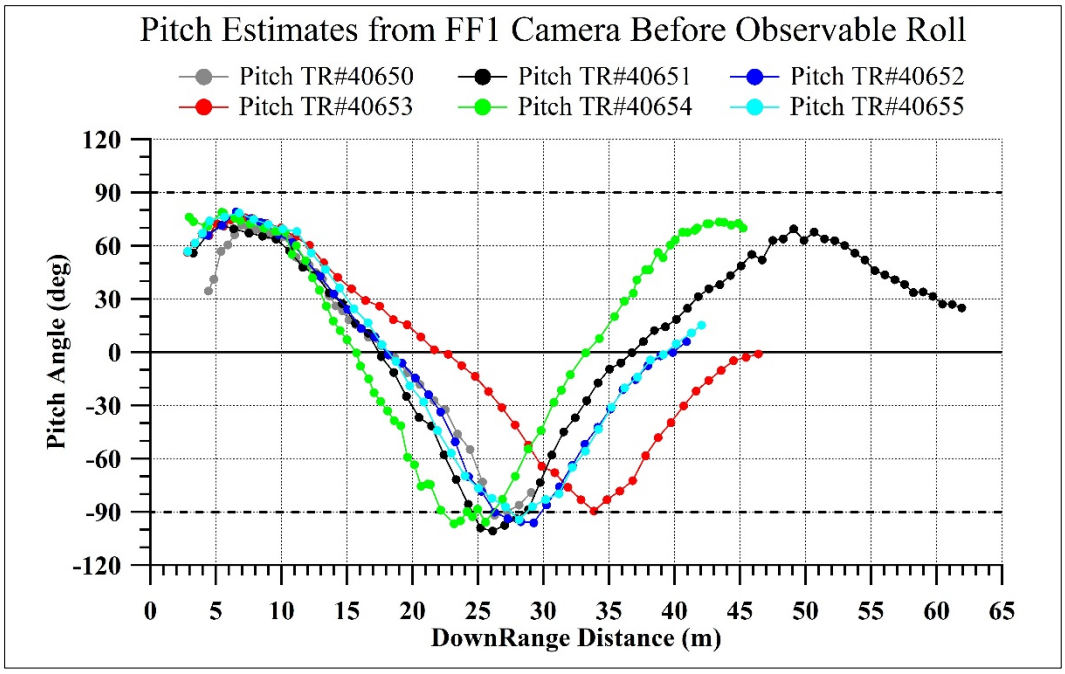

Fig. 39 CobraMRV pitch vs. downrange distance before occurrence of significant roll

When the polynomial fits made to the pitch and yaw estimates from the FF 1 images of TR 40650 through TR 40655 for the intervals included in Fig. 39 are plotted (Fig. 40), they show repeatable yawing motion history in magnitude and direction. We believe that these data enable revised modelling efforts that may more accurately predict CobraMRV aerodynamic characteristics.

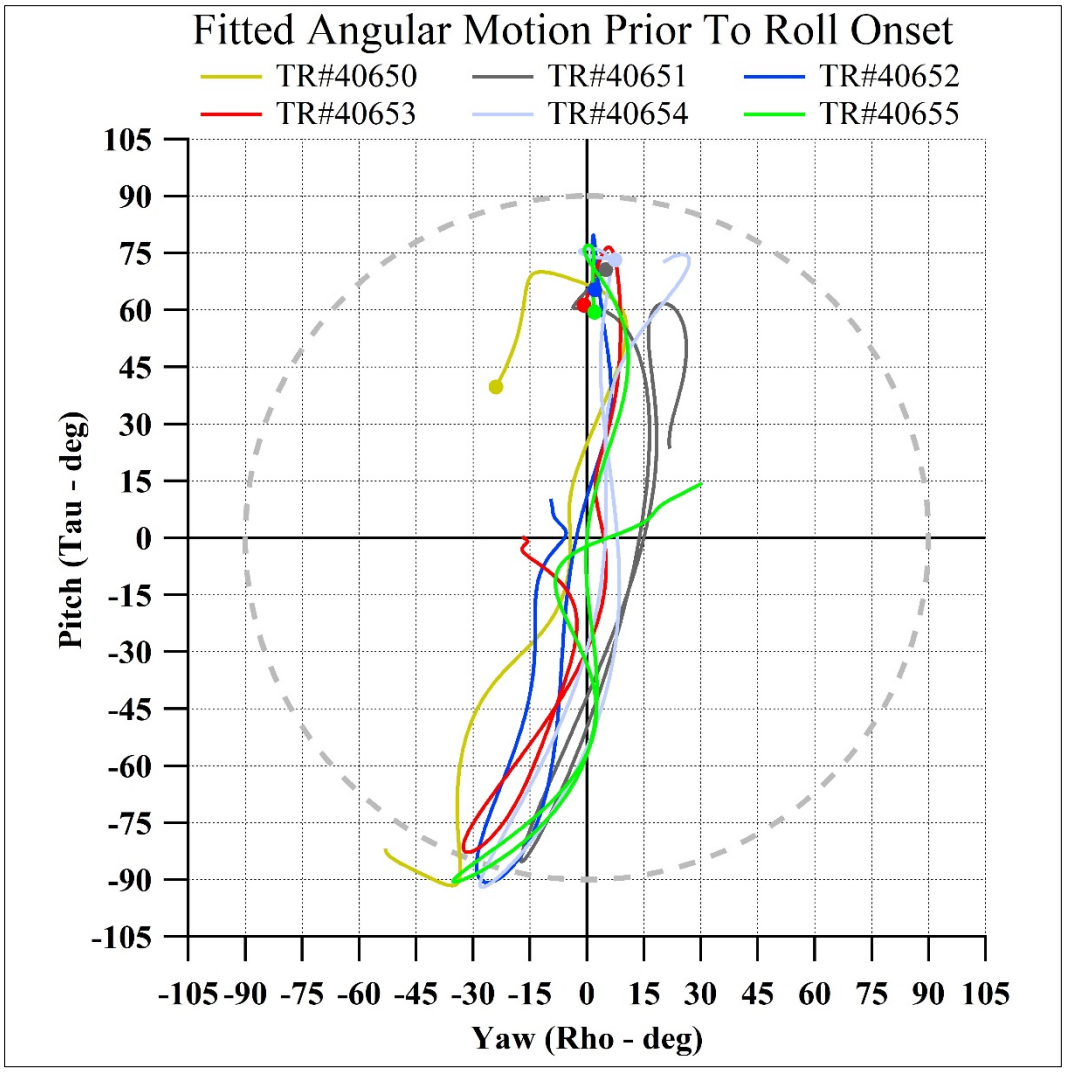

Fig. 40 CobraMRV axis orientation history before occurrence of significant roll for TR 40650 through TR 40655

5. Improving State Estimation Accuracy

Whenever possible, all the range instrumentation employed in future flight experiments should be connected to the test-range IRIG B time source. This not only would facilitate correlating data from different instruments, but also would provide some redundancy and allow direct comparison of time and position measurements from multiple sources.

Given a common time base, the accuracies of two sets of location and orientation measurements ultimately determine the accuracies of the flight-vehicle state estimates derived from an individual video frame. The first of these sets is the location and orientation of the projection of the flight vehicle onto that frame's

image plane. The second is the location and orientation of the image plane in the gun coordinate system.

5.1 Location and Orientation Estimation within an Individual Video Image

The accuracy achievable for the flight-vehicle projection measurements in a digital image is a function of the resolution of the image (i.e., the ratio of the pixel spatial extent at the instantaneous LOS distance and the test airframe's dimensions). Combining the CobraMRV's length of 99.6 mm and the Decker criterion of 100 pixels along the longitudinal axis for reliable automated-shape-extraction software functionality, pixel size on the CobraMRV body would ideally be less than or equal to 1 mm. When the camera characteristics given in Table 1 are considered, employing this pixel size results in FC total image frame sizes of no more than a square meter along the shot line: 0.8 × 0.6 m, 1.28 × 0.8 m, and 1.28 × 0.512 m. This frame size presents a coverage problem in two ways. First, very little of the trajectory would be potentially observable with any reasonable number of fixed cameras. Second, the dispersion occurring with multiple shots could result in some test items passing outside of the camera FOV. For the radar-derived CobraMRV trajectories, the height spread exceeds 0.5 m after approximately 50 m downrange travel (Fig. 41).

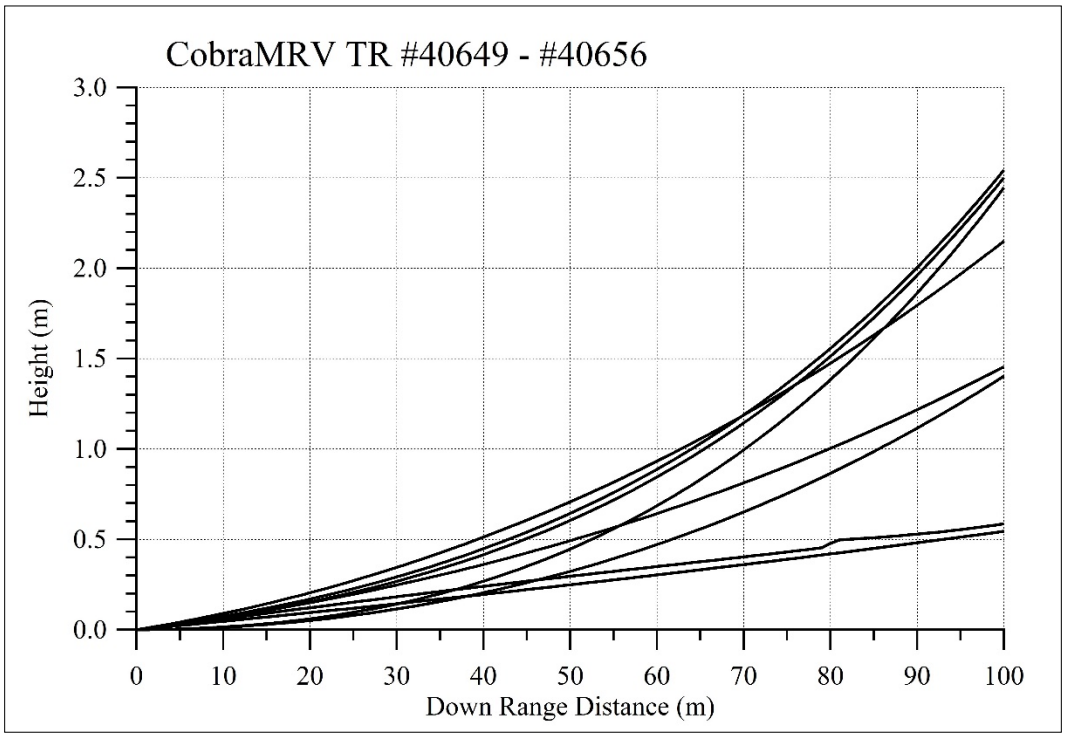

Fig. 41 CobraMRV height vs. range for all eight flight experiments

If resolution is 50 pixels along the flight body's length, the accuracy of automated axis orientation estimates for an individual image of the CobraMRV shape predicted by the Decker simulation is on the order of 1°. Qualitatively, the authors feel that in images with resolutions of 40 or more pixels along the CobraMRV axis and moderate yaw with respect to the image plane, the pixels corresponding to the endpoints of that axis can be reliably determined by manual inspection. With a 2.5-mm pixel size, FC image frame sizes then become 2 × 1.5 m, 3.2 × 2 m, and 3.2 × 1.28 m.

We strongly recommend that video coverage of future flight experiments be designed whenever possible to obtain images with no less than 40-pixel resolution along the flight body axis if those images are to be used to make orientation estimates. If future CobraMRV flight experiments are conducted with this same equipment, we recommend the following:

- Cameras FC 1–5 configured and positioned to achieve at least 40 (ideally 100)-pixel resolution at downrange distances of interest.
- FF 1 and 2 configured and repositioned so that FF 1 images meet or exceed the 40-pixel criterion from muzzle exit to whatever the associated maximum downrange distance,* with FF 2 picking up at that point with 40-pixel resolution and continuing thereafter.
- Reposition and/or re-aim the DR camera to begin to observe the flight body as early as possible.
- If additional cameras are available, include multiple DR cameras to segment the coverage and obtain better-resolution images throughout the trajectory. We also strongly recommend that, whenever possible, flight bodies have some kind of longitudinal markings that could be used for roll orientation estimation in video images: fiducials in the cameras; FOVs are also crucial for reference.

As the pixel size associated with any resolution criterion scales with the flight body's length, greater portions of trajectories of larger projectiles could be easily covered with cameras like those used in these experiments. For example, contemporary 120-mm kinetic energy projectiles are nearly 1 m in length. For the

* With the FF 1 pixel size of this experiment, a location 25 m downrange and 16 m offline would provide such resolution for the first 50 m of downrange travel. A second such camera 75 m downrange and 16 m offline would then provide 40+ pixel resolution 50–100 m downrange. Both FFs would track and record video throughout the flights, but these considerations would assure high-quality imagery in desired intervals. Alternatively, a different lens configuration could be applied to provide needed resolution.

100-pixel criterion, the pixel size becomes 1 cm and the corresponding frame sizes are 8 × 6 m, 12.8 × 8 m, and 12.8 × 5.12 m.

5.2 Location and Orientation Estimation of a Video Image in Gun Coordinates

Accurate location and orientation of images in the gun coordinate system is achieved in aerodynamic spark ranges by having rigidly fixed cameras and screens in surveyed locations along the flightpath. Additionally, within the cameras' FOVs are fiducials that are adjusted for each shot to account for current ambient conditions of temperature, pressure, and so on within the enclosed range. Clearly, this level of accuracy cannot be achieved at an outdoor range where camera characteristics and positioning are adapted to the particular test requirements. However, we believe that installing improved fiducials along the flight path at this flat-fire range would significantly improve overall state measurement accuracy. A conceptually simple possibility would be to pour a concrete slab parallel to the shot line with accurately plumbed "slots" at surveyed locations (x,y,z) into which rigid striated "posts" of environmentally insensitive material could be inserted. With one or (preferably) more posts within a digital image, calculations based on the line-of-bearing to multiple fiducial points can yield within-image adjustments to the estimated camera pose and focal length. These camera characteristics would enable computer vison measurements of improved accuracy over those made using the simplifying assumptions presented for this experiment. The accuracies obtained depend on line-of-bearing uncertainty due to pixel subtense quantization and the number of line-of-bearing observations (see Thompson and Durfee 1992). Alternatively, location measurement of temporary fiducials (stakes) can be done before each shot or daily if it can be assumed they will not move due to gun blast. Routine measurements can be made at the beginning of the setup or each morning, but caution should be made to ensure no camera or fiducial adjustments or movement between shots.

The combination of better data correlation from multiple sources, satisfying an image resolution requirement, and inclusion of quality fiducials within the images would enable greater accuracy of test-item state measurements.

6. Conclusions

Flight experiments of gun-launched scale models of a conceptual airframe called CobraMRV being considered by NASA for future manned Mars missions were conducted at ARL in the fall of 2017. Inflight observations by test range radars and high-speed video cameras were recorded and postprocessed to obtain CobraMRV

state estimates useful for aerodynamic characterization of the CobraMRV shape. Eight flight experiments were conducted.

A subset of the recorded data was processed with computerized image-processing software that computed the orientation of the CobraMRV longitudinal axis within the image. These orientation data were used to match simulated flight data as reported by Sostaric et al. (2019). Most of the recorded video data were not of adequate resolution for reliable employment of this software.

In this effort, CobraMRV longitudinal axis endpoint pixel locations within the recorded images were obtained via manual frame-by-frame examination of all the usable recorded video from the eight flight experiments. These were used to compute the axis' orientation within that image. In addition, out-of-image plane axial orientation components were estimated, radar-derived position data were incorporated into the estimation methodologies, angular- and distance-related pixel foreshortenings were considered, and correspondences between images from multiple cameras were examined when making CobraMRV position and attitude estimates in the gun coordinate system. Though the manual axis endpoint estimates are likely of lesser accuracy than those obtained via the computerized processing, they enabled a great quantity of additional position and attitude estimates that hopefully aid in the understanding of the CobraMRV airframe performance.

Finally, recommendations are made of notionally modest test range changes that would enable improved accuracy of airframe state estimates with the same radar and video instrumentation used in these experiments.

7. References

Brown JL, Garcia JA, Kinney DJ, Bowles JV, Mansour NN, inventors; National Aeronautics & Space Administration, assignee. Co-optimization of blunt body shapes for moving vehicles. United States patent US 8,725,470B1. 2014a May 13.

Brown TG, Harkins T, Don M, Hall R, Davis B. Development and demonstration of a new capability for aerodynamic characterization of medium caliber projectiles. 28th International Symposium on Ballistics; 2014b Sep 22–26; Atlanta, GA.

Brown TG, Sostaric RR, Garcia JA, Harkins TE, Johnson BJ, Decker R. Launch techniques for high angle of attack non-symmetric projectiles and characterization of aerodynamic damping. 69th Aeroballistic Range Association Meeting; 2018 Oct 8–11; Bath, UK.

Cerimele C, Robertson E, Sostaric R, Campbell C, Robinson P, Matz D, Johnson B, Stachowak S, Garcia, J, Bowles, et al. A rigid mid-lift-to-drag ratio approach to human Mars entry, descent, and landing. AIAA SciTech Guidance, Navigation, and Control Conference; 2017 Jan 9–13; Grapevine, TX.

Decker RJ. Cobra sabot test video analysis results. Program Review Briefing at Army Research, Development and Engineering (ARDEC); 2017 Nov; Picatinny Arsenal, NJ.

Decker R, Davis B, Harkins T. Pitch and yaw trajectory measurement comparison between automated video analysis and onboard sensor data analysis techniques. Army Research Laboratory (US); 2013a Sep. Report No.: ARL-TR-6576.

Decker R, Kolsch M, Yakimenko O. An automated method for computer vision: analysis of cannon-launched artillery video. 27th International Ballistics Symposium; 2013b; Freiburg, Germany.

Murphy C. Data reduction for the free flight spark ranges. Army Ballistic Research Laboratory (US); 1954 Feb. Report No.: BRL Report 900.

Sostaric RR, Johnson BJ, Doll JA, Garcia JA, Nikaido BE, Brown TG, Harkins TE, Decker R. Aeroballistic range testing of the Cobra Mid Lift-to-Drag Entry Vehicle. Proceedings of the AIAA SciTech 2019 Conference; 2019 Jan 7–11; San Diego, CA.

Thompson AA, Durfee GL. Techniques for evaluating line of bearing (LOB) sstems. Ballistics Research Laboratory; 1992 Sep. Report No.: BRL-TR-3390.

Appendix A. Mechanical Design

Design and mechanical drawings of the fabricated hardware are depicted in this appendix. Three launch package designs were fabricated. First, a simple surrogate mass simulant was made for verification of the charge mass to produced the desired launch velocity. This package consisted of a right circular cylinder with a slightly larger rear obturator to seal the high-pressure gun gases (Fig. A-1). Based on previous designs, these slugs employed a material and a geometery suitable to match the mass of the Co-Optimization Bluntbody Re-entry Analysis Cobra Mid-Lift-to-Drag Rigid Vehicle (CobraMRV) models. The length-to-diameter ratio was held to not exceed approximately 1.5 to maintain static stability. Second, a solid aluminum (Al) MRV scaled replica (1:200) was fabricated for the first sabot-integrity experiment. Al was chosen as an easy to machine and readily available material to verify external geometry characheristics, as shown in Appendix D. Third, the 1:200 scale model of the CobraMRV with physical characteristics associated with aerodymanic performance matching those of the full-size MRV was designed. This flight body was made of titanium (Ti) and incorporated a void and an Al lid. As demonstrated in previous work by Brown et al.,[1] a small cavity provides the possibility of incorporating a notional inertial measument system capable of measuring motion along the entire flight path in future experimentation, thus supplementing the photogrammetry techniques for flight dynamics measurement used in this effort.

[1] Brown TG, Harkins T, Don M, Hall R, Garner J, Davis B. Techniques and methodologies for aerodynamically characterizing medium caliber ammunition. 28th International Symposium on Ballistics; 2004 Sep 22–26; Atlanta, GA.

A.1 Slug (Low-Density Polyethylene)

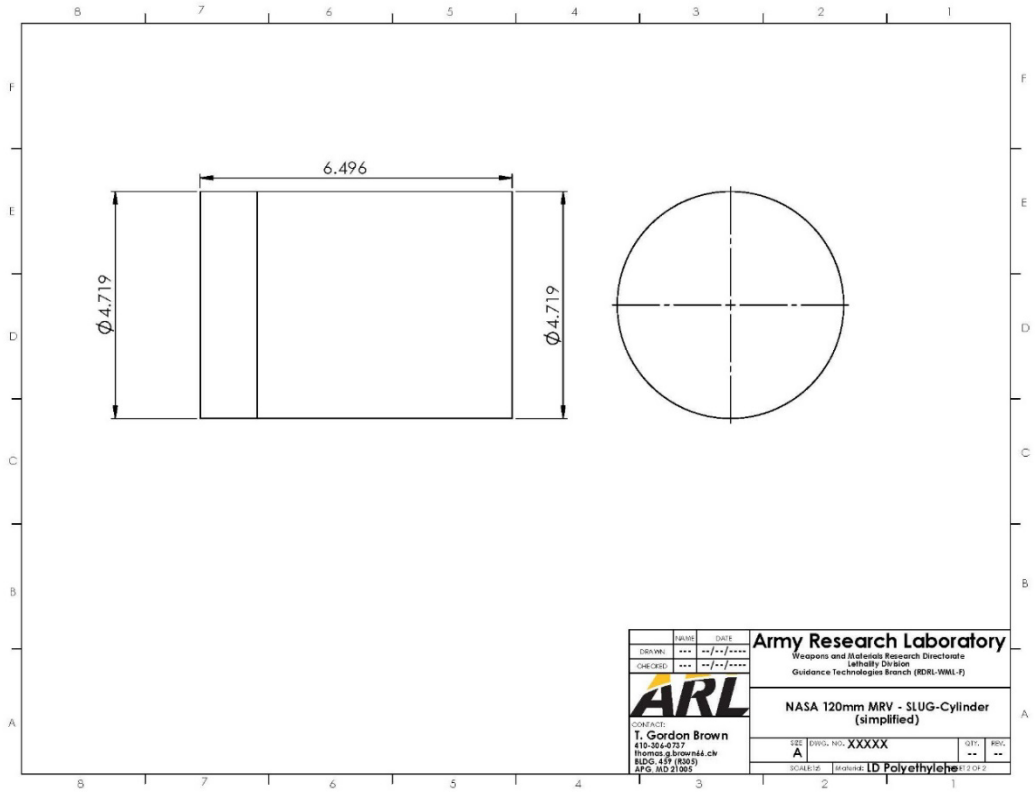

Fig. A-1 Slug, simplified projectile, solid polyethylene cylindrical shape with obturator

A.2 CobraMRV Design at 1:200 Scale

The nonsymmetric projectile is referred to as the CobraMRV.[2] The design resembles the NASA Space Shuttle without wings: a cylinder with blunt rounded nose and flattened bottom, yet with small tail fins at the rear. A representation is shown in Fig. A-2. Drawings of the package are included in Figs. A-3 through A-5. This scale model's design incorporates the external shape as well as internal features to replicate the MRV's physical characteristics (center of gravity, moment of inertial, mass), as shown in Table B-2 in Appendix B.

[2] Cerimele C, Robertson E, Sostaric R, Campbell C, Robinson P, Matz D, Johnson B, Stachowak S, Garcia, J, Bowles, et al. A rigid mid-lift-to-drag ratio approach to human Mars entry, descent, and landing. AIAA SciTech Guidance, Navigation, and Control Conference; 2017 Jan 9–13; Grapevine, TX.

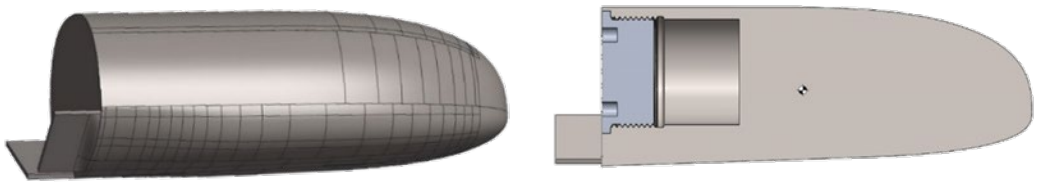

Fig. A-2 Computer-aided design model of CobraMRV

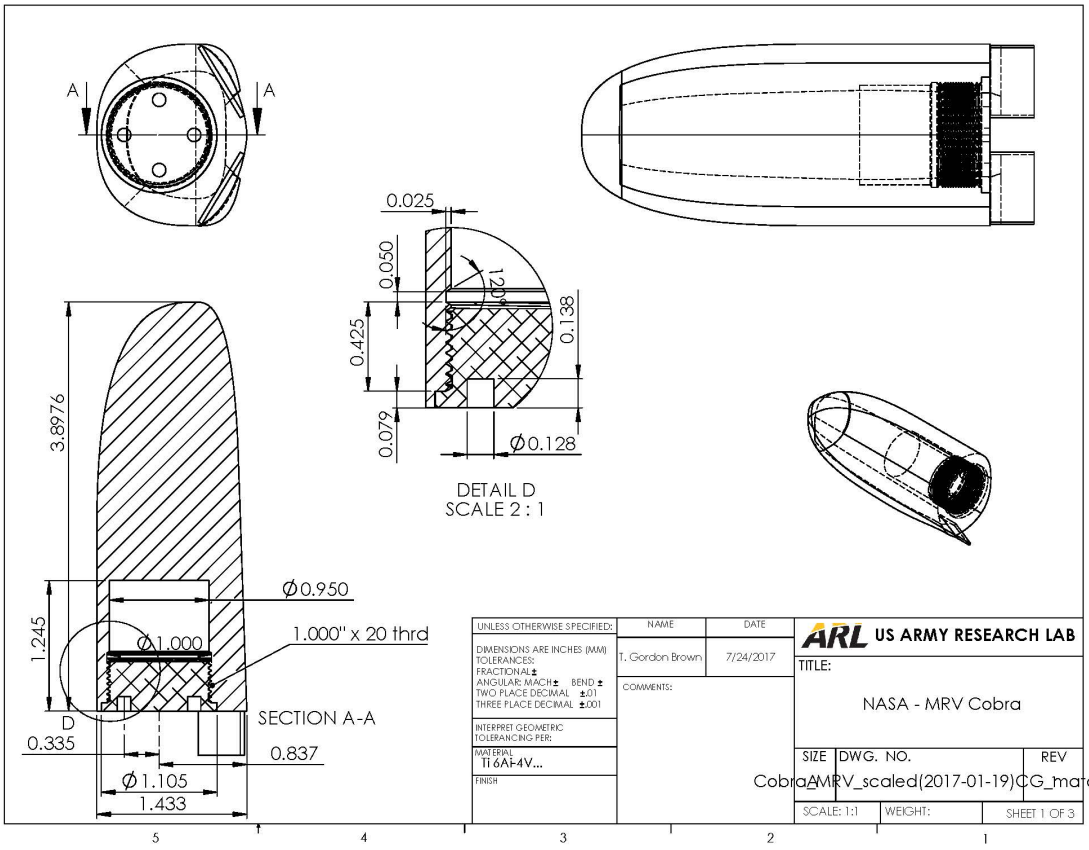

Fig. A-3 Drawing 1 (overview) of MRV 1:200 scale at design physical characteristics

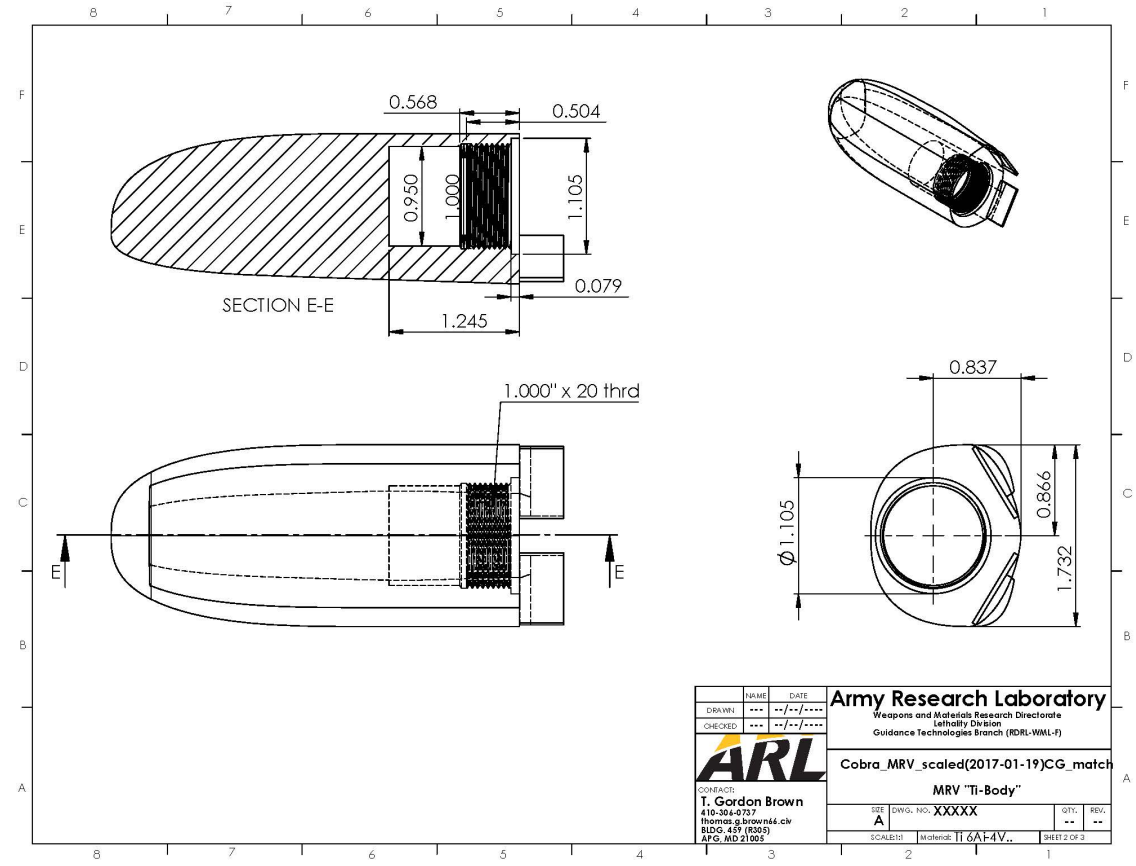

Fig. A-4 Drawing 2 (Ti body) of MRV 1:200 scale at design physical characteristics

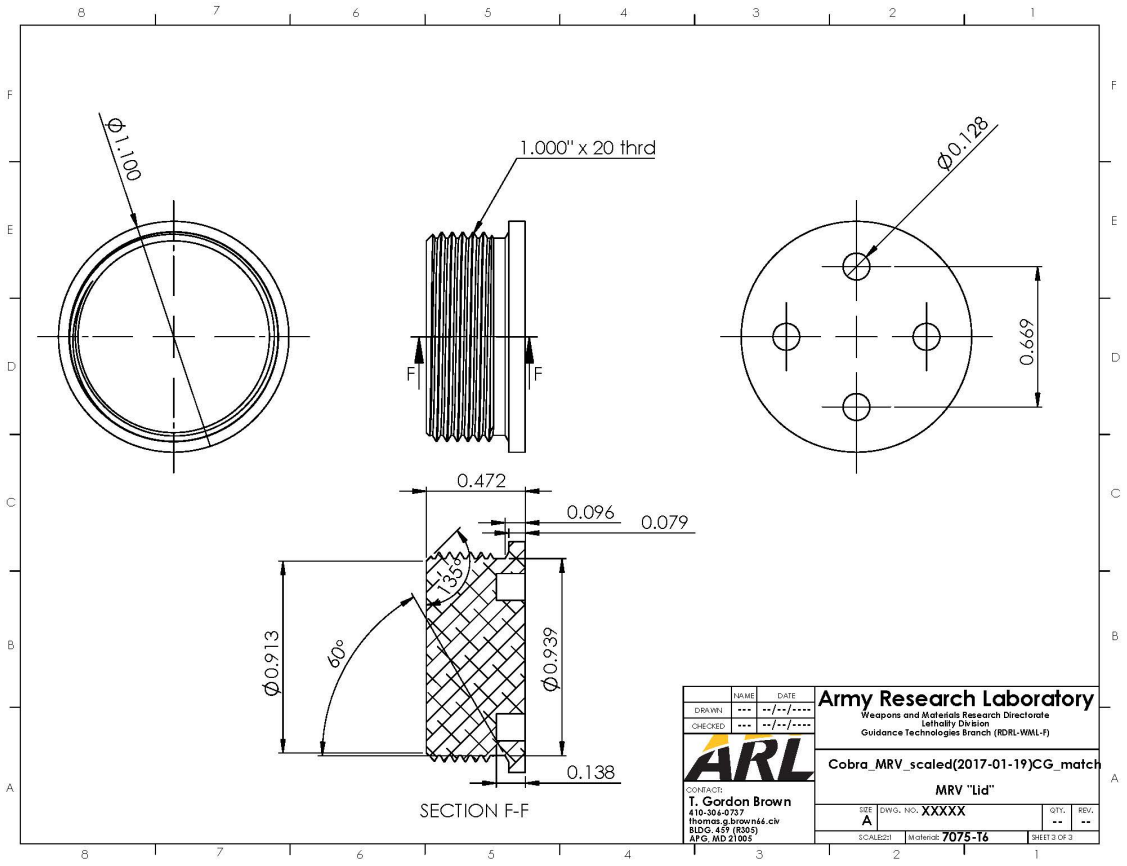

Fig. A-5 Drawing 3 (Al lid) of MRV 1:200 scale at design physical characteristics

A.3 Sabot Design

Sabot design was accomplished by extending the state of art of symmetric sabot design features and materials used previously for NASA and other customer programs (Fig. A-6).

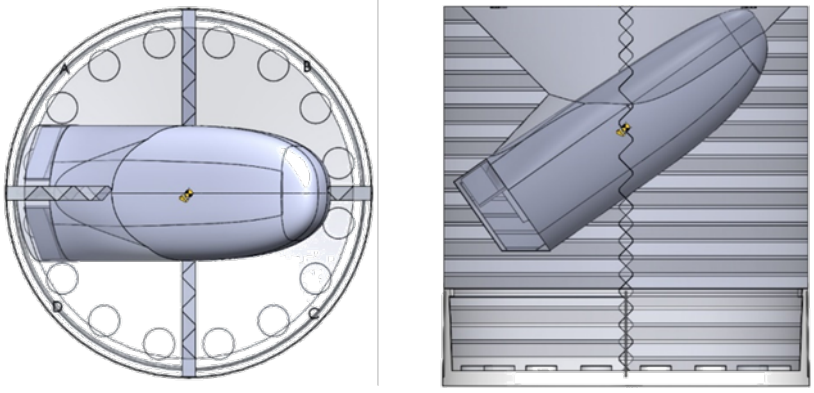

Fig. A-6 Transparent sabot package assembly

Figure A-7 shows a high-angle-of-attack, nonsymmetric vehicle sabot. For these experiments, a separate obturator cup that doubles as the sabot retainer keeps the four petals together and the projectile intact as well as protected from the high-pressure gun gases and temperature. Minimal material is used in the obturator cup since it serves only to seal the configuration. Using silicon grease around the outside can help seal the gun gases as well.

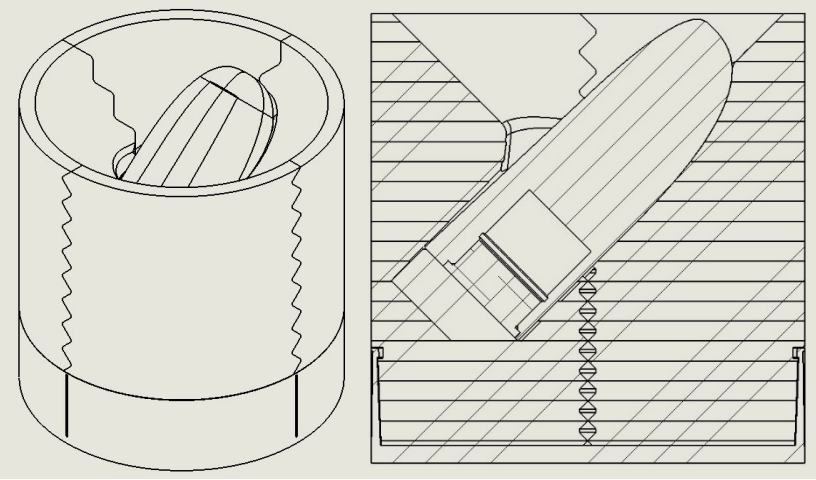

Fig. A-7 Sabot package (nonsymmetric): (left) orthogonal and (right) cutaway view

Finite element analysis (FEA) was used to help design the sabot. Almost 400,000 elements were included in the mesh to run static load analysis. Results are depicted in Fig. A-8, and von Mises stress is shown in Fig. A-9. The factor of safety is shown in Fig. A-10, yet safety margin is related to approximate values due to incomplete material property availability of the rapid prototype material (glass-filled nylon). However, it acts as a good reference for design iteration due to relative stress concentrations. Notice that most areas are less than 1 in this static simulation, yet for the most part, remain above one-tenth the assumed yield stress. For this particular dynamic case of constrained gun tube environment and relatively mundane loading rates, the definition of yield strength could be exaggerated and ultimately exceeded. This assumption was verified in a realistic gun launch test case before the ultimate experimental evaluation. In the results section, a view of the sabot piece integrity upon separation from the gun is demonstrated.

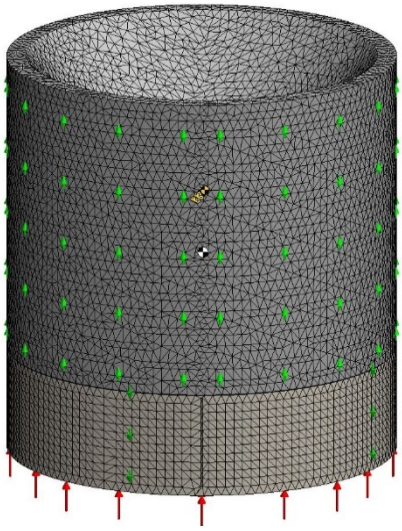

Fig. A-8 Mesh of sabot package (384.5e03 elements)

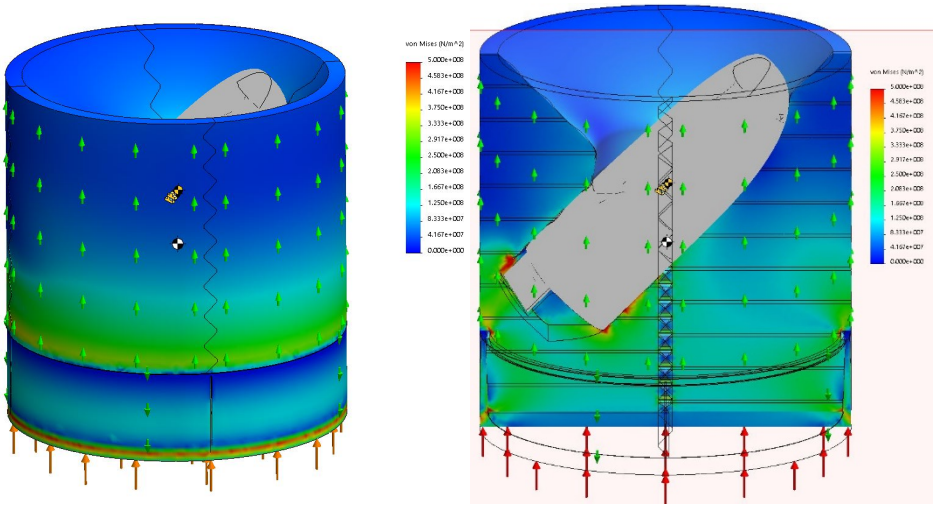

Fig. A-9 Sabot FEA: von Mises stress (exterior and interior)

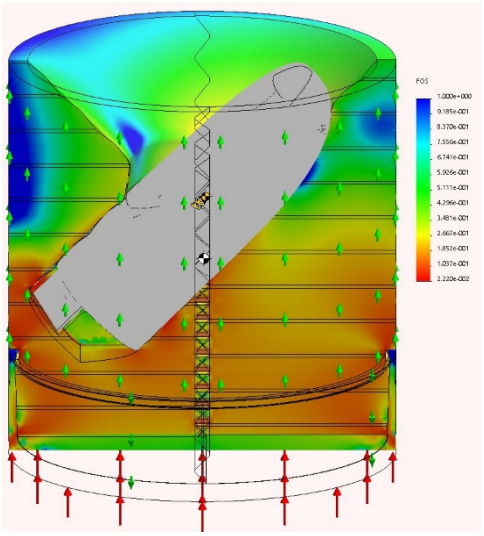

Fig. A-10 Sabot FEA: factor of safety (interior)

Appendix B. Experimental Flight Log

The design of the series of experiments was simple in nature: shoot a payload from a gun at high angle of attack and observe its resulting flight motion. The motion could be evaluated using multiple methods. One method proven extremely useful at characterizing free-flight motion is to use in situ sensors (solar, inertial, magnetic, or surface pressure) via telemetry link, or use an onboard recorder as described in previous work by Mermagen and Clay,[1] Brown et al.,[2] Topper et al.,[3] and Brown et al.[4–6] Another method is to measure in flight motion externally from a stationary location with a camera via shadowgraphs[7] or direct imaging[8] or a combination of radar, shadowgraphs, and sensors.[9] Due to limited time and budget constraints, the method implemented for the firings detailed in this report was designed to minimize risks. Image-based diagnostics were deemed most efficient given our short time frame. The experimental setup was also designed to include evaluation of as much of the Co-Optimization Bluntbody Re-entry Analysis Cobra Mid-Lift-to-Drag Rigid Vehicle (CobraMRV) trajectory as possible within the confines of the Transonic Experimental Facility.

Two flight experiments (FEs) were conducted. The objective of the first, FE 1.1, was to confirm the internal ballistics performance of the gun system and to verify the performance of the sabot design. Two slugs approximating the mass of the

[1] Mermagen WH, Clay WH. The design of a second generation yawsonde. Army Ballistic Research Laboratory (US); 1974 Apr. Report No.: BRL-MR-2368.

[2] Brown TG, Bukowski E, Ilg M, Brandon F. Measurement of in-flight motion characteristics of a high-g launched flare stabilized projectile with on-board telemetry. International Telemetry Conference (ITC); 2007 Nov. Paper No.: 07-1051.

[3] Topper B, Brown T, Bukowski E, Davis B, Hall R, Muller P, Vong T, Brandon F. Feasibility of determining aerodynamic coefficients for a NASA Apollo body with the use of telemetry data from free flight range testing. Army Research Laboratory (US); 2007 Sep. Report No.: ARL-TR-4271.

[4] Brown TG, Harkins T, Don M, Hall R, Davis B. Development and demonstration of a new capability for aerodynamic characterization of medium caliber projectiles. 28th International Symposium on Ballistics; 2014b Sep 22–26; Atlanta, GA.

[5] Brown TG, Schoenenberger M, Bukowski E, Don M, Garner J, Yates L, Hallameyer J. Novel technique to measure simultaneous leeward and windward pressure with correlation to ground-based aerodynamic range measurements. Aeroballistic Range Association Meeting; 2016 Oct; Toledo, Spain.

[6] Brown TG, Sostaric RR, Garcia JA, Harkins TE, Johnson BJ, Decker R. Launch techniques for high angle of attack non-symmetric projectiles and characterization of aerodynamic damping. 69th Aeroballistic Range Association Meeting; 2018 Oct 8–11, Bath, UK.

[7] Murphy C. Data reduction for the free flight spark ranges. Army Ballistic Research Laboratory (US); 1954 Feb. Report No.: BRL Report 900.

[8] Decker R, Kolsch M, Yakimenko O. An automated method for computer vision: analysis of cannon-launched artillery video. Proceedings of the 27th International Ballistics Symposium; 2013; Freiburg, Germany.

[9] Davis B, Guidos B, Harkins T. Complementary roles of spark range and onboard free-flight measurements for projectile development. Army Research Laboratory; 2009 Aug. Report No.: ARL-TR-4910.

scaled MRV models were fired to confirm the 5-kg charge mass would produce desired launch velocities. This was followed by a single-shot evaluation of the sabot design using a surrogate aluminum (Al) MRV shape. The experiment was successful at verifying structural integrety and sabot separation. Physical characteristics of the slugs and the Al MRV launch body are given in Table B-1. Also included are launch characteristics and notes associated with the experiment.

Table B-1 FE 1.1 Al MRV: sabot integrity

FE1.1 - Sabot Integrity (Aluminum MRV)												
Date	Time	TR#	Config.	Launch Mass (kg)	Payload Mass (kg)	Ix (g cm^2)	Iy	Iz	cg (x) (cm - nose)	cg (z) (cm-nose)	Charge Mass (kg)	Velocity (m/s)
9/19/2017		40613	Slug#1	1.78	1.78						5.0	1126.0
9/19/2017		40614	Slug#2	1.782	1.782						5.0	1100.0
9/19/2017		40615	MRV Alum. Model#1	1.626	282.25	604.55	2185.37	2303.64	5.273	-0.284	5.0	1117.0

	FE1.1 - Sabot Integrity (Aluminum MRV)							
TR#	HS 1 (10m)	HS 2 (26)	HS 3 (40)	HS 4 (56)	FF 1	FF 2	Notes	
40613							2 wraps tape to seal	
40614							2 wraps tape to seal	
40615					yes		No grease in grooves, but greased outside, model nose up	vel - radar1, radar2(faint trace low sn), video 35m analysis (703, 1145, 1117)

For the second flight experiment, FE 1.2, scaled CobraMRV flight bodies were designed with physical parameters to mimic center of gravity (CG) location with respect to aerodynamic shape with moments of inertia and mass of the full-scale MRV design. This body design used titanium and included a small void with an Al lid. The void was included in the design to accommodate possible insertion of onboard sensors. The experimental matrix is included in Table B-2. Data not recorded or in question are either left blank or annotated accordingly. Eight MRV rounds were fired. Physical characteristics of each are recorded in Table B-2 along with launch characteristics. A log of the video coverage for each of the eight shots along with notes recorded during the experiment are also included for reference.

Table B-2 FE 1.2 Ti MRV: video characterization

FE1.2 Titanium MRV - Video Characterization												
Date	Time	TR#	Config.	Launch Mass (kg)	Payload Mass (kg)	Ix (g cm^2)	Iy	Iz	cg (x) (cm - nose)	cg (z) (cm-nose)	Charge Mass (kg)	Velocity (m/s)
10/31/2017	1530	40649	MRV#1	1.7755	0.45243	943.24	3402.45	3595.98	5.175	-0.183	5.0	1138.4
11/1/2017	1115	40650	MRV#2	1.7678	0.45036	942.65	3413.99	3597.29	5.154	-0.361	5.0	1113.8
11/1/2017	1337	40651	MRV#3	1.7553	0.44895	923.24	3410.05	3597.80	4.969	-0.350	5.0	1109.3
11/1/2017	1433	40652	MRV#4	1103.7	0.44918	991.01	3287.40	3513.99	4.998	-0.102	5.0	1103.7
11/2/2017	1110	40653	MRV#5	1.7905	0.44794	1008.88	3186.71	3425.04	5.248	0.043	5.0	1116.0
11/2/2017	1157	40654	MRV#6	1.8137	0.44624	982.81	3246.44	3440.94	5.277	-0.086	5.0	1080.0
11/2/2017	1354	40655	MRV#7	1.7715	0.44862	996.54	3260.86	3493.79	5.288	-0.011	5.0	1144.7
11/2/2017	1428	40656	MRV#8	1.7858	0.45376	1019.72	3356.98	3543.68	5.277	0.003	5.0	1094.4

FE1.2 Titanium MRV - Video Characterization								
TR#	HS 1 (10m)	HS 2 (26)	HS 3 (40)	HS 4 (56)	FF 1	FF 2	Notes	
40649	round low	round low	no	no	flat, ran out top	no	low and right, @366m - 37m r, 94m up, 0.5s, 240m, 16m r, 32m up	
40650	yes	yes	no	no	yes outran	no	0.05m/s/s FF1, 50mm@9microsec (10,26m), 15micros 2.8(40m)	adjusted HS1-4 down, but not quite enough, FF1 ret 0.05m/s/m(too low)
40651	yes	yes	yes	yes	yes	no	5m/s/m, 40,56m bottom frame,	adjusted 40, 56m to top 3.5' of 12' pole
40652	yes	yes	yes	yes	yes	outran	5m/s/m, 40,56m bottom frame,	tightened fov (40)
40653	yes	yes	yes	yes	yes	?		
40654	yes	yes	yes	yes	yes	?		
40655	yes	yes	yes	yes	great	?	Great Flight Follower	
40656	yes	yes	yes	yes	didn't save	late	Lost FF1 - cut cable	

Appendix C. Mechanical Fabrication

Fabricated hardware was accomplished through translating the computer-aided design files to G-Code for controlling the milling machine. Usually this is an automated process but at times requires manual modifications as needed. Initially, an aluminum (Al) model was constructed to ensure the external shape consistencey. The final shape of the Co-Optimization Bluntbody Re-entry Analysis Mid-Lift-to-Drag Rigid Vehicle (CobraMRV) is shown in Fig. C-1.

Fig. C-1 CobraMRV 1:200 scale model as fabricated

In general, the Al and titanium (Ti) parts met expected tolerance specifications as built. The Al body was measured to have a root mean square (RMS) error of 0.140 mm and average error of 0.096 mm given 3-D comparison results. In five 2-D comparisons of the Al body, measurements varied by a maximum of 0.051–0.610 mm with a standard deviation of approximately 0.152 mm or less. The Ti body was measured to have RMS error of 0.302 mm and average error of 0.284 mm given 3-D comparison results. In four 2-D comparisons of the Ti body, measurements varied by a maximum of 0.051–0.787 mm with a standard deviation of approximately 0.152 mm or less.

C.1 CobraMRV Inspection

Date Inspected: 5/25/2017
Date Generated: 5/25/2017,
12:46 pm

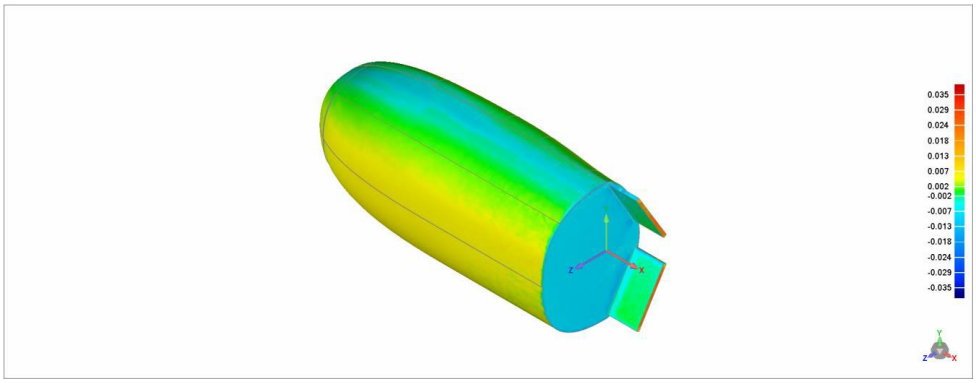

Author: Ryan Gilley

Client Name: ARL GTB
Reference Model: Cobra_MRV_scaled (2017-01-19)
Test Model: CobraMRV Aluminum

Alignment Statistics: **Alignment Name: Best fit alignment: Cobra_MRV_scaled(2017-01-19) (1)**

RMS Error: 0.005511817in
Model Max. Length: 4.319952717in
Average Error: 0.003760457in

3D Comparison Results

Reference Model	Cobra_MRV_scaled(2017-01-19)
Test Model	CobraMRV Aluminum
No. of Data Points	572970

Tolerance Type	3D Deviation
Units	In
Max. Critical	0.035
Max. Nominal	0.002
Min. Nominal	-0.002
Min. Critical	-0.035

Deviation	
Max. Upper Deviation	0.024
Max. Lower Deviation	-0.035
Average Deviation	0.004 / -0.003
Standard Deviation	0.004

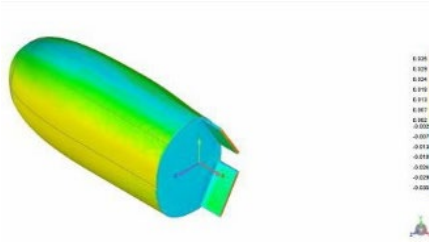

Deviation Distribution

>=Min	<Max	Points	%
-0.035	-0.029	1	0.000
-0.029	-0.024	1	0.000
-0.024	-0.018	33	0.006
-0.018	-0.013	513	0.090
-0.013	-0.007	15274	2.666
-0.007	-0.002	100330	17.511
-0.002	0.002	106847	18.648
0.002	0.007	349108	60.930
0.007	0.013	658	0.115
0.013	0.018	30	0.005
0.018	0.024	166	0.029
0.024	0.029	8	0.001
0.029	0.035	0	0.000

Out of Upper Critical	0	0.000
Out of Lower Critical	1	0.000

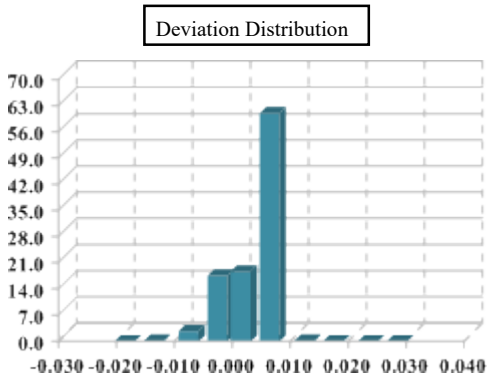

Standard Deviations

Distribution (+/-	Points	%
-6 * Std. Dev.	97	0.017
-5 * Std. Dev.	361	0.063
-4 * Std. Dev.	2528	0.441
-3 * Std. Dev.	21355	3.727
-2 * Std. Dev.	83361	14.549
-1 * Std. Dev.	114641	20.008
1 * Std. Dev.	303855	53.032
2 * Std. Dev.	46484	8.113
3 * Std. Dev.	84	0.015
4 * Std. Dev.	17	0.003
5 * Std. Dev.	45	0.008
6 * Std. Dev.	142	0.025

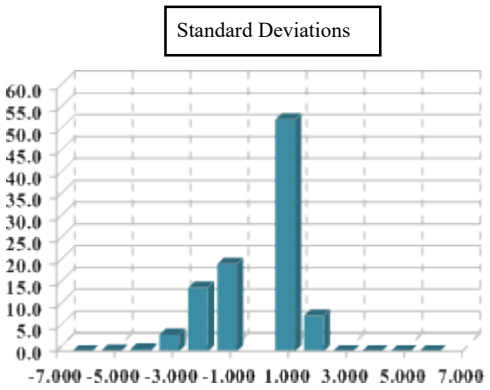

Annotated View: Annotation View 1

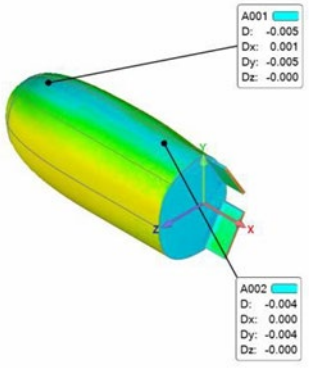

CSYS: Annotation View 1 (Units: in)

Name	Dev	Ref X	Ref Y	Ref Z	Dev Radius	Dev X	Dev Y	Dev Z	Meas. X	Meas. Y	Meas. Z	Normal X	Normal Y	Normal Z
A001	-0.005	-3.158	0.731	0.163	0.039	0.001	-0.005	-0.000	-3.157	0.726	0.163	-0.249	0.966	0.073
A002	-0.004	-0.671	0.861	0.175	0.039	0.000	-0.004	-0.000	-0.671	0.857	0.174	0.000	0.998	0.066

Annotated View: Annotation View 2

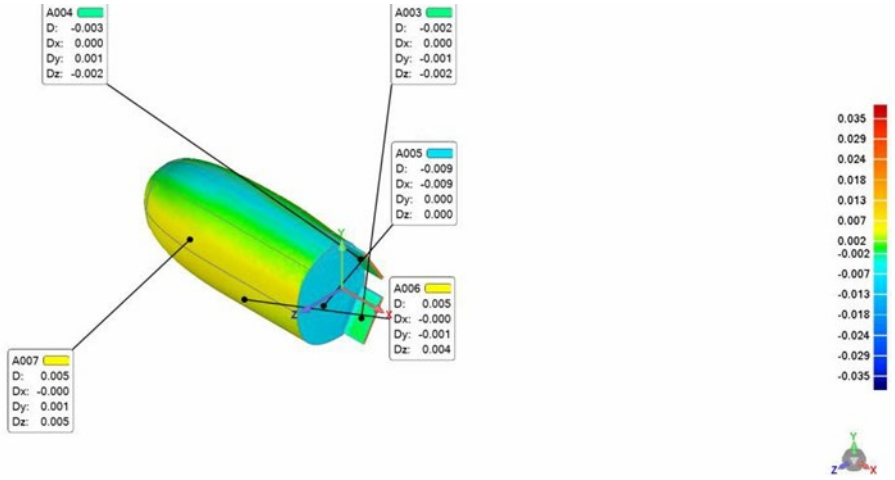

CSYS: Annotation View 2 (Units: in)

Name	Dev	Ref X	Ref Y	Ref Z	Dev Radius	Dev X	Dev Y	Dev Z	Meas. X	Meas. Y	Meas. Z	Normal X	Normal Y	Normal Z
A003	-0.002	0.218	-0.543	-0.197	0.039	0.000	-0.001	-0.002	0.218	-0.544	-0.199	0.000	0.515	0.857
A004	-0.003	0.205	0.549	-0.194	0.039	0.000	0.001	-0.002	0.205	0.550	-0.196	0.000	-0.515	0.857
A005	-0.009	0.000	-0.125	0.392	0.039	-0.009	0.000	0.000	-0.009	-0.125	0.392	1.000	0.000	0.000
A006	0.005	-1.182	-0.341	0.907	0.039	0.000	-0.001	0.004	-1.182	-0.342	0.911	0.000	-0.274	0.962
A007	0.005	-2.335	0.198	0.918	0.039	-0.000	0.001	0.005	-2.335	0.199	0.923	-0.062	0.129	0.990

Annotated View: Annotation View 3

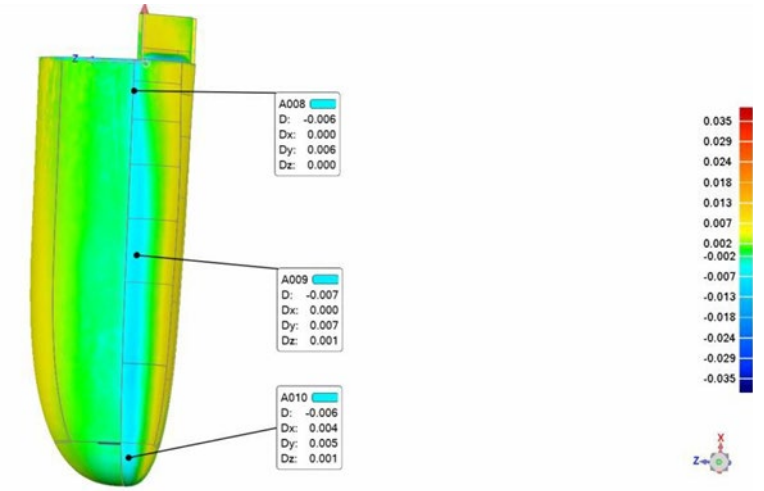

CSYS: Annotation View 3 (Units: in)

Name	Dev	Ref X	Ref Y	Ref Z	Dev Radius	Dev X	Dev Y	Dev Z	Measured X	Measured Y	Measured Z	Normal X	Normal Y	Normal Z
A008	-0.006	-0.291	-0.866	-0.009	0.039	0.000	0.006	0.000	-0.291	-0.860	-0.008	-0.003	-0.997	-0.076
A009	-0.007	-1.798	-0.862	-0.096	0.039	0.000	0.007	0.001	-1.798	-0.856	-0.096	-0.008	-0.996	-0.094
A010	-0.006	-3.650	-0.522	-0.072	0.039	0.004	0.005	0.001	-3.647	-0.517	-0.071	-0.579	-0.803	-0.137

Annotated View: Annotation View 4

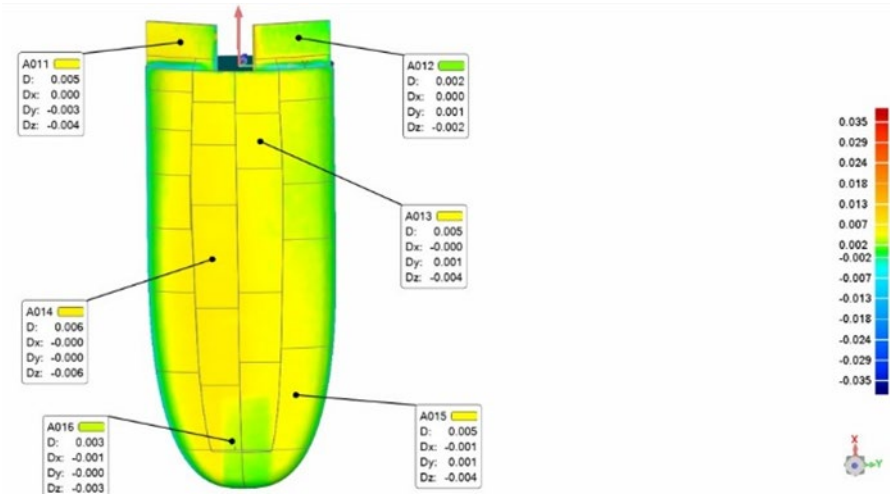

CSYS: Annotation View 4 (Units: in)

Name	Dev	Ref X	Ref Y	Ref Z	Dev Radius	Dev X	Dev Y	Dev Z	Measured X	Measured Y	Measured Z	Normal X	Normal Y	Normal Z
A011	0.005	0.247	-0.518	-0.261	0.039	0.000	-0.003	-0.004	0.247	-0.521	-0.266	0.000	-0.522	-0.853
A012	0.002	0.280	0.574	-0.228	0.039	0.000	0.001	-0.002	0.280	0.575	-0.230	0.000	0.522	-0.853
A013	0.005	-0.652	0.226	-0.453	0.039	-0.000	0.001	-0.004	-0.652	0.227	-0.457	-0.002	0.122	-0.993
A014	0.006	-1.740	-0.235	-0.427	0.039	-0.000	-0.000	-0.006	-1.740	-0.235	-0.433	-0.033	-0.039	-0.999
A015	0.005	-3.006	0.514	-0.329	0.039	-0.001	0.001	-0.004	-3.007	0.515	-0.333	-0.117	0.266	-0.957
A016	0.003	-3.434	-0.086	-0.310	0.039	-0.001	-0.000	-0.003	-3.435	-0.086	-0.313	-0.202	-0.008	-0.979

Annotated View: Annotation ALL

Name	Dev	Ref X	Ref Y	Ref Z	Dev Radius	Dev X	Dev Y	Dev Z	Measured X	Measured Y	Measured Z	Normal X	Normal Y	Normal Z
A001	-0.005	-3.158	0.731	0.163	0.039	0.001	-0.005	-0.000	-3.157	0.726	0.163	-0.249	0.966	0.073
A002	-0.004	-0.671	0.861	0.175	0.039	0.000	-0.004	-0.000	-0.671	0.857	0.174	0.000	0.998	0.066
A003	-0.002	0.218	-0.543	-0.197	0.039	0.000	-0.001	-0.002	0.218	-0.544	-0.199	0.000	0.515	0.857
A004	-0.003	0.205	0.549	-0.194	0.039	0.000	0.001	-0.002	0.205	0.550	-0.196	0.000	-0.515	0.857
A005	-0.009	0.000	-0.125	0.392	0.039	-0.009	0.000	0.000	-0.009	-0.125	0.392	1.000	0.000	0.000
A006	0.005	-1.182	-0.341	0.907	0.039	0.000	-0.001	0.004	-1.182	-0.342	0.911	0.000	-0.274	0.962
A007	0.005	-2.335	0.198	0.918	0.039	-0.000	0.001	0.005	-2.335	0.199	0.923	-0.062	0.129	0.990
A008	-0.006	-0.291	-0.866	-0.009	0.039	0.000	0.006	0.000	-0.291	-0.860	-0.008	-0.003	-0.997	-0.076
A009	-0.007	-1.798	-0.862	-0.096	0.039	0.000	0.007	0.001	-1.798	-0.856	-0.096	-0.008	-0.996	-0.094
A010	-0.006	-3.650	-0.522	-0.072	0.039	0.004	0.005	0.001	-3.647	-0.517	-0.071	-0.579	-0.803	-0.137
A011	0.005	0.247	-0.518	-0.261	0.039	0.000	-0.003	-0.004	0.247	-0.521	-0.266	0.000	-0.522	-0.853
A012	0.002	0.280	0.574	-0.228	0.039	0.000	0.001	-0.002	0.280	0.575	-0.230	0.000	0.522	-0.853
A013	0.005	-0.652	0.226	-0.453	0.039	-0.000	0.001	-0.004	-0.652	0.227	-0.457	-0.002	0.122	-0.993
A014	0.006	-1.740	-0.235	-0.427	0.039	-0.000	-0.000	-0.006	-1.740	-0.235	-0.433	-0.033	-0.039	-0.999
A015	0.005	-3.006	0.514	-0.329	0.039	-0.001	0.001	-0.004	-3.007	0.515	-0.333	-0.117	0.266	-0.957
A016	0.003	-3.434	-0.086	-0.310	0.039	-0.001	-0.000	-0.003	-3.435	-0.086	-0.313	-0.202	-0.008	-0.979

2-D Compare View: 2-D Comparison 2

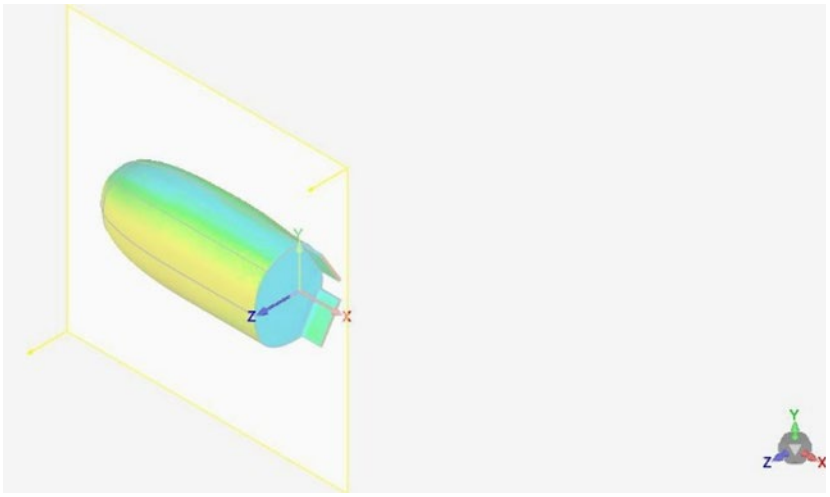

Z = 0.229 in

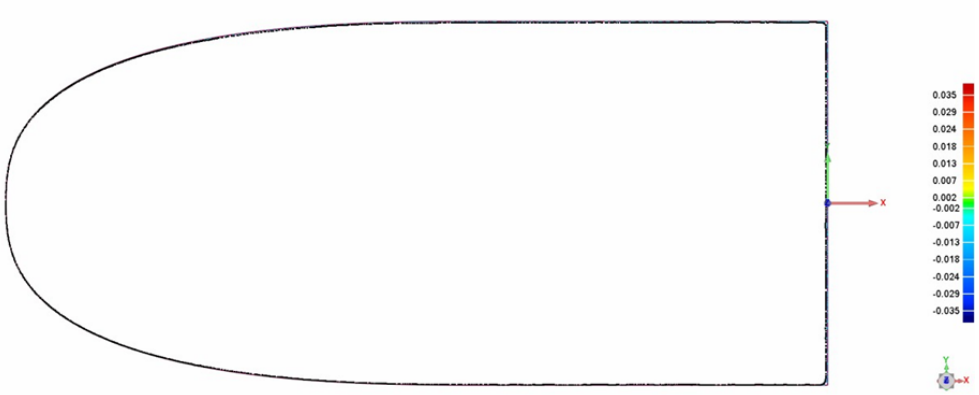

Method: Planar Deviation
Whisker Scale: 1.000

2D Comparison Results CSYS: World CSYS

Reference Model	Cobra_MRV_scaled(2017-01-19)
Test Model	CobraMRV Aluminum

Name	2D Comparison 2
Location	Z = 0.229 in
No. of Data Points	2674

Units	in
Max. Critical	0.035
Max. Nominal	0.002
Min. Nominal	-0.002
Min. Critical	-0.035

Deviation	
Max Dev +	0.002
Max Dev -	-0.012
Standard Deviation	0.002

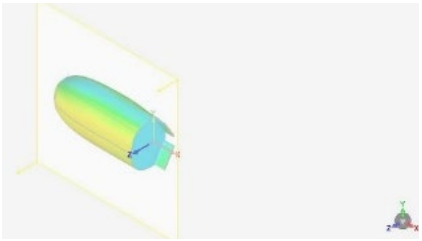

Percentage Deviations

>=Min	<Max	Points	%
-0.035	-0.029	0	0.000
-0.029	-0.024	0	0.000
-0.024	-0.018	0	0.000
-0.018	-0.013	0	0.000
-0.013	-0.007	286	10.696
-0.007	-0.002	1867	69.820
-0.002	0.002	521	19.484
0.002	0.007	0	0.000
0.007	0.013	0	0.000
0.013	0.018	0	0.000
0.018	0.024	0	0.000
0.024	0.029	0	0.000
0.029	0.035	0	0.000

Out of Upper Critical +	0	0.000
Out of Lower Critical -	0	0.000

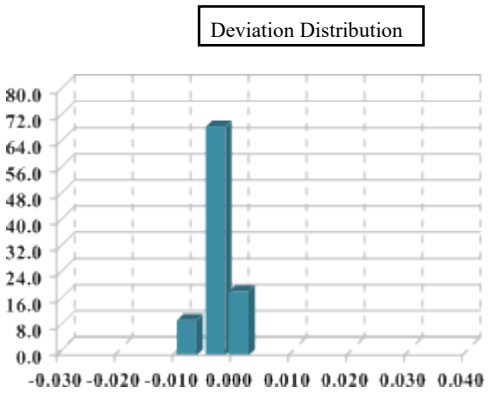

Standard Deviations

Distribution (+/-)	Points	%
-6 * Std. Dev.	1	0.037
-5 * Std. Dev.	10	0.374
-4 * Std. Dev.	274	10.247
-3 * Std. Dev.	577	21.578
-2 * Std. Dev.	745	27.861
-1 * Std. Dev.	936	35.004
1 * Std. Dev.	131	4.899
2 * Std. Dev.	0	0.000
3 * Std. Dev.	0	0.000
4 * Std. Dev.	0	0.000
5 * Std. Dev.	0	0.000
6 * Std. Dev.	0	0.000

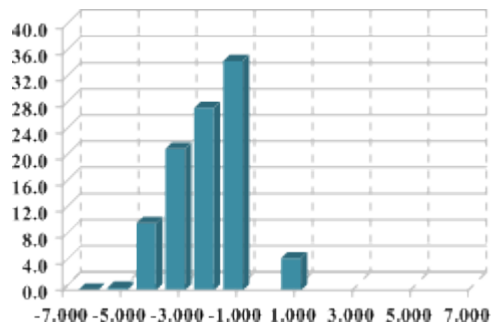

2-D Compare View: 2-D Comparison 3

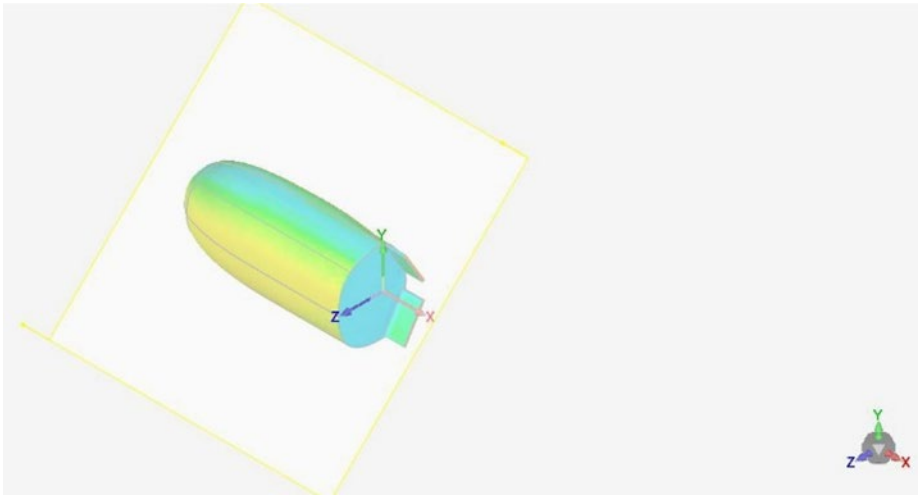

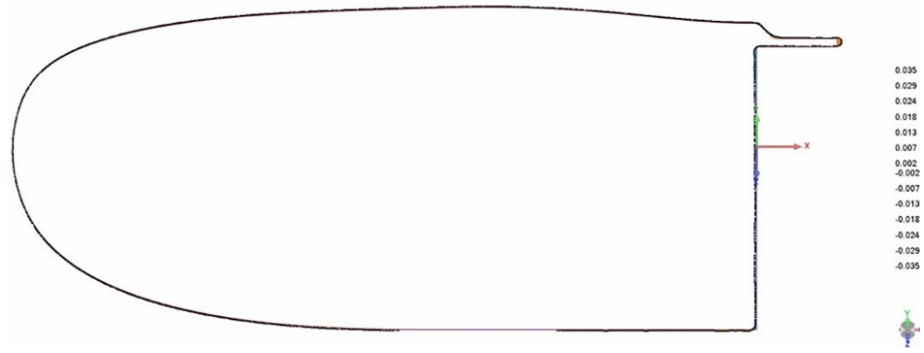

Method: Planar Deviation Whisker Scale: 1.000

2D Comparison Results CSYS: World CSYS

Reference Model	Cobra_MRV_scaled(2017-01- 19)
Test Model	CobraMRV Aluminum

Name	2D Comparison 3
Location	
No. of Data Points	3070

Units	in
Max. Critical	0.035
Max. Nominal	0.002
Min. Nominal	-0.002
Min. Critical	-0.035

Deviation	
Max Dev +	0.022
Max Dev -	-0.013
Standard Deviation	0.004

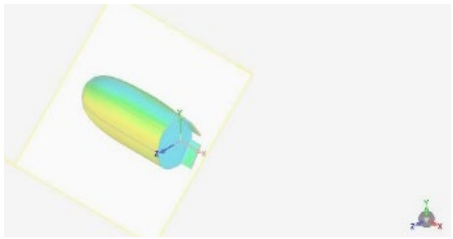

Percentage Deviations

>=Min	<Max	Points	%
-0.035	-0.029	0	0.000
-0.029	-0.024	0	0.000
-0.024	-0.018	0	0.000
-0.018	-0.013	0	0.000
-0.013	-0.007	250	8.143
-0.007	-0.002	107	3.485
-0.002	0.002	190	6.189
0.002	0.007	2500	81.433
0.007	0.013	12	0.391
0.013	0.018	6	0.195
0.018	0.024	5	0.163
0.024	0.029	0	0.000
0.029	0.035	0	0.000

Out of Upper Critical +	0	0.000
Out of Lower Critical -	0	0.000

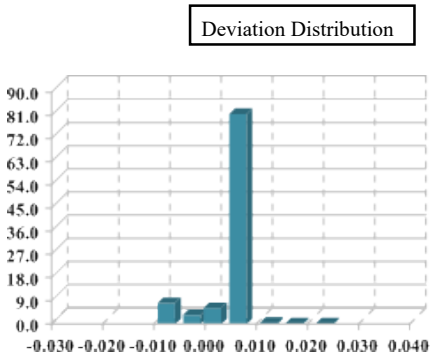

Standard Deviations

Distribution (+/-)	Points	%
-6 * Std. Dev.	0	0.000
-5 * Std. Dev.	0	0.000
-4 * Std. Dev.	3	0.098
-3 * Std. Dev.	230	7.492
-2 * Std. Dev.	48	1.564
-1 * Std. Dev.	99	3.225
1 * Std. Dev.	1123	36.580
2 * Std. Dev.	1548	50.423
3 * Std. Dev.	8	0.261
4 * Std. Dev.	1	0.033
5 * Std. Dev.	6	0.195
6 * Std. Dev.	4	0.130

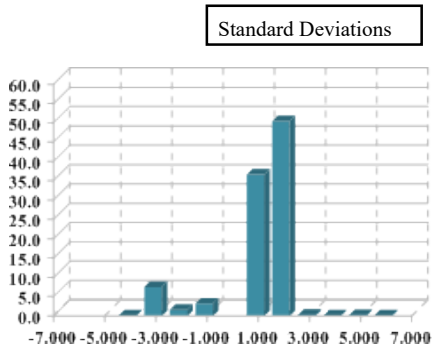

2D Compare View: 2D Comparison 4

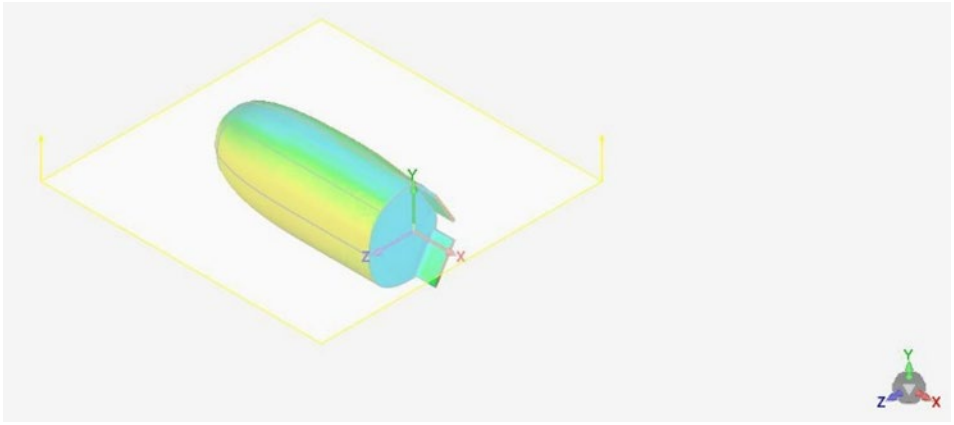

Y = 0.162 in

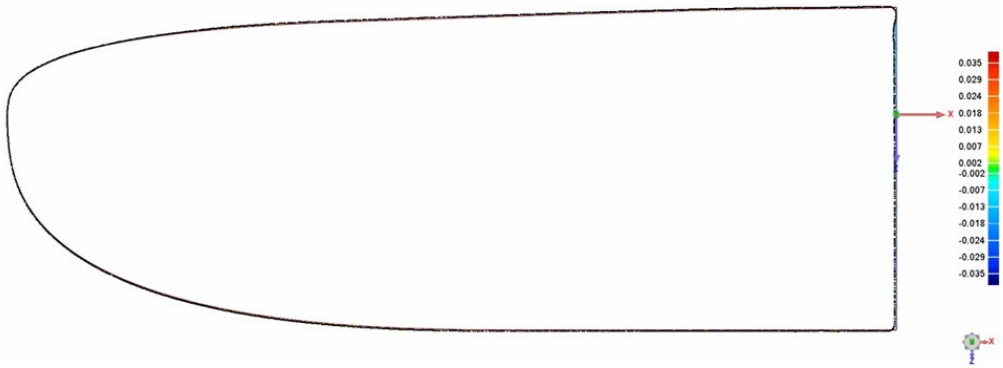

Method: Planar Deviation Whisker Scale: 1.000

2D Comparison Results CSYS: World CSYS

Reference Model	Cobra_MRV_scaled(2017-01- 19)
Test Model	CobraMRV Aluminum

Name	2D Comparison 4
Location	Y = 0.162 in
No. of Data Points	2878

Units	in
Max. Critical	0.035
Max. Nominal	0.002
Min. Nominal	-0.002
Min. Critical	-0.035

Deviation	
Max Dev +	0.006
Max Dev -	-0.014
Standard Deviation	0.004

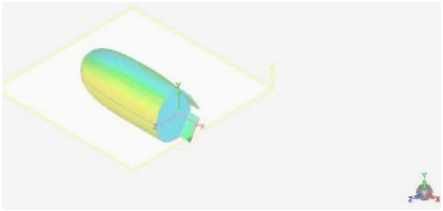

Percentage Deviations

>=Min	<Max	Points	%
-0.035	-0.029	0	0.000
-0.029	-0.024	0	0.000
-0.024	-0.018	0	0.000
-0.018	-0.013	5	0.174
-0.013	-0.007	241	8.374
-0.007	-0.002	16	0.556
-0.002	0.002	175	6.081
0.002	0.007	2441	84.816
0.007	0.013	0	0.000
0.013	0.018	0	0.000
0.018	0.024	0	0.000
0.024	0.029	0	0.000
0.029	0.035	0	0.000

Out of Upper Critical +	0	0.000
Out of Lower Critical -	0	0.000

Deviation Distribution

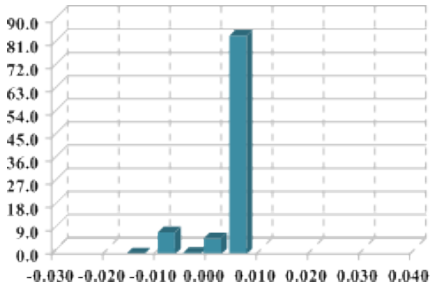

Standard Deviations

Distribution (+/-)	Points	%
-6 * Std. Dev.	0	0.000
-5 * Std. Dev.	0	0.000
-4 * Std. Dev.	13	0.452
-3 * Std. Dev.	232	8.061
-2 * Std. Dev.	7	0.243
-1 * Std. Dev.	44	1.529
1 * Std. Dev.	585	20.327
2 * Std. Dev.	1997	69.388
3 * Std. Dev.	0	0.000
4 * Std. Dev.	0	0.000
5 * Std. Dev.	0	0.000
6 * Std. Dev.	0	0.000

Standard Deviations

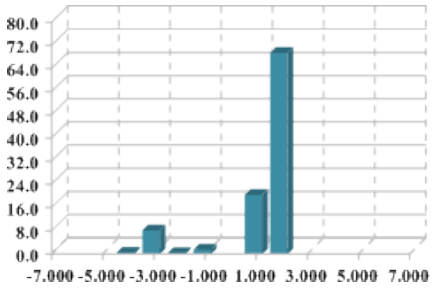

2D Compare View: 2D Comparison 5

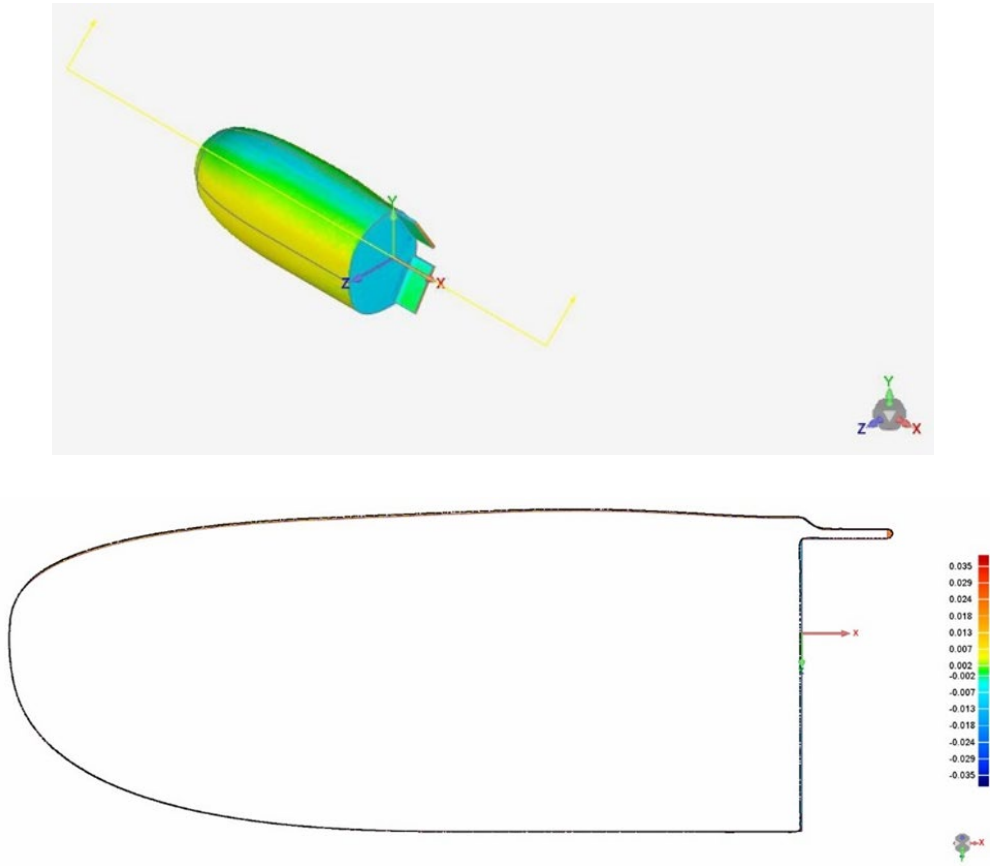

Method: Planar Deviation Whisker Scale: 1.000

2D Comparison Results CSYS: World CSYS

Reference Model	Cobra_MRV_scaled (2017-01- 19)
Test Model	CobraMRV Aluminum

Name	2D Comparison 5
Location	
No. of Data Points	3226

Units	in
Max. Critical	0.035
Max. Nominal	0.002
Min. Nominal	-0.002
Min. Critical	-0.035

Deviation	
Max Dev +	0.024
Max Dev -	-0.012
Standard Deviation	0.005

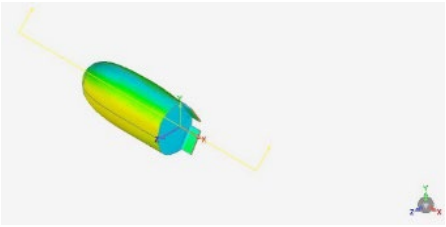

Percentage Deviations

>=Min	<Max	Points	%
-0.035	-0.029	0	0.000
-0.029	-0.024	0	0.000
-0.024	-0.018	0	0.000
-0.018	-0.013	0	0.000
-0.013	-0.007	284	8.803
-0.007	-0.002	112	3.472
-0.002	0.002	1352	41.909
0.002	0.007	796	24.675
0.007	0.013	668	20.707
0.013	0.018	5	0.155
0.018	0.024	9	0.279
0.024	0.029	0	0.000
0.029	0.035	0	0.000

Out of Upper Critical +	0	0.000
Out of Lower Critical -	0	0.000

Deviation Distribution

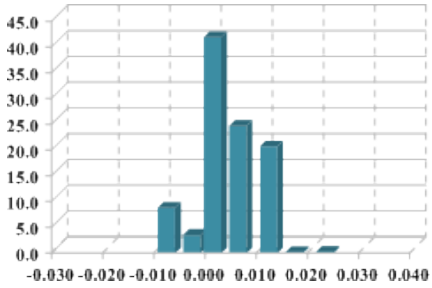

Standard Deviations

Distribution (+/-)	Points	%
-6 * Std. Dev.	0	0.000
-5 * Std. Dev.	0	0.000
-4 * Std. Dev.	0	0.000
-3 * Std. Dev.	22	0.682
-2 * Std. Dev.	290	8.989
-1 * Std. Dev.	192	5.952
1 * Std. Dev.	1580	48.977
2 * Std. Dev.	1127	34.935
3 * Std. Dev.	1	0.031
4 * Std. Dev.	5	0.155
5 * Std. Dev.	9	0.279
6 * Std. Dev.	0	0.000

Standard Deviations

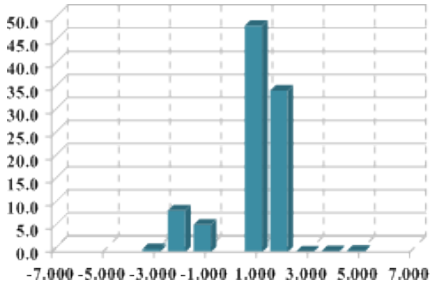

Location Set: 2D Comparison 1 Upper and Lower Deviations

Name	Dev	Ref X	Ref Y	Ref Z	Radius	Dev X	Dev Y	Dev Z	Measured X	Measured Y	Measured Z
2D Comparison 1 Lower Dev.	-0.012	0.000	-0.841	0.229	n/a	-0.012	0.000	0.000	-0.012	-0.841	0.229
2D Comparison 1 Upper Dev.	0.002	-3.878	0.006	0.229	n/a	-0.002	0.000	0.000	-3.880	0.006	0.229

Location Set: 2D Comparison 2 Upper and Lower Deviations

Name	Dev	Ref X	Ref Y	Ref Z	Radius	Dev X	Dev Y	Dev Z	Measured X	Measured Y	Measured Z
2D Comparison 2 Lower Dev.	-0.012	0.000	-0.841	0.229	n/a	-0.012	0.000	0.000	-0.012	-0.841	0.229
2D Comparison 2 Upper Dev.	0.002	-3.878	0.006	0.229	n/a	-0.002	0.000	0.000	-3.880	0.006	0.229

Location Set: 2D Comparison 3 Upper and Lower Deviations

Name	Dev	Ref X	Ref Y	Ref Z	Radius	Dev X	Dev Y	Dev Z	Measured X	Measured Y	Measured Z
2D Comparison 3 Lower Dev.	-0.013	0.000	0.510	-0.187	n/a	-0.013	0.000	0.000	-0.013	0.510	-0.187
2D Comparison 3 Upper Dev.	0.022	0.422	0.547	-0.223	n/a	0.022	0.000	0.000	0.444	0.547	-0.223

Location Set: 2D Comparison 4 Upper and Lower Deviations

Name	Dev	Ref X	Ref Y	Ref Z	Radius	Dev X	Dev Y	Dev Z	Measured X	Measured Y	Measured Z
2D Comparison 4 Lower Dev.	-0.014	0.000	0.162	-0.342	n/a	-0.014	0.000	0.000	-0.014	0.162	-0.342
2D Comparison 4 Upper Dev.	0.006	-0.255	0.162	0.939	n/a	0.000	0.000	0.006	-0.255	0.162	0.945

Location Set: 2D Comparison 5 Upper and Lower Deviations

Name	Dev	Ref X	Ref Y	Ref Z	Radius	Dev X	Dev Y	Dev Z	Measured X	Measured Y	Measured Z
2D Comparison 5 lower Dev.	-0.012	0.000	-0.291	-0.291	n/a	-0.012	0.000	0.000	-0.012	-0.291	-0.291
2D Comparison 5 Upper Dev.	0.024	0.422	-0.345	-0.345	n/a	0.024	0.000	0.000	0.446	-0.345	-0.345

C.2 Laser Scan Results: Design Comparison to Fabricated Hardware (Titanium)

Titanium fabrication topographical measurments.

CobraMRV Inspection

Date Inspected: 5/25/2017
Date Generated: 5/25/2017, 1:13 pm

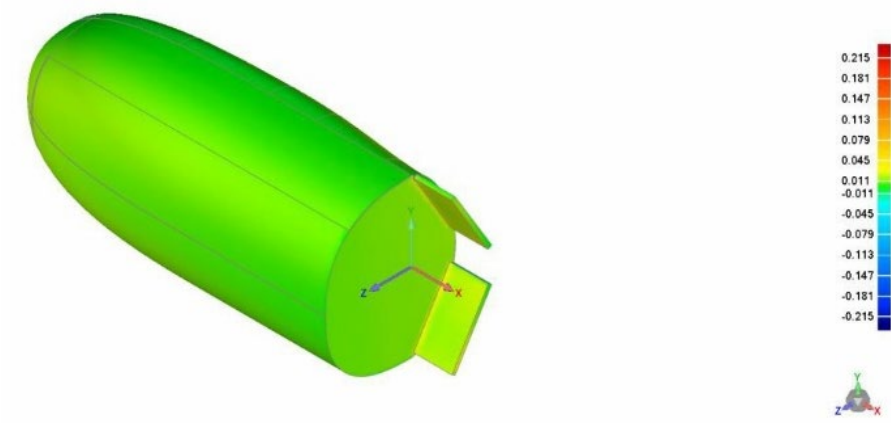

Author: Ryan Gilley
Client Name: ARL GTB

Reference Model: Cobra_MRV_scaled(2017-01-19)
Test Model: CobraMRV Titanium

Alignment Statistics: **Alignment Name: Best fit alignment: Cobra_MRV_scaled(2017-01-19) (1)**

RMS Error: 0.011871525in
Model Max. Length: 4.319952717in
Average Error: 0.011189016in

3D Comparison Results

Reference Model	Cobra_MRV_scaled(2017-01-19)
Test Model	CobraMRV Titanium
No. of Data Points	591023

Tolerance Type	3D Deviation
Units	in
Max. Critical	0.215
Max. Nominal	0.011
Min. Nominal	-0.011
Min. Critical	-0.215

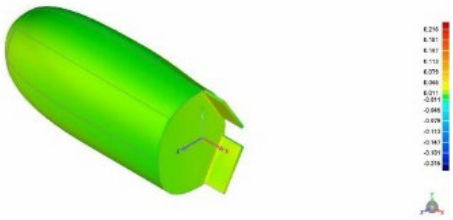

Deviation	
Max. Upper Deviation	0.207
Max. Lower Deviation	-0.215
Average Deviation	0.012 / -0.003
Standard Deviation	0.007

Deviation Distribution

>=Min	<Max	Points	%
-0.215	-0.181	2	0.000
-0.181	-0.147	3	0.001
-0.147	-0.113	1	0.000
-0.113	-0.079	0	0.000
-0.079	-0.045	2	0.000
-0.045	-0.011	1930	0.327
-0.011	0.011	257203	43.518
0.011	0.045	331877	56.153
0.045	0.079	0	0.000
0.079	0.113	0	0.000
0.113	0.147	0	0.000
0.147	0.181	3	0.001
0.181	0.215	1	0.000
Out of Upper Critical		0	0.000
Out of Lower Critical		1	0.000

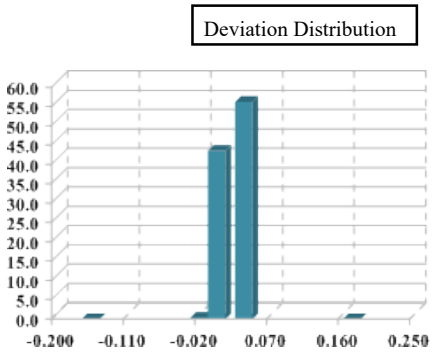

Standard Deviations

Distribution (+/-)	Points	%
-6 * Std. Dev.	160	0.027
-5 * Std. Dev.	734	0.124
-4 * Std. Dev.	1180	0.200
-3 * Std. Dev.	9564	1.618
-2 * Std. Dev.	99745	16.877
-1 * Std. Dev.	146227	24.741
1 * Std. Dev.	243949	41.276
2 * Std. Dev.	88521	14.978
3 * Std. Dev.	908	0.154
4 * Std. Dev.	31	0.005
5 * Std. Dev.	0	0.000
6 * Std. Dev.	4	0.001

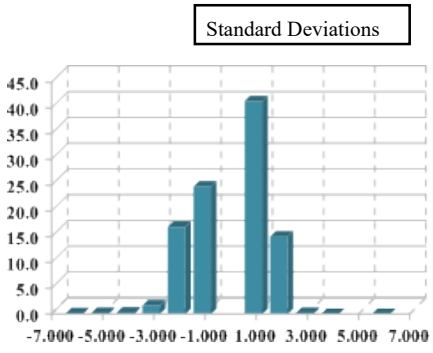

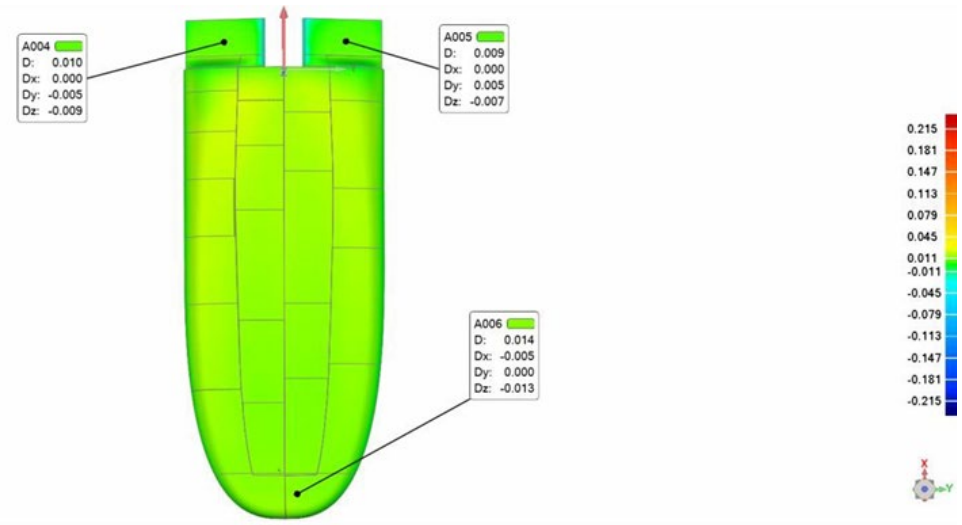

Units: in

CSYS: Annotation View 1

Name	Dev	Ref X	Ref Y	Ref Z	Dev Radius	Dev X	Dev Y	Dev Z	Meas. X	Meas. Y	Meas. Z	Normal X	Normal Y	Normal Z
A004	0.010	0.225	-0.518	-0.261	0.039	0.000	-0.005	-0.009	0.225	-0.524	-0.270	0.000	-0.522	-0.853
A005	0.009	0.232	0.540	-0.248	0.039	0.000	0.005	-0.007	0.232	0.544	-0.256	0.000	0.522	-0.853
A006	0.014	-3.695	0.107	-0.236	0.039	-0.005	0.000	-0.013	-3.700	0.108	-0.249	-0.372	0.022	-0.928

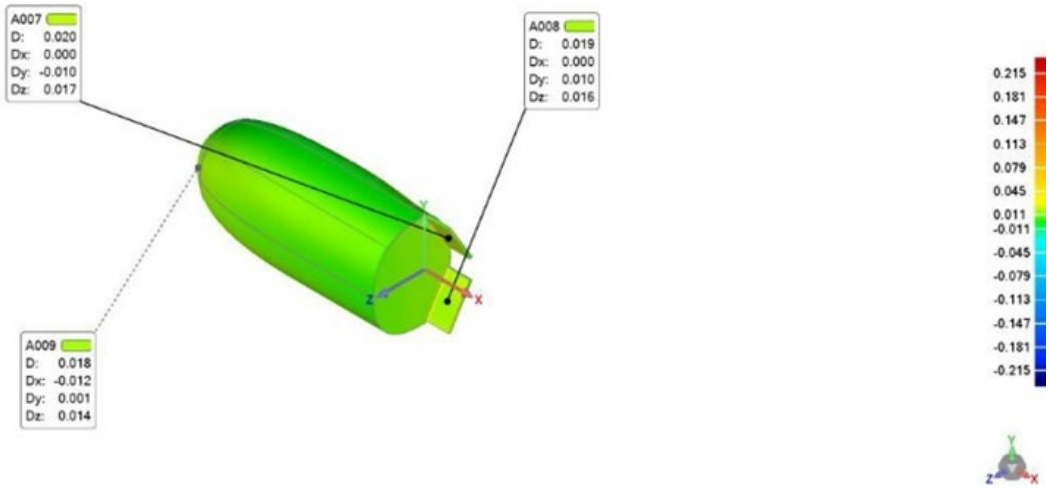

Units: in

CSYS: Annotation View 2

Name	Dev	Ref X	Ref Y	Ref Z	Dev Radius	Dev X	Dev Y	Dev Z	Meas. X	Meas. Y	Meas. Z	Normal X	Normal Y	Normal Z
A007	0.020	0.225	0.501	-0.222	0.039	0.000	-0.010	0.017	0.225	0.491	-0.205	0.000	-0.515	0.857
A008	0.019	0.208	-0.515	-0.214	0.039	0.000	0.010	0.016	0.208	-0.506	-0.198	0.000	0.515	0.857
A009	0.018	-3.667	0.077	0.558	0.039	-0.012	0.001	0.014	-3.679	0.078	0.572	-0.637	0.047	0.769

Annotated View: All Units: in

Name	Dev	Ref X	Ref Y	Ref Z	Dev Radius	Dev X	Dev Y	Dev Z	Meas. X	Meas. Y	Meas. Z	Normal X	Normal Y	Normal Z
A004	0.010	0.225	-0.518	-0.261	0.039	0.000	-0.005	-0.009	0.225	-0.524	-0.270	0.000	-0.522	-0.853
A005	0.009	0.232	0.540	-0.248	0.039	0.000	0.005	-0.007	0.232	0.544	-0.256	0.000	0.522	-0.853
A006	0.014	-3.695	0.107	-0.236	0.039	-0.005	0.000	-0.013	-3.700	0.108	-0.249	-0.372	0.022	-0.928
A007	0.020	0.225	0.501	-0.222	0.039	0.000	-0.010	0.017	0.225	0.491	-0.205	0.000	-0.515	0.857
A008	0.019	0.208	-0.515	-0.214	0.039	0.000	0.010	0.016	0.208	-0.506	-0.198	0.000	0.515	0.857
A009	0.018	-3.667	0.077	0.558	0.039	-0.012	0.001	0.014	-3.679	0.078	0.572	-0.637	0.047	0.769

2D Compare View: 2D Comparison 1

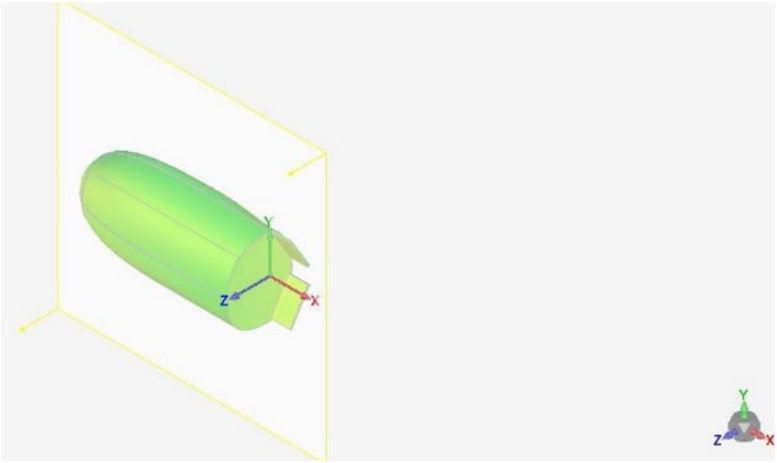

Z = 0.000 in

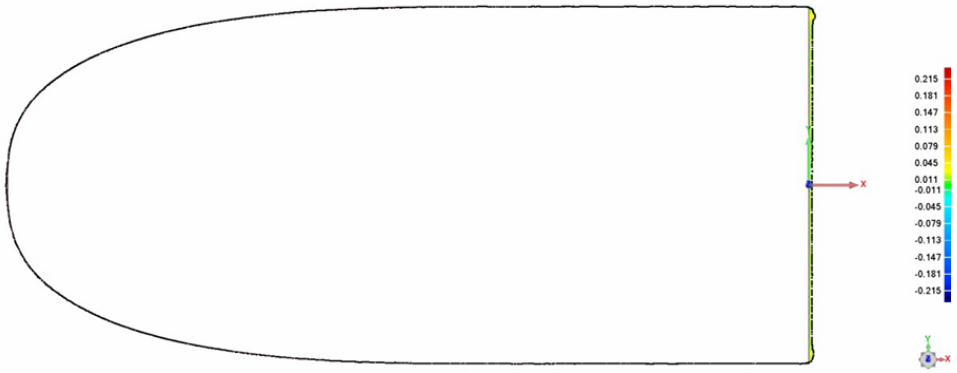

Method: Planar Deviation Whisker Scale: 1.000

2D Comparison Results CSYS: World CSYS

Reference Model	Cobra_MRV_scaled(2017 01_19)
Test Model	CobraMRV Titanium

Name	2D Comparison 1
Location	Z = 0.000 in
No. of Data Points	2938

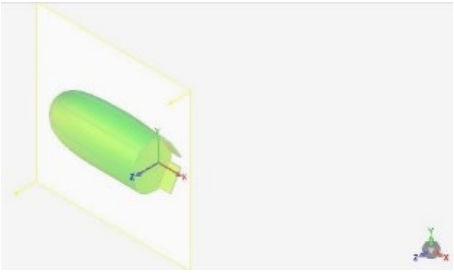

Units	in
Max. Critical	0.215
Max. Nominal	0.011
Min. Nominal	-0.011
Min. Critical	-0.215

Deviation	
Max Dev +	0.031
Max Dev -	-0.005
Standard Deviation	0.005

Percentage Deviations

>=Min	<Max	Points	%
-0.215	-0.181	0	0.000
-0.181	-0.147	0	0.000
-0.147	-0.113	0	0.000
-0.113	-0.079	0	0.000
-0.079	-0.045	0	0.000
-0.045	-0.011	0	0.000
-0.011	0.011	2619	89.142
0.011	0.045	319	10.858
0.045	0.079	0	0.000
0.079	0.113	0	0.000
0.113	0.147	0	0.000
0.147	0.181	0	0.000
0.181	0.215	0	0.000

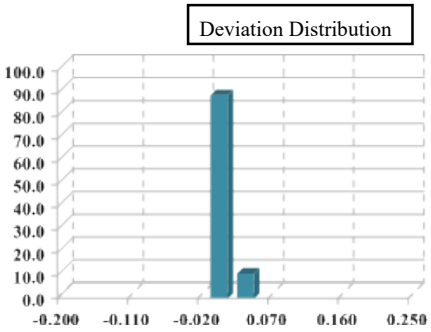

Out of Upper Critical +	0	0.000
Out of Lower Critical -	0	0.000

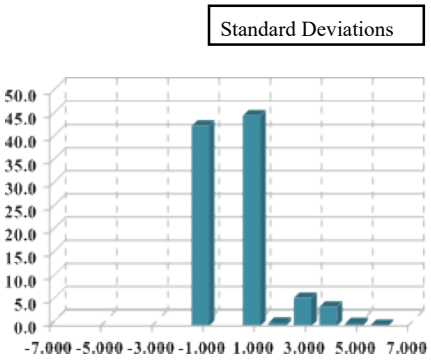

Standard Deviations

Distribution (+/-)	Points	%
-6 * Std. Dev.	0	0.000
-5 * Std. Dev.	0	0.000
-4 * Std. Dev.	0	0.000
-3 * Std. Dev.	0	0.000
-2 * Std. Dev.	0	0.000
-1 * Std. Dev.	1268	43.159
1 * Std. Dev.	1332	45.337
2 * Std. Dev.	18	0.613
3 * Std. Dev.	177	6.025
4 * Std. Dev.	121	4.118
5 * Std. Dev.	17	0.579
6 * Std. Dev.	5	0.170

2D Compare View: 2D
Comparison 2

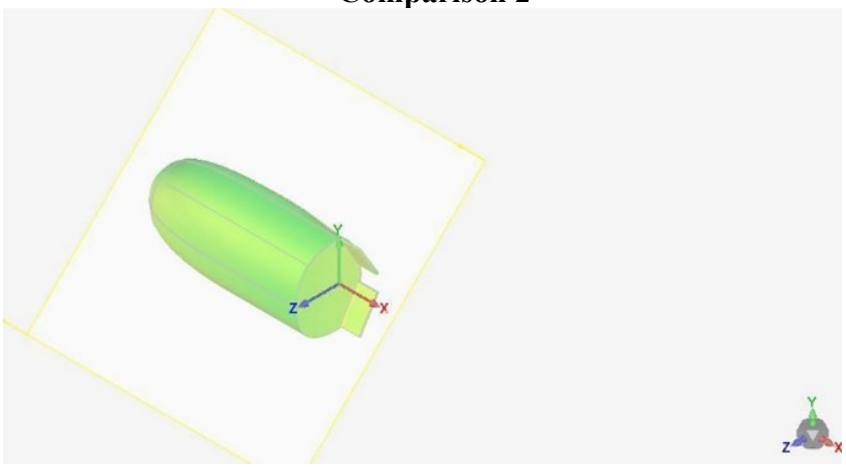

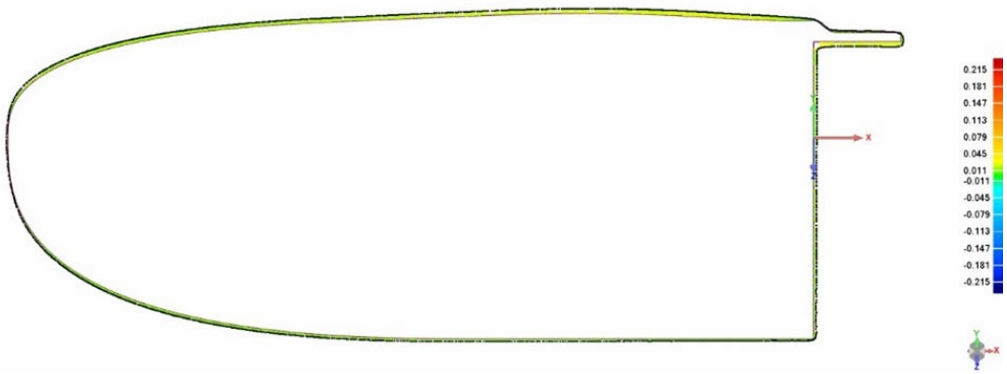

Method: Planar Deviation Whisker Scale: 1.000

2D Comparison Results CSYS: World CSYS

Reference Model	Cobra_MRV_scaled(2017-01-19)
Test Model	CobraMRV Titanium

Name	2D Comparison 2
Location	
No. of Data Points	3302

Units	in
Max. Critical	0.215
Max. Nominal	0.011
Min. Nominal	-0.011
Min. Critical	-0.215

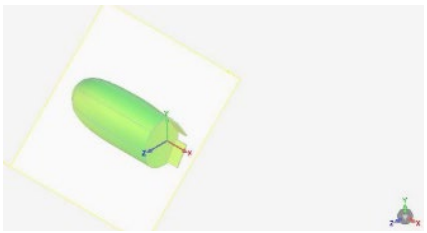

Deviation	
Max Dev +	0.029
Max Dev -	-0.004
Standard Deviation	0.006

Percentage Deviations

>=Min	<Max	Points	%
-0.215	-0.181	0	0.000
-0.181	-0.147	0	0.000
-0.147	-0.113	0	0.000
-0.113	-0.079	0	0.000
-0.079	-0.045	0	0.000
-0.045	-0.011	0	0.000
-0.011	0.011	812	24.591
0.011	0.045	2490	75.409
0.045	0.079	0	0.000
0.079	0.113	0	0.000
0.113	0.147	0	0.000
0.147	0.181	0	0.000
0.181	0.215	0	0.000

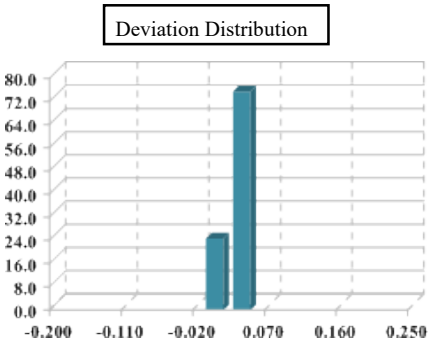

Out of Upper Critical +	0	0.000
Out of Lower Critical -	0	0.000

Standard Deviations

Distribution (+/-)	Points	%
-6 * Std. Dev.	0	0.000
-5 * Std. Dev.	0	0.000
-4 * Std. Dev.	0	0.000
-3 * Std. Dev.	0	0.000
-2 * Std. Dev.	0	0.000
-1 * Std. Dev.	9	0.273
1 * Std. Dev.	171	5.179
2 * Std. Dev.	704	21.320
3 * Std. Dev.	1068	32.344
4 * Std. Dev.	923	27.953
5 * Std. Dev.	425	12.871
6 * Std. Dev.	2	0.061

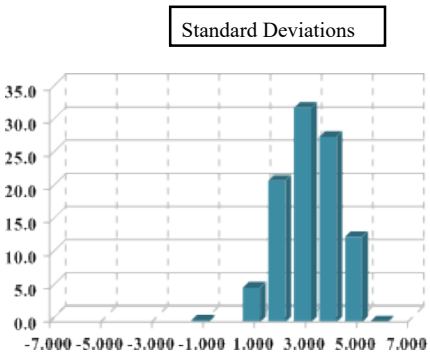

2D Compare View: 2D
Comparison 3

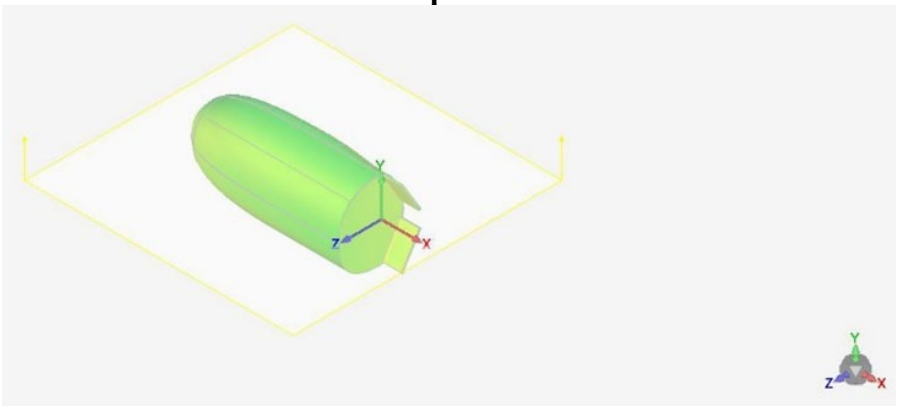

Y = 0.000 in

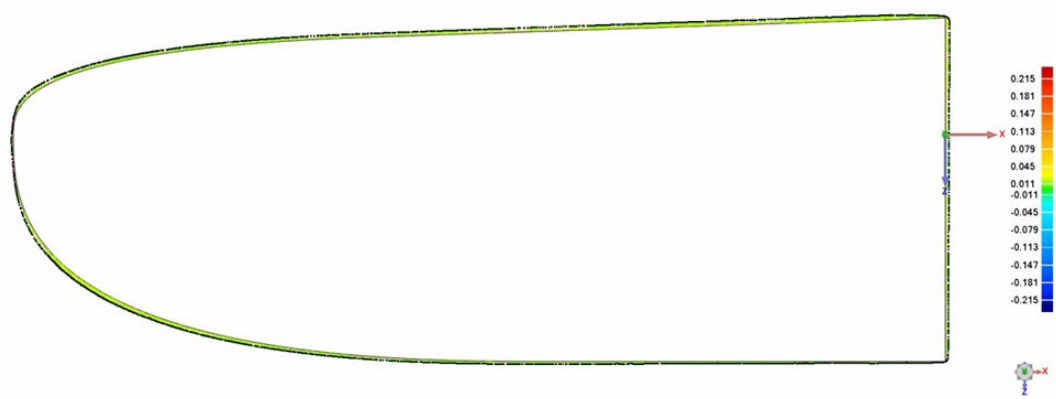

Method: Planar Deviation Whisker Scale: 1.000

2D Comparison Results CSYS: World CSYS

Reference Model	Cobra_MRV_scaled(2017-01-19)
Test Model	CobraMRV Titanium

Name	2D Comparison 3
Location	Y = 0.000 in
No. of Data Points	2895

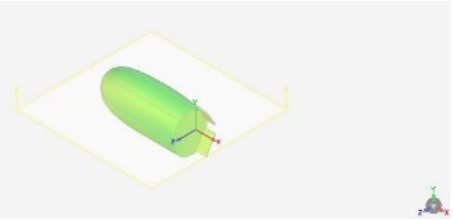

Units	in
Max. Critical	0.215
Max. Nominal	0.011
Min. Nominal	-0.011
Min. Critical	-0.215

Deviation	
Max Dev +	0.020
Max Dev -	0.000
Standard Deviation	0.004

Percentage Deviations

>=Min	<Max	Points	%
-0.215	-0.181	0	0.000
-0.181	-0.147	0	0.000
-0.147	-0.113	0	0.000
-0.113	-0.079	0	0.000
-0.079	-0.045	0	0.000
-0.045	-0.011	0	0.000
-0.011	0.011	718	24.801
0.011	0.045	2177	75.199
0.045	0.079	0	0.000
0.079	0.113	0	0.000
0.113	0.147	0	0.000
0.147	0.181	0	0.000
0.181	0.215	0	0.000

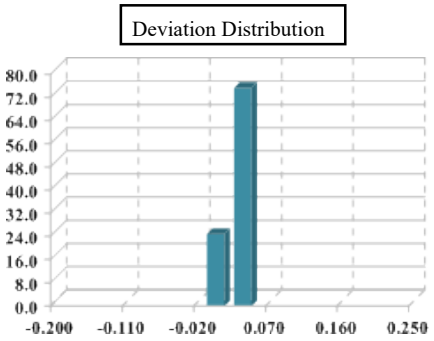

Out of Upper Critical +	0	0.000
Out of Lower Critical -	0	0.000

Standard Deviations

Distribution (+/-)	Points	%
-6 * Std. Dev.	0	0.000
-5 * Std. Dev.	0	0.000
-4 * Std. Dev.	0	0.000
-3 * Std. Dev.	0	0.000
-2 * Std. Dev.	0	0.000
-1 * Std. Dev.	0	0.000
1 * Std. Dev.	25	0.864
2 * Std. Dev.	432	14.922
3 * Std. Dev.	484	16.718
4 * Std. Dev.	1072	37.029
5 * Std. Dev.	882	30.466
6 * Std. Dev.	0	0.000

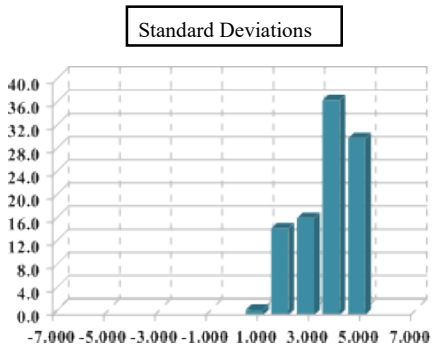

2D Compare View: 2D
Comparison 4

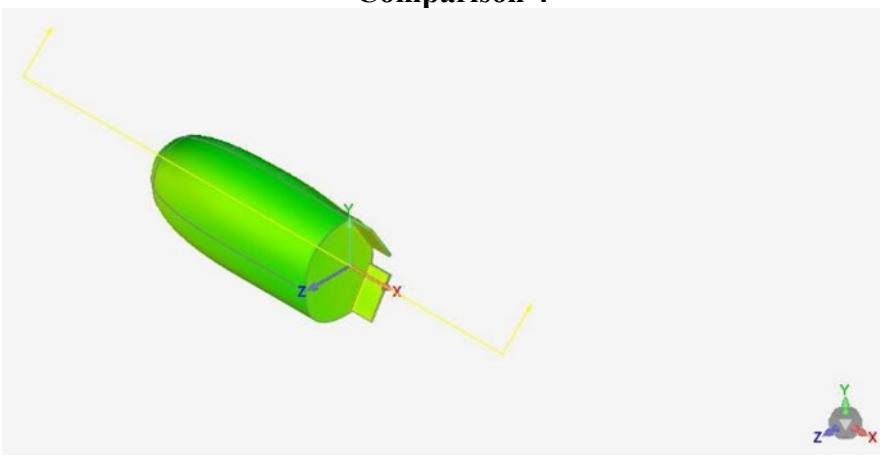

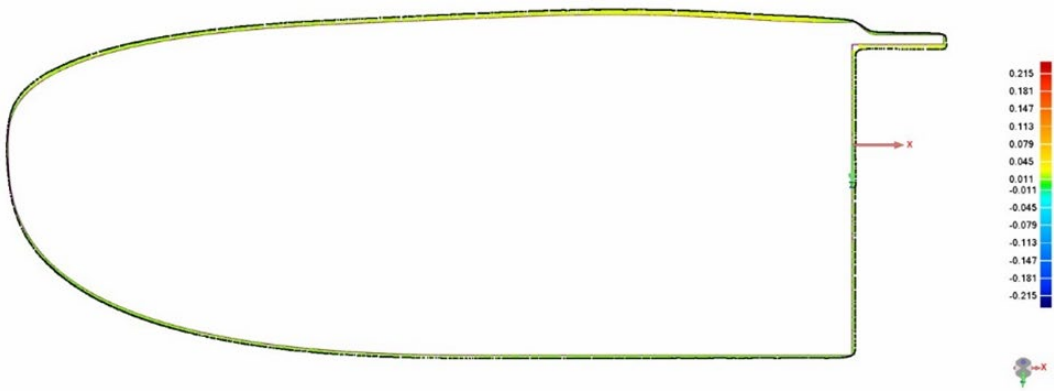

Method: Planar Deviation Whisker Scale: 1.000

2D Comparison Results CSYS: World CSYS

Reference Model	Cobra_MRV_scaled(2017-01-19)
Test Model	CobraMRV Titanium

Name	2D Comparison 4
Location	
No. of Data Points	3234

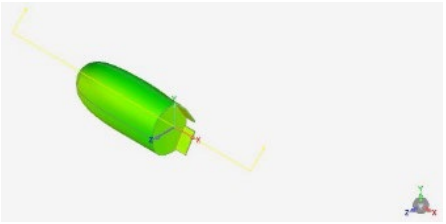

Units	in
Max. Critical	0.215
Max. Nominal	0.011
Min. Nominal	-0.011
Min. Critical	-0.215

Deviation	
Max Dev +	0.027
Max Dev -	0.000
Standard Deviation	0.005

Percentage Deviations

>=Min	<Max	Points	%
-0.215	-0.181	0	0.000
-0.181	-0.147	0	0.000
-0.147	-0.113	0	0.000
-0.113	-0.079	0	0.000
-0.079	-0.045	0	0.000
-0.045	-0.011	0	0.000
-0.011	0.011	351	10.853
0.011	0.045	2883	89.147
0.045	0.079	0	0.000
0.079	0.113	0	0.000
0.113	0.147	0	0.000
0.147	0.181	0	0.000
0.181	0.215	0	0.000

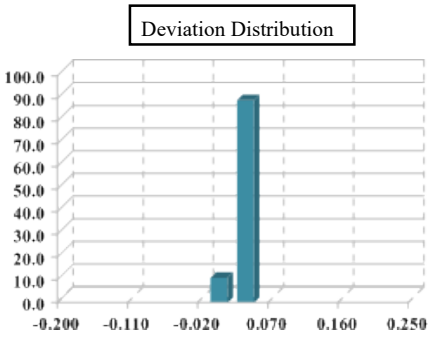

Out of Upper Critical +	0	0.000
Out of Lower Critical -	0	0.000

Standard Deviations

Distribution (+/-)	Points	%
-6 * Std. Dev.	0	0.000
-5 * Std. Dev.	0	0.000
-4 * Std. Dev.	0	0.000
-3 * Std. Dev.	0	0.000
-2 * Std. Dev.	0	0.000
-1 * Std. Dev.	0	0.000
1 * Std. Dev.	101	3.123
2 * Std. Dev.	237	7.328
3 * Std. Dev.	1513	46.784
4 * Std. Dev.	662	20.470
5 * Std. Dev.	719	22.233
6 * Std. Dev.	2	0.062

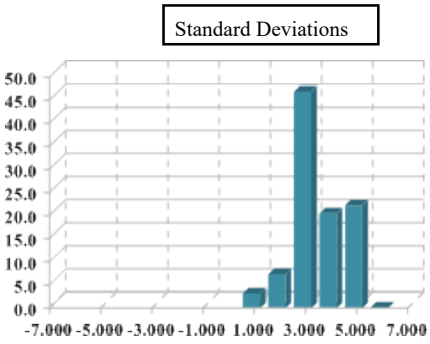

Location Set: 2D Comparison 1 Upper and Lower Deviations

Name	Dev	Ref X	Ref Y	Ref Z	Radius	Dev X	Dev Y	Dev Z	Meas. X	Meas. Y	Meas. Z
2D Comparison 1 Lower Dev.	-0.005	-0.007	-0.866	0.000	n/a	0.000	0.005	0.000	-0.007	-0.862	0.000
2D Comparison 1 Upper Dev.	0.031	0.000	0.824	0.000	n/a	0.031	0.000	0.000	0.031	0.824	0.000

Location Set: 2D Comparison 2 Upper and Lower Deviations

Name	Dev	Ref X	Ref Y	Ref Z	Radius	Dev X	Dev Y	Dev Z	Meas. X	Meas. Y	Meas. Z
2D Comparison 2 Lower Dev.	-0.004	0.416	0.359	-0.359	n/a	0.000	-0.003	0.003	0.416	0.356	-0.356
2D Comparison 2 Upper Dev.	0.029	0.033	0.327	-0.327	n/a	0.000	-0.020	0.020	0.033	0.307	-0.307

Location Set: 2D Comparison 3 Upper and Lower Deviations

Name	Dev	Ref X	Ref Y	Ref Z	Radius	Dev X	Dev Y	Dev Z	Meas. X	Meas. Y	Meas. Z
2D Comparison 3 Lower Dev.	0.000	-0.000	0.000	0.945	n/a	0.000	0.000	0.000	-0.000	0.000	0.945
2D Comparison 3 Upper Dev.	0.020	-3.641	0.000	0.581	n/a	-0.012	0.000	0.016	-3.652	0.000	0.597

Location Set: 2D Comparison 4 Upper and Lower Deviations

Name	Dev	Ref X	Ref Y	Ref Z	Radius	Dev X	Dev Y	Dev Z	Meas. X	Meas. Y	Meas. Z
2D Comparison 4 Lower Dev.	0.000	-0.001	0.684	0.684	n/a	0.000	0.000	0.000	-0.001	0.684	0.684
2D Comparison 4 Upper Dev.	0.027	0.032	-0.327	-0.327	n/a	0.000	0.019	0.019	0.032	-0.308	-0.308

Appendix D. Physical Measurements

The physical characteristics of the assembled Co-Optimization Bluntbody Re-entry Analysis Mid-Lift-to-Drag Rigid Vehicle (CobraMRV) 1:200-scale flight body were characterized prior to the flight experiment for use in later analysis of the observed dynamic flight response. The technique for measuring physical charateristics is based on the principle of moments, which states the moment of inertia (MOI) is proportional to the mass times the square of the distance from the rotation frame. The device used to make measurements is made by Space Electronics and consists of a spring-loaded air-bearing torsional table that measures the period of oscillation. The period is proportonal to the MOI of the moving parts. The fixture assembly and table is rotated only about 15° and released to oscillate freely. The average of about five periods is used to calculate the moment of inertia.

The MOI measurement table is shown in Fig. D-1 with a fixture designed to hold the MRV in a transverse orientation to the pivot point. Additional fixtures are required to hold the object at a given location and orientation to measure about the correct axis of the object. A tare of the apparatus (table and fixture) is subtracted from the objects sinusoidal motion and used to correct for the object's MOI directly. A time for a complete cycle of oscillation is recorded, and the moment is determined directly from that and the relation to mass and moment arm. Figure D-2 shows the MRV resting on a cylindrical fixture oriented for measurement in the axial direction. Again the cylindrical fixture and table were tared at various locations from the center to make measurements of MOI and center of gravity (CG) about the axial location of the body since the object was asymmetric about that axis. These measurements were recorded to gain insight into the axial offset of CG. Note the first image in Fig. D-2 is on center, and the second image is off center intentionally to measure the CG offset with reference to the intentional offset. Figure D-3 represents measurements made of the CobraMRV location within the fixture using an optical comparitor.

Fig. D-1 MOI measurement table with MRV and fixture assembly (transverse)

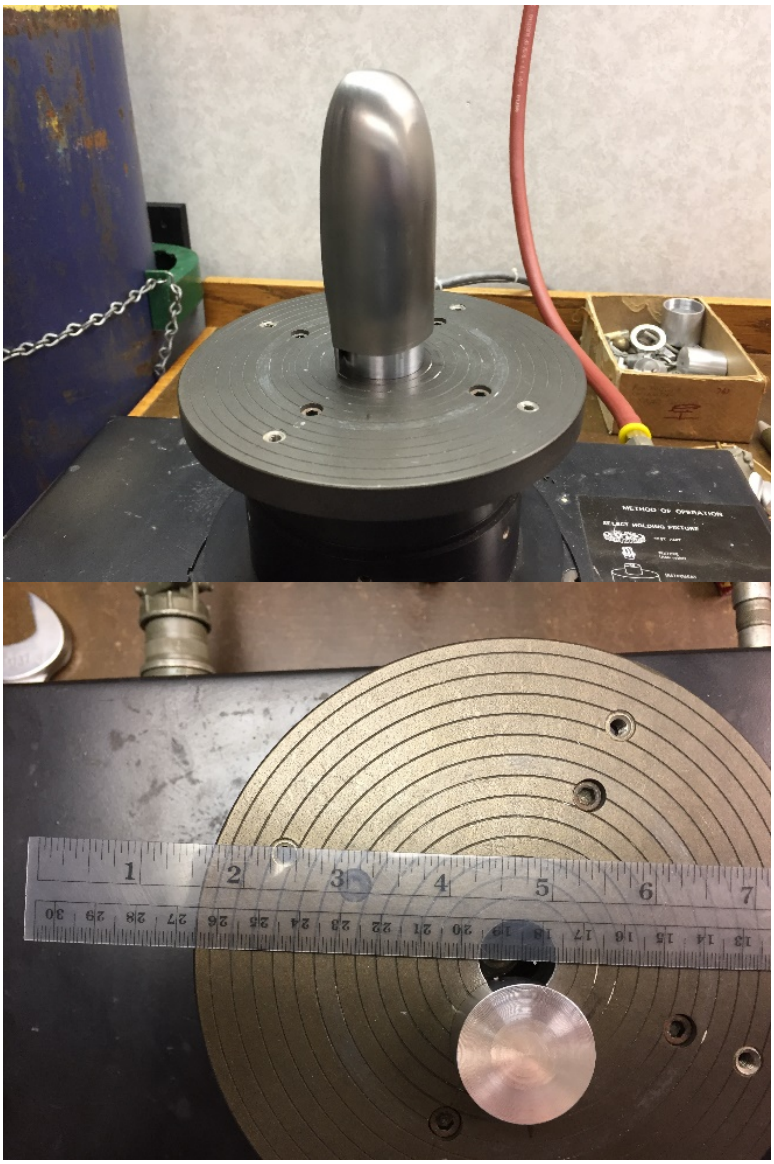

Fig. D-2 MOI measurement table with MRV and fixture assembly (axial)

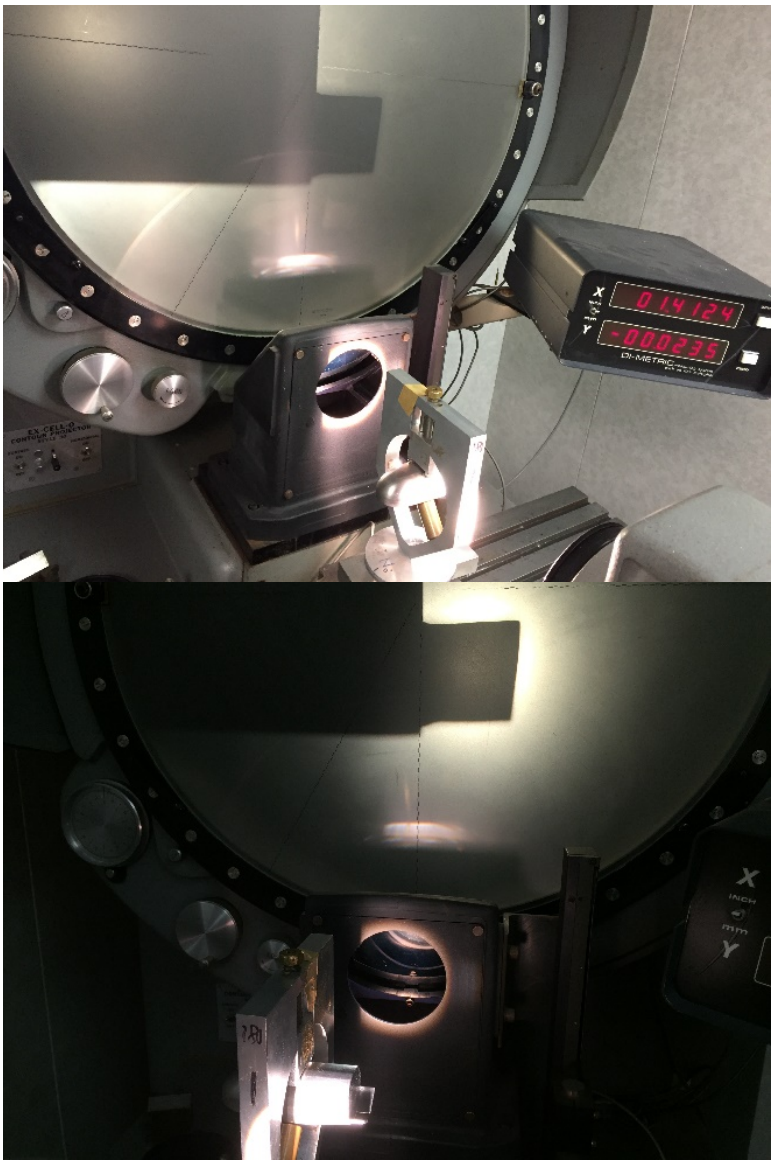

Fig. D-3 Optical comparitor measurement of MRV fixture location with reference to the pivot point

Since the MOI measurement table rotates about the center of the plate, careful measurement of the object with reference to the pivot point must be recorded. An optical comparitor was used to measure and record accurate displacements from a given reference point on the object. Since the relationship of MOI is related to mass and distance squared, a quadratic fit is required to gain an accurate location and value of MOI. A fit of the data is shown in Fig. D-4 with the minimum value indicating the CG location and MOI, respectively. Values for mass, CG, and MOI are included in Appendix A.

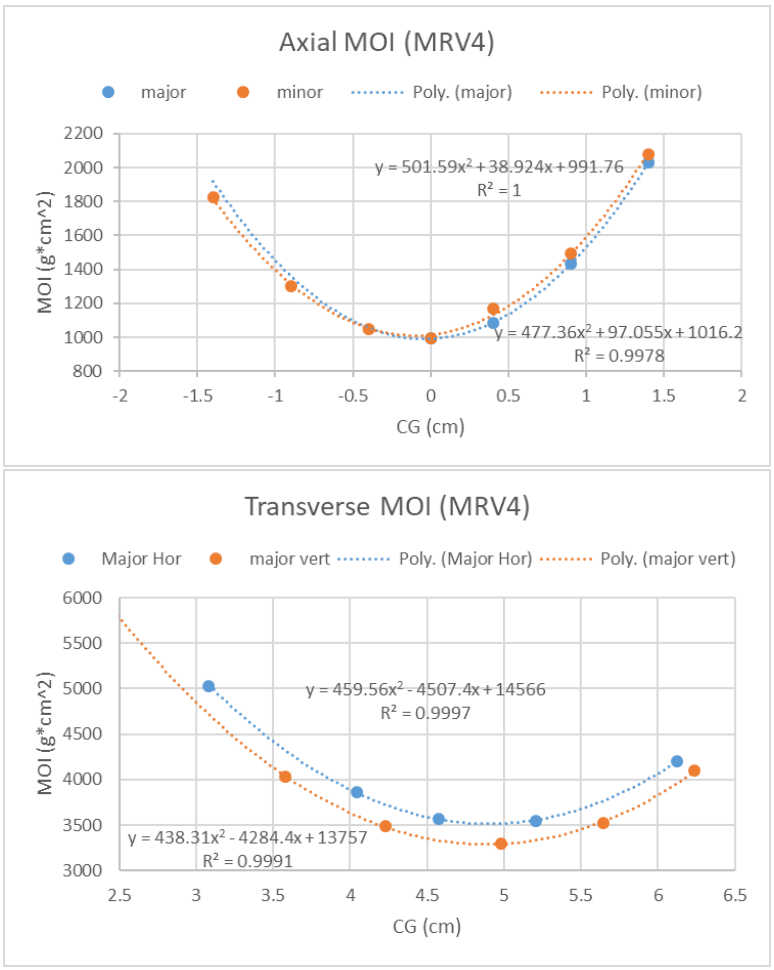

Fig. D-4 Typical quadratic fit of MOI and CG

Appendix E. Site Survey

The positions of the cameras and the visible fiducials were surveyed with respect to a local coordinate system using a Leica TS16 TotalStation survey instrument. Table E-1 provides locations of the cameras and the fiducials in local coordinates, with the origin located at the gun muzzle reference and the northing axis pointing down range. (Nonhighlighted values are reference measurements or duplicate measurements for error establishment.)

Table E-1 Survey results

Code	Northing (m)	Easting (m)	Ortho. height (m)	Adj. height (m)	Notes
	47.4907	–48.8641	–2.6949		TS
	0	0	0		Muzzle Ref
	10.2873	–22.8228	–2.4231		TS
	94.9588	0	–2.3476		GTL Ref
	0	0	0		Muzzle Ref
	94.9654	0	–2.3518		GTL Ref
FC4	56.1145	–7.0645	–2.6411	1.7648	High Speed 4
FC3	40.6559	–11.6288	–2.7064	–1.5888	High Speed 3
FC2	25.366	–12.0863	–2.5907	–1.3334	High Speed 2
	–0.0101	0.0003	–0.0005		Muzzle Meas
	–0.0093	0.0004	0.0008		Muzzle Meas
	–0.0037	–0.0013	0.0033		Muzzle Meas
FF1	45.0725	37.2676	–2.1254	–1.3634	Flight Follower 1
FC5	17.5286	40.356	–1.5868	–0.6724	High Speed 5
DB	12.5919	0.2033	–1.6024	–1.2976	High Speed (down bore)
DR	17.4308	–0.0431	–1.6189	–1.3141	High Speed (down range)
FF2	95.1891	–50.1139	–2.4378	–1.6758	Flight Follower 2
FD4	55.2849	1.3961	0.495		Fiducial 4
FD3	40.9895	1.4	0.4954		Fiducial 3
FD2b	25.8988	1.5898	0.5452		Fiducial 2b
FD2	22.9329	1.3555	0.5508		Fiducial 2
FD1b	9.4845	1.3413	1.3138		Fiducial 1b
FD1	7.9973	1.5511	1.3207		Fiducial 1
	–0.0153	–0.0281	–0.0138		Muzzle Meas
FC1	8.8942	–12.5641	–2.3414	–1.0333	High Speed 1
				Approximate	
				Measured	
				Ref. ground	

Appendix F. Results: Tube Round (TR) 40649

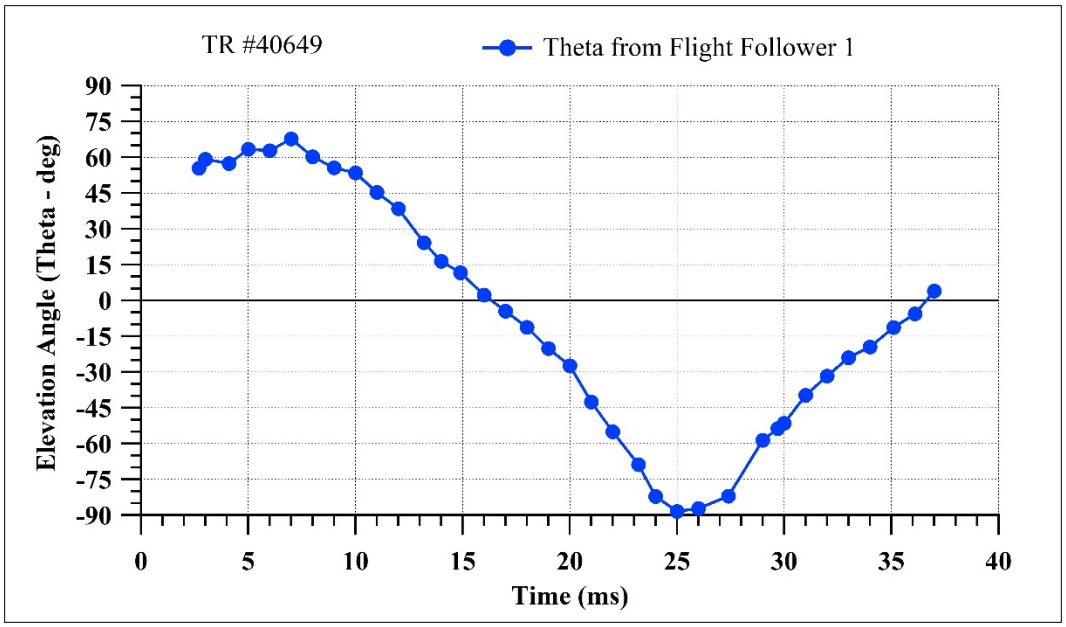

Fig. F-1 Elevation angle vs. flight time in gun coordinates, TR 40649

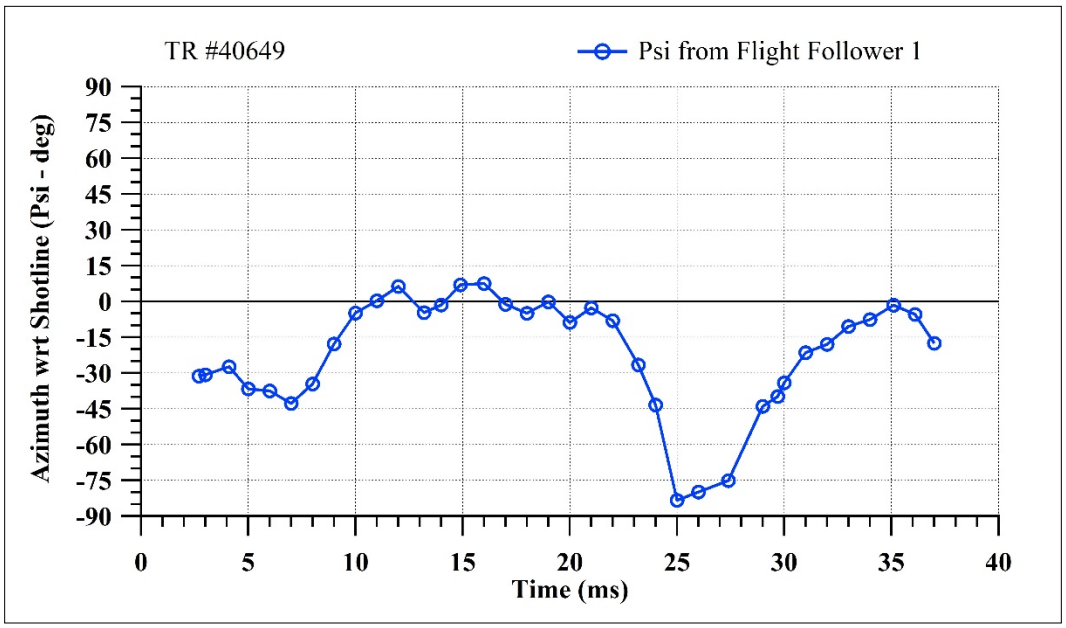

Fig. F-2 Azimuth angle vs. flight time in gun coordinates, TR 40649

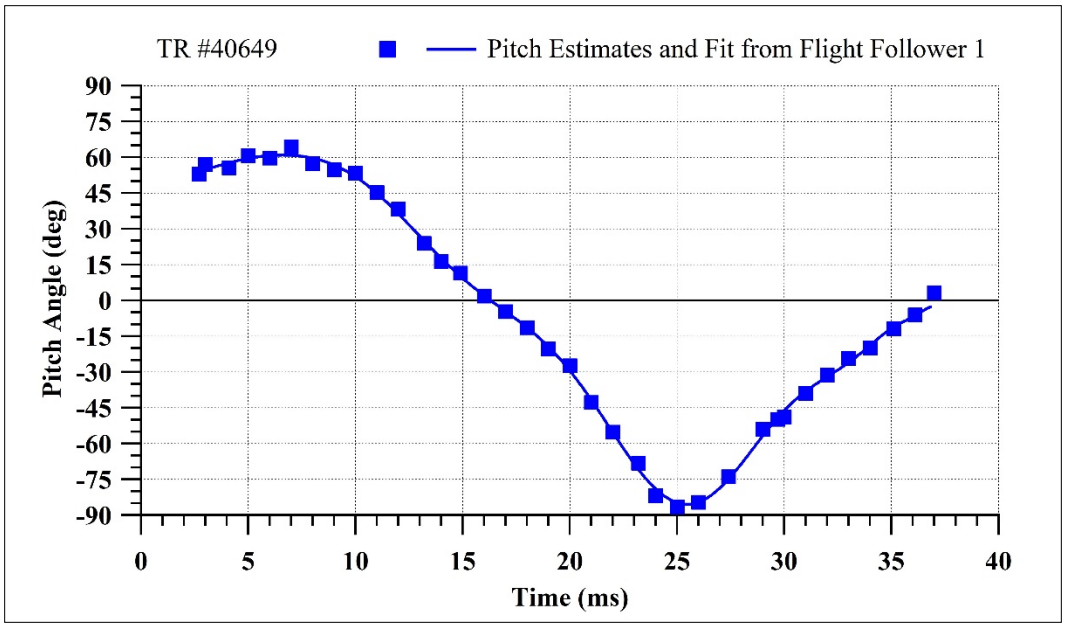

Fig. F-3 Pitch angle vs. flight time in gun coordinates, TR 40649

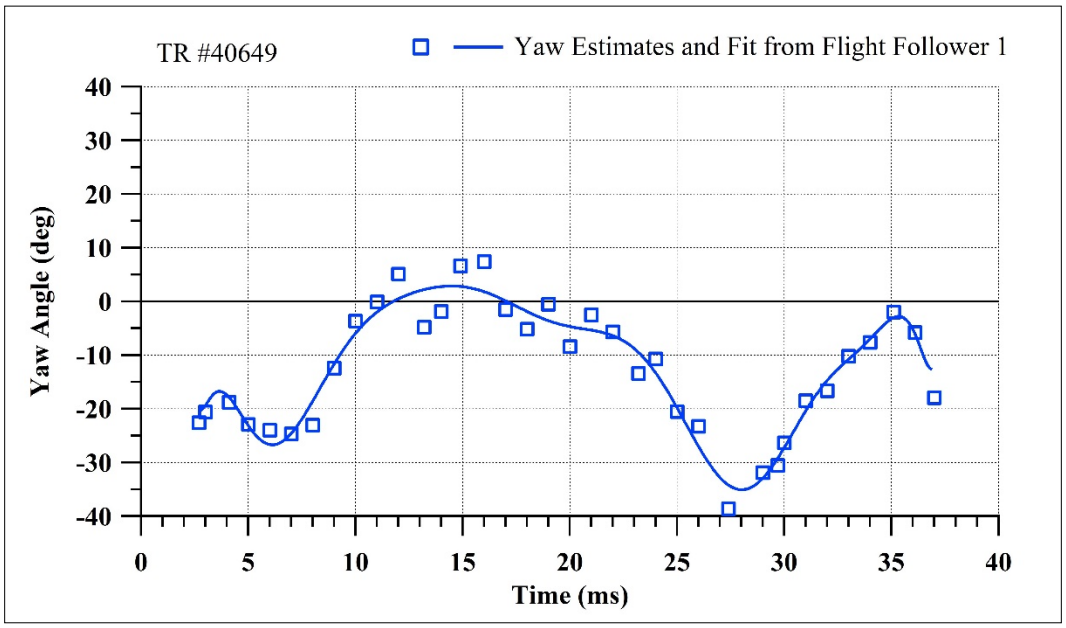

Fig. F-4 Yaw angle vs. flight time in gun coordinates, TR 40649

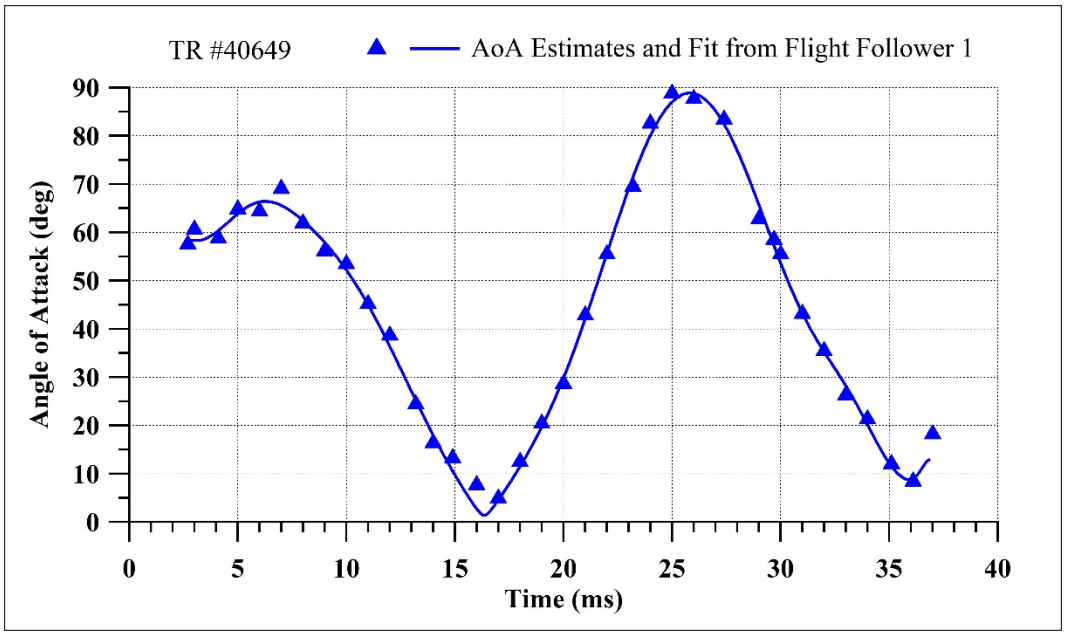

Fig. F-5 Angle of attack (AoA) vs. flight time in gun coordinates, TR 40649

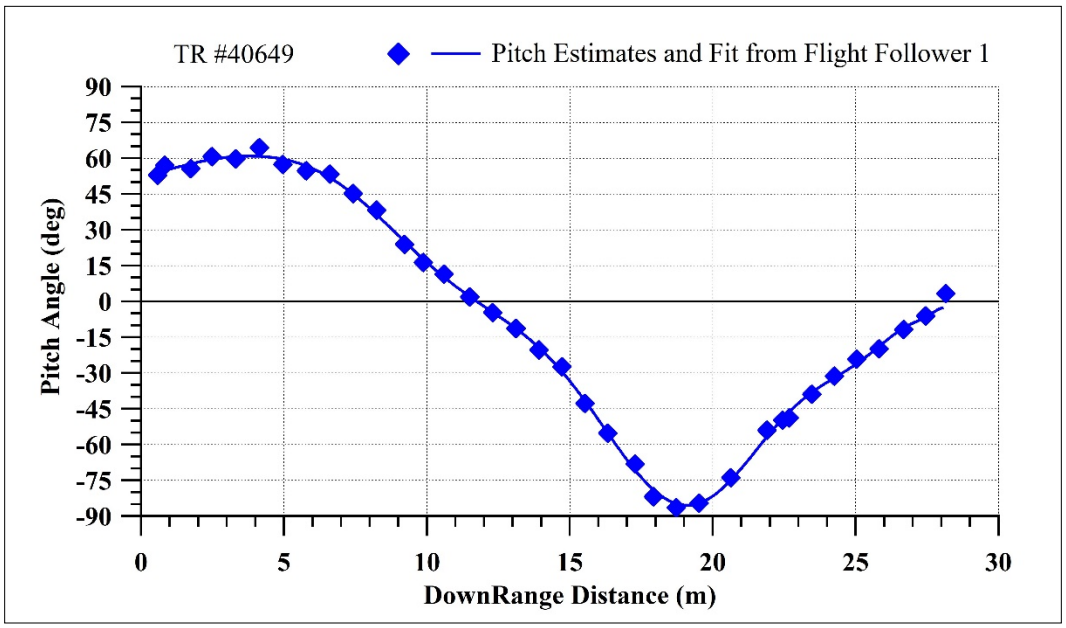

Fig. F-6 Pitch angle vs. downrange distance in gun coordinates, TR 40649

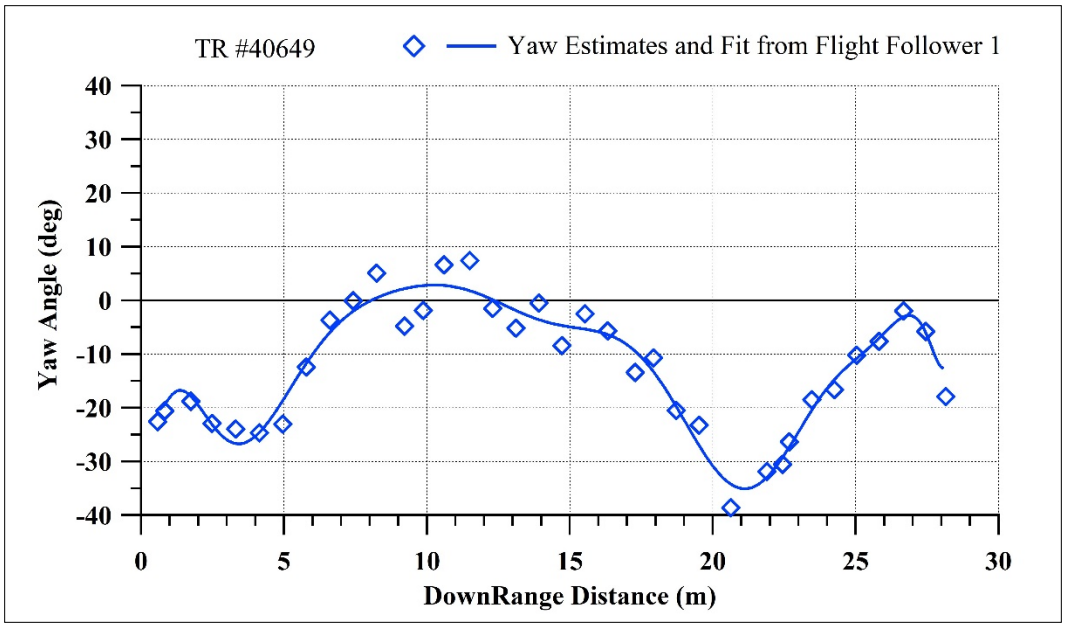

Fig. F-7 Yaw angle vs. downrange distance in gun coordinates, TR 40649

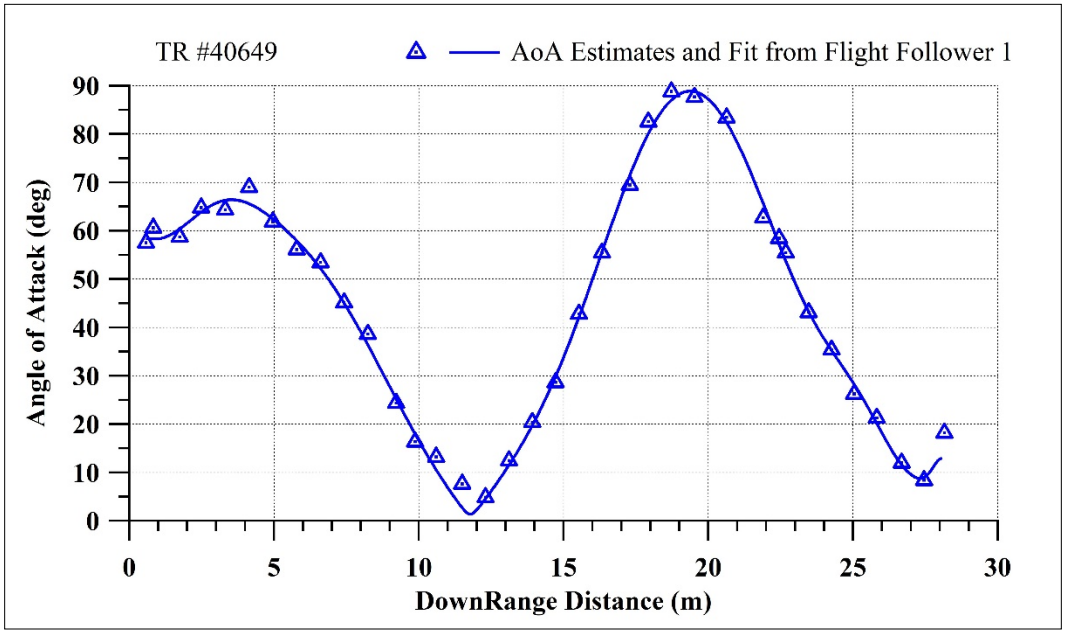

Fig. F-8 AoA vs. downrange distance in gun coordinates, TR 40649

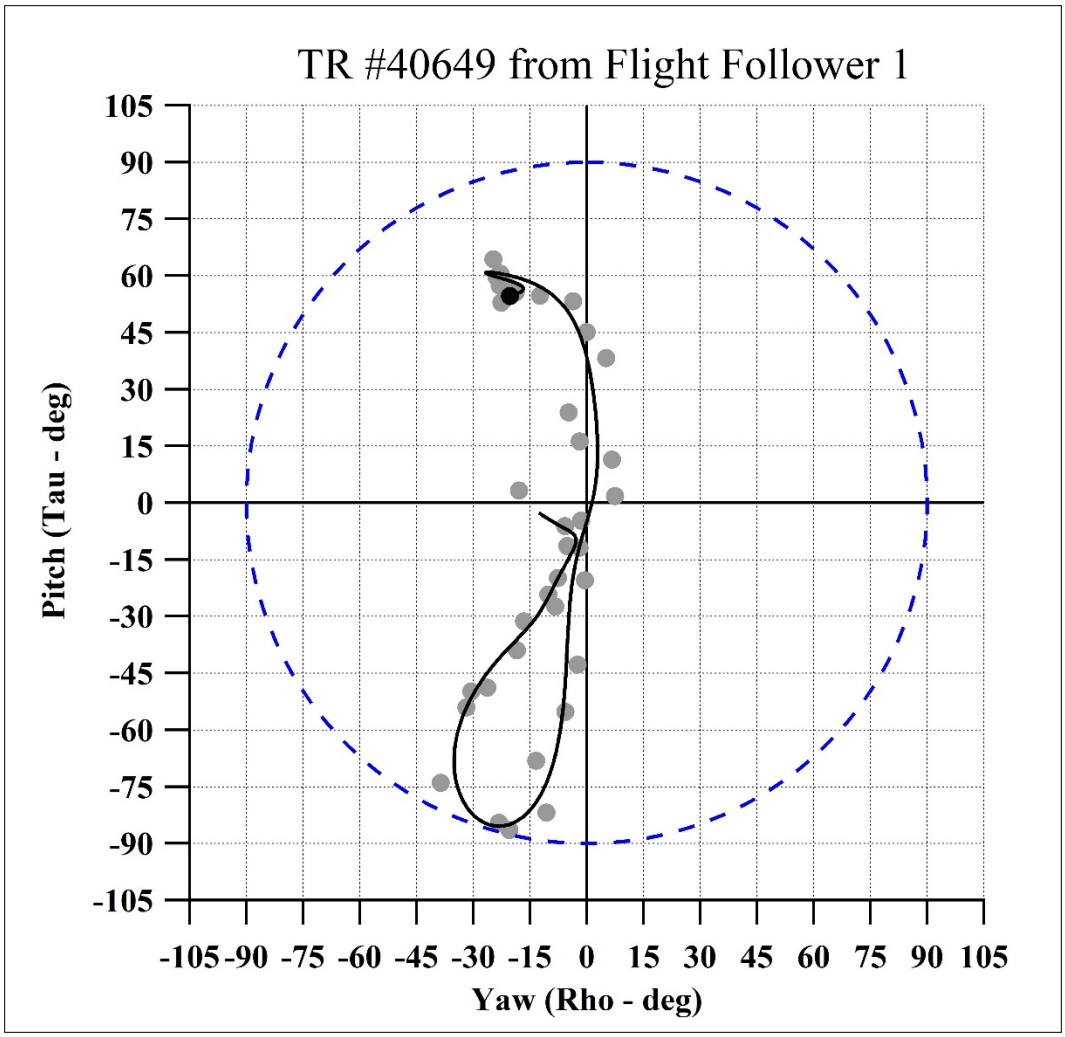

Fig. F-9 Pitch vs. yaw, TR 40649

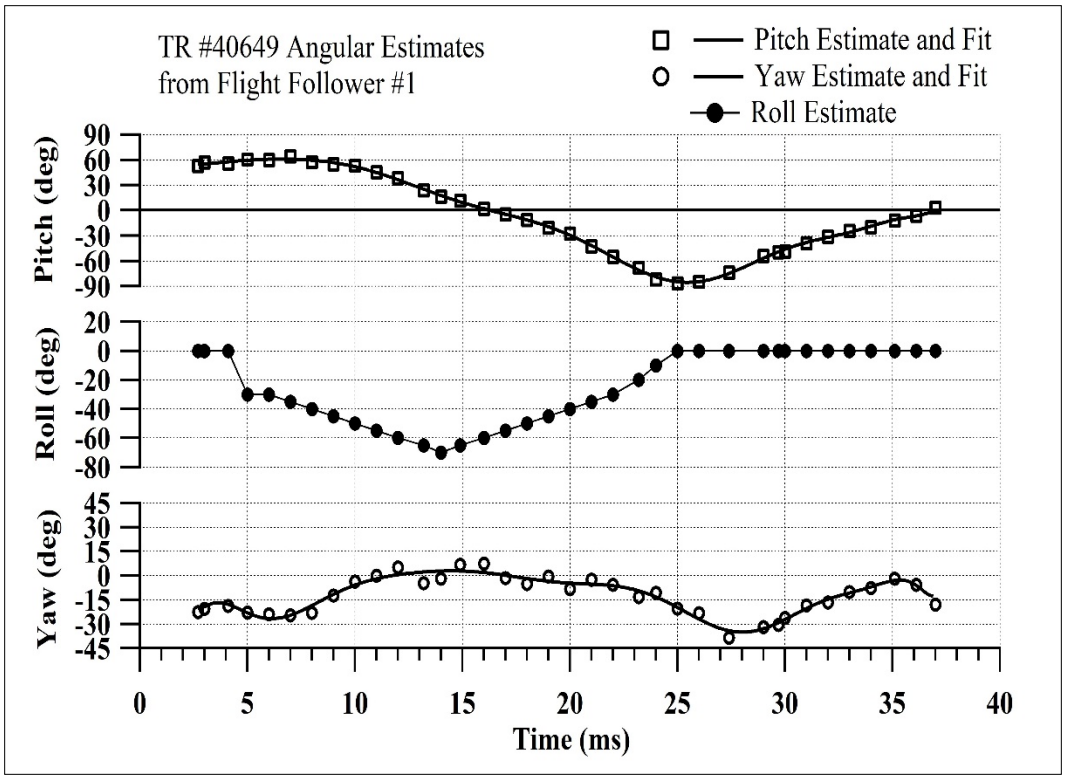

Fig. F-10 Pitch, yaw, and roll angle estimates from Flight Follower 1 vs. flight time in gun coordinates, TR 40649

Appendix G. Results: Tube Round (TR) 40650

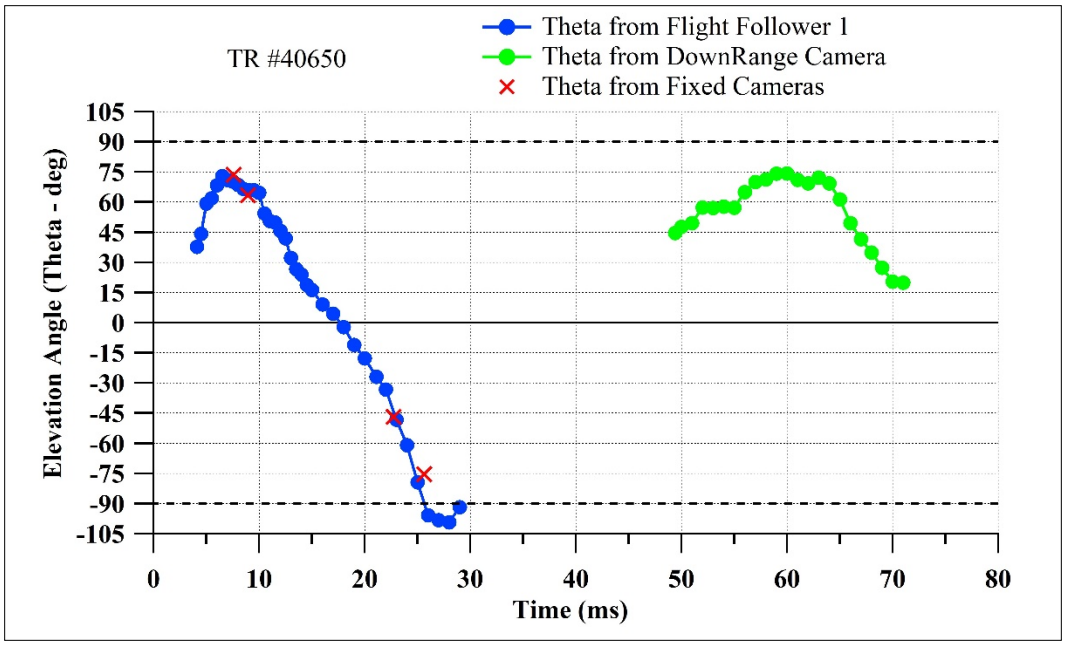

Fig. G-1 Elevation angle vs. flight time in gun coordinates, TR 40650

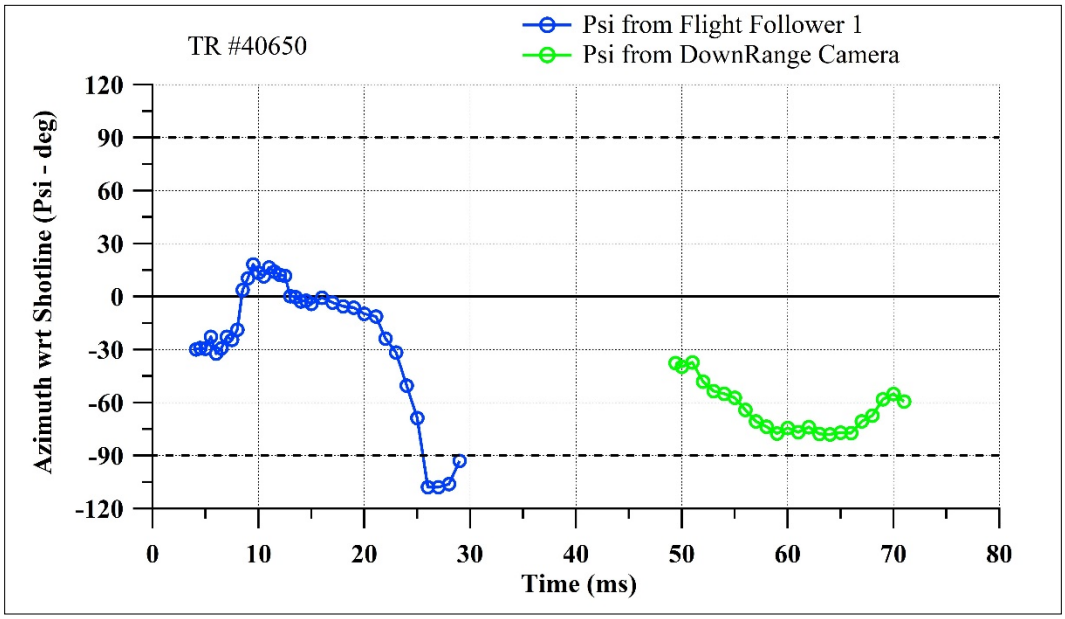

Fig. G-2 Azimuth angle vs. flight time in gun coordinates, TR 40650

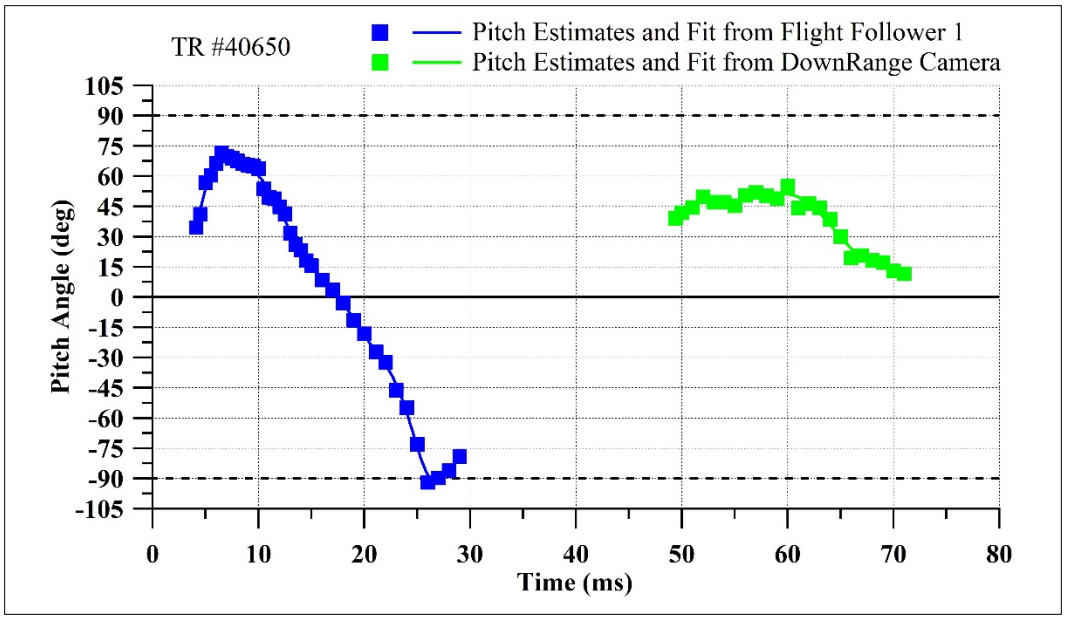

Fig. G-3 Pitch angle vs. flight time in gun coordinates, TR 40650

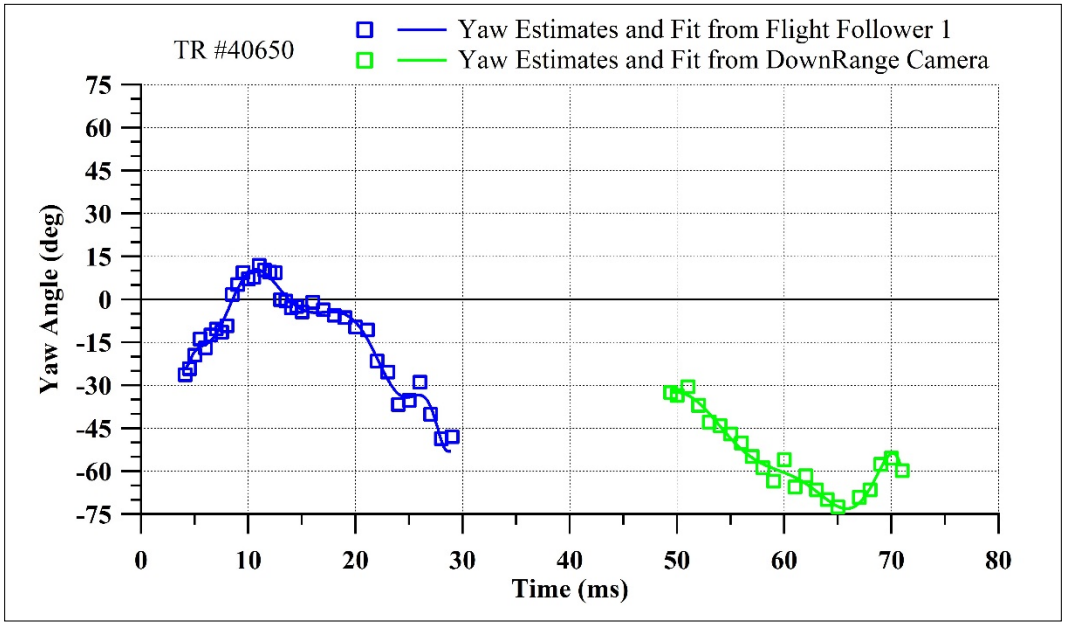

Fig. G-4 Yaw angle vs. flight time in gun coordinates, TR 40650

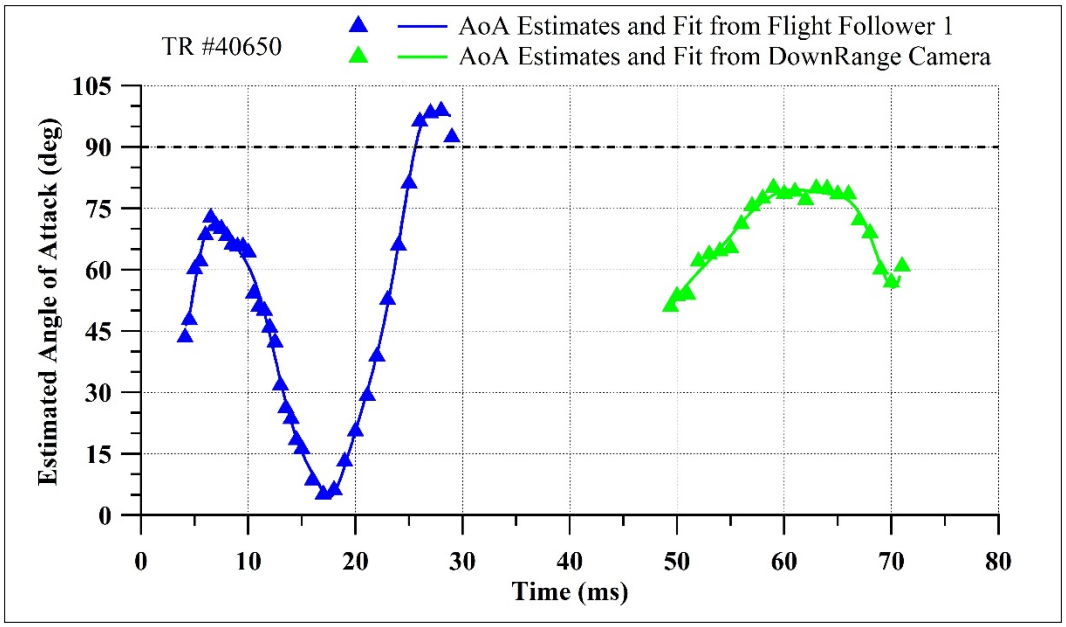

Fig. G-5 Angle of attack (AoA) vs. flight time in gun coordinates, TR 40650

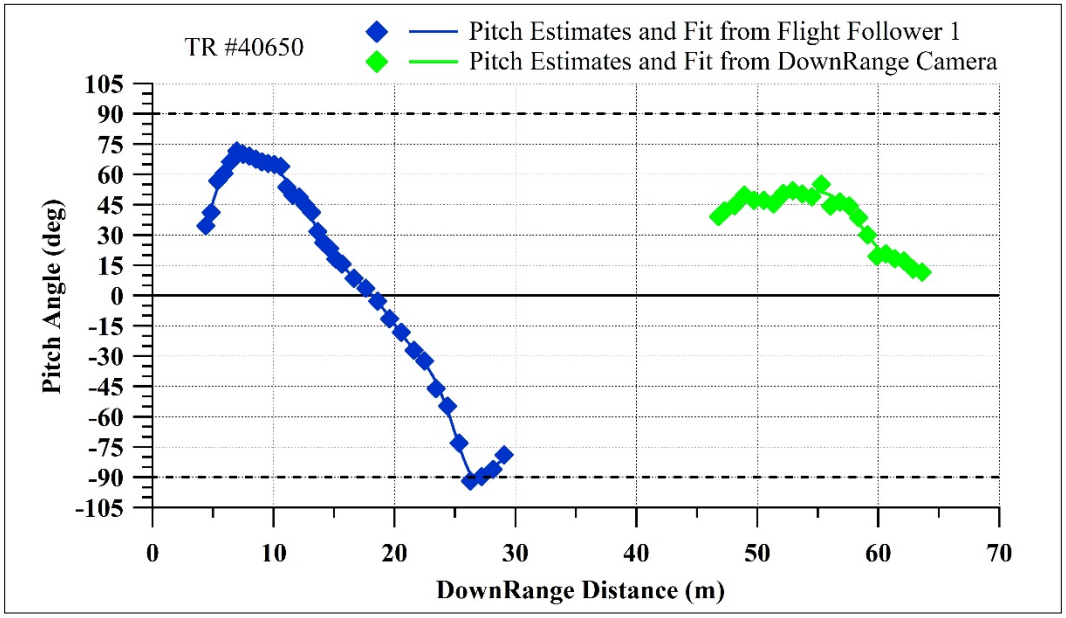

Fig. G-6 Pitch angle vs. downrange distance in gun coordinates, TR 40650

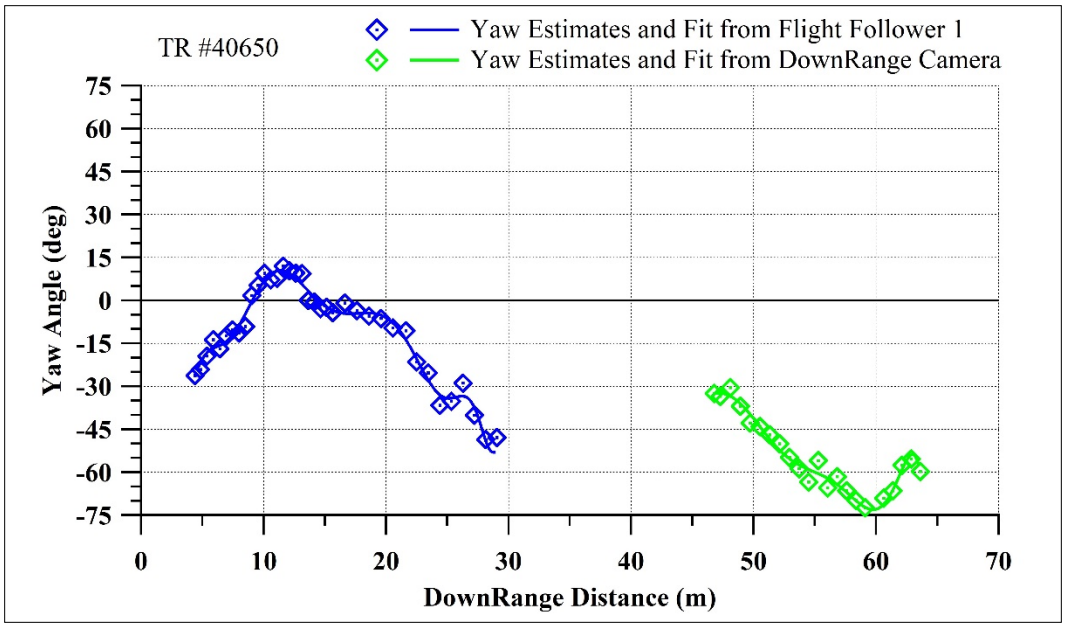

Fig. G-7 Yaw angle vs. downrange distance in gun coordinates, TR 40650

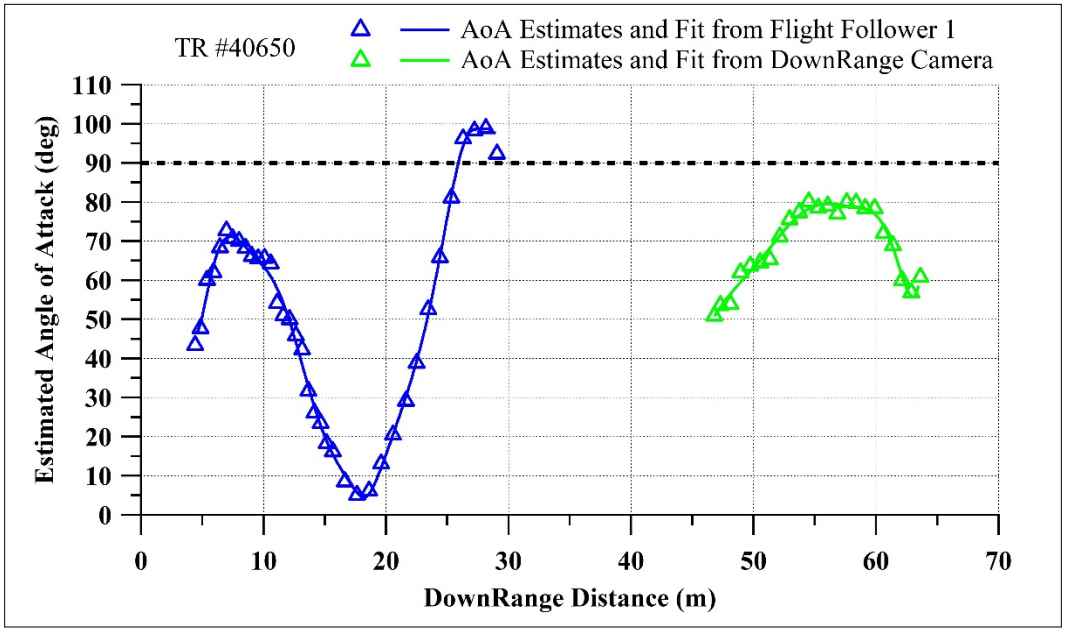

Fig. G-8 AoA vs. downrange distance in gun coordinates, TR 40650

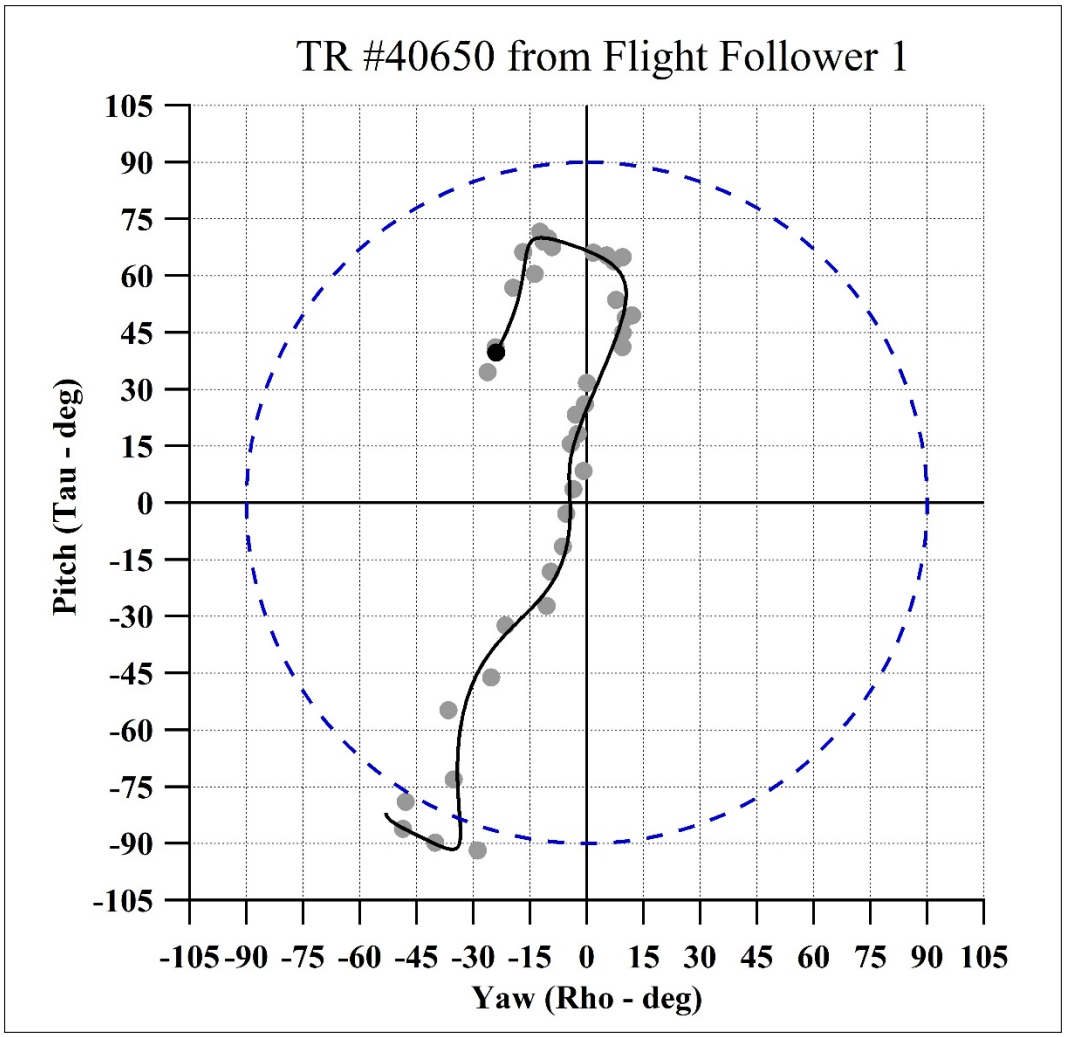

Fig. G-9 Pitch vs. yaw, TR 40650

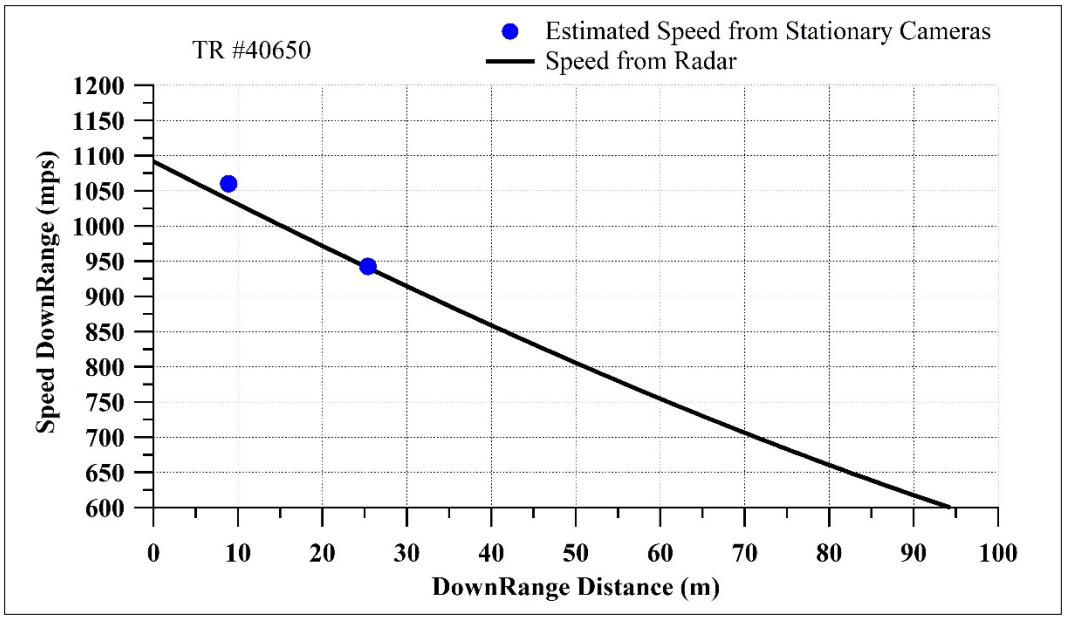

Fig. G-10 CobraMRV speed from video and radar vs. downrange distance, TR 40650

Appendix H. Results: Tube Round (TR) 40651

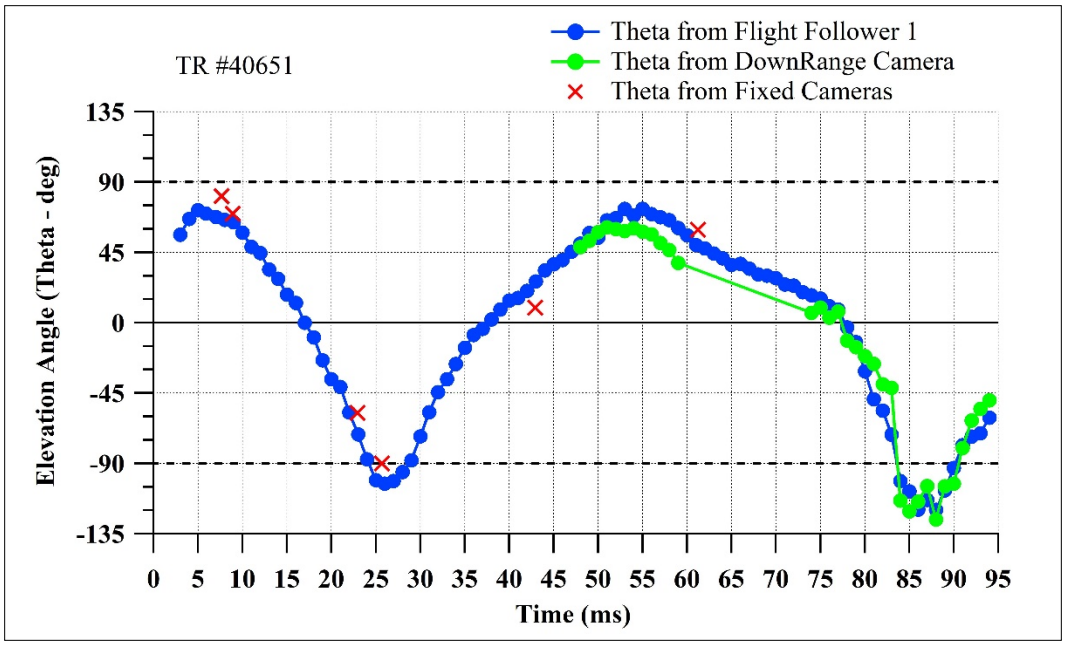

Fig. H-1 Elevation angle vs. flight time in gun coordinates, TR 40651

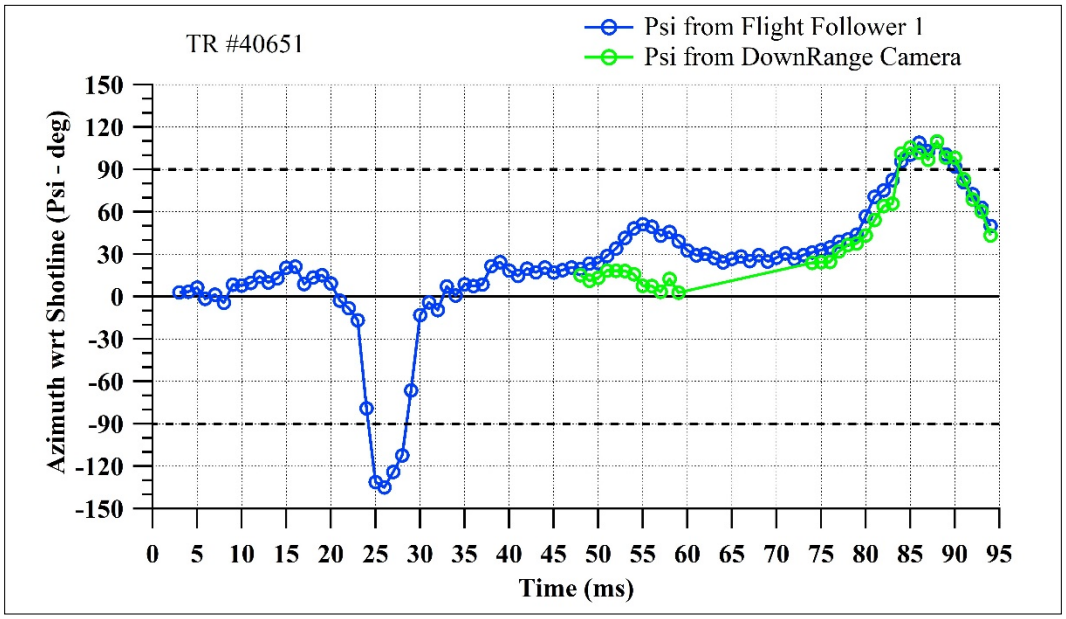

Fig. H-2 Azimuth angle vs. flight time in gun coordinates, TR 40651

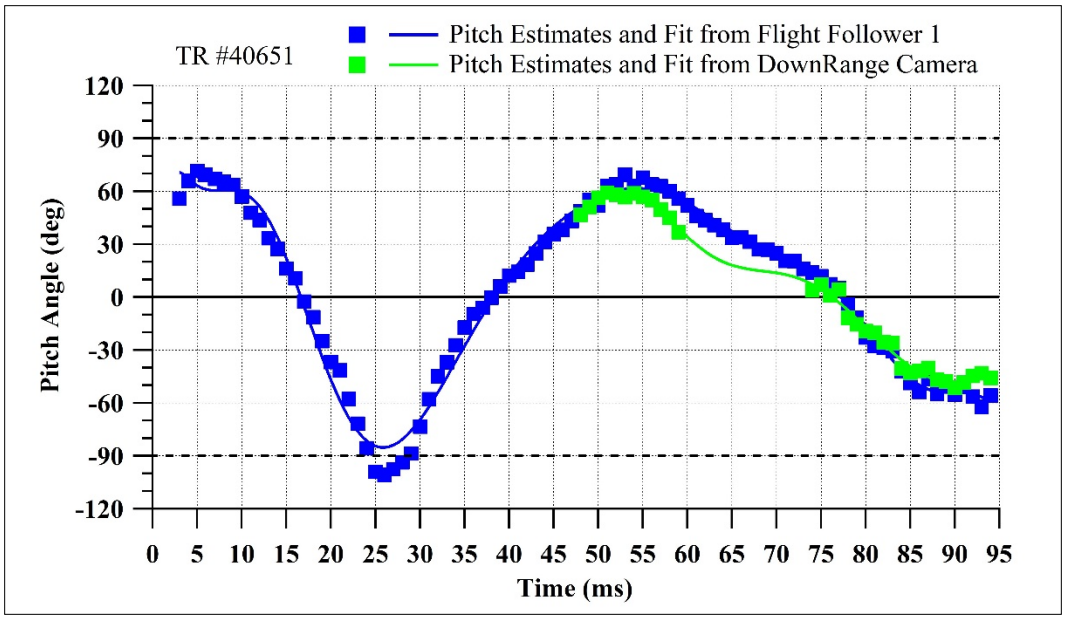

Fig. H-3 Pitch angle vs. flight time in gun coordinates, TR 40651

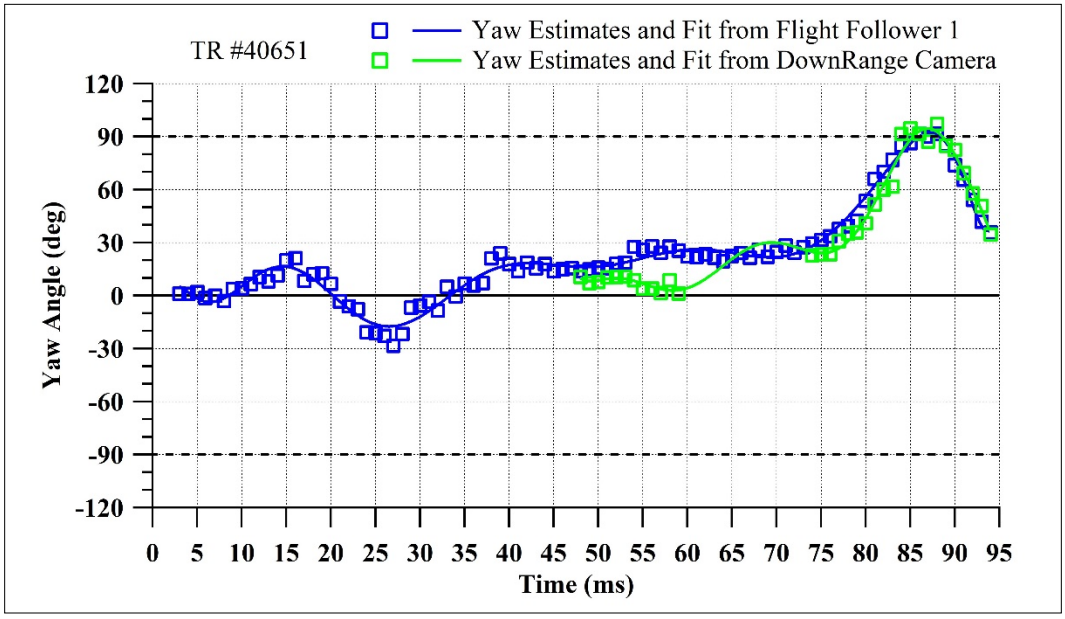

Fig. H-4 Yaw angle vs. flight time in gun coordinates, TR 40651

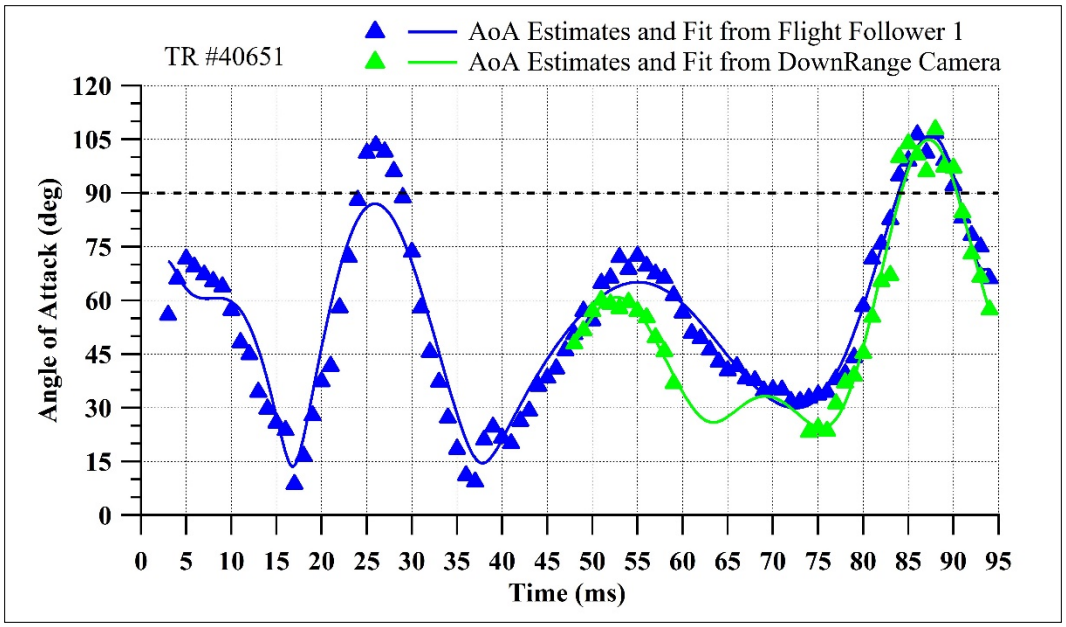

Fig. H-5 Angle of attack (AoA) vs. flight time in gun coordinates, TR 40651

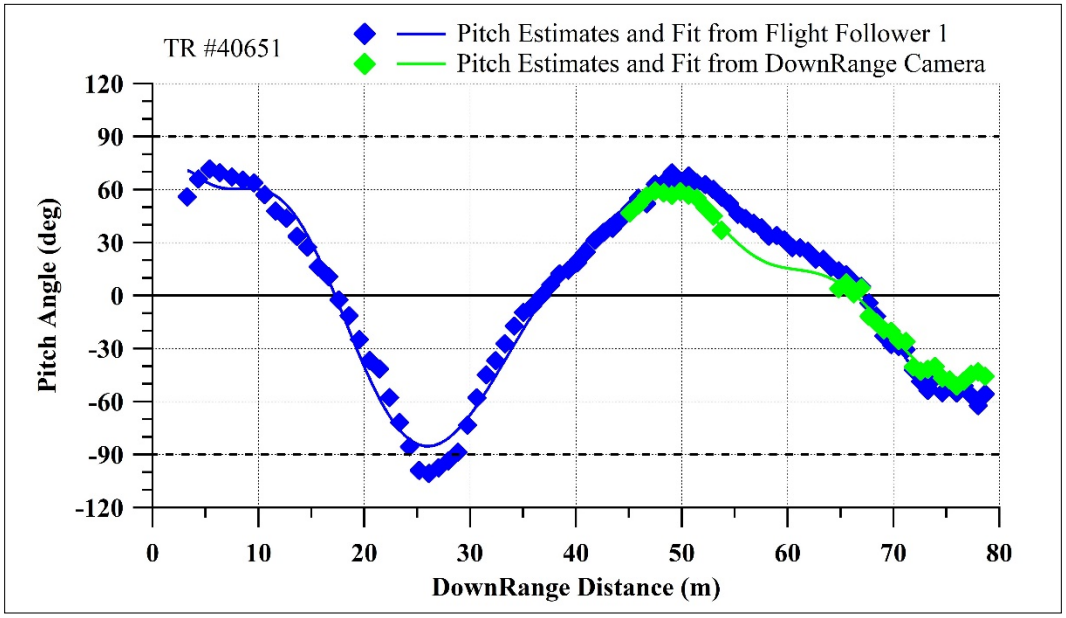

Fig. H-6 Pitch angle vs. downrange distance in gun coordinates, TR 40651

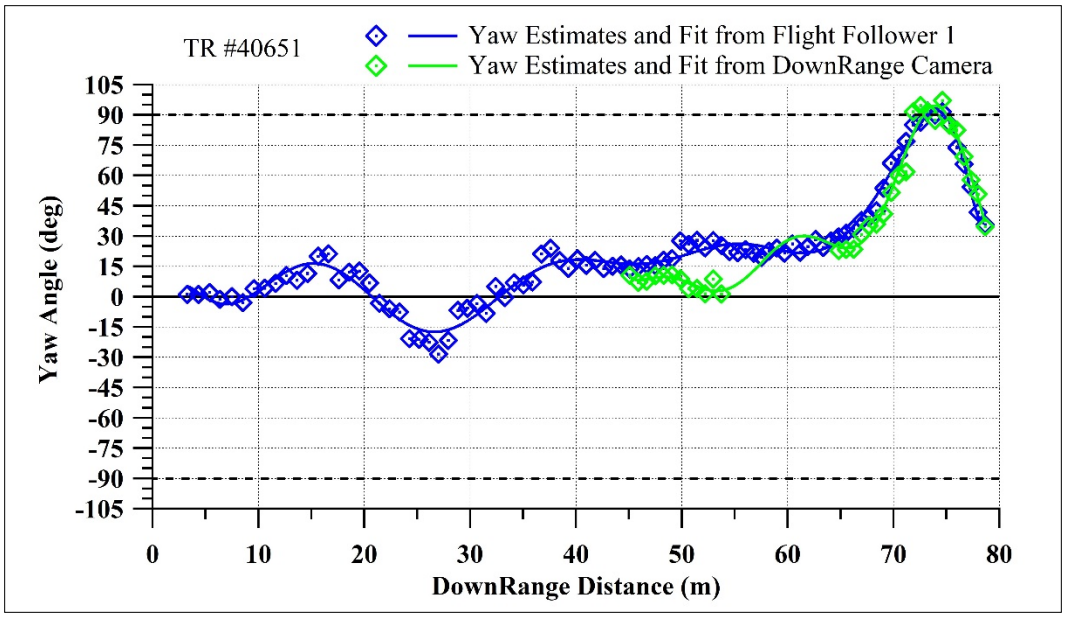

Fig. H-7 Yaw angle vs. downrange distance in gun coordinates, TR 40651

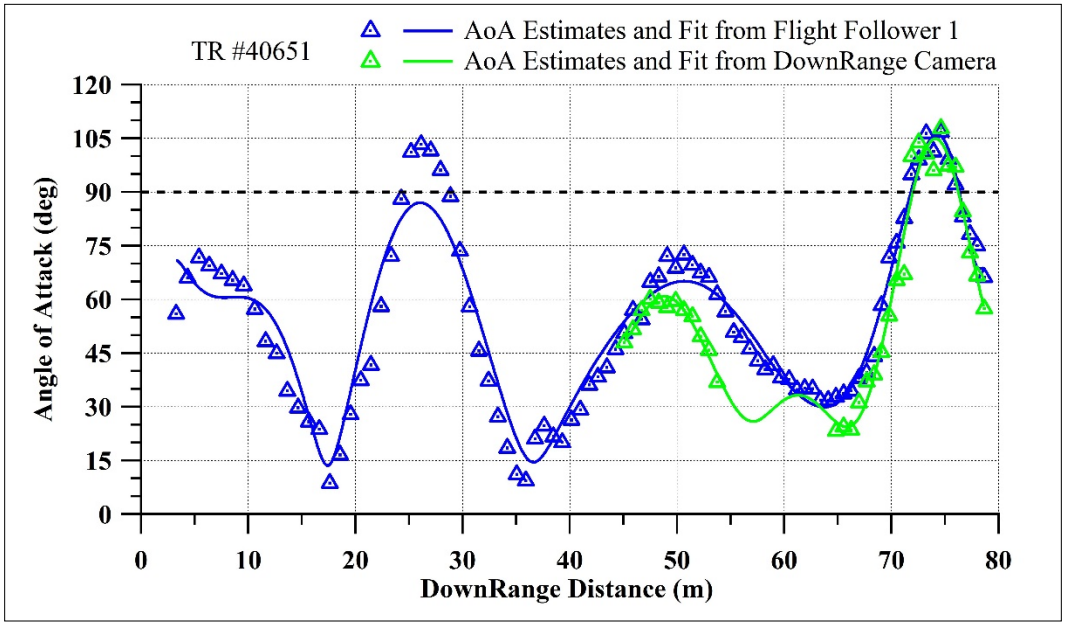

Fig. H-8 AoA vs. downrange distance in gun coordinates, TR 40651

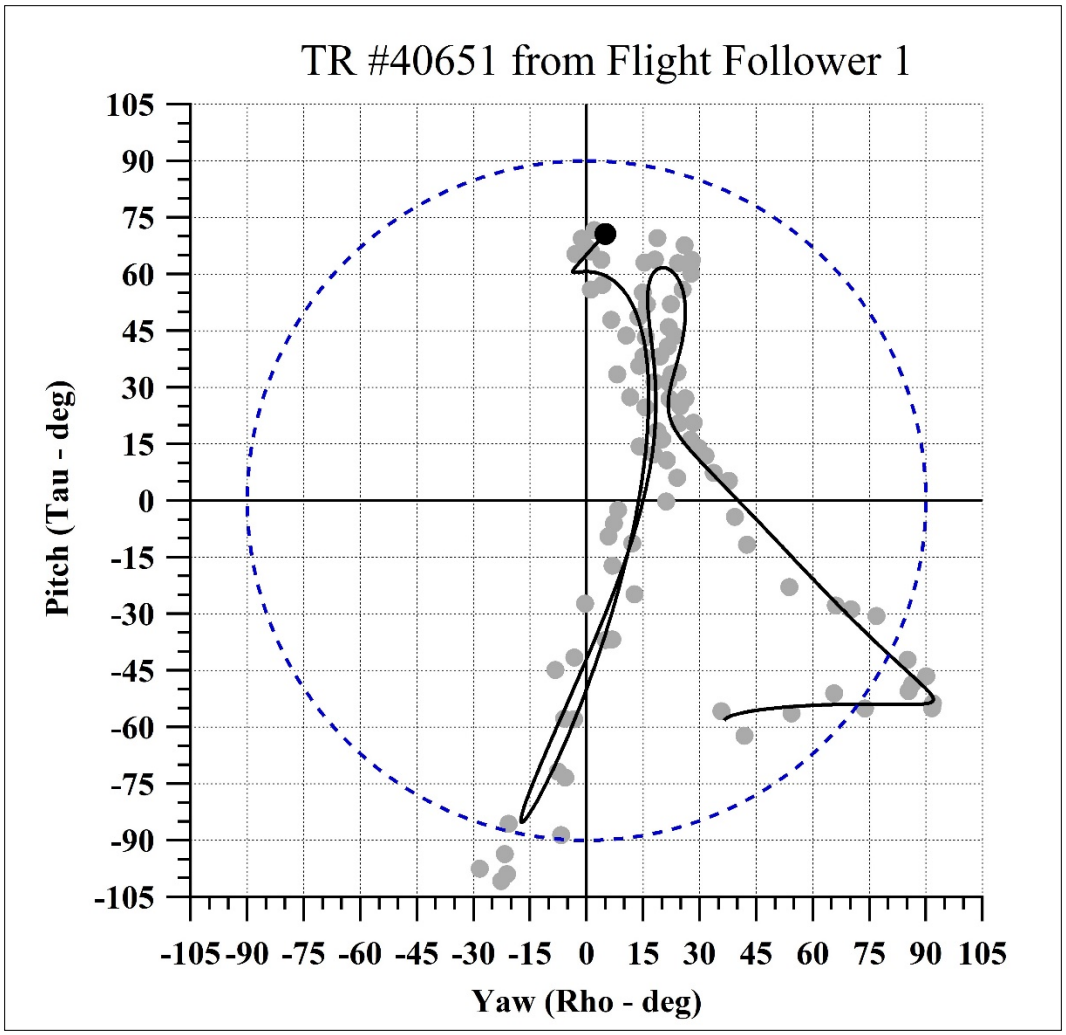

Fig. H-9 Pitch vs. yaw, TR 40651

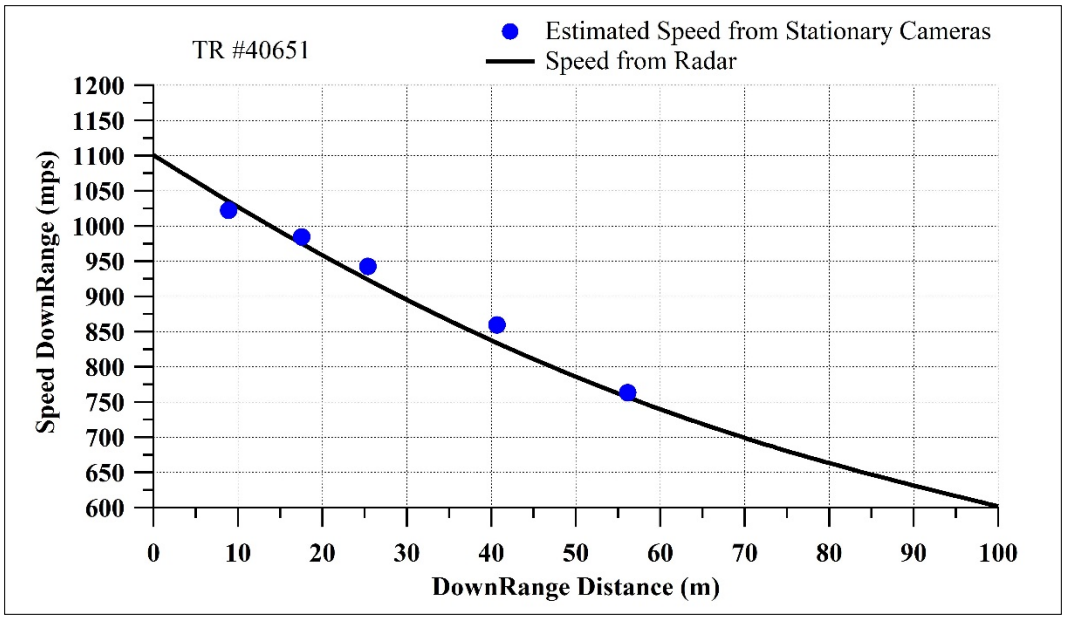

Fig. H-10 CobraMRV speed from video and radar vs. downrange distance, TR 40651

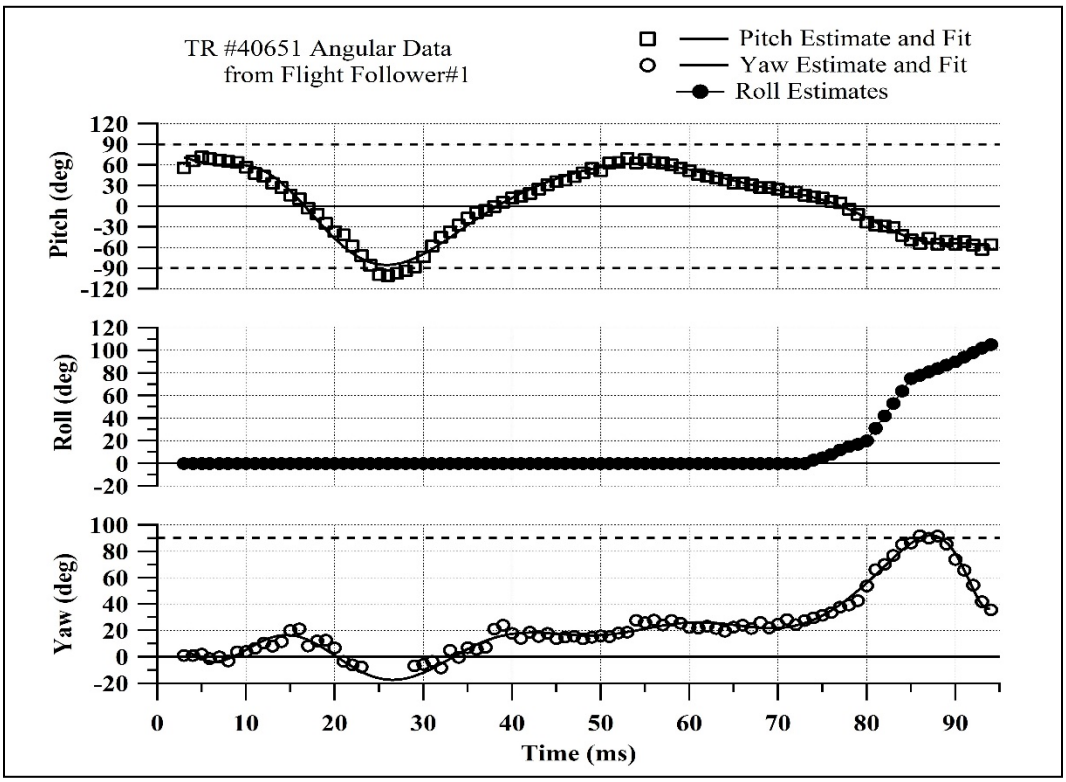

Fig. H-11 Pitch, yaw, and roll angle estimates from Flight Follower 1 vs. flight time in gun coordinates, TR 40651

Appendix I. Results: Tube Round (TR) 40652

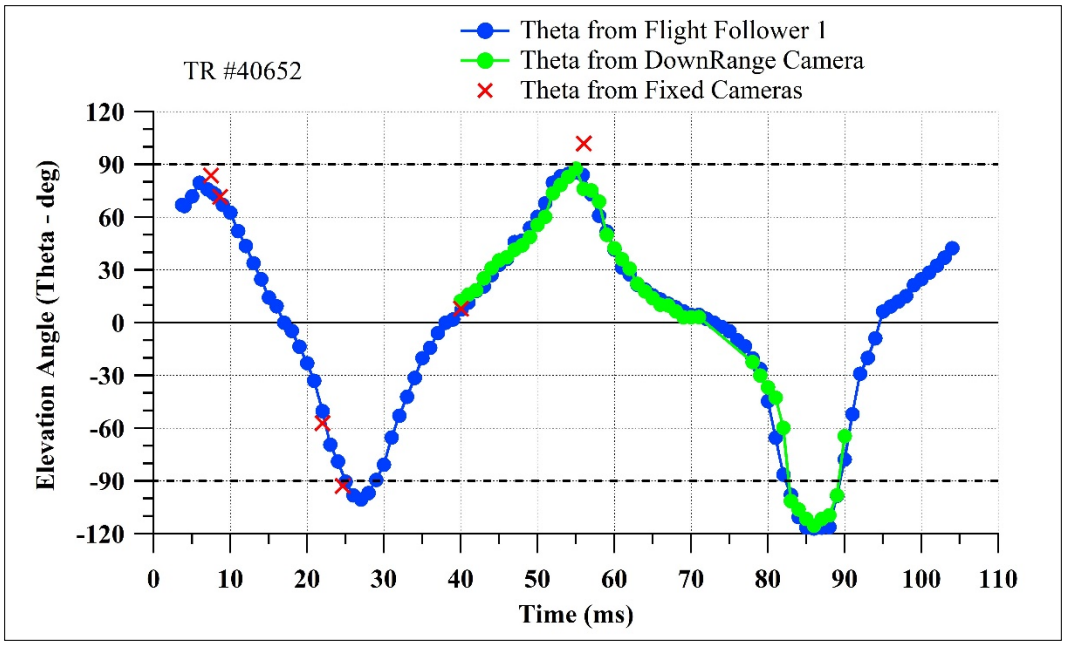

Fig. I-1 Elevation angle vs. flight time in gun coordinates, TR 40652

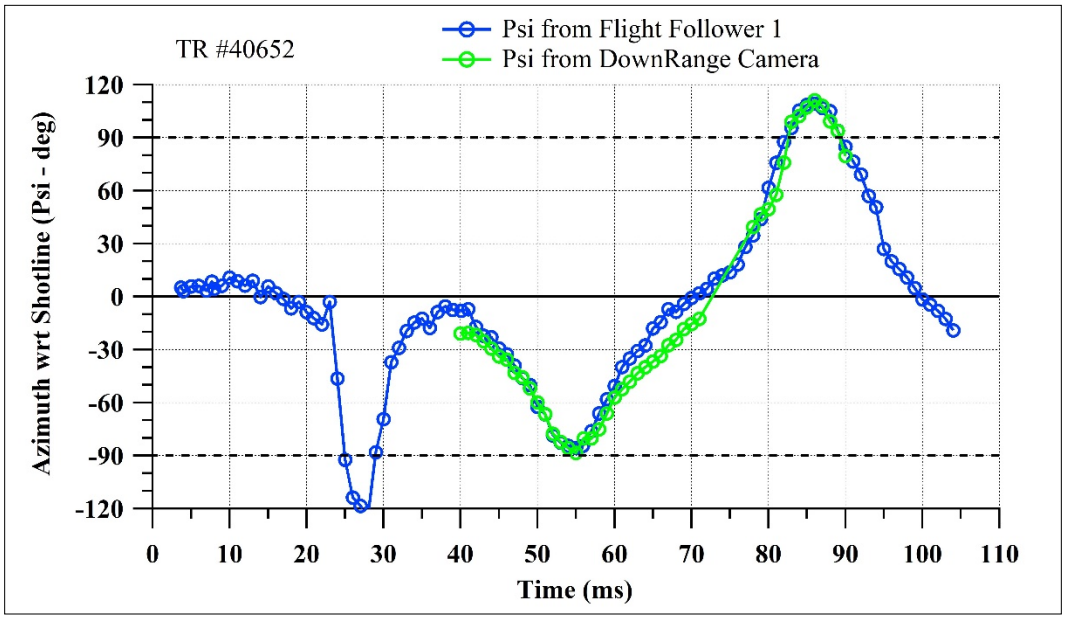

Fig. I-2 Azimuth angle vs. flight time in gun coordinates, TR 40652

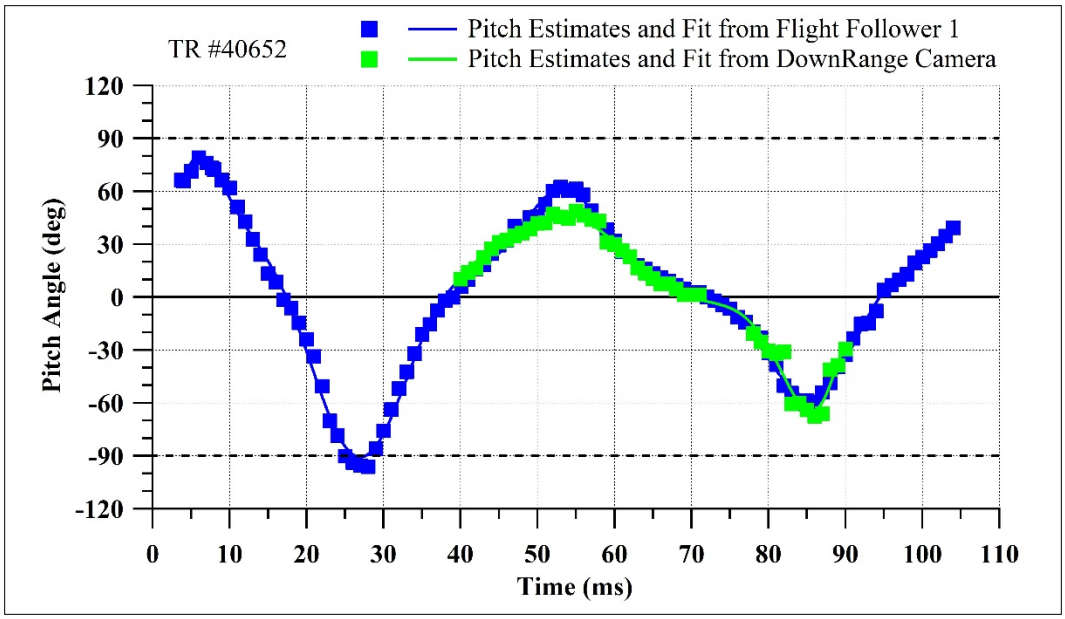

Fig. I-3 Pitch angle vs. flight time in gun coordinates, TR 40652

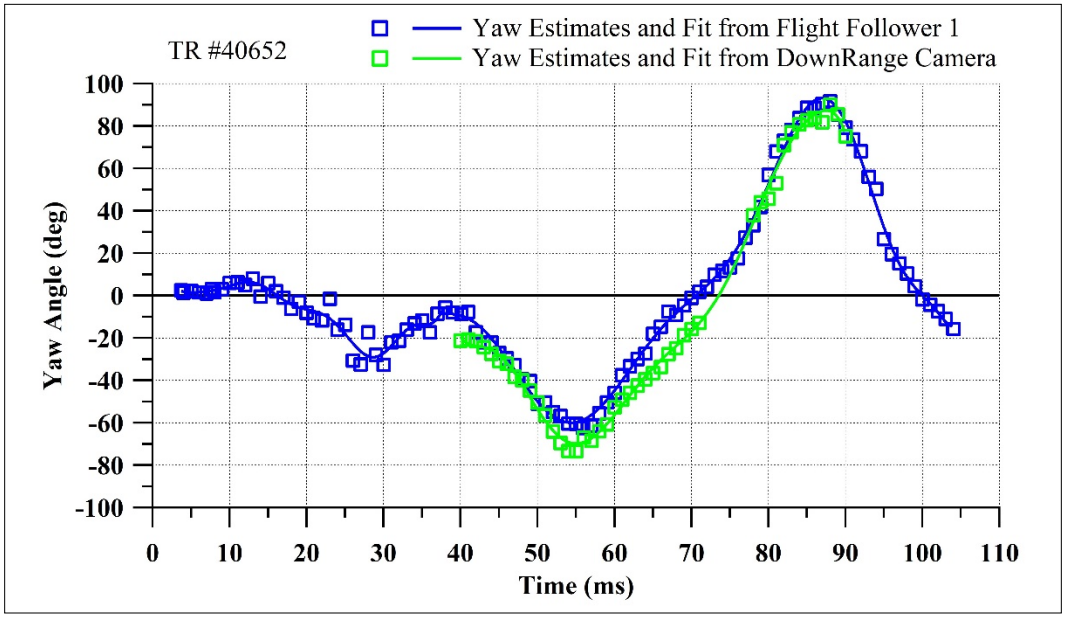

Fig. I-4 Yaw angle vs. flight time in gun coordinates, TR 40652

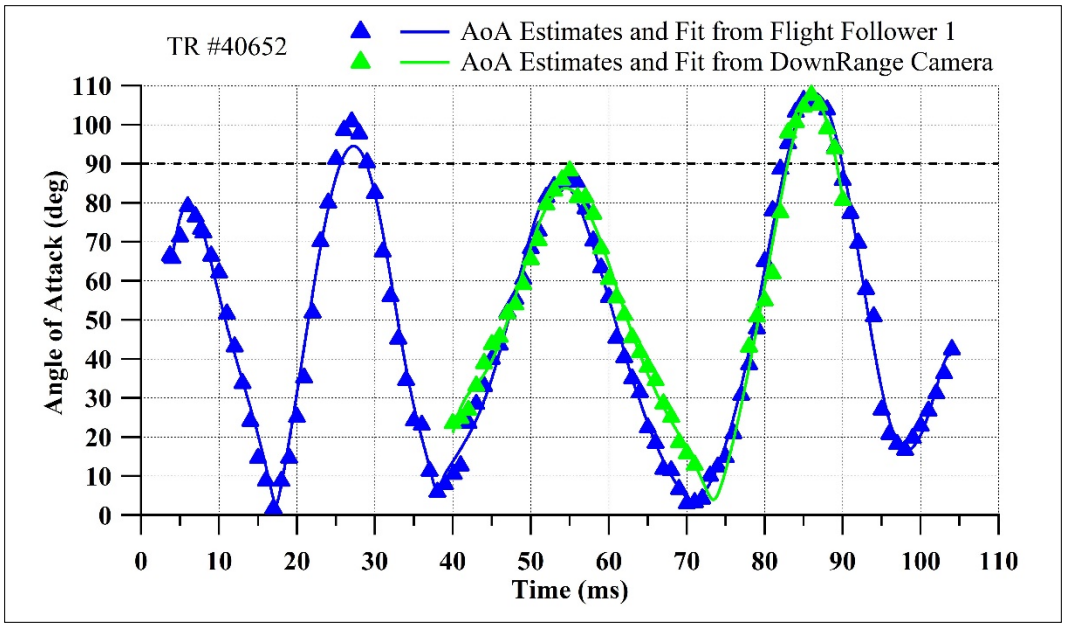

Fig. I-5 Angle of attack (AoA) vs. flight time in gun coordinates, TR 40652

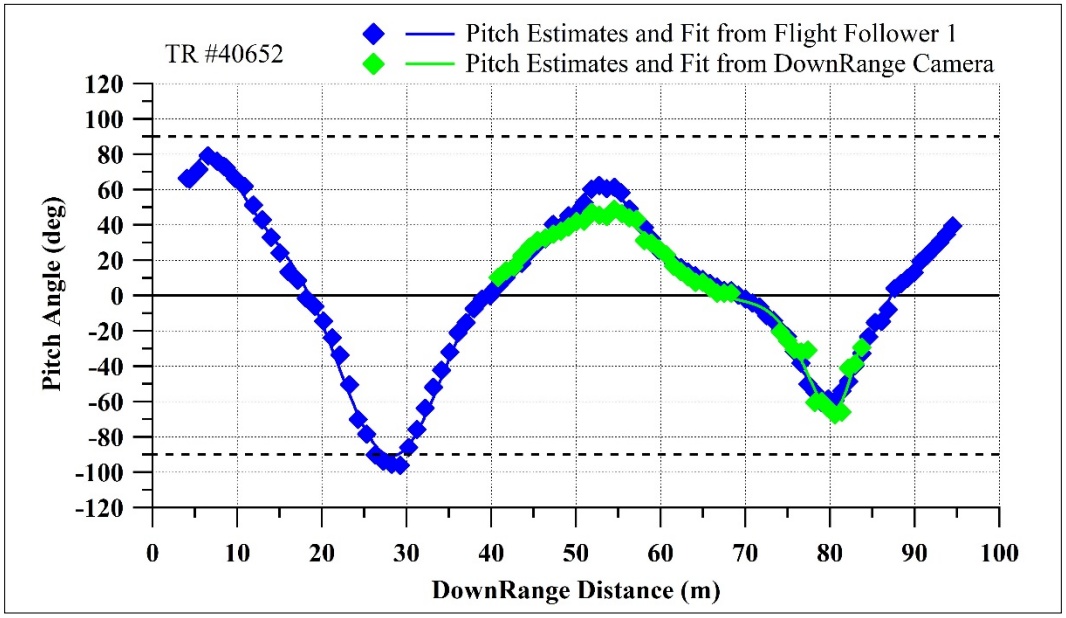

Fig. I-6 Pitch angle vs. downrange distance in gun coordinates, TR 40652

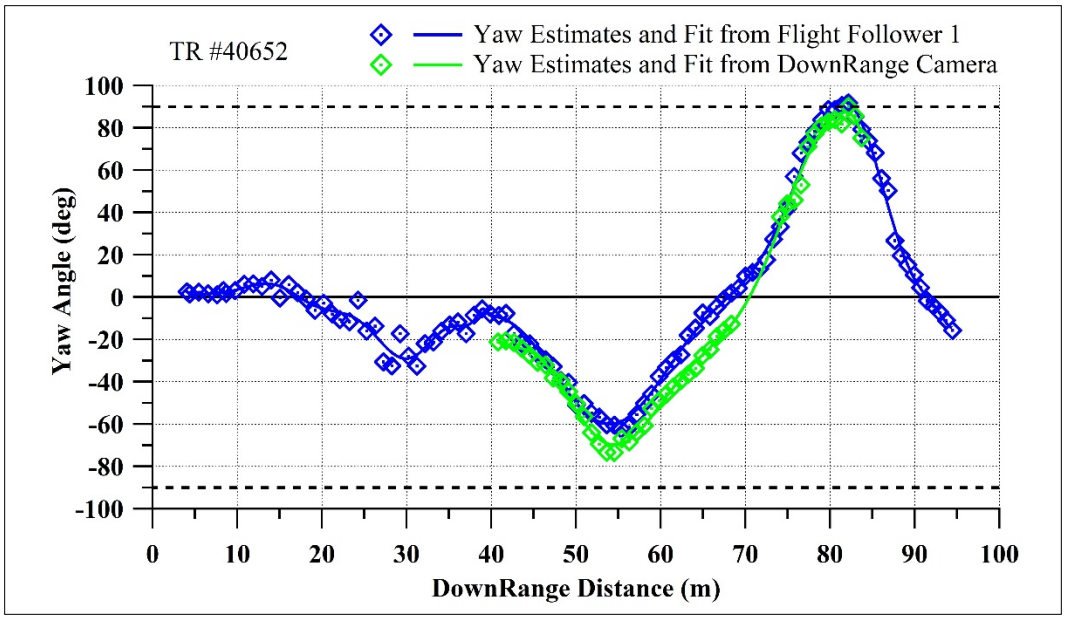

Fig. I-7 Yaw angle vs. downrange distance in gun coordinates, TR 40652

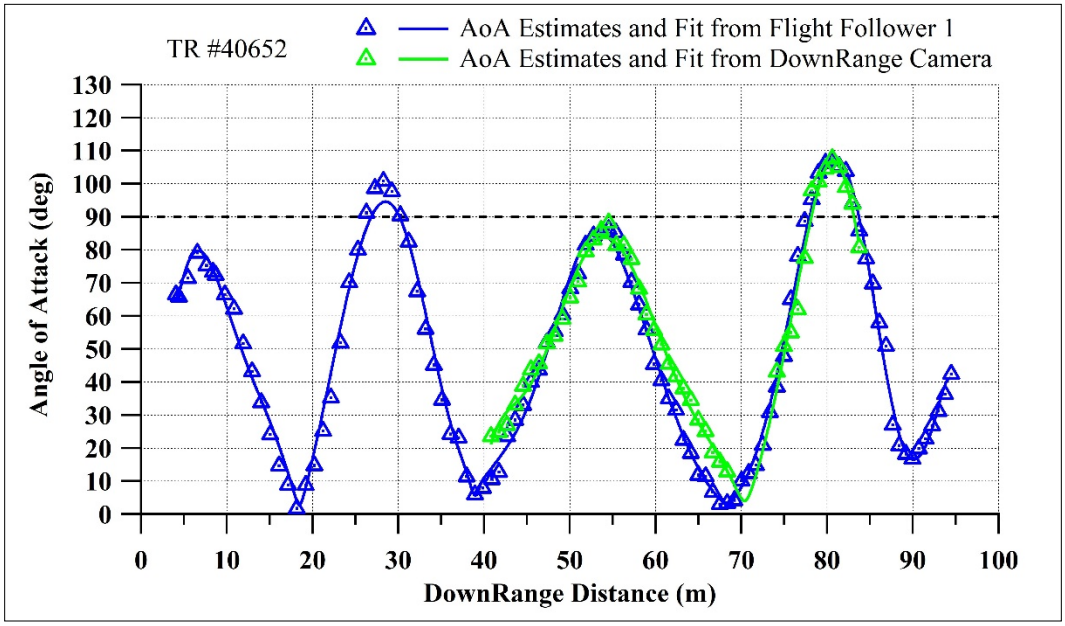

Fig. I-8 AoA vs. downrange distance in gun coordinates, TR 40652

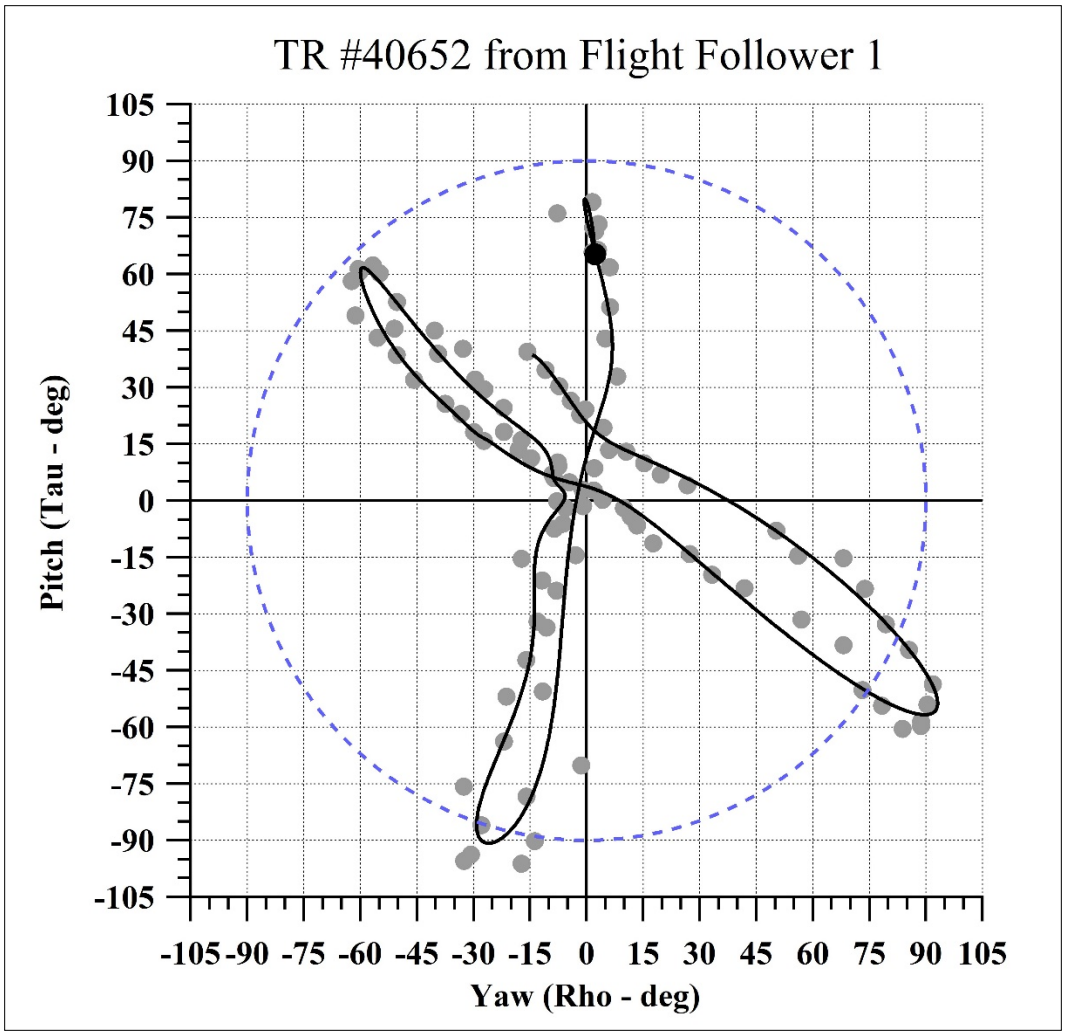

Fig. I-9 Pitch vs. yaw, TR 40652

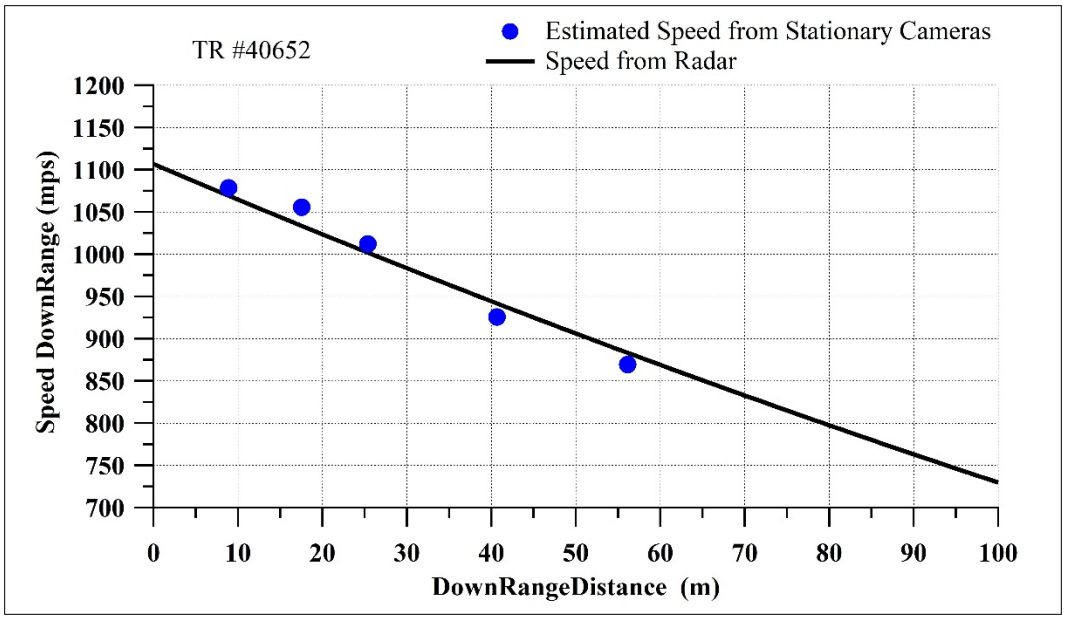

Fig. I-10 CobraMRV speed from video and radar vs. downrange distance, TR 40652

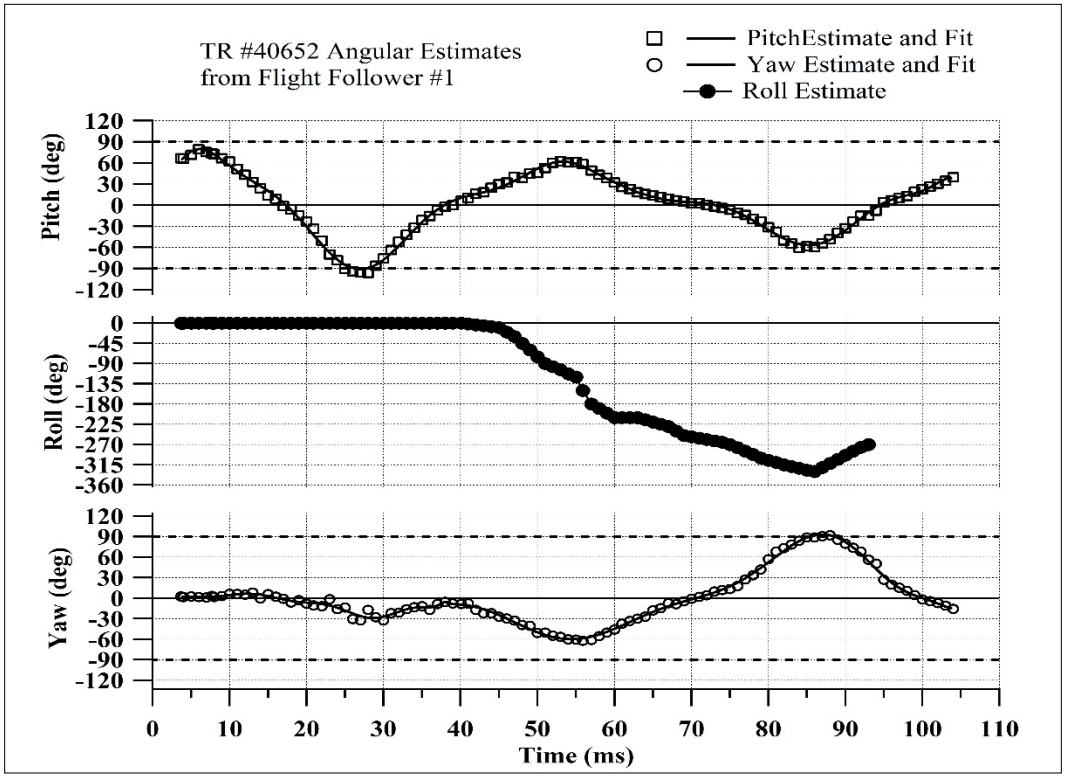

Fig. I-11 Pitch, yaw, and roll angle estimates from Flight Follower 1 vs. flight time in gun coordinates, TR 40652

Appendix J. Results: Tube Round (TR) 40653

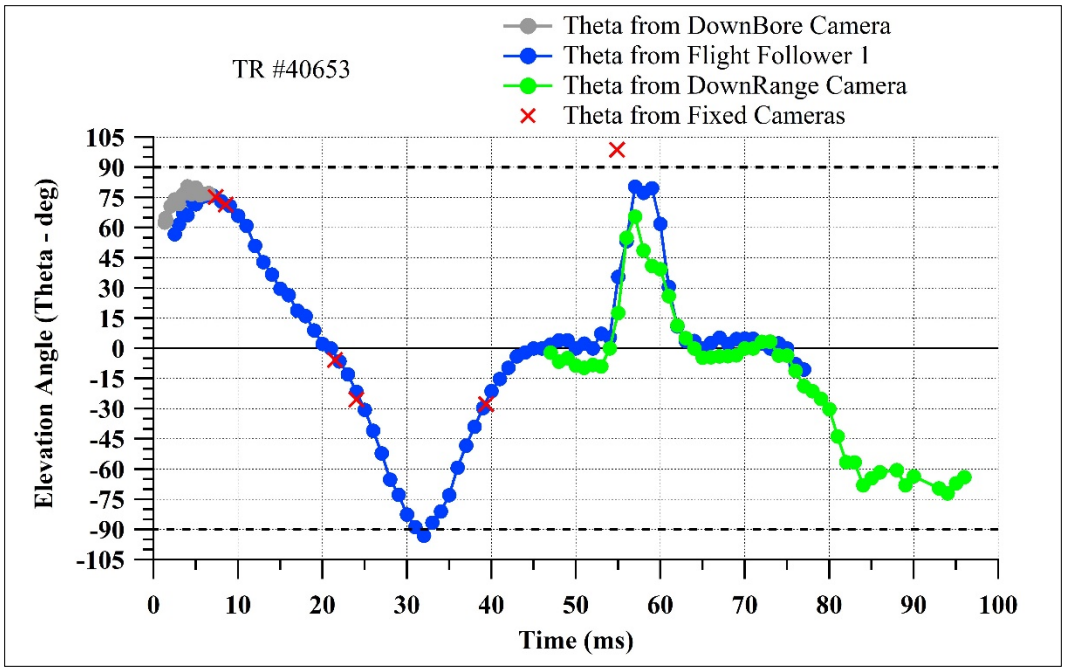

Fig. J-1 Elevation angle vs. flight time in gun coordinates, TR 40653

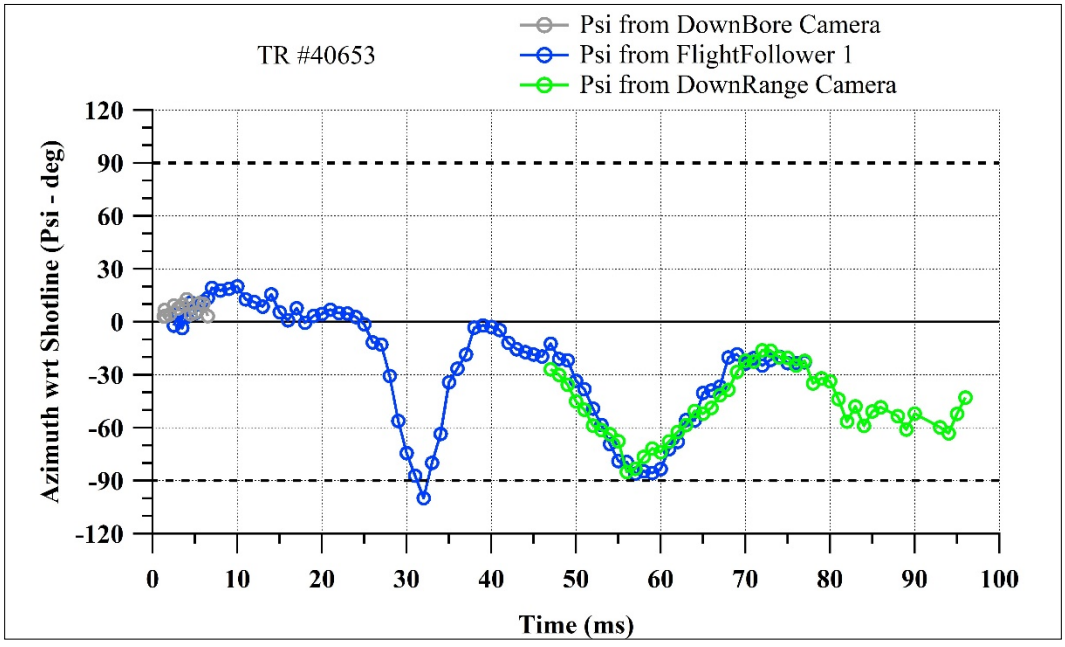

Fig. J-2 Azimuth angle vs. flight time in gun coordinates, TR 40653

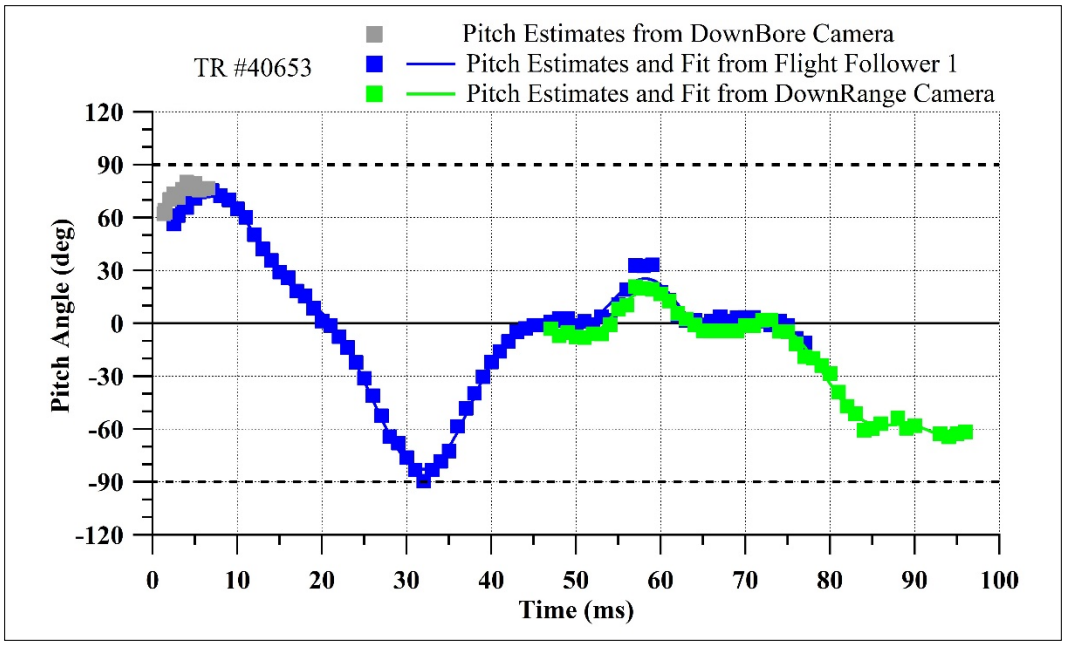

Fig. J-3 Pitch angle vs. flight time in gun coordinates, TR 40653

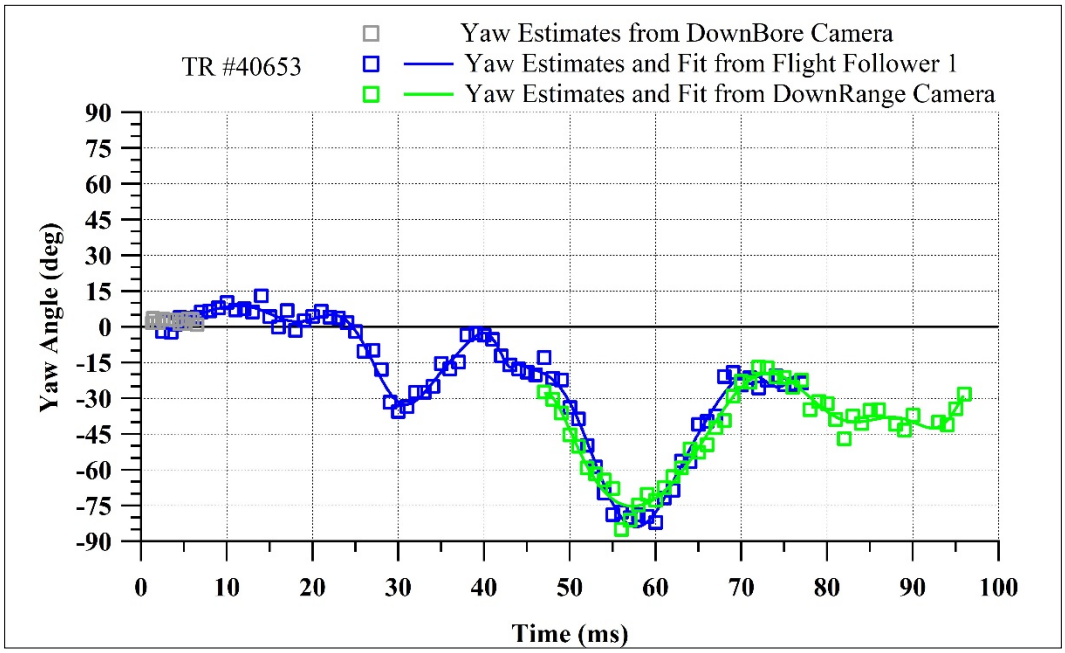

Fig. J-4 Yaw angle vs. flight time in gun coordinates, TR 40653

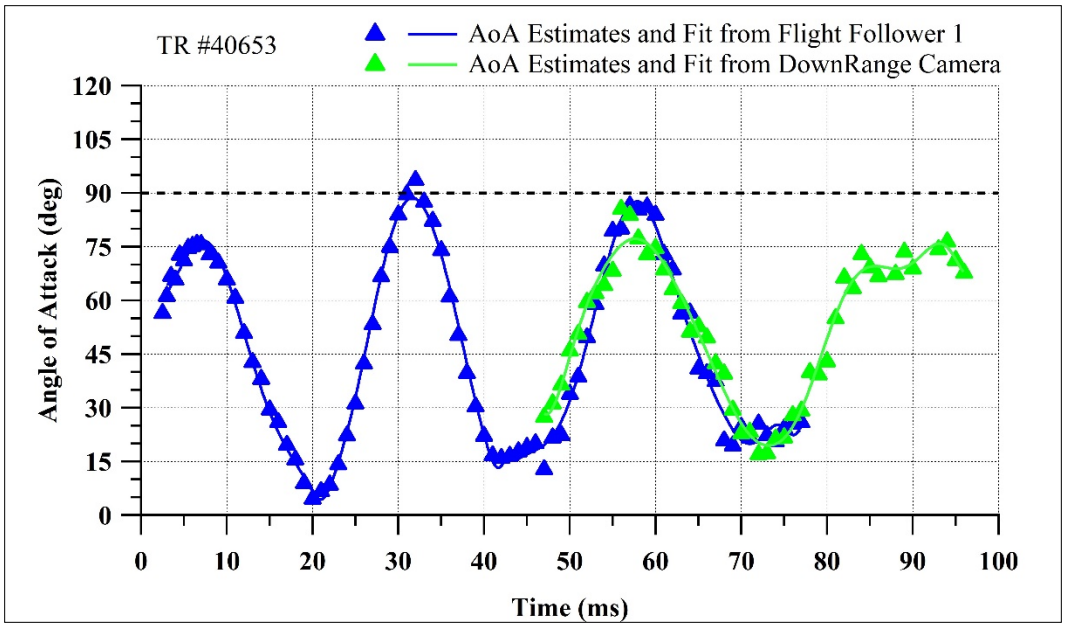

Fig. J-5 Angle of attack (AoA) vs. flight time in gun coordinates, TR 40653

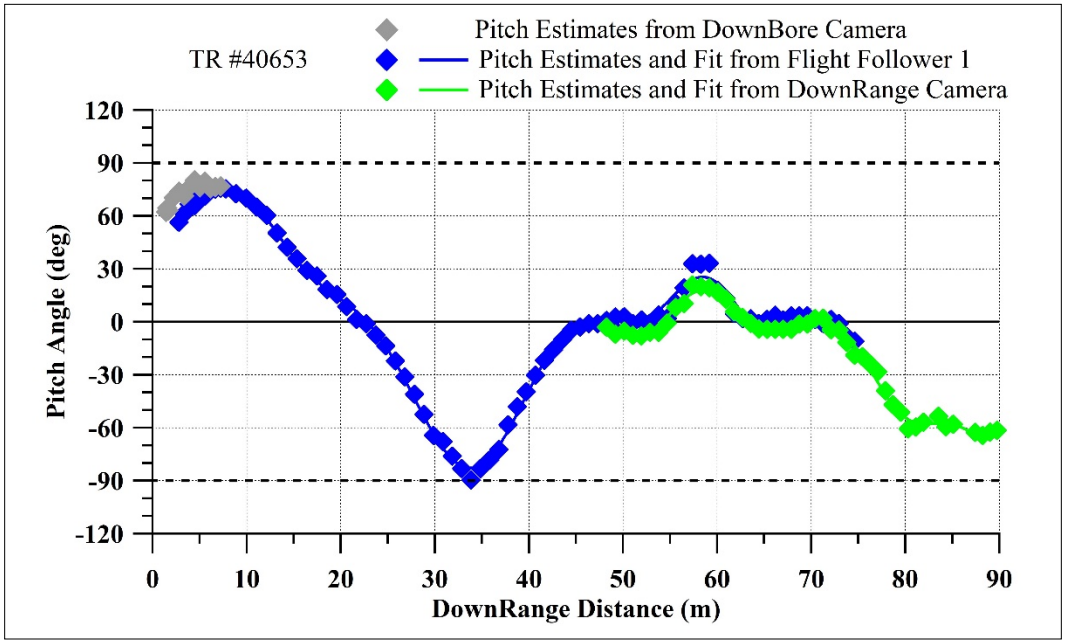

Fig. J-6 Pitch angle vs. downrange distance in gun coordinates, TR 40653

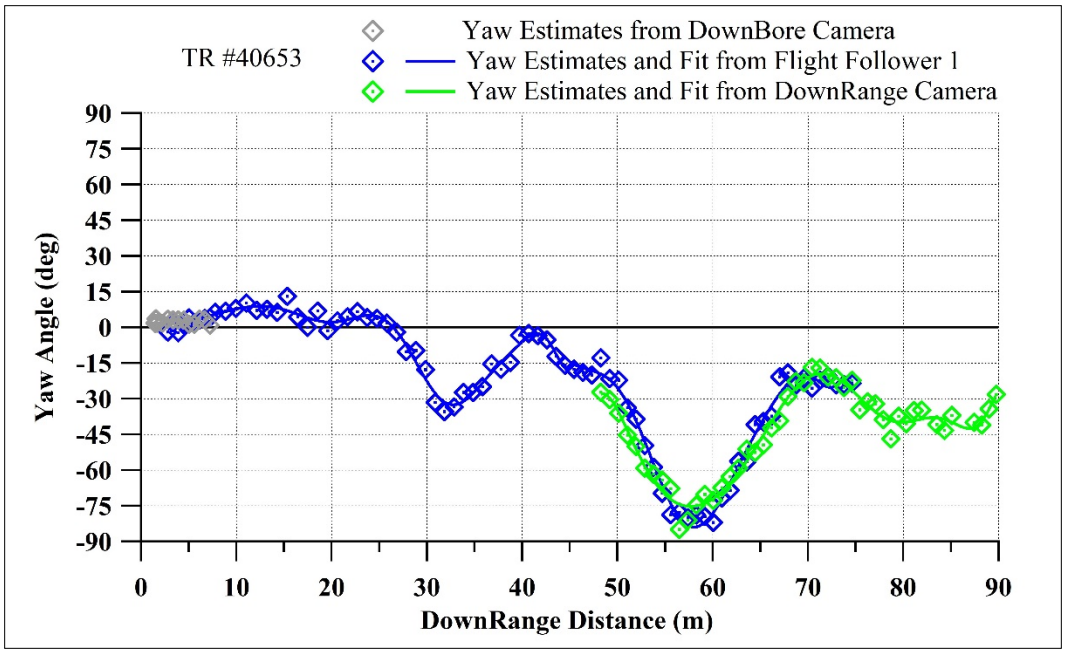

Fig. J-7 Yaw angle vs. downrange distance in gun coordinates, TR 40653

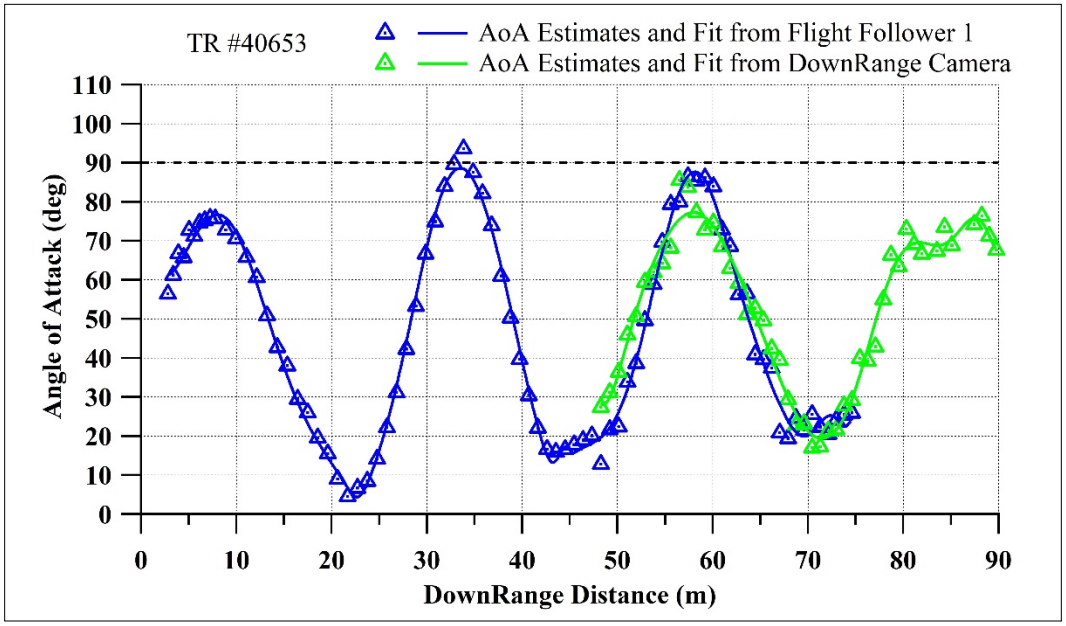

Fig. J-8 AoA vs. downrange distance in gun coordinates, TR 40653

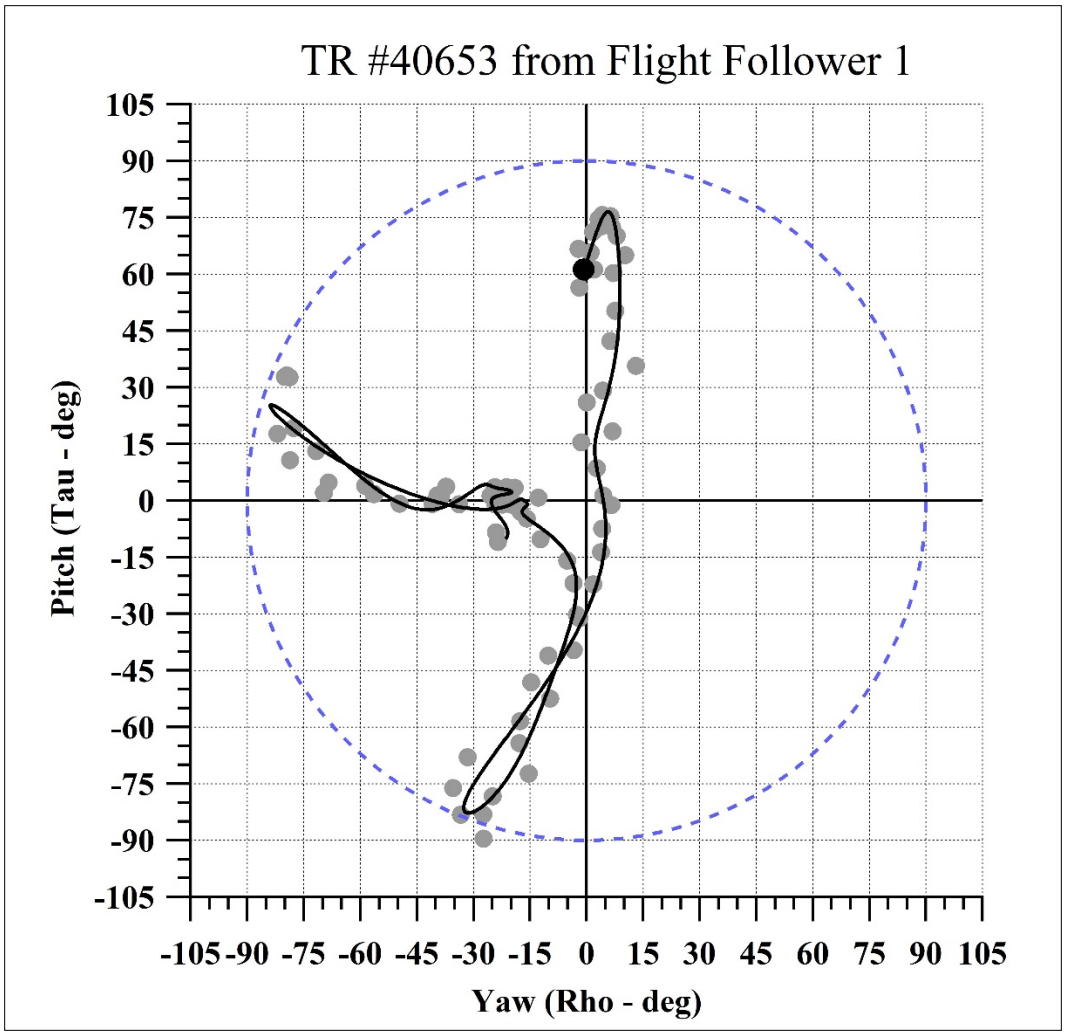

Fig. J-9 Pitch vs. yaw, TR 40653

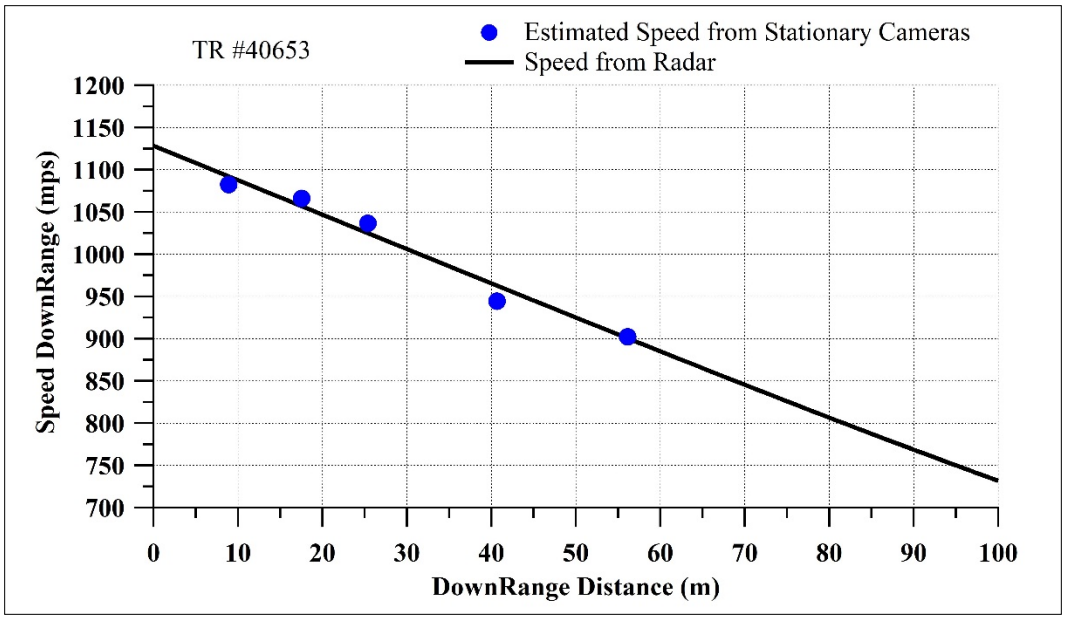

Fig. J-10 CobraMRV speed from video and radar vs. downrange distance, TR 40653

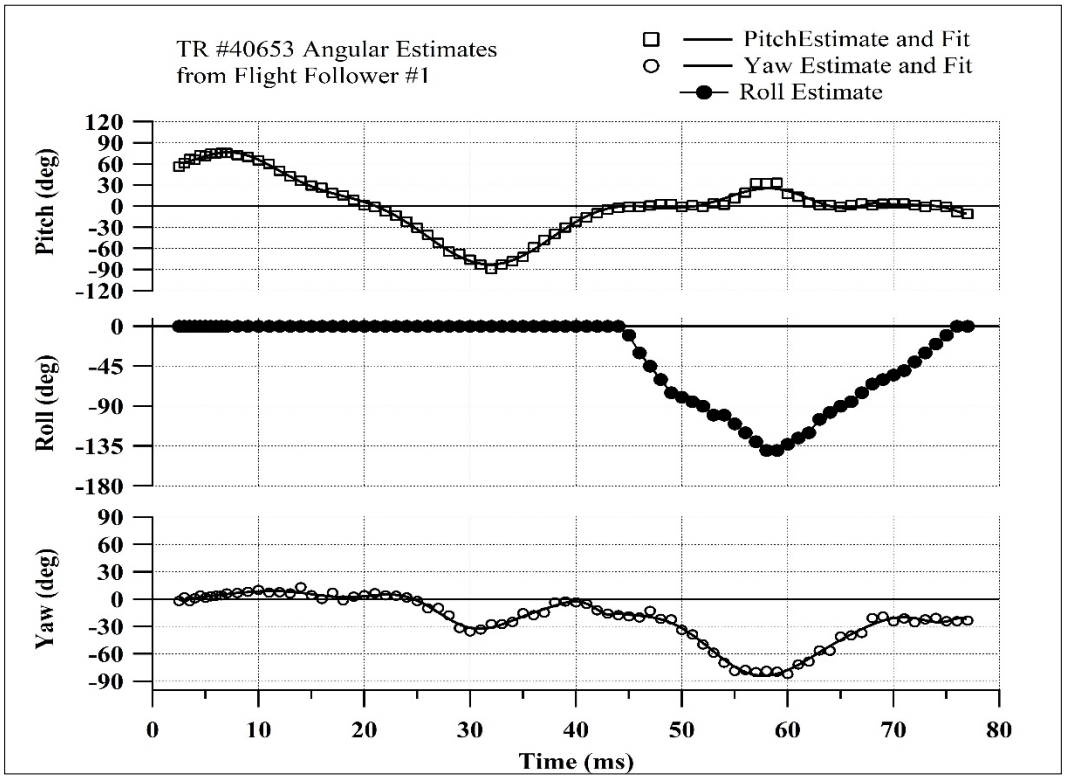

Fig. J-11 Pitch, yaw, and roll angle estimates from Flight Follower 1 vs. flight time in gun coordinates, TR 40653

Appendix K. Results: Tube Round (TR) 40654

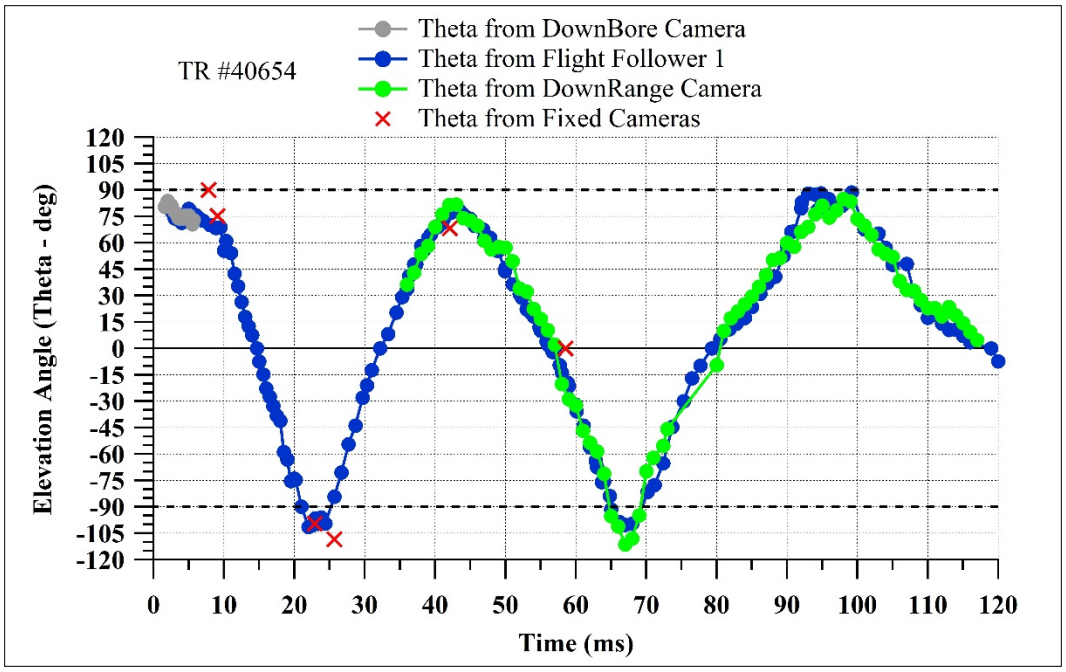

Fig. K-1 Elevation angle vs. flight time in gun coordinates, TR 40654

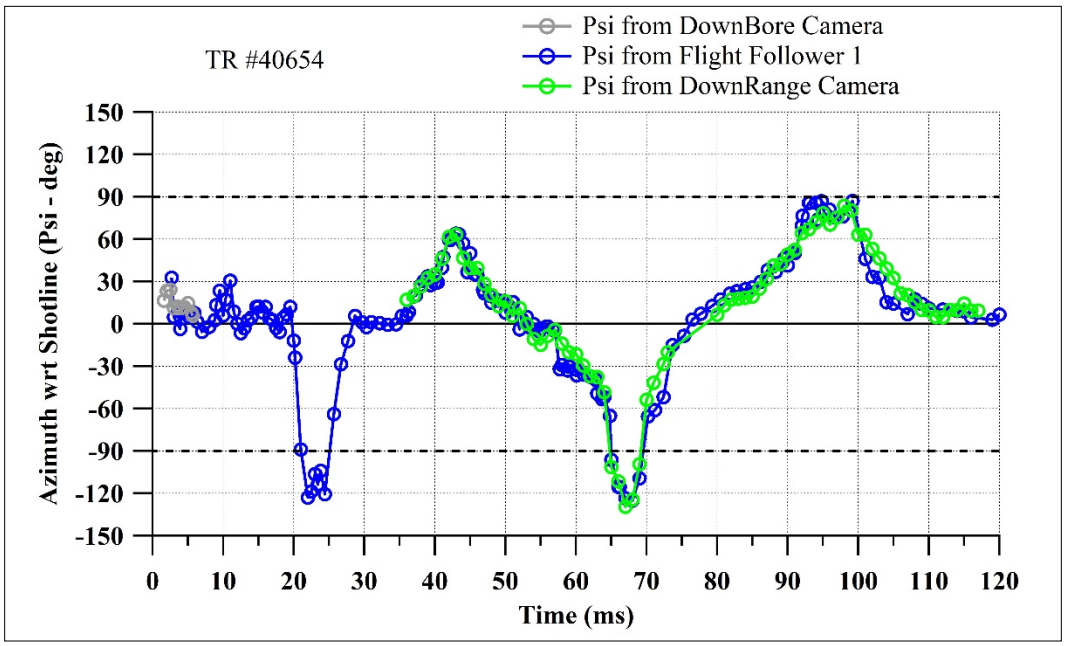

Fig. K-2 Azimuth angle vs. flight time in gun coordinates, TR 40654

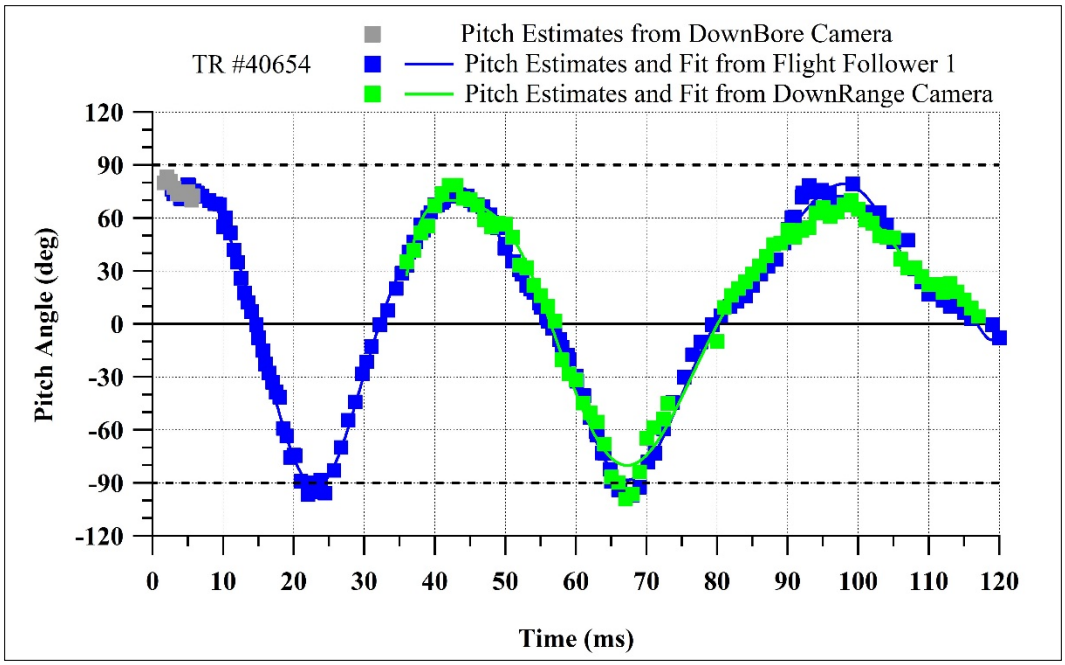

Fig. K-3 Pitch angle vs. flight time in gun coordinates, TR 40654

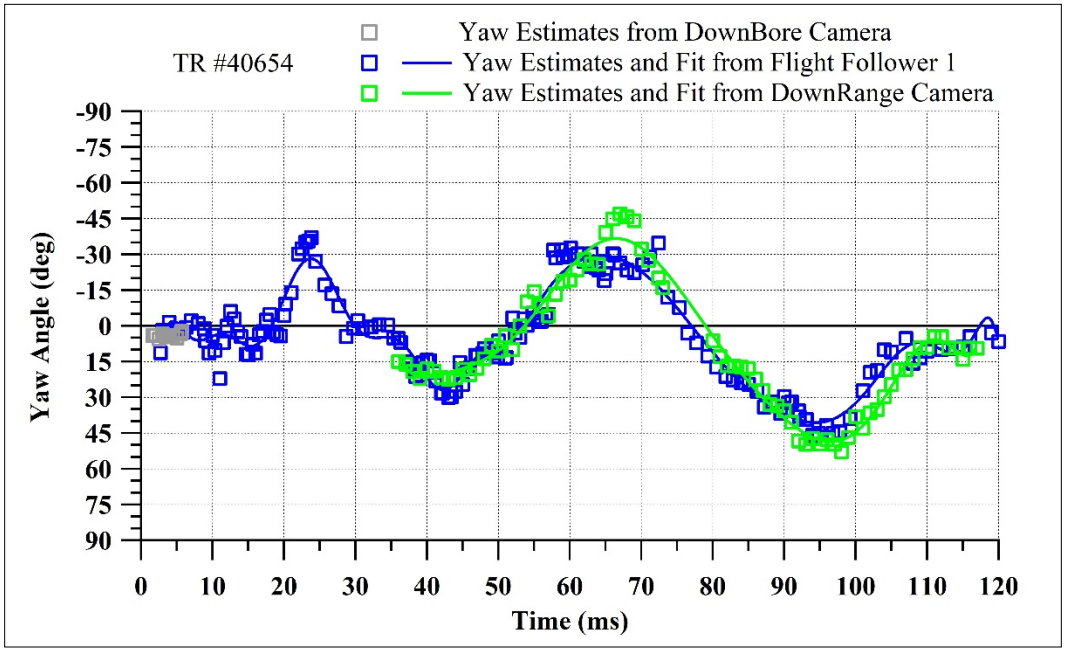

Fig. K-4 Yaw angle vs. flight time in gun coordinates, TR 40654

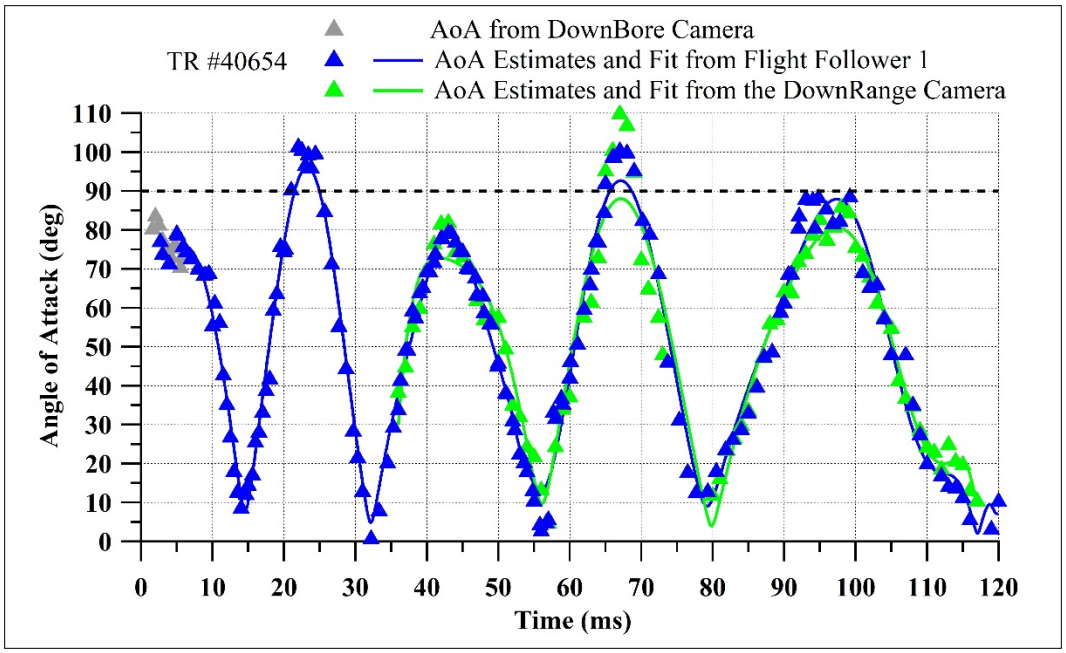

Fig. K-5 Angle of attack (AoA) vs. flight time in gun coordinates, TR 40654

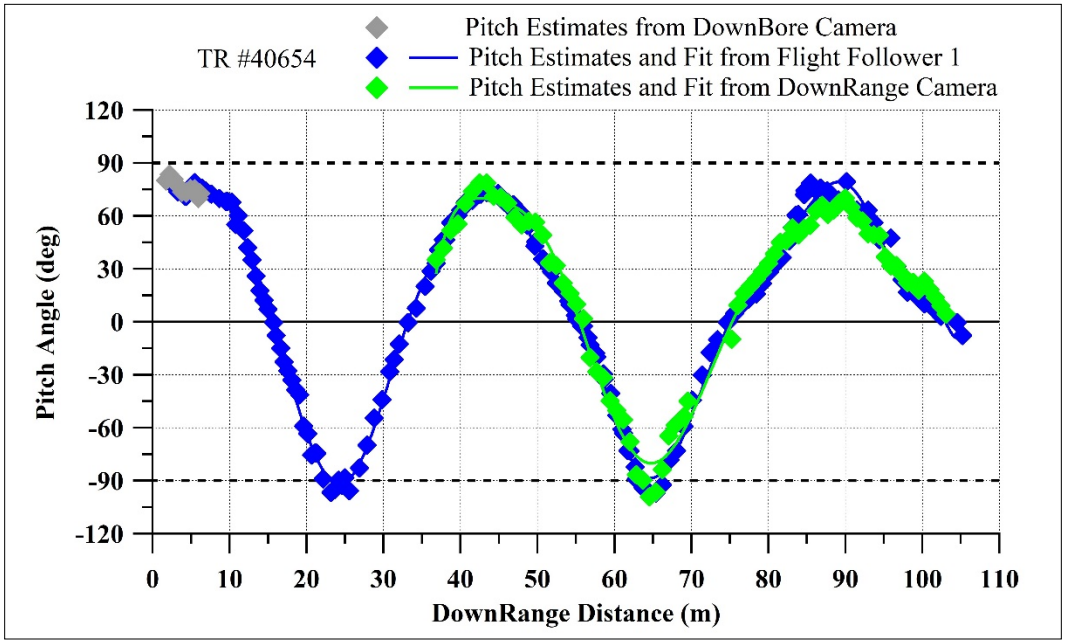

Fig. K-6 Pitch angle vs. downrange distance in gun coordinates, TR 40654

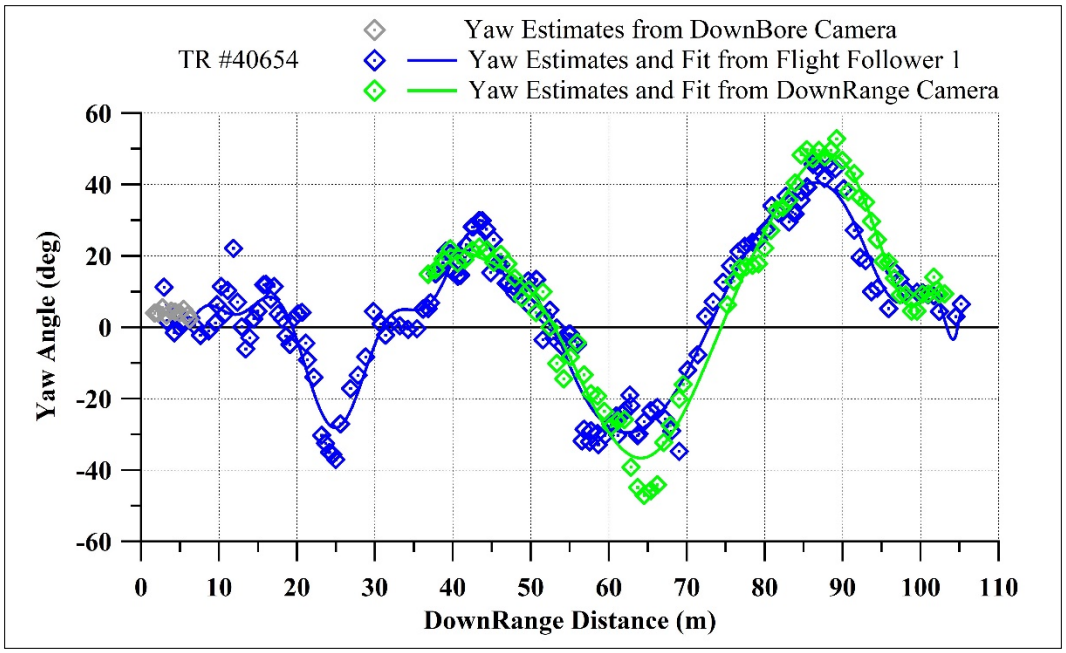

Fig. K-7 Yaw angle vs. downrange distance in gun coordinates, TR 40654

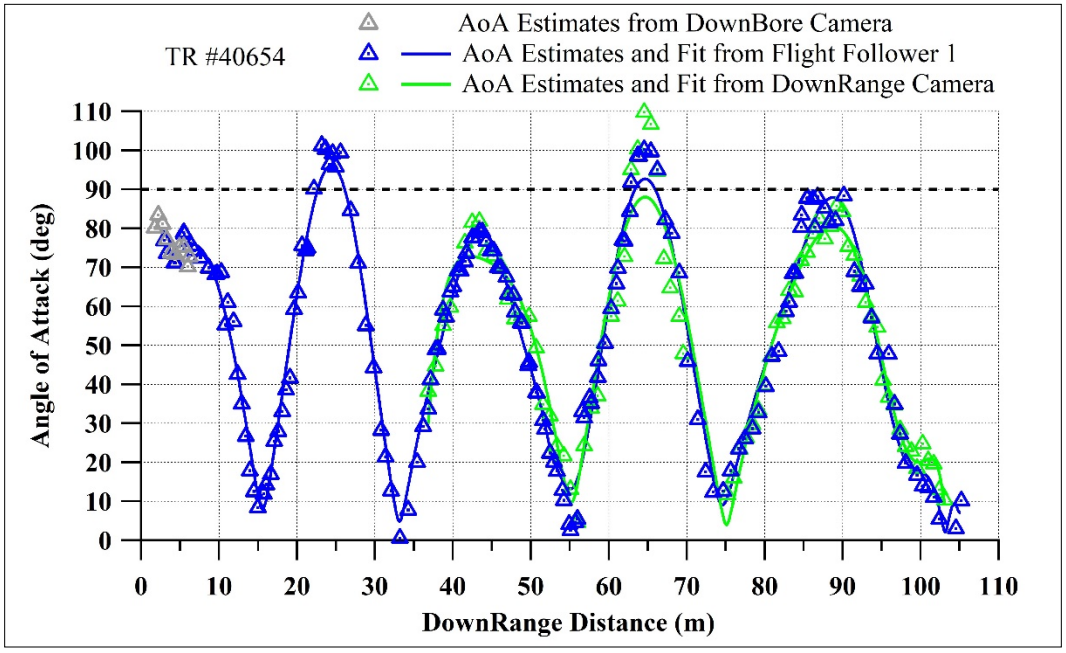

Fig. K-8 AoA vs. downrange distance in gun coordinates, TR 40654

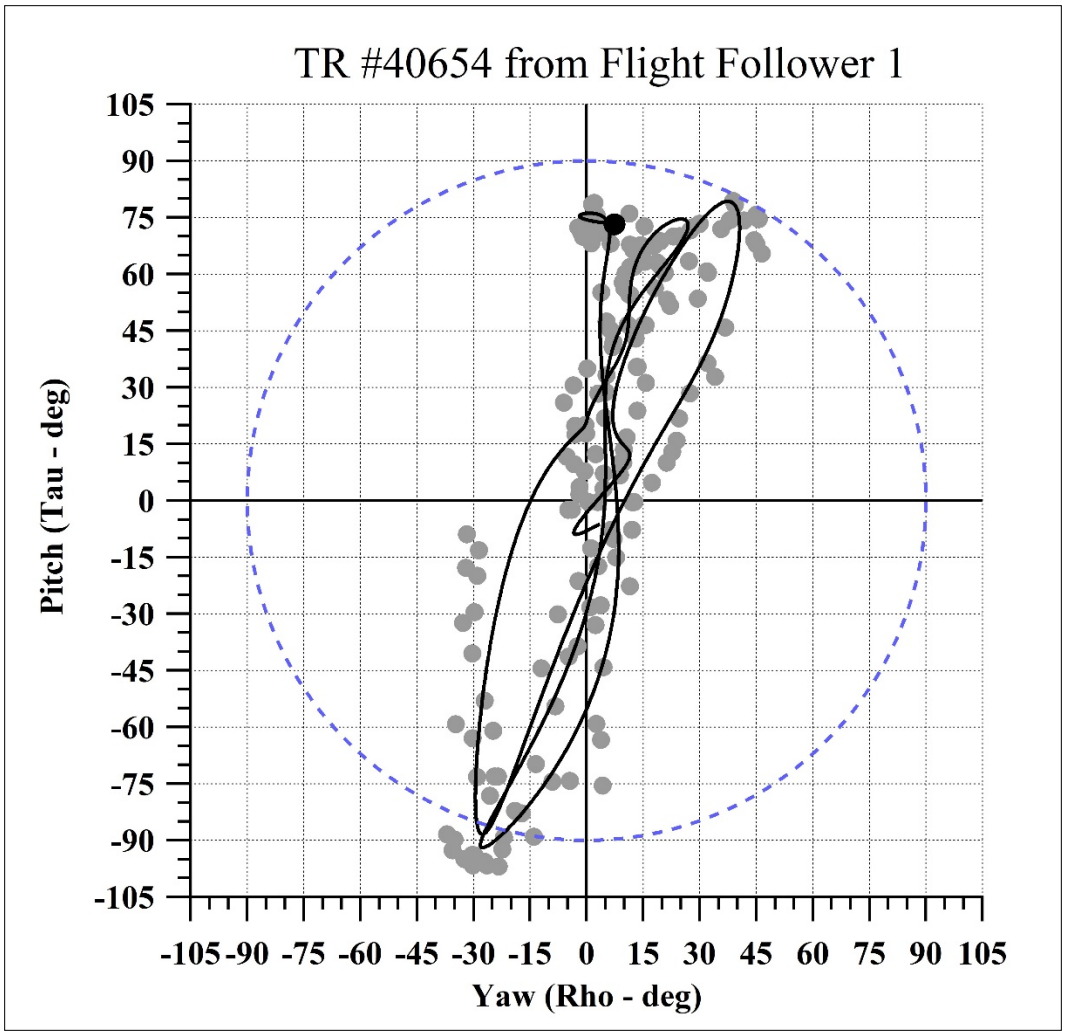

Fig. K-9 Pitch vs. yaw, TR 40654

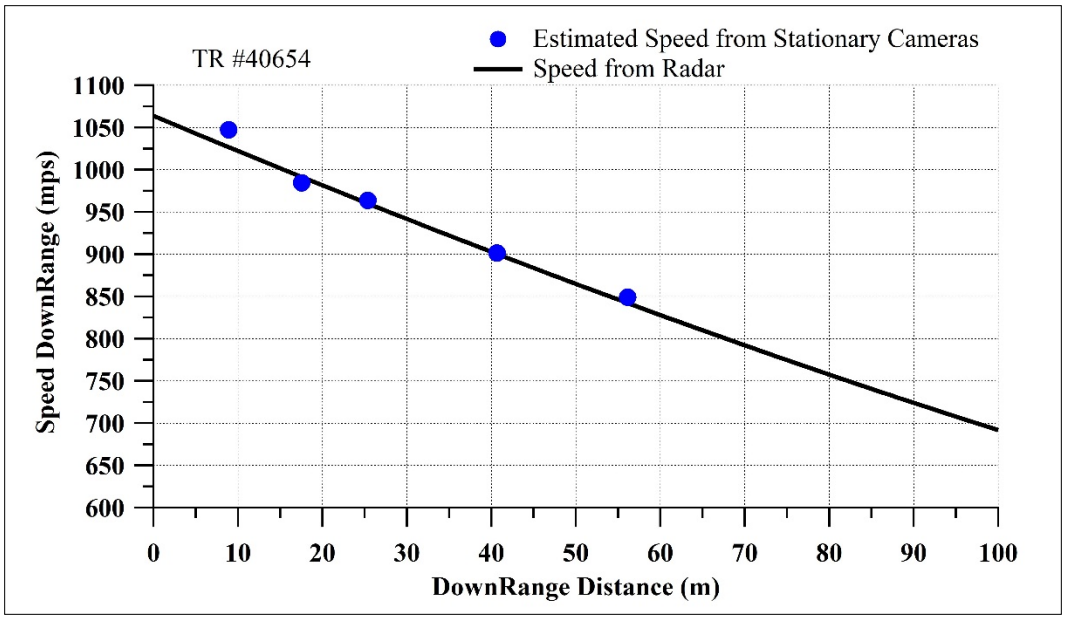

Fig. K-10 CobraMRV speed from video and radar vs. downrange distance, TR 40654

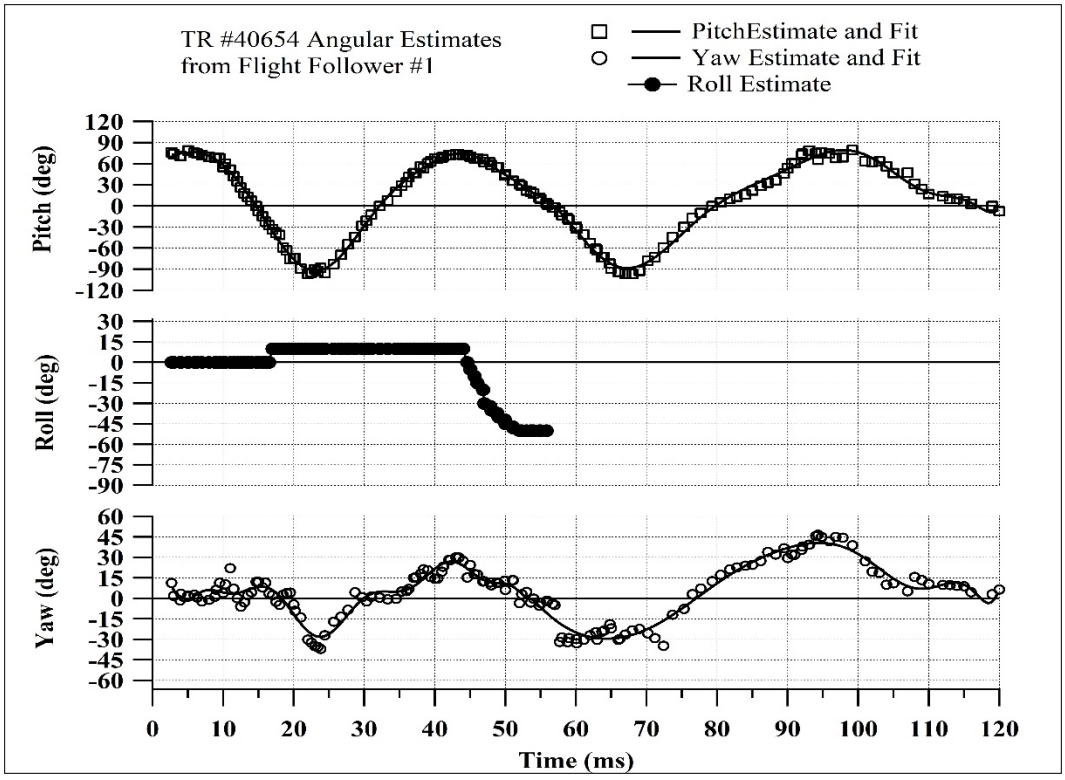

Fig. K-11 Pitch, yaw, and roll angle estimates from Flight Follower 1 vs. flight time in gun coordinates, TR 40654

Appendix L. Results: Tube Round (TR) 40655

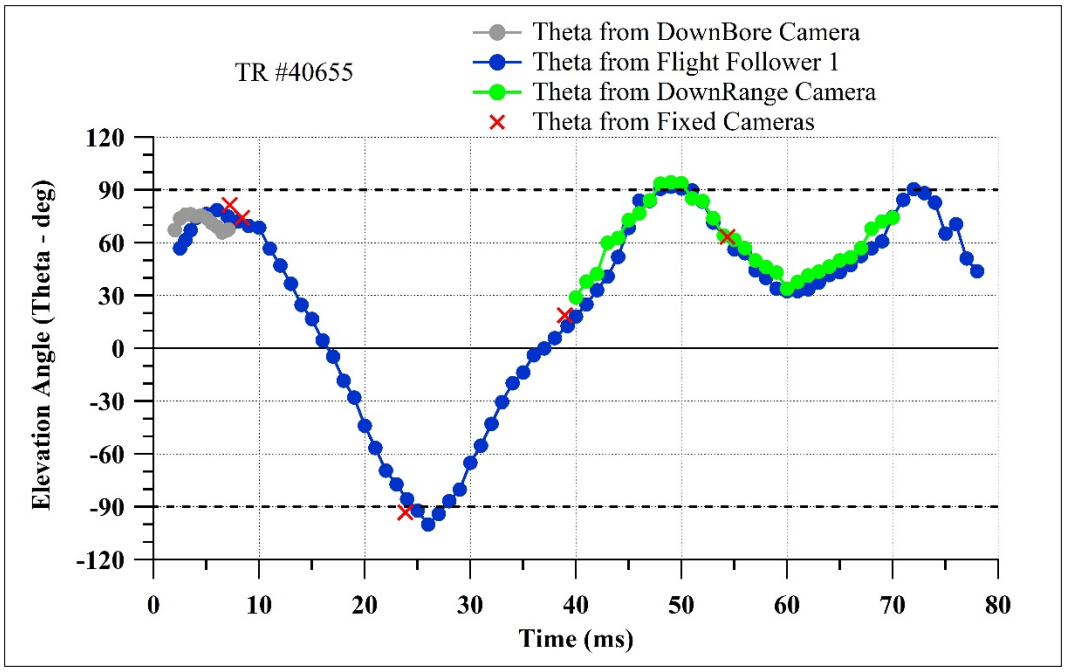

Fig. L-1 Elevation angle vs. flight time in gun coordinates, TR 40655

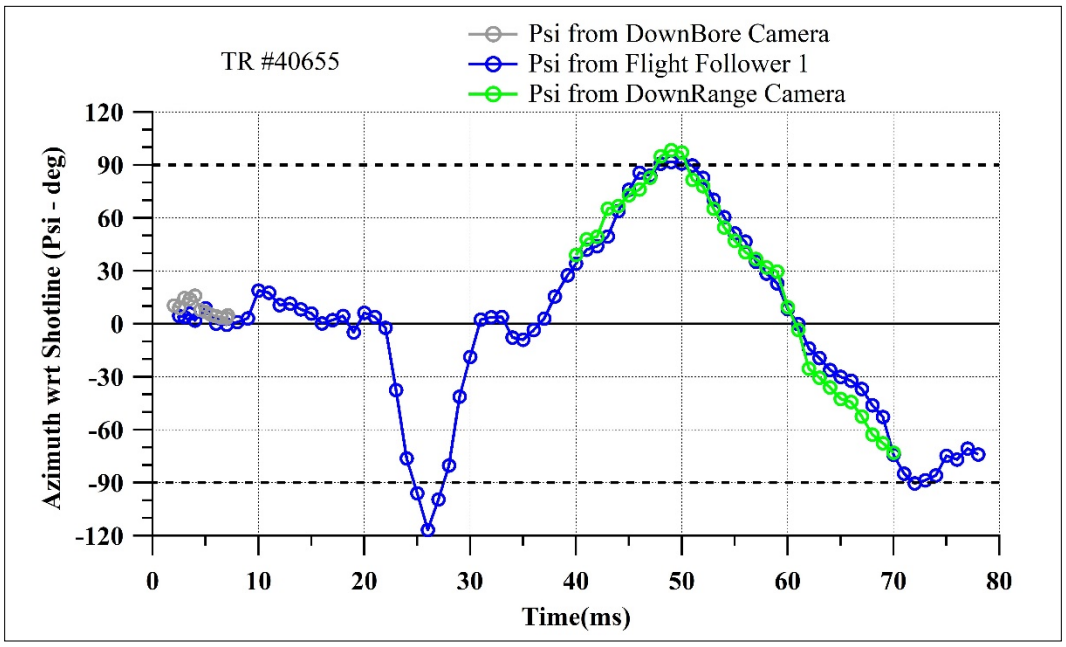

Fig. L-2 Azimuth angle vs. flight time in gun coordinates, TR 40655

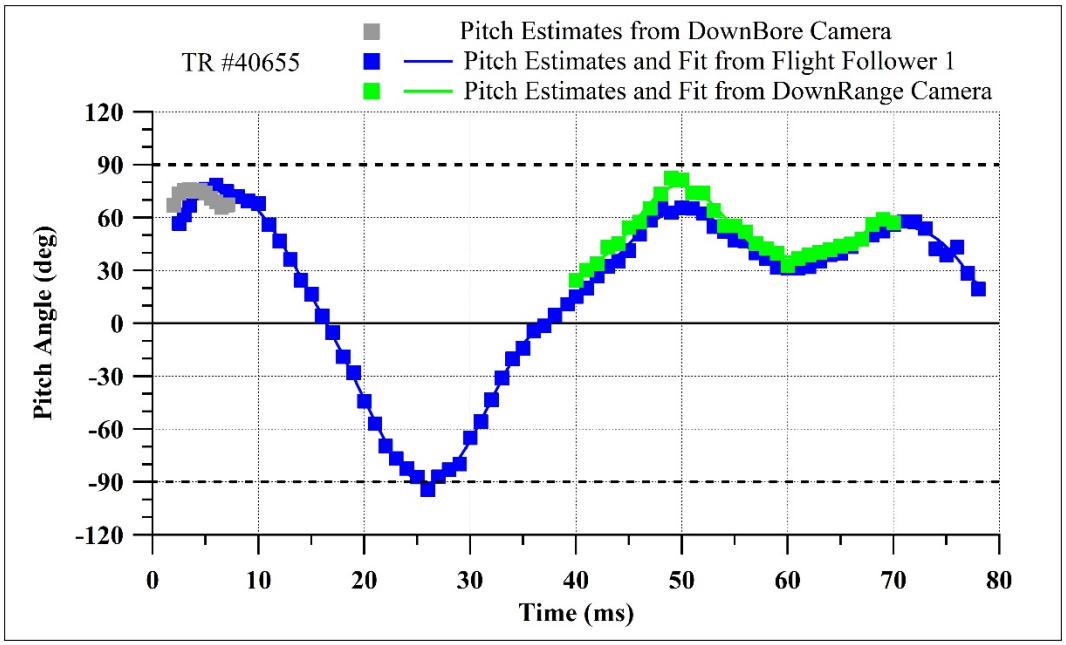

Fig. L-3 Pitch angle vs. flight time in gun coordinates, TR 40655

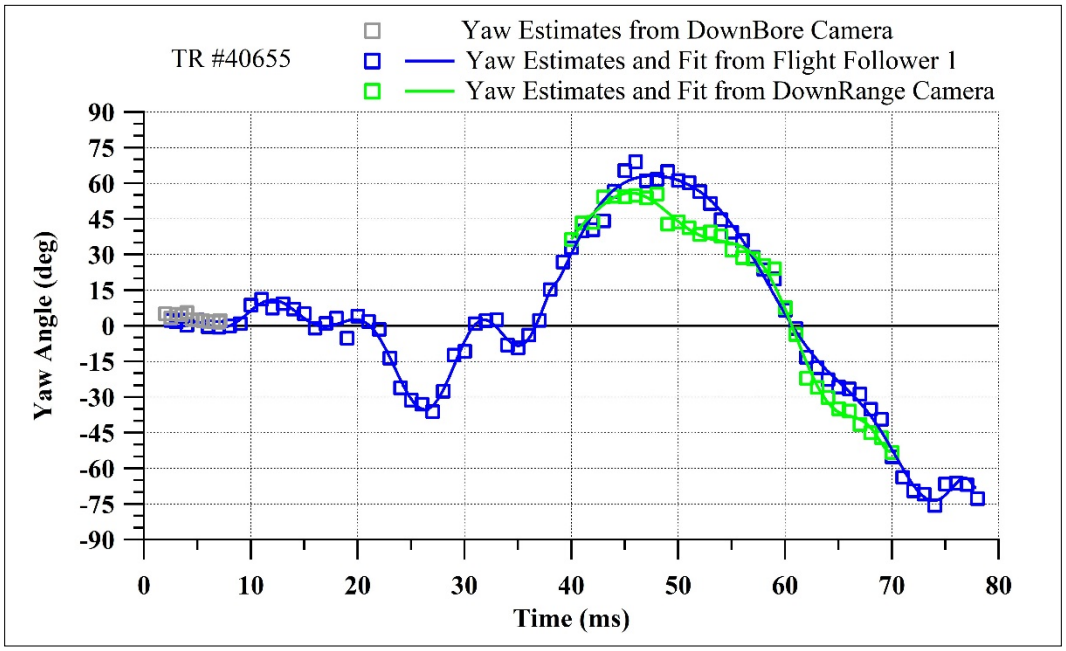

Fig. L-4 Yaw angle vs. flight time in gun coordinates, TR 40655

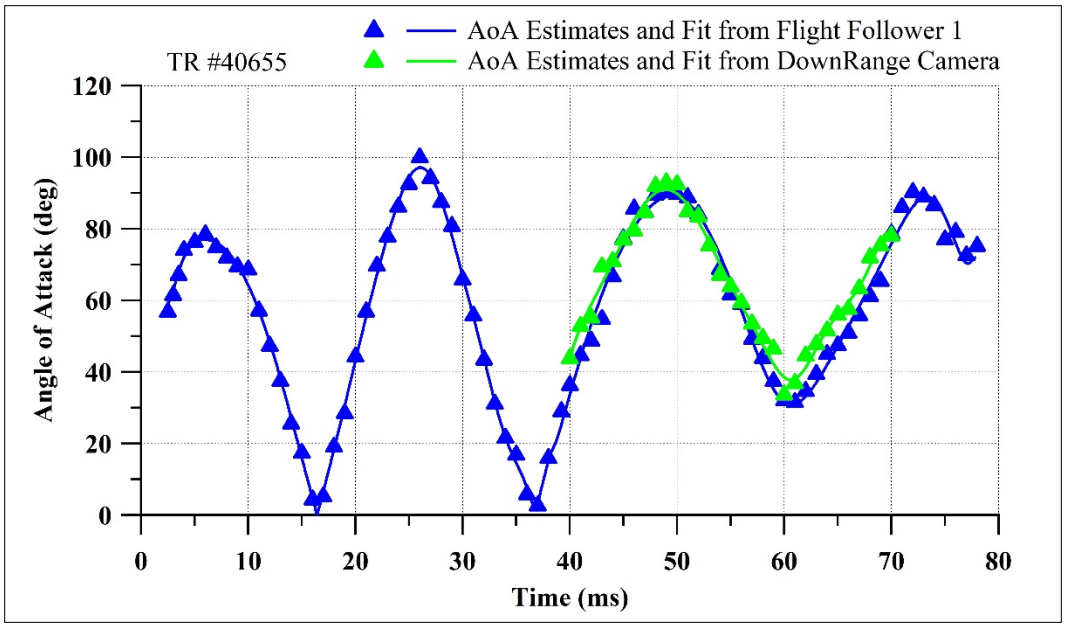

Fig. L-5 Angle of attack (AoA) vs. flight time in gun coordinates, TR 40655

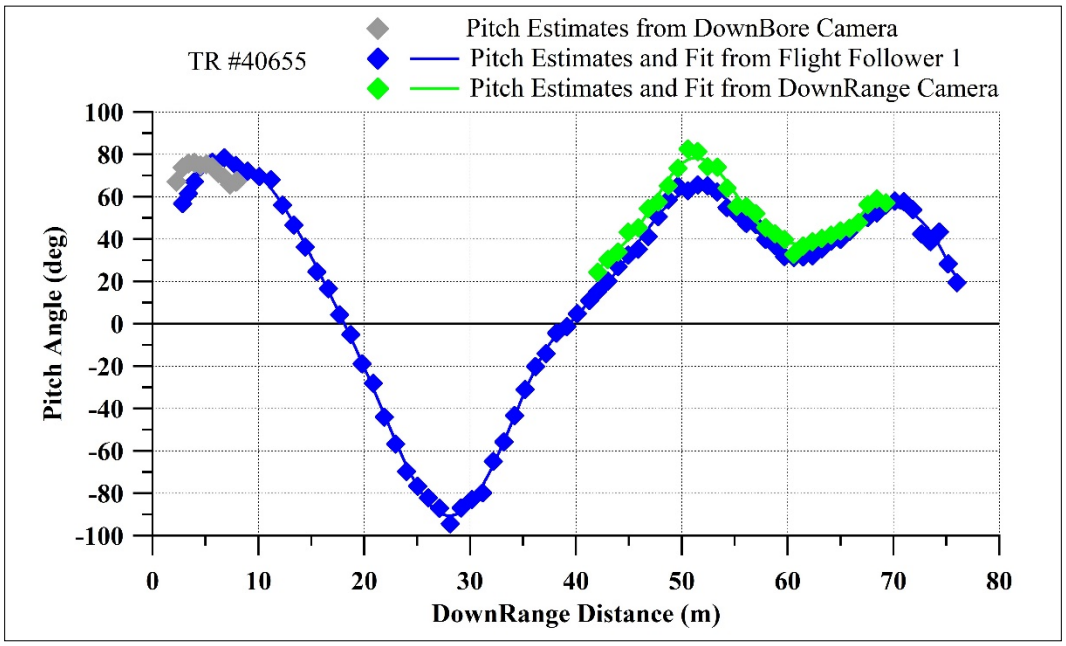

Fig. L-6 Pitch angle vs. downrange distance in gun coordinates, TR 40655

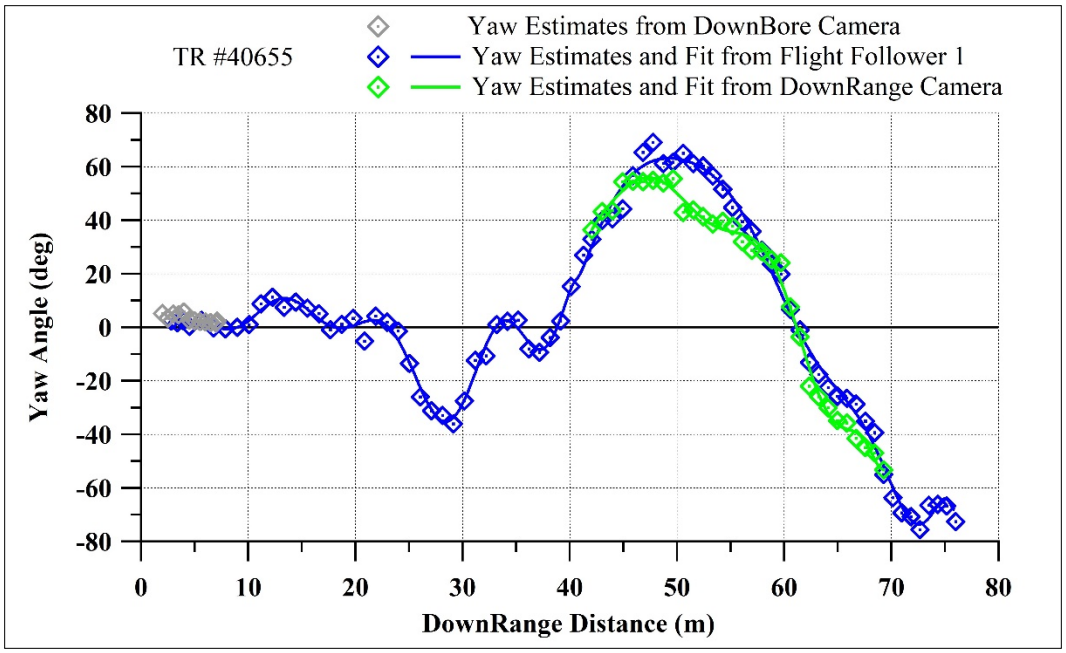

Fig. L-7 Yaw angle vs. downrange distance in gun coordinates, TR 40655

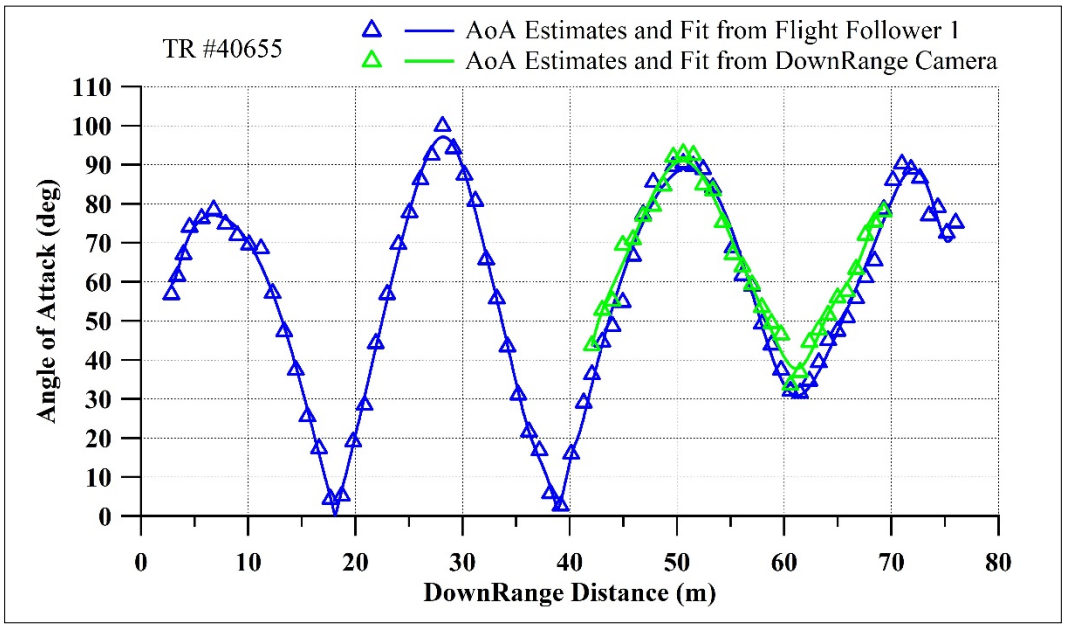

Fig. L-8 AoA vs. downrange distance in gun coordinates, TR 40655

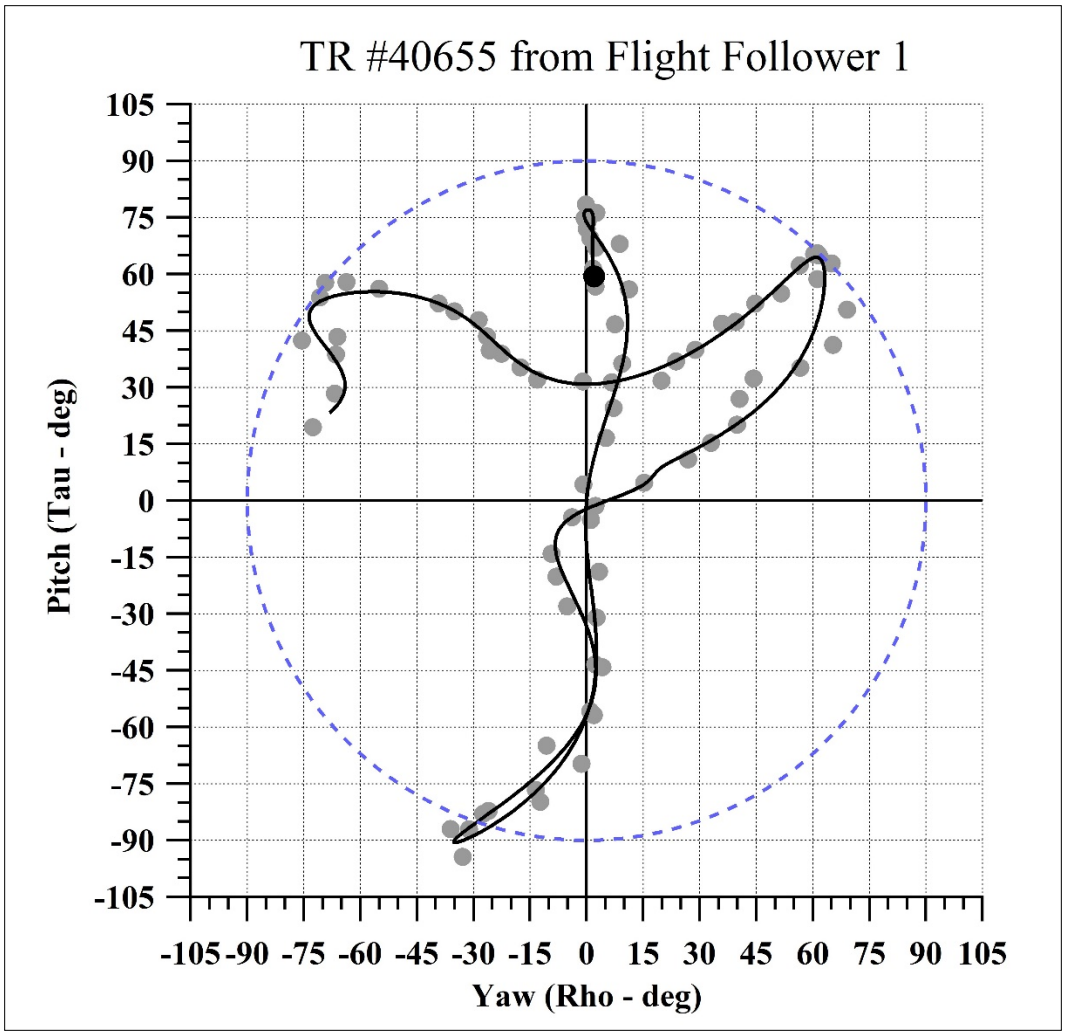

Fig. L-9 Pitch vs. yaw, TR 40655

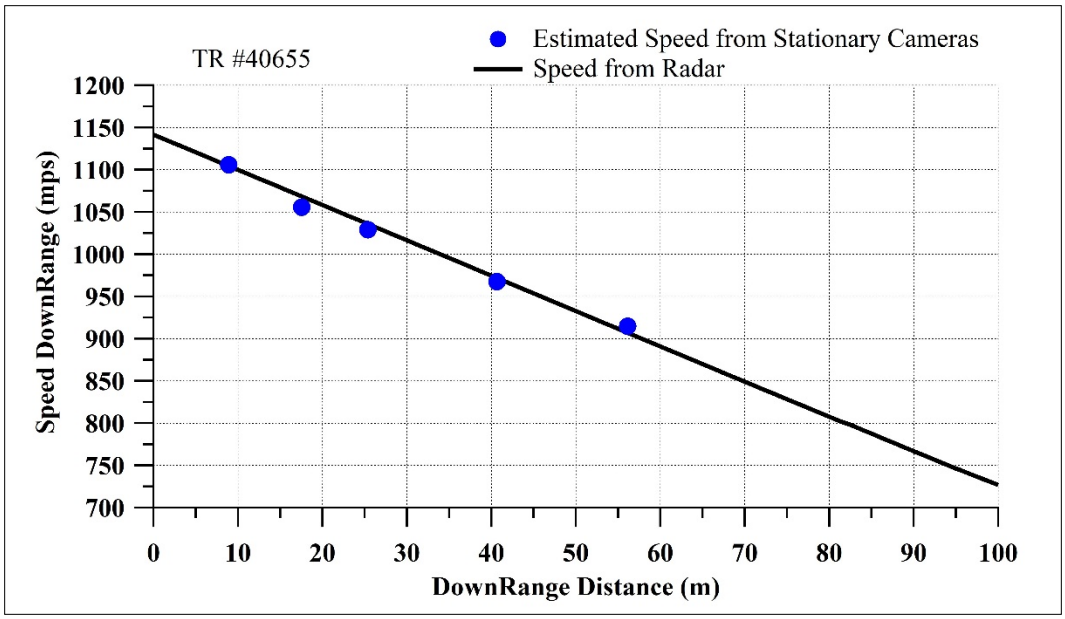

Fig. L-10 CobraMRV speed from video and radar vs. downrange distance, TR 40655

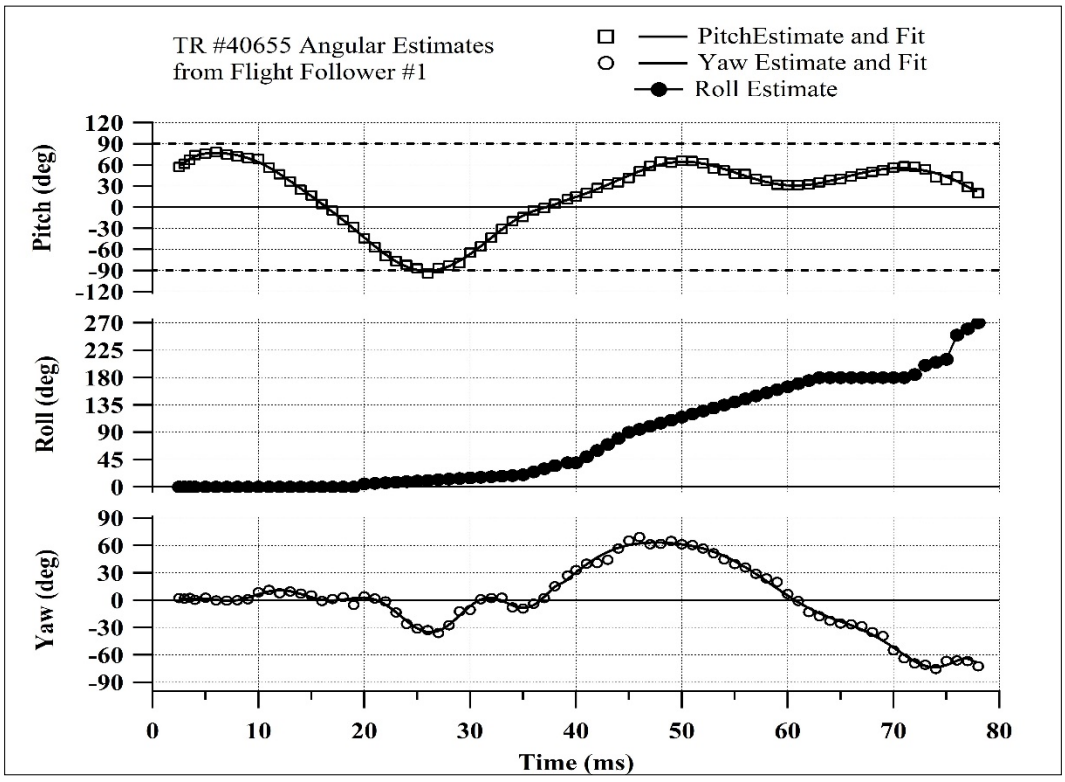

Fig. L-11 Pitch, yaw, and roll angle estimates from Flight Follower 1 vs. flight time in gun coordinates, TR 40655

Appendix M. Results: Tube Round (TR) 40656

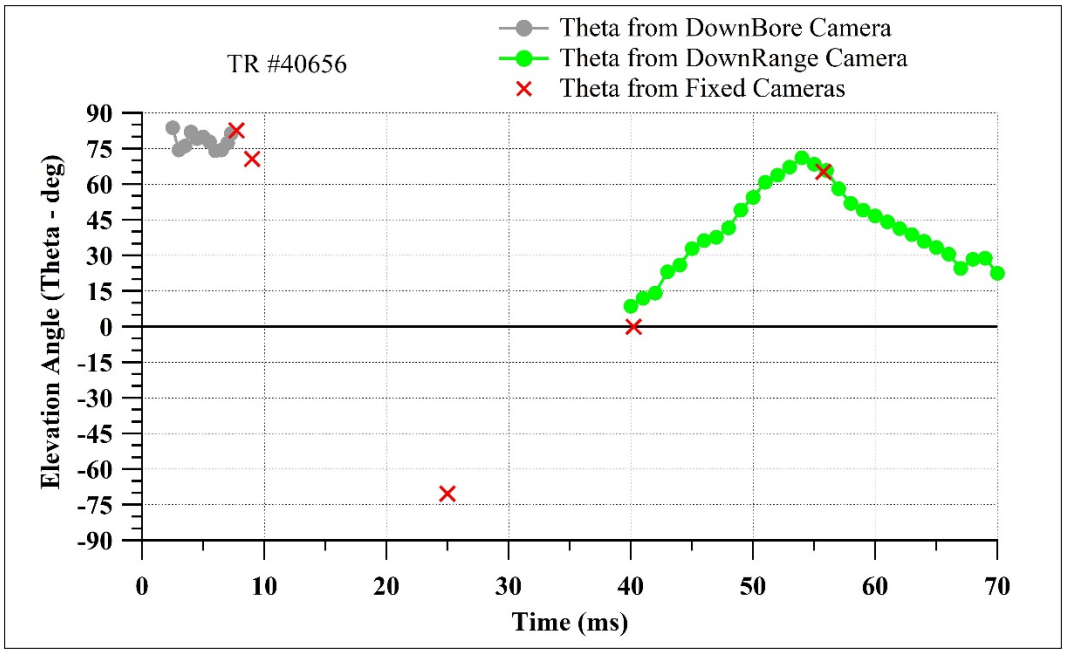

Fig. M-1 Elevation angle vs. flight time in gun coordinates, TR 40656

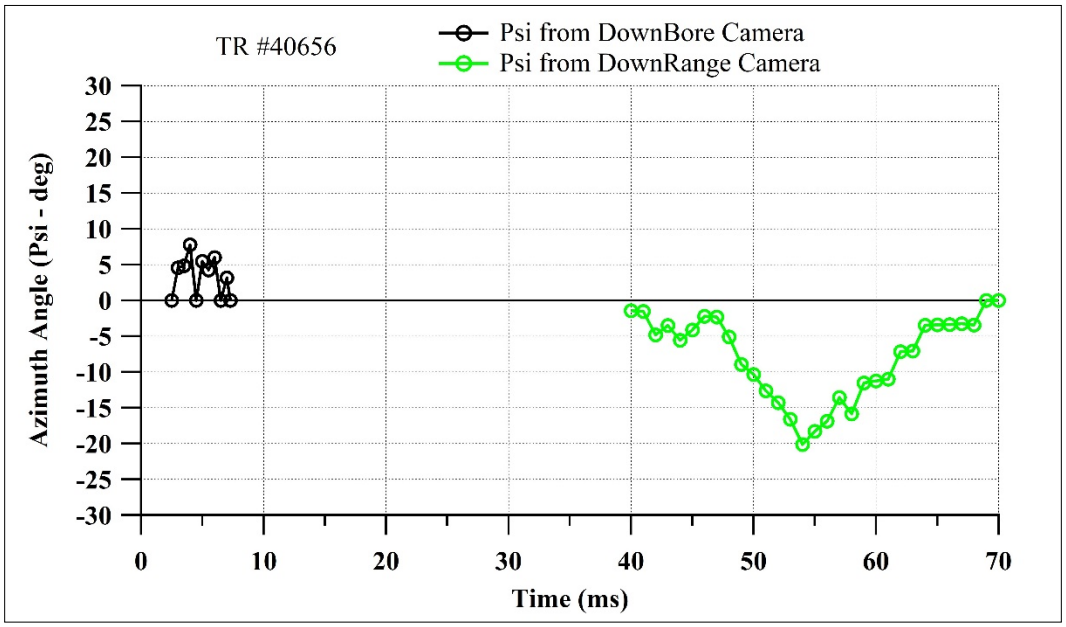

Fig. M-2 Azimuth angle vs. flight time in gun coordinates, TR 40656

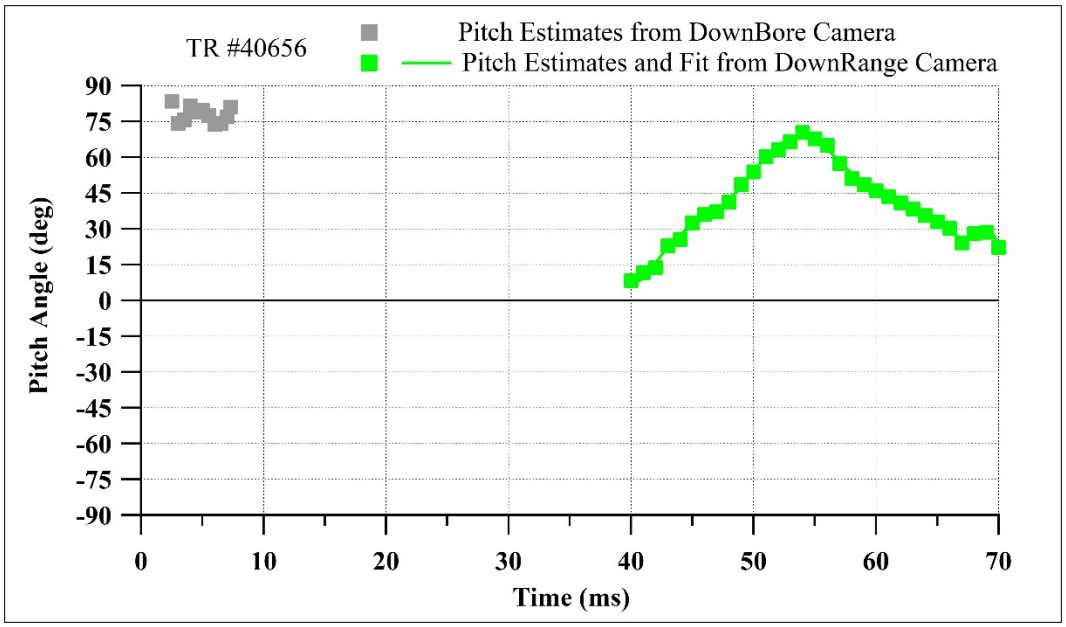

Fig. M-3 Pitch angle vs. flight time in gun coordinates, TR 40656

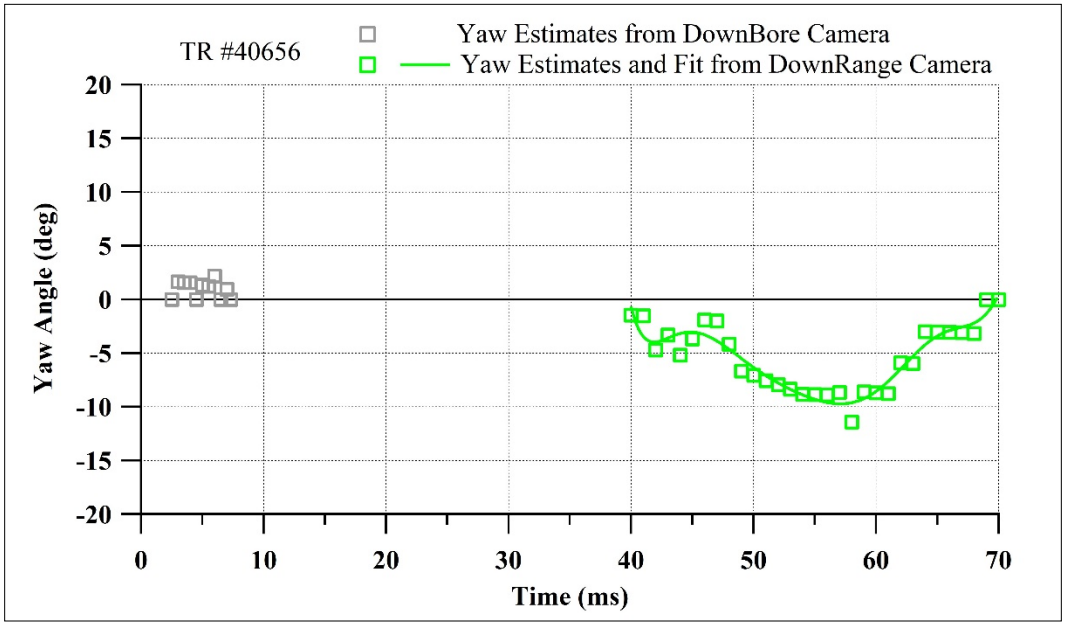

Fig. M-4 Yaw angle vs. flight time in gun coordinates, TR 40656

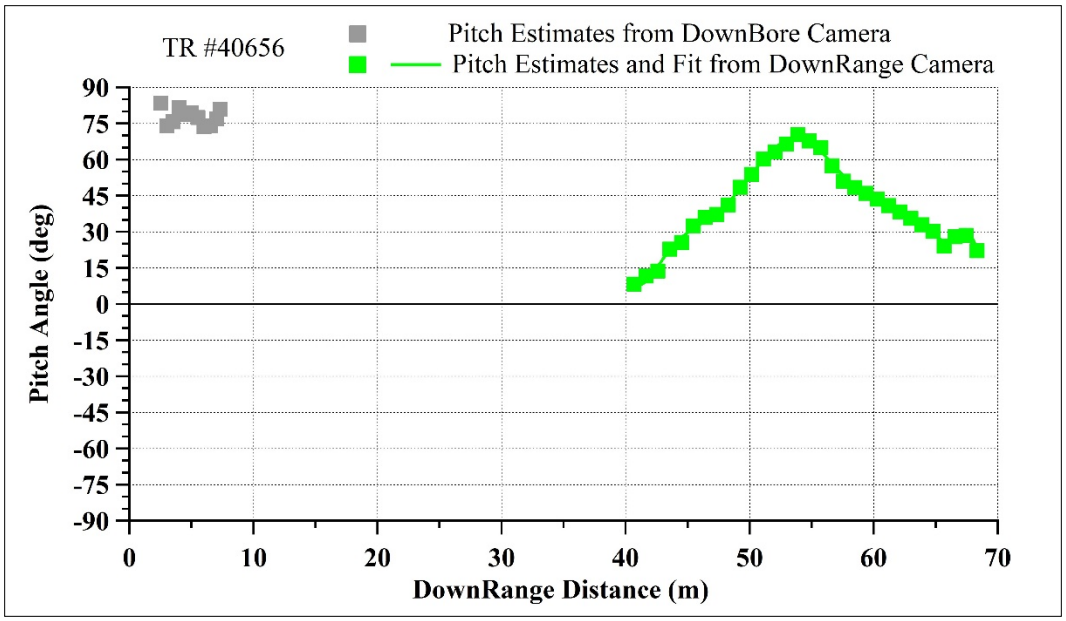

Fig. M-5 Pitch angle vs. downrange distance in gun coordinates, TR 40656

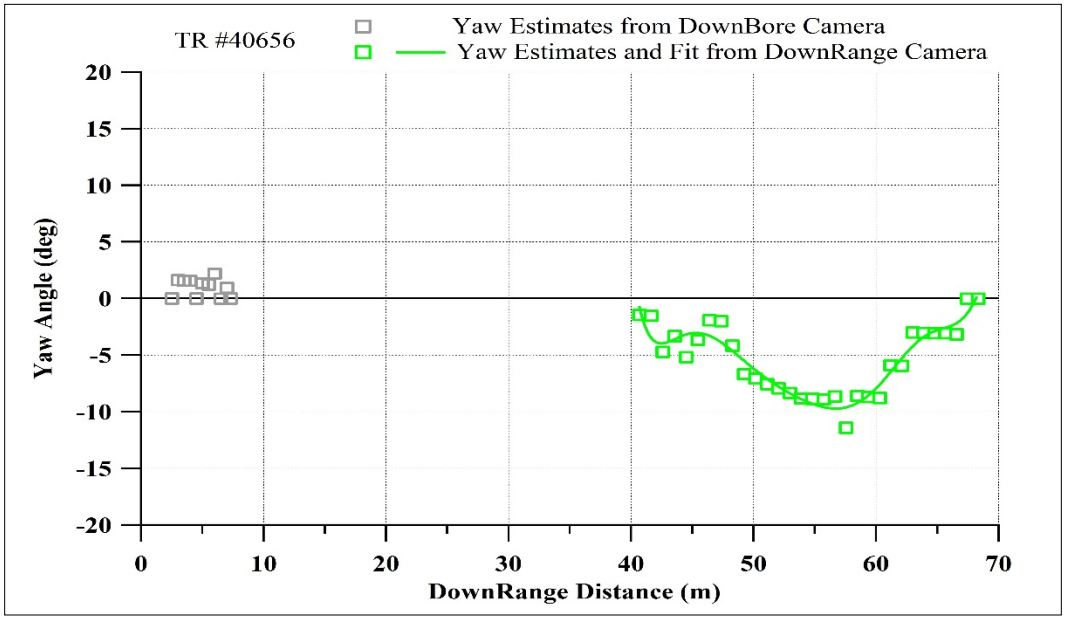

Fig. M-6 Yaw angle vs. downrange distance in gun coordinates, TR 40656

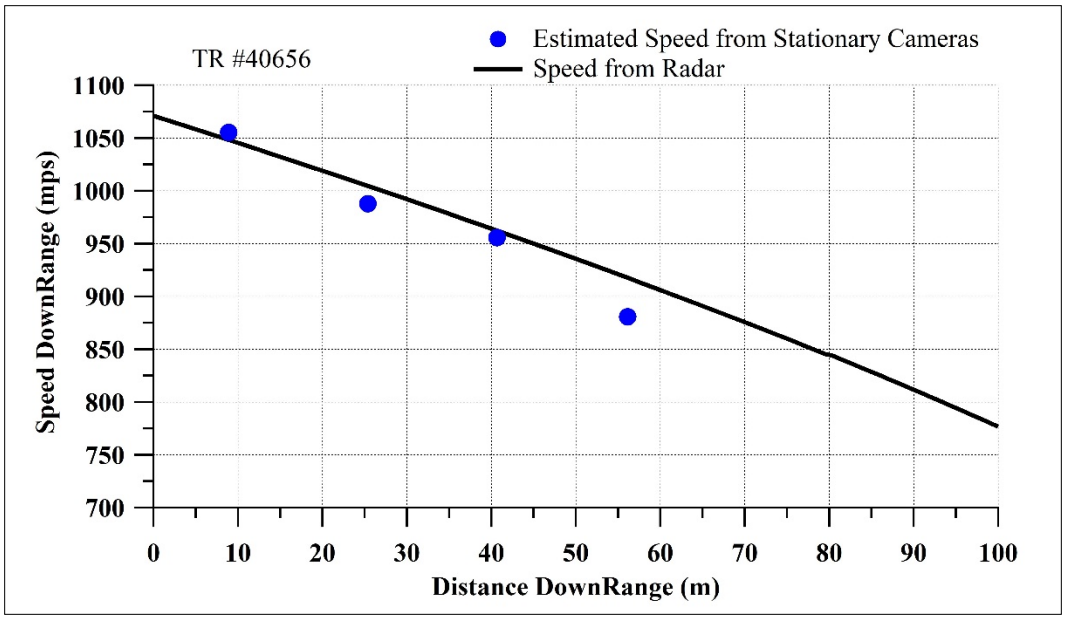

Fig. M-7 CobraMRV speed from video and radar vs. downrange distance, TR 40656

List of Symbols, Abbreviations, and Acronyms

2-D	two-dimensional
3-D	three-dimensional
Al	aluminum
AoA	angle of attack
APG	Aberdeen Proving Ground
ARL	Army Research Laboratory
ATC	Aberdeen Test Center
CCDC	US Army Combat Capabilities Development Command
CG	center of gravity
COBRA	Co-Optimization Bluntbody Re-entry Analysis
DB	downbore
DR	downrange
EDL	entry, descent, and landing
FC	fixed camera
FE	flight experiment
FEA	finite element analysis
FF	flight follower
FOV	field of view
IRIG	inter-range instrumentation group
LOS	line of sight
MOI	moment of inertia
MRV	Mid-Lift-to-Drag Rigid Vehicle
NASA	National Aeronautics and Space Administration
RMS	root mean square
Ti	titanium
TR	tube round

1 (PDF) DEFENSE TECHNICAL INFORMATION CTR DTIC OCA

1 (PDF) DEVCOM ARL FCDD RLD CL TECH LIB

26 (PDF) DEVCOM ARL FCDD RLW W T SHEPPARD W OBERLE P PEREGINO F FRESCONI FCDD RLW WD I CELMANS J DESPIRITO C MERMAGEN E MILLER L STROHM J VASILE FCDD RLW WE T G BROWN T HARKINS M IL B TOPPER B DAVIS D EVERSON J MALEY M DON E BUKOWSKI J CONDON D PETRICK D EVERSON N BRYANT M GRABNER O ROE J CONDON

1 (PDF) DEVCOM AC FCDD ACM AA R DECKER

3 (PDF) NASA JOHNSON R SOSTARIC B JOHNSON J DOLL

2 (PDF) NASA AMES J GARCIA B NIKAIDO